

Impact of modulation instability on distributed optical fiber sensors

THÈSE N° 7007 (2016)

PRÉSENTÉE LE 11 MAI 2016

À LA FACULTÉ DES SCIENCES ET TECHNIQUES DE L'INGÉNIEUR

GROUPE SCI STI LT

PROGRAMME DOCTORAL EN PHOTONIQUE

ÉCOLE POLYTECHNIQUE FÉDÉRALE DE LAUSANNE

POUR L'OBTENTION DU GRADE DE DOCTEUR ÈS SCIENCES

PAR

Mohammad Mehdi ALEM KARLADANI

acceptée sur proposition du jury:

Prof. S. Roke, présidente du jury
Prof. L. Thévenaz, directeur de thèse
Prof. H. Maillotte, rapporteur
Prof. S. Wabnitz, rapporteur
Prof. C.-S. Brès, rapporteuse



ÉCOLE POLYTECHNIQUE
FÉDÉRALE DE LAUSANNE

Suisse
2016

I hide my tears when I say your name,
But the pain in my heart is still the same.

In loving memory of Mom and Aunty...



Acknowledgements

Throughout these years as a doctoral student in Switzerland I had the great privilege of learning new things, sharing knowledge and experiencing delightful moments with wonderful people to whom my sincere gratitude goes forever.

First and foremost of all, I would like to express my warmest gratitude to my supervisor, Prof. Luc Thévenaz, for sharing his knowledge and experience with me and for providing a warm and stimulating environment in which I could learn and progress.

I thank my former and current colleagues in the Group for Fibre Optics at EPFL for sharing their time and thoughts with me discussing about life and science. In particular, I would like to thank our postdoctoral fellows Marcelo Soto and Kenny Hey Tow and our doctoral assistants, Nikolay Primerov, Isabelle Dicaire, Andrey Denisov, Xin Lu, Desmond Chow and Flavian Gyger and our master students, Simon Zaslawski and Konrad Rolle.

I am also grateful to the former and current administrative assistants of our group and the EPFL doctoral program in photonics, Alexandra Morrison, Svetlana Mashkina, Cathy Buchs and Pierrette Paulou-Vaucher for kindly helping me through all the paperwork.

I would like to thank the committee members of my doctoral exam for having accepted to assess my thesis and taking the time to read it through: Prof. Hervé Maillotte, Prof. Stefan Wabnitz and Prof. Camille-Sophie Brès. I would also like to thank Prof. Sylvie Roke for being the president of the thesis jury.

I am extremely grateful to my lovely friends who made my stay in Switzerland pleasant and unforgettable: Fatemeh Alishahi, Kamran Kalbasi, Hamed Izadi, Soonaz Malakzadeh, Armand Vedadi, Farhang Javaherian, Khashayar Mehrany, Mahmoud Jazayerifar, Mahdi Mashayekhi and Amin Shoaie. My special thanks go to Kamran for all the moments we have shared in our endless and thoughtful discussions. I would also like to thank my music teacher Sogol Mirzaei for being patient with me and giving positive encouragement.

Finally, I am deeply indebted to my family, especially my parents, Bahman and late Fatemeh, for the unconditional love and support they have given to me throughout my life. I am also most grateful to my dear brothers, Behrouz, Abbas, and Amin and my lovely sisters-in-law Elham and Negar for having always been supportive in difficult times. Many thanks also go to my brotherly cousins, Ali and Erfan, that in spite of a long distance have always been with me. I finish with expressing my deep affection for my sweet nephew, Sepehr, whose cuteness reminds me of good memories of the past.

Lausanne, April 2016
Mehdi Alem

Abstract

Modulation instability as the main limit to the sensing distance of distributed fiber sensors is thoroughly investigated in this thesis in order to obtain a model for predicting its characteristics and alleviating its effects. Starting from Maxwell's equations in optical fibers, the nonlinear Schrödinger equation describing the propagation of wave envelope in nonlinear dispersive media is derived. As the main tool for analyzing modulation instability, the nonlinear Schrödinger equation is numerically evaluated using the split-step Fourier method and its analytical closed-form solutions such as solitons are utilized to validate the numerical algorithms. As the direct consequence of the nonlinear Schrödinger equation, self-phase modulation is utilized to measure the nonlinear coefficient of optical fibers via a self-aligned interferometer.

The modulation instability gain is obtained by applying a linear stability analysis to the nonlinear Schrödinger equation assuming a white background noise as the seeding for the nonlinear interaction. The gain spectrum of modulation instability is expressed by hyperbolic functions for lossless fibers and by Bessel functions with complex orders for fibers with attenuation. An approximate gain spectrum is presented for lossy fibers based on the gain in lossless optical fibers. The accuracy of the analytical results and approximate formulas is evaluated by performing Monte Carlo simulations on the nonlinear Schrödinger equation. Moreover, the gain spectrum of modulation instability in several optical fibers of different types and lengths are experimentally observed to demonstrate its expected characteristics such as symmetric spectral sidebands, higher-order modulation instability, and power-dependence bandwidth.

The impact of background noise on the onset and evolution of modulation instability is analytically investigated and experimentally demonstrated. Power depletion due to the nonlinear process of modulation instability is modeled by integrating its gain spectrum using Laplace's method. Based on the depletion power, a critical power for modulation instability is proposed by introducing the notion of depletion ratio. The model is verified by numerical simulation and experimental measurement. An optimal input power for the distributed fiber sensors is proposed to maximize the output optical power and thus, the far end signal-to-noise ratio. The corresponding depleted power and maximal output power are derived analytically using optimization. Furthermore, the recurrence phenomenon of Fermi-Pasta-

Ulam is experimentally observed and numerically simulated, proving the accuracy of the numerical techniques employed in this dissertation.

A standard Brillouin optical time-domain analyser serves as the experimental test bench for the proposed model. As the physical phenomenon behind the experiment, stimulated Brillouin scattering is described based on a pump-probe interaction mechanism through an acoustic wave. A 25 km standard single-mode fiber is employed as a nonlinear medium with anomalous dispersion at the pump wavelength 1550 nm. The evolution of pump power propagating along the fiber is mapped using the Brillouin interaction with the probe lightwave. The measured longitudinal power traces are processed to extract the impact of modulation instability on the pump power.

It is experimentally demonstrated that distributed fiber sensors with orthogonally-polarized pumps at different wavelengths suffer less from modulation instability. As the scalar modulation instability of each pump reduces, vector modulation instability occurs because of interaction between the pumps; however, the overall performance improves. A version of the coupled nonlinear Schrödinger equations known as the Manakov system is shown to describe the behavior of two-pump distributed fiber sensors employing standard optical fibers with random birefringence. The excellent agreement between the experimental measurement and numerical simulation indicates that the performance limit of two-pump distributed fiber sensors with orthogonal polarizations is determined by polarization modulation instability.

Keywords: *nonlinear fiber optics, nonlinear Schrödinger equation, distributed fiber sensors, Kerr effect, modulation instability, stimulated Brillouin scattering, vector modulation instability, Manakov system, dispersion, polarization, parametric process, split-step Fourier method, gain spectrum, white noise.*

Résumé

L'instabilité de modulation, en tant que limite majeure à la portée des capteurs répartis à fibre optique, est traitée de façon approfondie dans cette thèse, dans le but d'obtenir un modèle prédisant ses caractéristiques et permettant d'en minimiser les effets. En partant des équations de Maxwell adaptées au cas de la fibre optique, l'équation de Schrödinger non linéaire en est déduite, qui décrit la propagation de l'enveloppe des ondes dans les milieux non linéaires dispersifs. Elle est résolue de manière numérique en utilisant la méthode de Fourier à pas fractionnaires (« split-step »), qui tient le rôle de principal outil d'analyse de l'instabilité de modulation. Les solutions analytiques de l'équation de Schrödinger non linéaire, telles que les solitons, sont utilisées pour valider les algorithmes numériques. Puis, l'auto-modulation de phase, conséquence naturelle de cette équation, est exploitée par l'intermédiaire d'un interféromètre auto-aligné, afin de mesurer le coefficient non linéaire des fibres optiques utilisées.

Le gain de l'instabilité de modulation est obtenu en effectuant une analyse de stabilité linéaire de l'équation de Schrödinger non linéaire, un bruit de fond blanc étant considéré comme initiateur de l'interaction non linéaire. Pour des fibres sans pertes, le spectre de gain de l'instabilité de modulation s'exprime à l'aide de fonctions hyperboliques, tandis que pour les fibres avec atténuation, il sera représenté par des fonctions de Bessel d'ordre complexe. Un spectre de gain approximatif est déduit pour des fibres avec atténuation, basé sur la solution obtenue dans des fibres optiques supposées sans perte. La précision des résultats analytiques et des expressions approximées est évaluée à l'aide de simulations de type Monte Carlo sur l'équation de Schrödinger non linéaire. De plus, les spectres de gain de l'instabilité de modulation ont pu être mesurés expérimentalement sur plusieurs types de fibres optiques de longueurs différentes, afin de mettre en évidence les caractéristiques prédites, telles que des bandes latérales spectralement symétriques, de l'instabilité de modulation d'ordre supérieur et une dépendance de la bande passante envers la puissance optique.

L'impact du bruit de fond sur la naissance et l'évolution de l'instabilité de modulation est analytiquement étudié et démontré expérimentalement. L'amenuisement de la puissance optique, comme conséquence du processus non linéaire d'instabilité de modulation, est modélisé en évaluant l'intégrale du spectre de gain par le biais de la méthode de Laplace. En se basant sur cette érosion de l'intensité de l'onde, une puissance critique pour l'instabilité

de modulation est proposée, en introduisant la notion de taux d'érosion. Ce modèle est validé par simulation numérique, ainsi que par des mesures expérimentales. Une puissance d'entrée optimale pour les capteurs à fibre optique répartis est proposée, afin de maximiser la puissance optique en sortie et, par conséquent, le rapport signal-sur-bruit en sortie de fibre. La puissance perdue par transfert spectral et la puissance maximale de sortie sont dérivées de façon analytique par optimisation. Par ailleurs, le phénomène de récurrence de Fermi-Pasta-Ulam est observé expérimentalement et simulé numériquement, ce qui fournit une preuve de l'exactitude des techniques numériques employées dans ce travail de thèse.

Un capteur réparti, basé sur la diffusion Brillouin et sur un schéma standard de temps de vol d'une impulsion, sert de banc d'essai expérimental pour le modèle proposé. En tant que phénomène physique à la base de l'expérience, la diffusion Brillouin stimulée est décrite comme un mécanisme d'interaction entre une pompe et une sonde par l'intermédiaire d'une onde acoustique. Une fibre unimodale standard, d'une longueur de 25 km, est utilisée comme milieu non linéaire et possède une dispersion anormale à la longueur d'onde de la pompe, soit 1550 nm. Une représentation de l'évolution de la puissance de pompe lors de sa propagation le long de la fibre est obtenue grâce à l'interaction Brillouin avec le signal continu de la sonde. Les graphes de la puissance en fonction de la distance sont analysés pour en extraire l'impact de l'instabilité de modulation sur la puissance de la pompe.

Au vu des expériences, il a pu être prouvé que les capteurs répartis sont plus robustes face à l'instabilité de modulation, si on utilise deux pompes à des longueurs d'onde distinctes et polarisées orthogonalement. L'instabilité de modulation scalaire de chaque pompe diminue, tandis qu'apparaît l'instabilité de modulation vectorielle due à l'interaction croisée entre les deux signaux de pompes. Une version des équations de Schrödinger non linéaires couplées, aussi connue sous la dénomination de système de Manakov, est utilisée pour décrire le comportement des capteurs à fibre répartis, à deux pompes et utilisant des fibres optiques standard avec une faible biréfringence aléatoire. L'excellent accord entre mesures et simulations numériques indique que la limite de performance, pour des capteurs répartis à deux pompes polarisées orthogonalement, est majoritairement dictée par l'instabilité de modulation vectorielle.

Mots-clés : *optique non linéaire, équation de Schrödinger non linéaire, capteurs à fibre optique répartis, effet Kerr, instabilité de modulation, diffusion Brillouin stimulée, instabilité de modulation vectorielle, système de Manakov, dispersion, polarisation, processus paramétrique, méthode de Fourier à pas fractionnaires, spectre de gain, bruit blanc.*

Contents

Acknowledgements	i
Abstract	iii
Résumé	v
Introduction	1
1 Preliminaries	5
1.1 Maxwell's Equations	5
1.1.1 Poynting's Theorem	6
1.1.2 Boundary Conditions	7
1.1.3 Electromagnetic Potentials	8
1.2 Constitutive Relations	9
1.2.1 Linear Response	11
1.2.2 Kramers–Kronig relations	12
1.3 Monochromatic Waves	14
1.3.1 Uniform Plane Waves	15
1.4 Wave Propagation in Optical Fibers	16
1.4.1 Cylindrical Wave Equation	19
1.4.2 Fundamental Mode	21
1.5 Nonlinear Fiber Optics	24
1.5.1 Kerr Effect	26
2 Nonlinear Schrödinger Equation	27
2.1 Nonlinear Wave Equation	27
2.1.1 Slowly Varying Envelope	29
2.1.2 Normalization of the NLSE	31
2.2 Solutions for the NLSE	32
2.2.1 Propagation in Linear and Dispersive Media	34
2.2.2 Propagation in Nonlinear and Nondispersive Media	35
2.2.3 Propagation in Nonlinear and Dispersive Media	38
2.3 Split-Step Fourier Method	40
2.4 SPM-Based Measurement of Nonlinear Coefficient	42

Contents

2.4.1	Mathematical Analysis of the Self-Aligned Interferometer	44
2.4.2	Experimental Results	46
3	Modulation Instability Gain	49
3.1	Dispersion Coefficients	49
3.1.1	Phase Matching in FWM	50
3.1.2	Phase Matching in Degenerate FWM	51
3.2	Linear Stability Analysis	52
3.2.1	Lossless Fibers	54
3.2.2	Optical Parametric Amplification	55
3.2.3	Modulation Instability Gain	57
3.3	Modulation Instability in Lossy Fibers	58
3.4	MI Gain Spectrum	63
3.5	Experimental Observation of MI Spectrum	66
4	MI Critical and Optimal Power	71
4.1	Power Evolution	72
4.1.1	Impact of Background Noise on the MI Evolution	74
4.2	Modeling the MI Critical Power	75
4.2.1	Optimal Input and Maximal Output Power	81
4.3	Brillouin Optical Time Domain Analysis	84
4.3.1	Pump-Probe Interaction in Stimulated Brillouin Scattering	85
4.3.2	Validating Experimental Setup	89
4.4	Experimental Validation of the Model	92
5	Polarization Modulation Instability	97
5.1	Manakov System	98
5.1.1	Mathematical Derivation of the Manakov System	99
5.1.2	Numerical Simulation of the Manakov System	101
5.2	BOTDA with Orthogonally Polarized Pumps	104
5.2.1	Experimental Setup of Two-Pump BOTDA	105
5.2.2	Comparison of the Model and Measurements	106
	Conclusions	109
	A White Noise	111
	B Laplace's Method	113
	Bibliography	124
	Curriculum Vitae	125

Introduction

Distributed Fiber Sensors

Facilities and structures such as buildings, bridges, dams, pipelines, etc. are continuously subject to stresses, strains and temperature variations that produce flaws. Tiny cracks that may appear due to heavy loads or temperature differences, over times will lead to failure. Manual checks are time-consuming and can cover only the easy-to-see parts of structures while most of damages start from inside and grow invisibly. Since the standard optical fibers used in telecom are sensitive to environmental factors like strain and temperature, structural health monitoring (SHM) can take the advantage of existing optical communication networks to establish a *distributed* sensing system for inspecting the health conditions of structures [1].

Changes in environment induce tiny alteration in optical fiber characteristics resulting in the scattering of light propagating in the fiber. Three optical scattering phenomena most often used in optical fiber sensors are Rayleigh, Raman and Brillouin scattering. Rayleigh scattering causes light to scatter elastically in all directions due to the sub-wavelength variations of refractive index [2]. Raman scattering is an inelastic process in which light is scattered by thermally activated molecular vibrations [3]. Brillouin scattering is due to the interaction between light waves and thermal sound waves causing a frequency shift in light [4]. Based on each scattering process, several implementations for distributed fiber sensors have been proposed among which, Raman-based distributed temperature sensing (DTS) [5], Brillouin optical time-domain analysis (BOTDA) [6], and Rayleigh-based phase-sensitive optical time-domain reflectometry (ϕ OTDR) [7] are most utilized depending upon applications.

The huge amount of research having been carried out in the past three decades has focused on two main paths: increasing the sensing distance and enhancing the spatial resolution. In order to achieve further distance, it is required to launch high power lightwave into the sensing fiber to compensate the fiber loss for obtaining a sufficient signal-to-noise ratio (SNR) at the most remote sensing point. However, increasing optical power gives rise to undesired nonlinear phenomena resulting in measurement distortion. The main source of distortion in distributed fiber sensors is the depletion of optical power [8] due to the nonlinear effects such as modulation instability (MI) [9] and stimulated Raman scattering (SRS) [10]. The exciting power of modulation instability has been shown experimentally to be less than that of stimulated Raman scattering [10]. Modulation instability also induces a visibility reduction in

ϕ OTDR, leading to loss of sensitivity at certain sensing positions [11]. Furthermore, in Brillouin optical time-domain reflectometry (BOTDR), MI contaminates the detected signal imposing an upward offset in the measured Brillouin frequency shift (BFS) that biases the extracted temperature or strain along the fiber [12]. Therefore, it can be stated with all confidence that modulation instability has the most detrimental impact on the performance of distributed fiber sensors. Hence, this work is meant to cope with modulation instability in optical fibers.

Modulation Instability

Observation of nonlinear phenomena in optical fibers is conveniently possible thanks to the high energy confinement, long-range guidance and low attenuation of optical fibers [3]. Among these nonlinear effects, modulation instability fundamentally covers a broad range of applications, from producing soliton pulses [13] to supercontinuum generation [14], while imposing a limitation on other applications such as coherent transmission systems [15] and coherent detection processes [16], because it alters the spectrum of lightwave dramatically.

Modulation instability is the break-up of an intense optical wave traveling in a nonlinear dispersive waveguide to a train of soliton-like pulses originating from residual minute modulations caused by intensity fluctuations [17]. MI in optical fibers has been treated theoretically by Hasegawa and Brinkman [18] and was experimentally observed for the first time in 1985 by Tai, Hasegawa, and Tomita using a mode-locked pulse laser [19]. Later in 1989, modulation instability of a continuous-wave (CW) laser was observed by Itoh, Davis, and Sudo [20]. In the frequency domain, MI generates two symmetric spectral sidebands around the laser central wavelength, resulting in a power exchange between the central frequency and the spectral components of the sidelobes as light propagates along the fiber [19].

Because of the cross-phase modulation (XPM) between two wavelengths [21, 22] or two polarization modes in high-birefringence (Hi-Bi) fibers [23, 24], modulation instability can occur in optical fibers having normal dispersion. Nonetheless, it is widely accepted that for a monochromatic light, no MI occurs in normal dispersion [3]. On the contrary, anomalous dispersion along with self-phase modulation (SPM) causes instability for optical waves in a relatively broad spectral band around the light central wavelength [19]. Hence, standard optical fibers having anomalous dispersion in the telecommunication window at 1550 nm are subject to modulation instability and thus, the performance of a broad range of fiber-optic systems, such as optical communication systems, optical signal processing methods, or distributed fiber sensors can be degraded by the distortion induced by modulation instability.

Although non-zero dispersion shifted fibers (DSF) with normal dispersion can be used to avoid modulation instability, most of existing fiber networks utilize standard single-mode fibers (SMF) and replacing them by DSFs requires a huge investment. It must be also noted that using DSFs can enhance other nonlinear phenomena such as four-wave mixing (FWM), because of lower dispersion favoring phase matching when compared to standard SMFs [3]. Therefore, modulation instability is unavoidable in most of the existing fiber-optics systems and thus, it must be dealt with properly from both experimental and analytical perspectives.

MI can be theoretically approached either by analysing a FWM framework [25] or by solving the nonlinear Schrödinger equation (NLSE) [26], which are essentially equivalent. The

Akhmediev breather formalism provides exact analytical solutions for the NLSE, describing the temporal evolution of optical pulses propagating in a dispersive Kerr medium [27, 28]. This formalism addresses the issues of pump depletion [29] and recurrence phenomenon [30] and can be effectively used to explain solitons and rogue waves in fiber optics [30, 31]. However, the analytical solution does not include the attenuation and another approach to the NLSE must be taken for dissipative systems. The method of linear stability analysis is the tool that can be efficiently utilized to analyze the nonlinear Schrödinger equation [18]. In this technique, a small perturbation modulates the stationary solution of the NLSE, and its evolution along the fiber is determined by linearizing the nonlinear equation [3, 32]. This resulted close-form solution also includes the effect of fiber attenuation. Such a solution of the NLSE is especially appropriate for conditions in which there are no multiple optical tones interacting coherently together [33], as it is the case of having only noise-seeded modulation instability; hence the linear stability analysis of the NLSE is considered as the approach to MI in this work, because distributed fiber sensors mainly use single-wavelength optical pulses.

There have been few attempts to obtain a critical power for modulation instability, limited to special conditions such as specific pulse shapes [34, 35] or noise characteristics [10]. An analytical formula is given in [36] for the critical length corresponding to the distance at which pump depletion is maximal. The result has been improved using the Akhmediev breather formalism in [28]. However, their analysis is focused on the interaction between coherent tones and not on the noise covering the whole MI spectrum. Therefore, a more general analysis of the critical power for modulation instability is needed.

Thesis Objective

The aim of this dissertation is to investigate the behavior of modulation instability in fiber-optic systems theoretically and experimentally in a way that its effect on the evolution of optical power propagating in the medium can be modeled and predicted accurately. In such a model, depletion of power as the most effective consequence of modulation instability in distributed fiber sensors must be taken into account. Moreover, since the model is used for long distance optical fiber systems, attenuation cannot be ignored and so the model must deal with the fiber attenuation properly.

It must be noted that by modulation instability in distributed fiber sensors, we mean a parametric amplification starting from the background noise propagating with the optical wave. Therefore, considering all the noise spectral components interacting with the lightwave is indispensable in order to have an accurate estimation of power exchange in noise-seeded modulation instability. Additionally, the model must take an appropriate approach to the randomness inherent in the background noise.

Based on the proposed model, explicit and easy-to-use mathematical expressions are expected to be provided for characterizing the system performance. The proposed analytical formulas must also be able to provide insight for designing optical fiber systems to prevent the consequences of modulation instability. The model should also propose techniques for mitigating modulation instability in the existing fiber-optic systems which is another goal for this thesis.

Outline of the Dissertation

The present work is organised as follows:

Chapter 1 provides some preliminary background needed for understanding electromagnetic wave propagation in a medium. A particular attention is given to optical fibers as a cylindrical waveguide and their optical properties. The propagation features of the fundamental mode in optical fibers is investigated regarding the use of SMFs in this work. A glance is also cast at the nonlinear phenomena in optical fibers in general and the Kerr effect in particular.

Chapter 2 is devoted to the nonlinear Schrödinger equation as the fundamental tool for modeling the wave propagation in a nonlinear dispersive medium. Starting from Maxwell's equations in an optical fiber, we derive the NLSE describing the evolution of wave envelope experiencing dispersion and intensity-dependent refractive index. The split-step Fourier method is studied and used to solve the the nonlinear Schrödinger equation numerically. Moreover, analytical solutions of the NLSE, e.g. solitons are employed to validate the numerical algorithm. A self-aligned interferometer based on the phenomenon of self-phase modulation is utilized to measure the nonlinear coefficients of several optical fibers of different types.

Chapter 3 investigates the gain spectrum of the nonlinear phenomena originating from the Kerr effect. Applying a linear stability analysis to the nonlinear Schrödinger equation with proper initial phase conditions and noise characteristics leads to the gain formula for different scenarios such as modulation instability, optical parametric amplification (OPA); to do so, the spectral samples of white noise are proved to be uncorrelated in Appendix A. The MI gain spectrum for lossy and lossless optical fibers is analytically derived and numerically verified using the Monte Carlo simulation. Finally, modulation instability gain spectrum is experimentally observed in different kinds of optical fibers to verify its characteristics expected from theory.

Chapter 4 presents the main results of this work. First, the longitudinal evolution of optical power traveling in optical fibers is analyzed and then, the impact of background noise level on the power evolution is investigated. The depleted power due to modulation instability is calculated analytically using Laplace's method of integration described in Appendix B. A model is proposed for the critical power of modulation instability based on the notion of depletion ratio corresponding to the power transferred from the pump to the MI spectral bands. An optimal input power for an optical fiber sensor is proposed in order to maximize the output pump power and thus, to achieve the maximum SNR at the far end of the sensing fiber. A BOTDA experimental test bench is employed to verify the theoretical results. For understanding the working principles of the experiment, a thorough analysis of stimulated Brillouin scattering (SBS) is provided.

Chapter 5 deals with the impact of vector modulation instability in a recently proposed BOTDA scheme employing two optical pumps with orthogonal polarizations at different wavelengths. A theoretical model for analyzing this scheme is presented based on a version of the coupled nonlinear Schrödinger equations referred to as the Manakov system which is extensively used for optical fibers with randomly varying birefringence. The model is verified by the experimental results obtained from a BOTDA with two orthogonally-polarized pumps.

The last chapter is devoted to the conclusions.

1 Preliminaries

Nonlinear fiber optics can be seen as perturbations in the well-ordered world of linear fiber optics. Therefore, understanding nonlinear effects in optical fiber systems needs basic knowledge of ordinary fiber optics and thus electromagnetism. In this chapter, several aspects of general electromagnetic optics, indispensable for the rest of this dissertation, are briefly discussed. For further details on each subject, appropriate references are cited throughout the text.

1.1 Maxwell's Equations

Classical electrodynamics was established by the Scottish mathematical physicist James Clerk Maxwell (1831–1879) in the second half of the nineteenth century, first by publishing the seminal article “*A Dynamical Theory of the Electromagnetic Field*” in 1865 [37] and then by writing a two-volume book named “*A Treatise on Electricity and Magnetism*” in 1873 [38]. Electromagnetic fields are represented through the *Lorentz force law* explaining the force \mathbf{F} [N] experienced by an electric charge q [C] moving with velocity \mathbf{v} [$\frac{\text{m}}{\text{s}}$] as follows [39]:

$$\mathbf{F} = q\mathbf{E} + q\mathbf{v} \times \mathbf{B}, \quad (1.1)$$

where \times denotes the vector cross product and \mathbf{E} [$\frac{\text{V}}{\text{m}}$] and \mathbf{B} [$\frac{\text{Wb}}{\text{m}^2}$] are the electric and magnetic fields, respectively. In order to take field-matter interactions into account it is necessary to introduce two auxiliary vector fields \mathbf{D} [$\frac{\text{C}}{\text{m}^2}$] and \mathbf{H} [$\frac{\text{A}}{\text{m}}$] associated to the electric and magnetic fields, respectively via the following relations [39]:

$$\mathbf{D} = \epsilon_0 \mathbf{E} + \mathbf{P}, \quad (1.2a)$$

$$\mathbf{H} = \mu_0^{-1} \mathbf{B} - \mathbf{M}, \quad (1.2b)$$

where \mathbf{P} and \mathbf{M} are the *polarization* and *magnetization* fields. The vector fields \mathbf{P} and \mathbf{M} indicate the response of matter to the applied electromagnetic fields and thus depend on the material and are given via the *constitutive* relations $\mathbf{P} = \mathbf{P}(\mathbf{E}, \mathbf{B})$ and $\mathbf{M} = \mathbf{M}(\mathbf{E}, \mathbf{B})$. The vacuum *permittivity* in Eq. (1.2a) is given by $\epsilon_0 = 8.8542 \times 10^{-12} \frac{\text{F}}{\text{m}}$ and the vacuum *permeability* in Eq. (1.2b) is expressed by $\mu_0 = 4\pi \times 10^{-7} \frac{\text{H}}{\text{m}}$. It should be noted that in vacuum there is no polarization or magnetization; so the corresponding constitutive relations are $\mathbf{D} = \epsilon_0 \mathbf{E}$ and

$\mathbf{B} = \mu_0 \mathbf{H}$. The general form of *Maxwell's equations* governing the four electromagnetic vector fields \mathbf{E} , \mathbf{D} , \mathbf{H} and \mathbf{B} independent from matter are given by the following dynamical partial differential equations [39]:

$$\nabla \times \mathbf{E} = -\partial_t \mathbf{B}, \quad (1.3a)$$

$$\nabla \times \mathbf{H} = \mathbf{J} + \partial_t \mathbf{D}, \quad (1.3b)$$

$$\nabla \cdot \mathbf{D} = \rho, \quad (1.3c)$$

$$\nabla \cdot \mathbf{B} = 0, \quad (1.3d)$$

where $\partial_t = \frac{\partial}{\partial t}$ denotes the time derivative. $\nabla \times$ and $\nabla \cdot$ are the *curl* and *divergence* operators, respectively. The source of electromagnetic fields is electric charges expressed by the scalar field of electric charge density ρ [$\frac{C}{m^3}$] and the vector field of electric current density $\mathbf{J} = \rho \mathbf{v}$ [$\frac{A}{m^2}$]. The principle of electric charge conservation dictates a *continuity* equation on the electric charge and current densities as follows:

$$\nabla \cdot \mathbf{J} + \partial_t \rho = 0. \quad (1.4)$$

Each of Maxwell's equations is a mathematical expression for a physical law in electromagnetism. Eq. (1.3a) explains Faraday's law of induction; while Eq. (1.3b) is Ampère's circuital law with Maxwell's extension. Eqs. (1.3c) and (1.3d) are Gauss's laws in electricity and magnetism, respectively. Besides establishing a mathematical framework for different physical laws, Maxwell contributed fundamentally in electromagnetism by adding the so-called *displacement* current $\partial_t \mathbf{D}$ to Ampère's law in Eq. (1.3b). This term makes Maxwell's equations compatible with the principle of charge conservation given in Eq. (1.4). It can be simply seen that the continuity equation is the direct result of Eqs. (1.3b) and (1.3c). For every vector fields \mathbf{A} the vector identity $\nabla \cdot (\nabla \times \mathbf{A}) = 0$ always holds; so taking the divergence of Eq. (1.3b) and using Eq. (1.3c) result in

$$\begin{aligned} \nabla \cdot (\nabla \times \mathbf{H}) &= \nabla \cdot \mathbf{J} + \nabla \cdot (\partial_t \mathbf{D}) = \nabla \cdot \mathbf{J} + \partial_t (\nabla \cdot \mathbf{D}) \\ &= \nabla \cdot \mathbf{J} + \partial_t \rho = 0, \end{aligned} \quad (1.5)$$

which is exactly the continuity equation given in Eq. (1.4). Having modified Ampère's law by adding the displacement current, Maxwell predicted the existence of electromagnetic waves traveling at the speed of light. Nevertheless, electromagnetic waves were experimentally demonstrated by the German physicist Heinrich Hertz (1857–1894) in 1887, a few years after Maxwell's death [40].

1.1.1 Poynting's Theorem

The principle of energy conservation in electromagnetism is mathematically stated by Poynting's theorem due to the English physicist John Henry Poynting (1852–1914). The starting point for deriving the theorem is the vector identity $\nabla \cdot (\mathbf{A} \times \mathbf{B}) = \mathbf{B} \cdot (\nabla \times \mathbf{A}) - \mathbf{A} \cdot (\nabla \times \mathbf{B})$ valid for every vector fields \mathbf{A} and \mathbf{B} . Applying this vector identity to the so-called Poynting vector

$\mathbf{S} = \mathbf{E} \times \mathbf{H}$ and using Eqs. (1.3a) and (1.3b) lead to

$$\begin{aligned}\nabla \cdot \mathbf{S} &= \nabla \cdot (\mathbf{E} \times \mathbf{H}) = \mathbf{H} \cdot (\nabla \times \mathbf{E}) - \mathbf{E} \cdot (\nabla \times \mathbf{H}) = \mathbf{H} \cdot (-\partial_t \mathbf{B}) - \mathbf{E} \cdot (\mathbf{J} + \partial_t \mathbf{D}) \\ &= -(\mathbf{H} \cdot \partial_t \mathbf{B} + \mathbf{E} \cdot \partial_t \mathbf{D} + \mathbf{E} \cdot \mathbf{J}).\end{aligned}\quad (1.6)$$

So the differential form of Poynting's theorem is expressed by

$$\nabla \cdot \mathbf{S} + \mathbf{H} \cdot \partial_t \mathbf{B} + \mathbf{E} \cdot \partial_t \mathbf{D} + \mathbf{E} \cdot \mathbf{J} = 0. \quad (1.7)$$

To obtain the integral form of the theorem, Eq. (1.7) is integrated over a finite volume V surrounded in a closed surface ∂V . Thus,

$$\int_V \nabla \cdot \mathbf{S} dv + \int_V \mathbf{H} \cdot \partial_t \mathbf{B} dv + \int_V \mathbf{E} \cdot \partial_t \mathbf{D} dv + \int_V \mathbf{E} \cdot \mathbf{J} dv = 0. \quad (1.8)$$

The divergence theorem associates the volume integral to its corresponding surface integral as follows:

$$\int_V \nabla \cdot \mathbf{S} dv = \oint_{\partial V} \mathbf{S} \cdot d\mathbf{a}. \quad (1.9)$$

Substituting Eq. (1.9) in Eq. (1.8) results in the integral form of Poynting's theorem as follows:

$$-\oint_{\partial V} \mathbf{S} \cdot d\mathbf{a} = \int_V \mathbf{H} \cdot \partial_t \mathbf{B} dv + \int_V \mathbf{E} \cdot \partial_t \mathbf{D} dv + \int_V \mathbf{E} \cdot \mathbf{J} dv. \quad (1.10)$$

The Poynting vector has the unit of $\frac{W}{m^2}$ and so its magnitude represents the intensity of electromagnetic fields. The left-hand side of Eq. (1.10) explains the incident power entering the surface, while the right-hand terms show the power saved in magnetic and electric fields and also dissipated in the volume, respectively [39].

1.1.2 Boundary Conditions

Maxwell's equations in their differential forms cannot be applied to the interface of two different media due to the discontinuity of electromagnetic fields at the boundary. Applying the integral form of Maxwell's equations to the boundary of medium 1 and medium 2 provides a set of boundary conditions explaining the behaviour of electromagnetic fields at the interface of the media. Suppose that \mathbf{n}_{12} is a unit vector directing from medium 1 to medium 2; four boundary conditions corresponding to four Maxwell's equations are given below

$$\mathbf{n}_{12} \times (\mathbf{E}_2 - \mathbf{E}_1) = 0, \quad (1.11a)$$

$$\mathbf{n}_{12} \times (\mathbf{H}_2 - \mathbf{H}_1) = \mathbf{J}_s, \quad (1.11b)$$

$$\mathbf{n}_{12} \cdot (\mathbf{D}_2 - \mathbf{D}_1) = \rho_s, \quad (1.11c)$$

$$\mathbf{n}_{12} \cdot (\mathbf{B}_2 - \mathbf{B}_1) = 0, \quad (1.11d)$$

where $\rho_s [\frac{C}{m^2}]$ is the surface charge density and $\mathbf{J}_s [\frac{A}{m}]$ is the surface current density. Eq. (1.11a) guarantees the continuity of the tangential component of \mathbf{E} and Eq. (1.11d) implies that the

normal component of \mathbf{B} is continuous across the interface. Based on Eq. (1.11b) the tangential component of \mathbf{H} is continuous across the surface if no surface current exists. Moreover, If there is no surface charge on the interface, according to Eq. (1.11c) the normal component of \mathbf{D} is continuous.

1.1.3 Electromagnetic Potentials

The wave nature of electromagnetic fields can be described by attributing two potential functions, i.e. an electric scalar potential and a magnetic vector potential to the fields. These potentials satisfy the wave equation regardless of the charge and current densities. Since every vector field \mathbf{A} satisfies the identity $\nabla \cdot (\nabla \times \mathbf{A}) = 0$ and from Eq. (1.3d) we have $\nabla \cdot \mathbf{B} = 0$, the magnetic field can be expressed by $\mathbf{B} = \nabla \times \mathbf{A}$ where \mathbf{A} [$\frac{\text{Wb}}{\text{m}}$] is called magnetic vector potential. Substituting the potential representation of magnetic field in Faraday's law of induction given by Eq. (1.3a) results in

$$\nabla \times (\mathbf{E} + \partial_t \mathbf{A}) = 0. \quad (1.12)$$

On the other hand, for any scalar field ϕ the vector identity $\nabla \times (-\nabla \phi) = 0$ holds, where $\nabla \phi$ denotes the *gradient* of the scalar field ϕ . Comparing this identity with Eq. (1.12) leads to the expression $\mathbf{E} + \partial_t \mathbf{A} = -\nabla \phi$, where ϕ [V] is called electric scalar potential. This way, electromagnetic fields can be expressed in terms of the potential functions as follows:

$$\mathbf{E} = -\nabla \phi - \partial_t \mathbf{A}, \quad (1.13a)$$

$$\mathbf{B} = \nabla \times \mathbf{A}. \quad (1.13b)$$

Therefore, instead of calculating electromagnetic fields directly it is possible to calculate the scalar and vector potentials first and then by use of Eqs. (1.13a) and (1.13b) the fields can be obtained. As an example consider the free space where $\mathbf{D} = \epsilon_0 \mathbf{E}$ and $\mathbf{B} = \mu_0 \mathbf{H}$. Maxwell's equations are simplified to:

$$\nabla \times \mathbf{E} = -\partial_t \mathbf{B}, \quad (1.14a)$$

$$\nabla \times \mathbf{B} = \mu_0 \mathbf{J} + \epsilon_0 \mu_0 \partial_t \mathbf{E}, \quad (1.14b)$$

$$\nabla \cdot \mathbf{E} = \frac{\rho}{\epsilon_0}, \quad (1.14c)$$

$$\nabla \cdot \mathbf{B} = 0. \quad (1.14d)$$

Substituting Eqs. (1.14) in Eqs. (1.13) results in the following coupled equations governing the scalar and vector potentials.

$$\nabla^2 \mathbf{A} - \frac{1}{c^2} \partial_t^2 \mathbf{A} - \nabla (\nabla \cdot \mathbf{A} + \frac{1}{c^2} \partial_t \phi) = -\mu_0 \mathbf{J}, \quad (1.15a)$$

$$\nabla^2 \phi + \partial_t (\nabla \cdot \mathbf{A}) = -\frac{\rho}{\epsilon_0}, \quad (1.15b)$$

where the constant $c = \frac{1}{\sqrt{\epsilon_0 \mu_0}}$ is the speed of light in vacuum which is $299792458 \frac{\text{m}}{\text{s}}$ and is often approximated by $c \approx 3 \times 10^8 \frac{\text{m}}{\text{s}}$. The Laplacian ∇^2 is defined as $\nabla \cdot \nabla \phi$ for the scalar potential and as $\nabla(\nabla \cdot \mathbf{A}) - \nabla \times (\nabla \times \mathbf{A})$ for the vector potential. Since the divergence of the magnetic potential is arbitrary and it does not affect the fields we can set it so that Eqs. (1.15) become uncoupled. Such a condition given below is called the *Lorenz gauge* [39].

$$\nabla \cdot \mathbf{A} = -\frac{1}{c^2} \partial_t \phi \quad (1.16)$$

Applying the Lorenz gauge to Eqs. (1.15) we obtain the following set of uncoupled inhomogeneous *wave* equations for the scalar and vector potentials:

$$\nabla^2 \mathbf{A} - \frac{1}{c^2} \partial_t^2 \mathbf{A} = -\mu_0 \mathbf{J}, \quad (1.17a)$$

$$\nabla^2 \phi - \frac{1}{c^2} \partial_t^2 \phi = -\frac{\rho}{\epsilon_0}. \quad (1.17b)$$

As it is clear from Eqs. (1.17), electric and magnetic potentials have a wave nature propagating with the speed of light and are generated by charge and current densities, respectively.

1.2 Constitutive Relations

The response of matter to the electromagnetic fields is determined by the constitutive relations expressing the polarization \mathbf{P} and magnetization \mathbf{M} of the material in the presence of the electromagnetic fields \mathbf{E} and \mathbf{B} . Most of materials used in optical devices such as silica have so little magnetic properties that their magnetization can be safely neglected [41]; therefore, $\mathbf{M} = 0$ and thus $\mathbf{B} = \mu_0 \mathbf{H}$. However, the situation for the polarization density is totally different. In its general form the constitutive relation $\mathbf{P} = \mathbf{P}(\mathbf{E})$ is extremely complicated and beyond our need, so we apply several assumptions on the nature of the material to simplify the expressions. Locality, causality and time invariance of the response are widely accepted throughout the classical treatment of field matter interactions. With these assumptions the polarization density is given by

$$\mathbf{P}(\mathbf{r}, t) = \epsilon_0 \int_{-\infty}^t \chi(\mathbf{r}, t - t'; \mathbf{E}) \mathbf{E}(\mathbf{r}, t') dt', \quad (1.18)$$

where the electric susceptibility $\chi(\mathbf{r}, t; \mathbf{E})$ is the impulse response of the material to the electric field. The position vector \mathbf{r} in the argument of χ shows the inhomogeneity of the medium which is responsible for the spatial nonconformity of the material and the time parameter t represents the dynamics of the material response which shows the dispersion effect. The upper limit of the integral is set to the observation time t to guarantee the causality principle; while by assuming $\chi(\mathbf{r}, t; \mathbf{E}) = 0$ for $t < 0$, it can be extended to $+\infty$ which is assumed hereafter. In its general form χ is a function of \mathbf{E} indicating the nonlinearity of the response; however, this nonlinearity emerges when high-intensity fields are applied to the medium, so the electric

susceptibility can be expanded using the Taylor series as follows:

$$\chi(\mathbf{E}) = \sum_{n=1}^{\infty} \chi^{(n)} \mathbf{E}^{n-1} = \chi^{(1)} + \chi^{(2)} \mathbf{E} + \chi^{(3)} \mathbf{E}^2 + \dots, \quad (1.19)$$

where $\chi^{(n)}$ is an $n+1$ order tensor. Substituting Eq. (1.19) into Eq. (1.18) results in the following constitutive relation:

$$\begin{aligned} \mathbf{P}(\mathbf{r}, t) &= \varepsilon_0 \sum_{n=1}^{\infty} \int_{-\infty}^{+\infty} \chi^{(n)}(\mathbf{r}, t-t') \mathbf{E}^n(\mathbf{r}, t') dt' \\ &= \varepsilon_0 \int_{-\infty}^{+\infty} \chi^{(1)}(\mathbf{r}, t-t') \mathbf{E}(\mathbf{r}, t') dt' + \varepsilon_0 \int_{-\infty}^{+\infty} \chi^{(2)}(\mathbf{r}, t-t') \mathbf{E}^2(\mathbf{r}, t') dt' \\ &\quad + \varepsilon_0 \int_{-\infty}^{+\infty} \chi^{(3)}(\mathbf{r}, t-t') \mathbf{E}^3(\mathbf{r}, t') dt' + \dots \end{aligned} \quad (1.20)$$

The first term on the right-hand side of Eq. (1.20) is the linear response of the material while the other terms are responsible for the nonlinearities in the material response. Therefore, the polarization density can be decomposed to its linear and nonlinear parts as follows:

$$\mathbf{P} = \mathbf{P}_L + \mathbf{P}_{NL}, \quad (1.21)$$

where the linear part of the polarization field is simply given by

$$\mathbf{P}_L(\mathbf{r}, t) = \varepsilon_0 \int_{-\infty}^{+\infty} \chi^{(1)}(\mathbf{r}, t-t') \mathbf{E}(\mathbf{r}, t') dt'. \quad (1.22)$$

For the nonlinear part of the polarization density it is usually assumed that the second and the third nonlinear coefficients are dominant and the higher-order nonlinearities are negligible. Therefore, the nonlinear polarization density is expressed by

$$\mathbf{P}_{NL}(\mathbf{r}, t) = \varepsilon_0 \int_{-\infty}^{+\infty} \chi^{(2)}(\mathbf{r}, t-t') \mathbf{E}^2(\mathbf{r}, t') dt' + \varepsilon_0 \int_{-\infty}^{+\infty} \chi^{(3)}(\mathbf{r}, t-t') \mathbf{E}^3(\mathbf{r}, t') dt'. \quad (1.23)$$

Materials like fused silica used in fiber optics that have an inversion center as one of their symmetry elements are called *centrosymmetric* and they lack any even-order nonlinearities; so, $\chi^{(2n)} = 0$ and the main part of their nonlinear response is third order [2]. Denominating the first- and third-order susceptibilities as $\chi_L = \chi^{(1)}$ and $\chi_{NL} = \chi^{(3)}$, the constitutive relation can be given by

$$\mathbf{P} = \mathbf{P}_L + \mathbf{P}_{NL} = \varepsilon_0 \int_{-\infty}^{+\infty} \chi_L(\mathbf{r}, t-t') \mathbf{E}(\mathbf{r}, t') dt' + \varepsilon_0 \int_{-\infty}^{+\infty} \chi_{NL}(\mathbf{r}, t-t') \mathbf{E}^3(\mathbf{r}, t') dt'. \quad (1.24)$$

Another assumption that is pertinent, especially in standard optical fibers, is the homogeneity of medium resulting in the position independent susceptibilities, i.e. $\chi_L(\mathbf{r}, t) = \chi_L(t)$ and $\chi_{NL}(\mathbf{r}, t) = \chi_{NL}(t)$. Strictly speaking, optical fibers are not homogeneous because the core and cladding have different refractive indices. However, they are *piecewise* homogenous that means it is possible to break the medium into a few homogenous regions with clear

boundaries. Maxwell's equations are solved in each homogeneous region and then appropriate boundary conditions are applied to obtain the electromagnetic fields in the whole medium. It is worth mentioning that some media such as photonic crystal fibers must be treated as inhomogeneous media [42]. With the assumption of homogeneity Eq. (1.24) is rewritten as

$$\mathbf{P}(\mathbf{r}, t) = \mathbf{P}_L + \mathbf{P}_{NL} = \epsilon_0 \int_{-\infty}^{+\infty} \chi_L(t - t') \mathbf{E}(\mathbf{r}, t') dt' + \epsilon_0 \int_{-\infty}^{+\infty} \chi_{NL}(t - t') \mathbf{E}^3(\mathbf{r}, t') dt'. \quad (1.25)$$

Most of materials like silicon, silica, etc. behave as a *dielectric* at optical frequencies and so there are no free electric charge and current interacting with fields. Therefore, we can set charge and current densities to zero, i.e. $\rho = 0$ and $\mathbf{J} = \mathbf{0}$. It is important to note that in some cases like plasmons where there are free charges the electric charge and current must be taken into account [43].

1.2.1 Linear Response

Generally speaking, the nonlinear response of a material compared to its linear response is so tiny that it can be considered as a perturbation. It means that we can analyze an electromagnetic system first in the linear regime and then add nonlinearities to the linear solution as perturbations, the approach that is taken throughout this work. Considering only the *linear* response of the medium the constitutive relation can be expressed by the *convolution* operator as follows:

$$\mathbf{P}(\mathbf{r}, t) = \epsilon_0 \int_{-\infty}^{+\infty} \chi_L(t - t') \mathbf{E}(\mathbf{r}, t') dt' = \epsilon_0 \chi_L(t) * \mathbf{E}(\mathbf{r}, t). \quad (1.26)$$

Therefore, the electric flux density can be given by

$$\mathbf{D}(\mathbf{r}, t) = \epsilon_0 \mathbf{E} + \mathbf{P} = \epsilon_0 \mathbf{E}(\mathbf{r}, t) + \epsilon_0 \chi_L(t) * \mathbf{E}(\mathbf{r}, t) = \epsilon_0 (\delta(t) + \chi_L(t)) * \mathbf{E}(\mathbf{r}, t), \quad (1.27)$$

where $\delta(t)$ denotes the Dirac delta function. Since the medium is free of charge we have $\nabla \cdot \mathbf{D} = 0$; considering Eq. (1.27) it can be easily seen that $\nabla \cdot \mathbf{E} = 0$ and thus, Maxwell's equations in a linear, homogenous and source-free medium are reduced to

$$\nabla \times \mathbf{E} = -\partial_t \mathbf{B}, \quad (1.28a)$$

$$\nabla \times \mathbf{B} = \frac{1}{c^2} \partial_t ((\delta(t) + \chi_L(t)) * \mathbf{E}), \quad (1.28b)$$

$$\nabla \cdot \mathbf{E} = 0, \quad (1.28c)$$

$$\nabla \cdot \mathbf{B} = 0. \quad (1.28d)$$

Decoupling Eqs. (1.28) results in the following uncoupled homogenous wave equations:

$$\nabla^2 \mathbf{E}(\mathbf{r}, t) = \frac{1}{c^2} \partial_t^2 ((\delta(t) + \chi_L(t)) * \mathbf{E}(\mathbf{r}, t)), \quad (1.29a)$$

$$\nabla^2 \mathbf{B}(\mathbf{r}, t) = \frac{1}{c^2} \partial_t^2 ((\delta(t) + \chi_L(t)) * \mathbf{B}(\mathbf{r}, t)). \quad (1.29b)$$

Eqs. (1.29) are often represented in the frequency domain. To do so, the pair of Fourier and inverse Fourier transforms are defined by

$$\hat{x}(\omega) = \mathcal{F}[x(t)] = \int_{-\infty}^{+\infty} x(t) e^{i\omega t} dt, \quad (1.30a)$$

$$x(t) = \mathcal{F}^{-1}[\hat{x}(\omega)] = \frac{1}{2\pi} \int_{-\infty}^{+\infty} \hat{x}(\omega) e^{-i\omega t} d\omega, \quad (1.30b)$$

where ω [$\frac{\text{rad}}{\text{s}}$] is the angular frequency and is equal to $2\pi f$, where f [Hz] is the frequency. Based on this definition of Fourier transform, the time derivative ∂_t is replaced by the factor $-i\omega$ in the frequency domain. Taking the Fourier transform of the wave equation given in Eq. (1.29a) leads to the following Helmholtz equation:

$$\nabla^2 \hat{\mathbf{E}}(\mathbf{r}, \omega) + \frac{\omega^2 (1 + \hat{\chi}_L(\omega))}{c^2} \hat{\mathbf{E}}(\mathbf{r}, \omega) = 0. \quad (1.31)$$

The relative permittivity of the medium is defined as $\epsilon_r(\omega) = 1 + \hat{\chi}_L(\omega)$ and the material refractive index is represented by $n = \sqrt{\epsilon_r}$. So the Helmholtz equation can be expressed in terms of refractive index by

$$\left(\nabla^2 + \frac{\omega^2 n^2}{c^2} \right) \hat{\mathbf{E}}(\mathbf{r}, \omega) = 0. \quad (1.32)$$

According to Eq. (1.32), in a linear homogeneous medium the electromagnetic fields propagate with velocity $\frac{c}{n}$. Since the refractive index is frequency dependent, the propagation speed changes with frequency; it is a linear phenomenon called *dispersion* and is responsible for making rainbows in the sky.

1.2.2 Kramers–Kronig relations

Causality in physical systems induces some properties on the susceptibility of materials. For instance, the response function $\chi(t) = 0$ for $t < 0$. It means that $\hat{\chi}(\omega)$ is a complex function with nonzero real and imaginary parts, i.e. $\hat{\chi}(\omega) = \hat{\chi}_r(\omega) + i\hat{\chi}_i(\omega)$ whose real and imaginary parts indicate the phase and amplitude responses, respectively; so, a material is lossy when $\hat{\chi}_i(\omega) \neq 0$. Unless $\chi(t)$ is a Dirac delta function, $\hat{\chi}(\omega)$ cannot be purely real. Therefore, a physical system is lossless if its response is instantaneous. In other words, any physical system that has dynamics suffers from energy dissipation. Causality adds also a more important property on the response function which is *analyticity*, i.e. $\hat{\chi}(\omega)$ is an analytic complex function. Analyticity implies that the real part of a function can be obtained from its imaginary part and vice versa. The useful tool for explaining the Kramers–Kronig relations is the Hilbert transform defined as

$$w(p) = \mathcal{H}[v(p)] = \frac{1}{\pi} \text{p.v.} \int_{-\infty}^{+\infty} \frac{v(q)}{p - q} dq, \quad (1.33)$$

where p.v. denotes the Cauchy principal value. It can also be proved that $\mathcal{H}^{-1} = -\mathcal{H}$. As examples, the Hilbert transform of $\cos(p)$ is $\sin(p)$ and thus, that of $\sin(p)$ is $-\cos(p)$. For an analytic function $\hat{\chi}(\omega) = \hat{\chi}_r(\omega) + i\hat{\chi}_i(\omega)$ that decays as fast as or faster than $|\omega|^{-1}$, its imaginary

part is the Hilbert transform of its real part, i.e. $\hat{\chi}_i(\omega) = \mathcal{H}[\hat{\chi}_r(\omega)]$, known as the Titchmarsh theorem [44]. Therefore, a version of the Kramers–Kronig relations is given by

$$\hat{\chi}_i(\omega) = \frac{1}{\pi} \text{p.v.} \int_{-\infty}^{+\infty} \frac{\hat{\chi}_r(\omega')}{\omega - \omega'} d\omega', \quad (1.34a)$$

$$\hat{\chi}_r(\omega) = \frac{1}{\pi} \text{p.v.} \int_{-\infty}^{+\infty} \frac{\hat{\chi}_i(\omega')}{\omega' - \omega} d\omega'. \quad (1.34b)$$

Moreover, the susceptibility $\chi(t)$ is a real-valued function, i.e. $\chi^*(t) = \chi(t)$ and so its Fourier transform has the Hermitian symmetry, i.e. $\hat{\chi}^*(-\omega) = \hat{\chi}(\omega)$. Therefore, the real part of $\hat{\chi}$ is an even function or $\hat{\chi}_r(\omega) = \hat{\chi}_r(-\omega)$ and its imaginary part is an odd function or $\hat{\chi}_i(-\omega) = -\hat{\chi}_i(\omega)$. These symmetries make it possible to calculate the integral in Eqs. (1.34) over positive frequencies. This way, another version of the Kramers–Kronig relations is expressed as

$$\hat{\chi}_i(\omega) = \frac{2}{\pi} \text{p.v.} \int_0^{\infty} \frac{\omega' \hat{\chi}_r(\omega')}{\omega^2 - \omega'^2} d\omega', \quad (1.35a)$$

$$\hat{\chi}_r(\omega) = \frac{2}{\pi} \text{p.v.} \int_0^{\infty} \frac{\omega' \hat{\chi}_i(\omega')}{\omega'^2 - \omega^2} d\omega'. \quad (1.35b)$$

One application of the Kramers-Kronig relations is to calculate one part of the susceptibility from the measurement of the other part. For instance, suppose that the refractive index of a fictitious material is measured at different frequencies by a refractometry method and so the real part of its susceptibility $\chi_r = (n - 1)^2$ is obtained as follows:

$$\hat{\chi}_r(\omega) = \frac{\chi_0}{1 + \tau_0^2 \omega^2}, \quad (1.36)$$

where χ_0 is the low frequency susceptibility and τ_0 is a fitting parameter obtained by measurement. The imaginary part of the material susceptibility is obtained via the Kramers-Kronig relation or actually by taking the Hilbert transform of the absorption spectrum as follows:

$$\hat{\chi}_i(\omega) = \mathcal{H}[\hat{\chi}_r(\omega)] = \frac{\chi_0 \tau_0 \omega}{1 + \tau_0^2 \omega^2}. \quad (1.37)$$

Therefore, the normalized susceptibility of the material is given by

$$\hat{\chi}(\omega) = \hat{\chi}_r(\omega) + i \hat{\chi}_i(\omega) = \chi_0 \frac{1 + i \tau_0 \omega}{1 + \tau_0^2 \omega^2} = \frac{\chi_0}{1 - i \tau_0 \omega}. \quad (1.38)$$

The response function of the material is obtained by taking the inverse Fourier transform of $\hat{\chi}(\omega)$, that is

$$\chi(t) = \frac{\chi_0}{\tau_0} e^{-\frac{t}{\tau_0}}. \quad (1.39)$$

Eq. (1.39) shows that τ_0 is actually the decay time of the response. Fig. 1.1 shows an example of such a susceptibility versus frequency when its low-frequency value is $\chi_0 = 4$. For more on the theory and applications of the Kramers-Kronig relations in optics see [44].

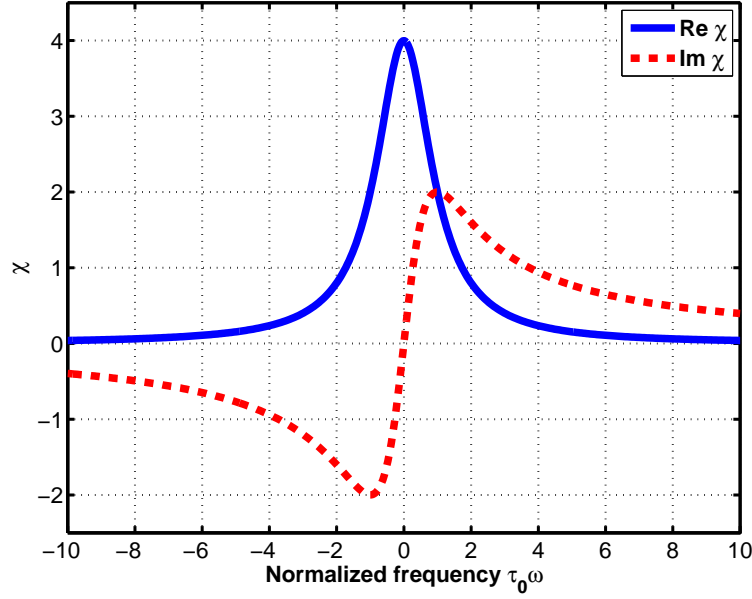


Figure 1.1 – Real and imaginary parts of a hypothetical material's susceptibility versus frequency.

1.3 Monochromatic Waves

Time harmonic analysis of dynamical systems such as Maxwell's equations is a strong tool for describing oscillatory phenomena and gives an insight to their spectral behavior. Time-harmonic fields are intertwined with the notion of wave envelope. The envelope function of a wave is a curve outlining the wave's extremes. So it varies smoothly and slowly with respect to the wave oscillation. Since the variation of the envelope function is much lower than the optical frequency ($\approx 10^{14}$ Hz), it is widely accepted in optics to use the envelope analysis even in ultrafast phenomena [45]. In the case of monochromatic or time-harmonic waves that oscillate harmonically with a single frequency ω , the fields are given by

$$\mathbf{E}(\mathbf{r}, t) = \Re[\mathbf{E}(\mathbf{r})e^{-i\omega t}] = \frac{1}{2}(\mathbf{E}(\mathbf{r})e^{-i\omega t} + \mathbf{E}^*(\mathbf{r})e^{i\omega t}) = \frac{1}{2}\mathbf{E}(\mathbf{r})e^{-i\omega t} + \text{c.c.}, \quad (1.40a)$$

$$\mathbf{H}(\mathbf{r}, t) = \Re[\mathbf{H}(\mathbf{r})e^{-i\omega t}] = \frac{1}{2}(\mathbf{H}(\mathbf{r})e^{-i\omega t} + \mathbf{H}^*(\mathbf{r})e^{i\omega t}) = \frac{1}{2}\mathbf{H}(\mathbf{r})e^{-i\omega t} + \text{c.c.}, \quad (1.40b)$$

where c.c. denotes the complex conjugate of the previous terms. To obtain the flow of energy it is necessary to calculate the average of the Poynting vector $\mathbf{S} = \mathbf{E} \times \mathbf{H}$ as follows:

$$\begin{aligned} \langle \mathbf{S} \rangle &= \frac{1}{4} \langle (\mathbf{E}e^{-i\omega t} + \mathbf{E}^*e^{i\omega t}) \times (\mathbf{H}e^{-i\omega t} + \mathbf{H}^*e^{i\omega t}) \rangle \\ &= \frac{1}{4} \langle \mathbf{E} \times \mathbf{H}^* + \mathbf{E}^* \times \mathbf{H} + \mathbf{E} \times \mathbf{H}e^{-2i\omega t} + \mathbf{E}^* \times \mathbf{H}^*e^{2i\omega t} \rangle = \frac{1}{4}(\mathbf{E} \times \mathbf{H}^* + \mathbf{E}^* \times \mathbf{H}) \\ &= \frac{1}{2}(\mathbf{S}_c + \mathbf{S}_c^*) = \Re[\mathbf{S}_c], \end{aligned} \quad (1.41)$$

where $\langle \rangle$ denotes the time average operation and \mathbf{S}_c is called the *complex* Poynting vector. The wave intensity I [$\frac{W}{m^2}$] is defined as the magnitude of the averaged Poynting vector and thus calculated by taking the real part of the complex Poynting vector,

$$I = |\langle \mathbf{S} \rangle| = |\Re[\mathbf{S}_c]|. \quad (1.42)$$

1.3.1 Uniform Plane Waves

The wavefront of an electromagnetic propagation is defined as the locus of points having the same phase. The wave is categorized based on the shape of this locus, for instance plane, spherical, parabolic, etc. Among them, the plane wave is the most useful, especially for long distance propagation or far-field approximation. In plane waves, the propagation direction is determined by a wave vector \mathbf{k} and so for any position vector \mathbf{r} the phase variation due to propagation is given by $e^{i\mathbf{k}\cdot\mathbf{r}}$. Moreover, if the wave is monochromatic with frequency ω , the phase variation due to oscillation is expressed by $e^{-i\omega t}$ and thus the phase term is represented as $e^{i(\mathbf{k}\cdot\mathbf{r}-\omega t)}$. The simplest type of plane waves is the uniform plane wave whose electromagnetic fields have constant amplitudes so that they can be expressed by

$$\mathbf{E}(\mathbf{r}, t) = \Re[\mathbf{E}_0 e^{i(\mathbf{k}\cdot\mathbf{r}-\omega t)}] = \frac{1}{2}\mathbf{E}_0 e^{i(\mathbf{k}\cdot\mathbf{r}-\omega t)} + \text{c.c.}, \quad (1.43a)$$

$$\mathbf{H}(\mathbf{r}, t) = \Re[\mathbf{H}_0 e^{i(\mathbf{k}\cdot\mathbf{r}-\omega t)}] = \frac{1}{2}\mathbf{H}_0 e^{i(\mathbf{k}\cdot\mathbf{r}-\omega t)} + \text{c.c.}, \quad (1.43b)$$

where \mathbf{E}_0 and \mathbf{H}_0 are constant vectors. Rigorously speaking, uniform plane waves do not exist because they need infinite energy. Moreover, the medium in which uniform plane waves propagate must be boundless like the free space and ideal, i.e. linear, homogeneous, isotropic, source-free and lossless. However, uniform plane waves provide an acceptable approximation for wave propagation in a broad variety of conditions. This approximation transforms the differential equations of Maxwell into vector equations by changing the space differential operator ∇ to the vector form $i\mathbf{k}$ and replacing the time derivative ∂_t by the scalar $-i\omega$. This way, Maxwell's equations given in Eqs. (1.28) can be rewritten as

$$\mathbf{k} \times \mathbf{E}_0 = \omega\mu_0\mathbf{H}_0, \quad (1.44a)$$

$$\mathbf{k} \times \mathbf{H}_0 = -\omega\epsilon_0\epsilon_r\mathbf{E}_0, \quad (1.44b)$$

$$\mathbf{k} \cdot \mathbf{E}_0 = 0, \quad (1.44c)$$

$$\mathbf{k} \cdot \mathbf{H}_0 = 0. \quad (1.44d)$$

Eqs. (1.44c) and (1.44d) demonstrate that the electromagnetic fields are orthogonal to the propagation direction, i.e. $\mathbf{E}_0 \perp \mathbf{k}$ and $\mathbf{H}_0 \perp \mathbf{k}$. Eqs. (1.44a) and (1.44b) show that $\mathbf{E}_0 \perp \mathbf{H}_0$ and the triplet $(\mathbf{E}_0, \mathbf{H}_0, \mathbf{k})$ makes a right-handed trihedral so that $\mathbf{E}_0 \times \mathbf{H}_0$ is in the direction of \mathbf{k} . The wave vector can be derived from Eqs. (1.44) as $\mathbf{k} = \frac{\omega}{c}\sqrt{\epsilon_r}\hat{\mathbf{k}}$ where $\hat{\mathbf{k}}$ is the unit vector in the direction of \mathbf{k} ; and thus the Poynting vector is

$$\mathbf{S}_c = \frac{1}{2}\mathbf{E}_0 \times \mathbf{H}_0^* = \frac{1}{2}|\mathbf{E}_0||\mathbf{H}_0|\hat{\mathbf{k}} = \frac{1}{2}n\epsilon_0 c|\mathbf{E}_0|^2\hat{\mathbf{k}}, \quad (1.45)$$

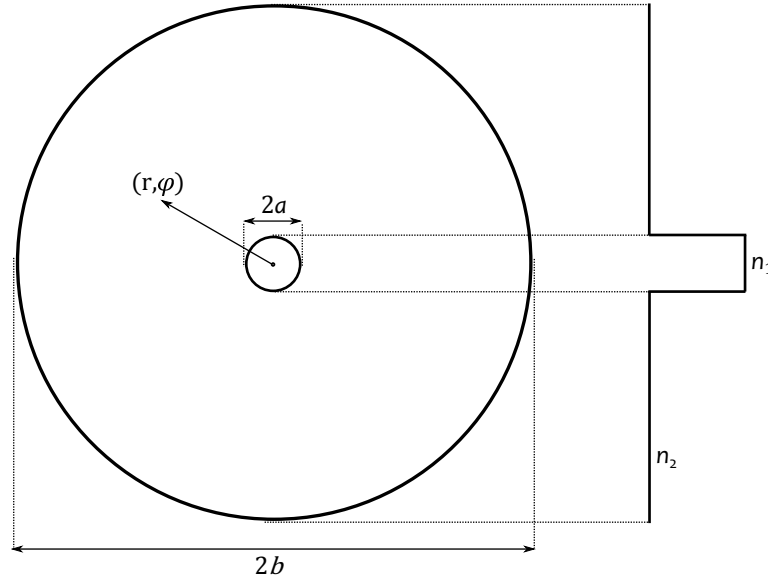


Figure 1.2 – The cross section of an optical fiber along with a step-index profile.

where the refractive index is given by $n = \sqrt{\epsilon_r}$. In this case the complex Poynting vector is a real vector and according to Eq. (1.42) the intensity of an optical signal in a medium with refractive index n , in terms of its electric field envelope \mathbf{E} , is given by

$$I = \frac{1}{2} n \epsilon_0 c |\mathbf{E}|^2. \quad (1.46)$$

This is a general formula for defining optical intensity and thus optical power and energy in optical systems.

1.4 Wave Propagation in Optical Fibers

Standard optical fibers are cylindrical dielectric waveguides made of silica (SiO_2). They consist of a core with refractive index n_1 and a cladding with refractive index n_2 . The cladding is usually made of pure silica with $n_2 = 1.457$ measured at He-Ne laser's wavelength 632.8 nm. The core refractive index is raised by doping germania (GeO_2), phosphorus pentoxide (P_2O_5), and alumina (Al_2O_3). Silica's refractive index can be also decreased by other dopants such as boron trioxide (B_2O_3) and fluorine (F). The slight difference between the core and cladding refractive indices is given by

$$\Delta = \frac{n_1^2 - n_2^2}{2n_1^2} \approx \frac{n_1 - n_2}{n_1}, \quad (1.47)$$

where the approximation is obtained by assuming $n_1 + n_2 \approx 2n_1$. Fig. 1.2 depicts a typical cross section of an optical fiber. The standard value of cladding diameter is $2b = 125$ micron while the core diameter $2a$ varies for different fibers. The refractive index profile shown in Fig. 1.2 is a step-index profile widely used in standard single-mode fibers. Other refractive index profiles

are used to modify the propagation properties of optical fibers. Fig. 1.3 shows two different refractive index profiles for two most common optical fibers: standard single-mode fiber (SMF) and dispersion shifted fiber (DSF).

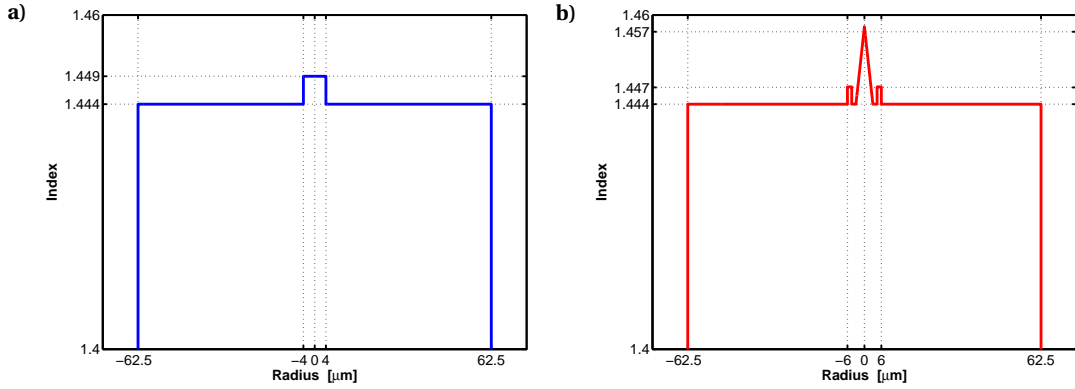


Figure 1.3 – Refractive index profile of single-mode optical fibers @ 1550 nm: a) Standard SMF and b) DSF

In order to obtain refractive index values at desired wavelengths, one can use a semi-empirical formula, namely, the Sellmeier equation, which is widely used in refractometry,

$$n^2(\lambda) = 1 + \sum_k \frac{A_k}{1 - (\frac{\lambda_k}{\lambda})^2}, \quad (1.48)$$

where A_k is a Sellmeier coefficient and λ_k is a resonance wavelength. The sellmeier coefficients are given in Table 1.1 for silica and germania along with their resonance wavelengths in micron [46].

	SiO ₂	GeO ₂
A_1	0.6961663	0.80686642
A_2	0.4079426	0.71815848
A_3	0.8974794	0.85416831
λ_1	0.0684043	0.068972606
λ_2	0.1162414	0.15396605
λ_3	9.8961610	11.841931

Table 1.1 – Sellmeier Coefficients.

As an example, the refractive index of pure silica at the telecom wavelength of 1.55 μm is obtained from Eq. (1.48) as $n_2 = 1.444$. Considering the linear response of material and low doping percentage, the relative permittivity $\epsilon_r = n^2$ of germania-doped silica can be represented by a linear combination of each component's permittivity so that for its refractive index we have $n^2 = xn_g^2 + (1 - x)n_s^2$ where x is germania's mole fraction. For instance, in a standard optical fiber with the core refractive index of $n_1 = 1.449$ at 1550 nm, the dopant percentage must be 3.2% which is rather low. The refractive index of a standard single-mode fiber (SMF-28TM in compliance with ITU-T Recommendation G.652) is shown in Fig. 1.4 for

the core and cladding. As it is clear from the figure, the refractive index of silica reduces by increasing wavelength (decreasing frequency) in the desired spectral bands of fiber usage; in other words, $\frac{dn}{d\lambda}$ is negative or equivalently, $\frac{dn}{d\omega}$ is positive.

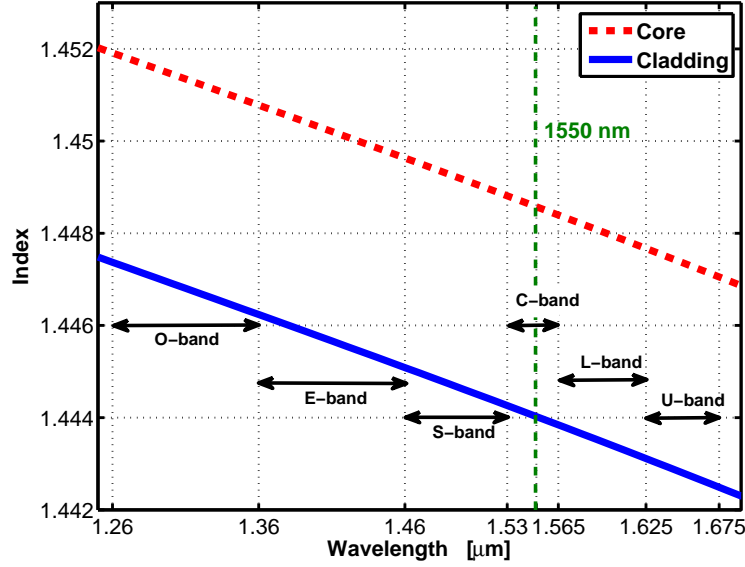


Figure 1.4 – Refractive index of the core and cladding of a standard SMF versus wavelength.

The main advantage of optical fibers that makes it the best communication channel for long-haul telecommunications is low attenuation at infrared (IR) wavelengths. The main sources of loss in optical fibers are the Rayleigh scattering in near-IR ($0.78 - 3 \mu\text{m}$) due to irregularities in the structure of amorphous silica, the absorption due to the electronic transition between the valence band and conduction band in ultra-violet (UV), and the vibration of Si-O and Ge-O bonds near 9 and $11 \mu\text{m}$, respectively, in mid-IR ($3 - 50 \mu\text{m}$). An extrinsic source of absorption at $1.38 \mu\text{m}$ is the OH vibration and there have been extensive efforts to reduce water in manufacturing processes and nowadays, low water-peak optical fibers are commercially available. A simple mathematical model for the uniform loss of an optical signal after travelling in a fiber of length L is an exponential function given by

$$P_L = P_0 e^{-\alpha L}, \quad (1.49)$$

where P_0 and P_L are input and output powers, respectively. α is called the power attenuation coefficient and its minimum value happens to be $\approx 5 \times 10^{-5} \text{ m}^{-1}$ at 1550 nm . The typical unit for fiber attenuation is $\frac{\text{dB}}{\text{km}}$ and the following relation can be used for unit transformation:

$$\alpha \text{ [m}^{-1}\text{]} = \ln(10) \alpha_{\text{dB}} \times 10^{-4} \text{ [dB/km]}, \quad (1.50)$$

where α_{dB} is the fiber attenuation coefficient in $\frac{\text{dB}}{\text{km}}$ and at 1550 nm it is around $0.2 \frac{\text{dB}}{\text{km}}$.

1.4.1 Cylindrical Wave Equation

Since the optical fiber waveguide has a cylindrical structure it is convenient to use the cylindrical coordinates system for solving the Helmholtz equation given in Eq. (1.32). In this coordinate system the vector field \mathbf{E} is expressed by (E_r, E_φ, E_z) that can be easily transformed to the Cartesian coordinate system by applying the following matrix transformation:

$$\begin{bmatrix} E_x \\ E_y \\ E_z \end{bmatrix} = \begin{bmatrix} \cos \varphi & -\sin \varphi & 0 \\ \sin \varphi & \cos \varphi & 0 \\ 0 & 0 & 1 \end{bmatrix} \begin{bmatrix} E_r \\ E_\varphi \\ E_z \end{bmatrix}, \quad (1.51)$$

where $x = r \cos \varphi$, $y = r \sin \varphi$ and (E_x, E_y, E_z) is the Cartesian representation of the field. The z -component of the field is the same in both coordinate system and thus, by considering the wave propagation in the z direction, it is possible to write the field in terms of its transverse and longitudinal components as follows:

$$\mathbf{E} = \mathbf{E}_\perp + E_z \hat{z}, \quad (1.52)$$

in which \mathbf{E}_\perp is either (E_r, E_φ) or (E_x, E_y) . In both coordinate systems the vector Laplacian operator can be written as follows:

$$\nabla^2 \mathbf{E} = \nabla^2 \mathbf{E}_\perp + (\nabla^2 E_z) \hat{z}, \quad (1.53)$$

where $\nabla^2 \mathbf{E}_\perp$ is perpendicular to the z direction and $\nabla^2 E_z$ is a scalar Laplacian operator. Substituting Eq. (1.53) in the Helmholtz equation results in the following uncoupled equations for transverse and longitudinal components of the vector field:

$$\nabla^2 \hat{\mathbf{E}}_\perp(\mathbf{r}, \omega) + \frac{\omega^2 n^2}{c^2} \hat{\mathbf{E}}_\perp(\mathbf{r}, \omega) = 0, \quad (1.54a)$$

$$\nabla^2 \hat{E}_z(\mathbf{r}, \omega) + \frac{\omega^2 n^2}{c^2} \hat{E}_z(\mathbf{r}, \omega) = 0. \quad (1.54b)$$

On the other hand, It can be deduced from Maxwell's equations that all the transverse components of electromagnetic fields can be obtained from their longitudinal components E_z and H_z ; so it is enough to obtain the longitudinal components of the fields. Moreover, H_z satisfies the same equation as E_z and thus it is sufficient to solve the scalar Helmholtz equation given in Eq. (1.54b) and then applying the boundary conditions at the core-cladding surface. In both Cartesian and cylindrical coordinate systems the scalar Laplacian operator can be decomposed to a transverse Laplacian and a longitudinal operator as follows:

$$\nabla^2 = \nabla_\perp^2 + \partial_z^2, \quad (1.55)$$

in which ∇_\perp^2 is $\partial_x^2 + \partial_y^2$ in the Cartesian system and $\partial_r^2 + \frac{1}{r} \partial_r + \frac{1}{r^2} \partial_\varphi^2$ in the cylindrical system. A typical way to solve the Helmholtz equation is the separation of variables, i.e. the electric field component $\hat{E}_z(\mathbf{r}, \omega)$ is decomposed to a transverse function F_\perp and a longitudinal propagation

$\hat{E}_z(z, \omega)$ so that

$$\hat{E}_z(\mathbf{r}, \omega) = F_\perp \hat{E}_z(z, \omega), \quad (1.56)$$

where F_\perp can be either $F_\perp(x, y)$ or $F_\perp(r, \varphi)$. Applying Eq. (1.55) and Eq. (1.56) to the Helmholtz equation in Eq. (1.54b) yields

$$\frac{\nabla_\perp^2 F_\perp}{F_\perp} + \frac{\partial_z^2 \hat{E}_z}{\hat{E}_z} + n^2 k^2 = 0, \quad (1.57)$$

in which $k = \frac{\omega}{c}$ is the wave number in vacuum. In a homogeneous waveguide where n is position-independent, Eq. (1.57) implies that all its three terms must be independent of the coordinate variables; assuming a propagation constant β for the z component, we have

$$(\partial_z^2 + \beta^2) \hat{E}_z = 0, \quad (1.58a)$$

$$(\nabla_\perp^2 + n^2 k^2 - \beta^2) F_\perp = 0. \quad (1.58b)$$

The solution of Eq. (1.58a) has the form of $e^{i\beta z}$, while Eq. (1.58b) has the solution of $J_m(ur)e^{im\varphi}$ in the core and $K_m(wr)e^{im\varphi}$ in the cladding, where J_m is the ordinary Bessel function of the first kind and K_m is the modified Bessel function of the second kind in which the integer m is the order of Bessel functions. $u = \sqrt{n_1^2 k^2 - \beta^2}$ and $w = \sqrt{\beta^2 - n_2^2 k^2}$ are transverse propagation constants in the core and cladding, respectively [47]. Since u and w must be real numbers, the propagation constant satisfies

$$n_2 k < \beta < n_1 k \quad (1.59)$$

β is the actual propagation constant in the fiber and so the effective refractive index is given by $n_{\text{eff}} = \frac{\beta}{k}$. According to Eq. (1.59), it is clear that $n_2 < n_{\text{eff}} < n_1$. Normalizing u and w to the core radius a as $U = au$ and $W = aw$ results in the normalized frequency V , defined as

$$V \triangleq \sqrt{U^2 + W^2} = ka\sqrt{n_1^2 - n_2^2} = ka\text{NA}, \quad (1.60)$$

where $\text{NA} \triangleq \sqrt{n_1^2 - n_2^2} = n_1 \sqrt{2\Delta}$ is referred to as the numerical aperture of the fiber. For example, NA is 0.12 for SMF-28TM at 1550 nm. In order to obtain the propagation constant β , the characteristic equation given in Eq. (1.61) must be solved for U or W (note that $U^2 + W^2 = V^2$). This equation actually relates the propagation constant to the frequency and so the dispersion relation $\beta = \beta(\omega)$ can be obtained by solving the characteristic equation

$$\left(\frac{J'_m(U)}{U J_m(U)} + \frac{K'_m(W)}{W K_m(W)} \right) \left(\frac{n_1^2}{n_2^2} \frac{J'_m(U)}{U J_m(U)} + \frac{K'_m(W)}{W K_m(W)} \right) = m^2 \left(\frac{1}{U^2} + \frac{1}{W^2} \right) \left(\frac{n_1^2}{n_2^2} \frac{1}{U^2} + \frac{1}{W^2} \right), \quad (1.61)$$

where prime denotes derivative. In order to have the propagation characteristics of a fiber such as phase and group velocities, group delay and group velocity dispersion it is indispensable to

solve Eq. (1.61). However, it is a transcendental equation that has no closed-form solution and must be solved by numerical methods. Next section is devoted to the solution of this equation for the fundamental mode of the fiber in which $m = 1$.

1.4.2 Fundamental Mode

The propagation modes in optical fibers can be categorized into transverse electric (TE), transverse magnetic (TM), hybrid EH and hybrid HE modes. Actually, every hybrid mode consists of two degenerate modes (modes with the same dispersion relation). The fundamental mode in optical fiber is HE_{11} which is a hybrid mode containing two degenerate modes. The cutoff frequency for the fundamental mode is theoretically zero and so it can potentially propagate at all wavelengths. The cutoff frequency of the first higher modes is given by the first zero of the Bessel function J_0 which is $V_c = 2.405$. Using the formula of the normalized frequency, the cutoff wavelength for an optical fiber to be in its single-mode regime is given by

$$\lambda_c = \frac{2\pi NA}{V_c} a. \quad (1.62)$$

For instance, the cutoff wavelength of an optical fiber with the core radius $a = 4$ micron and numerical aperture $NA = 0.12$ is $\lambda_c = 1.25$ micron obtained from Eq. (1.62). So for all wavelengths longer than 1.25 micron, the fiber is in its single-mode state and only the fundamental mode propagates in the fiber.

Conventional optical fibers have very low difference between the core and cladding refractive indices so that the ratio $\frac{n_1}{n_2}$ is close to unity. In the *weakly guiding approximation*, $\frac{n_1}{n_2} \approx 1$, different modes have the same propagation constant and can be rearranged to a set of *linearly polarized* (LP) modes. For example, the two-fold fundamental mode HE_{11} makes LP_{01} , while the next mode LP_{11} consists of TE_{01} , TM_{01} , and HE_{21} with the cutoff frequency of $V_c = 2.405$; or LP_{21} includes EH_{11} and HE_{31} with the cutoff frequency $V_c = 3.832$. It should be noted that this approximation is not applicable for silica-air guiding structures such as hollow-core fibers because the difference between the air and silica refractive indices is not negligible [46]. Considering the weakly guiding approximation, the fundamental mode LP_{01} has two linear polarizations: horizontal polarization LP_{01}^x with electric field $(E_x, 0, E_z)$ and vertical polarization LP_{01}^y with field $(0, E_y, E_z)$. The spatial variation of the transverse components E_x and E_y can be expressed by

$$F_{\perp}(r, \varphi) = \begin{cases} J_0(ur) & 0 \leq r \leq a \\ \frac{J_0(ua)}{K_0(ua)} K_0(wr) & r > a \end{cases}. \quad (1.63)$$

It is clear that the transverse distribution of the fundamental mode is independent from the azimuthal angle φ and thus has a circular symmetry. It is useful to approximate Eq. (1.63) with the following Gaussian distribution [48]:

$$F_{\perp}(r, \varphi) \approx \exp\left(-\frac{r^2}{\rho^2}\right), \quad (1.64)$$

Chapter 1. Preliminaries

where ρ is a parameter obtained by fitting Eq. (1.64) into Eq. (1.63) and can be expressed in terms of the normalised frequency as follows [48]:

$$\frac{\rho}{a} \approx 0.65 + 1.619V^{-\frac{3}{2}} + 2.879V^{-6}. \quad (1.65)$$

As an example, for SMF-28TM with $V = 1.91$ at 1550 nm, Eq. (1.65) results in $\rho = 1.32a = 5.3 \mu\text{m}$. An important parameter related to the transverse distribution of fields is the effective area defined as [3],

$$A_{\text{eff}} \triangleq \frac{\left(\iint_{-\infty}^{+\infty} |F_{\perp}(x, y)|^2 dx dy \right)^2}{\iint_{-\infty}^{+\infty} |F_{\perp}(x, y)|^4 dx dy} = \frac{\left(\int_0^{2\pi} \int_0^{\infty} |F_{\perp}(r, \varphi)|^2 r dr d\varphi \right)^2}{\int_0^{2\pi} \int_0^{\infty} |F_{\perp}(r, \varphi)|^4 r dr d\varphi}. \quad (1.66)$$

Substituting the Gaussian distribution given in Eq. (1.64) in the effective area definition yields

$$A_{\text{eff}} = \pi \rho^2. \quad (1.67)$$

Since the mode effective area is $\pi \rho^2$, the parameter ρ is called the mode field radius and so 2ρ is the mode field diameter (MFD). For a standard SMF at C-band the effective area is about $85 \mu\text{m}^2$, while for a typical DSF it is around $50 \mu\text{m}^2$ showing that the energy is more confined in DSFs than SMFs. The propagation characteristics of the electromagnetic mode traveling in the fiber are completely determined by the characteristic equation given in Eq. (1.61). Once the equation is solved, the dispersion relation $\beta = \beta(k)$ is known and so the effective refractive index $n_{\text{eff}} = \frac{\beta}{k}$ and the group index $n_g = \frac{d\beta}{dk}$ are obtained. This way the phase and group velocities are calculated as follows:

$$v_p = \frac{\omega}{\beta} = \frac{ck}{\beta} = \frac{c}{n_{\text{eff}}}, \quad (1.68a)$$

$$v_g = \frac{d\omega}{d\beta} = \frac{cdk}{d\beta} = \frac{c}{n_g}. \quad (1.68b)$$

Fig. 1.5 shows how the effective and group refractive indices versus wavelength in a standard SMF. It is clear from Fig. 1.5a that the effective refractive index is between the core and cladding indices and the longer the wavelength is, the closer to the cladding index the effective index will be. The group index plotted in Fig. 1.5b has a minimal point at around 1310 nm which means at this wavelength the group velocity is maximal. The figure also shows that the group index is larger than the effective index or equivalently the group velocity is less than the phase velocity. It can be mathematically deduced following the definition of effective and group indices,

$$n_g = \frac{d\beta}{dk} = \frac{d(kn_{\text{eff}})}{dk} = n_{\text{eff}} + k \frac{dn_{\text{eff}}}{dk} = n_{\text{eff}} + \omega \frac{dn_{\text{eff}}}{d\omega} = n_{\text{eff}} - \lambda \frac{dn_{\text{eff}}}{d\lambda}, \quad (1.69)$$

where the minus sign in the right-hand side of the expression is due to $\frac{d\omega}{d\lambda} = -\frac{d\lambda}{\lambda}$, because $\omega\lambda = 2\pi c$. It is evident from Fig. 1.5a that $\frac{dn_{\text{eff}}}{d\lambda}$ is negative and thus, Eq. (1.69) implies that

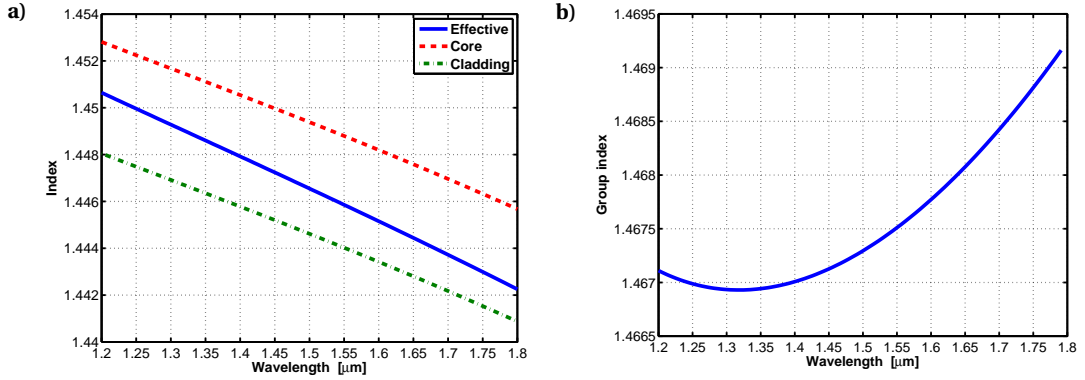


Figure 1.5 – Refractive index of a SMF-28™ versus wavelength: a) Effective index laid between the core and cladding indices and b) Group index.

$n_g > n_{\text{eff}}$ and so $v_g < v_p$. Another important concept related to the group velocity is the dispersion parameter D defined as

$$D \triangleq \frac{d}{d\lambda} \left(\frac{1}{v_g} \right) = \frac{1}{c} \frac{dn_g}{d\lambda}. \quad (1.70)$$

The dispersion parameter is normally given in $\frac{\text{ps}}{\text{nm.km}}$ and it can be expressed in terms of effective index using Eqs. (1.69) and (1.70),

$$D = \frac{1}{c} \frac{dn_g}{d\lambda} = \frac{1}{c} \frac{d}{d\lambda} \left(n_{\text{eff}} - \lambda \frac{dn_{\text{eff}}}{d\lambda} \right) = -\frac{\lambda}{c} \frac{d^2 n_{\text{eff}}}{d\lambda^2}. \quad (1.71)$$

The dependence of the effective and group indices on wavelength is due to two causes: first the wavelength dependence of the material refractive index, and second the characteristic equation given in Eq. (1.61); the former is called the *material* dispersion D_m and the latter the *waveguide* dispersion D_w so that the total dispersion is $D = D_m + D_w$.

Fig. 1.6 shows the dispersion coefficients of a standard SMF obtained by solving the characteristic equation numerically and considering the material dispersion through the Sellmeier equation given in Eq. (1.48). The wavelength at which the dispersion parameter is null is called the zero-dispersion wavelength (ZDW) which is around 1310 nm for SMF-28™, evidenced from Fig. 1.6. The zero-dispersion wavelength is a critical parameter for a variety of fiber optic applications from telecommunications to optical signal processing. Therefore, manipulating the dispersion profile of optical fibers is a key point in designing and manufacturing fibers. In order to modify the dispersion parameter of an optical fiber, one needs to play with the waveguide dispersion of the fiber through the refractive index profile. The most common dispersion-managed single mode fibers are dispersion-shifted fibers (DSF) and dispersion-compensating fibers (DCF). Fig. 1.7 shows the dispersion parameter of three common fibers, namely, standard SMF, DSF, and DCF. For standard SMFs the dispersion parameter in the C-band is positive ($\approx 17 \frac{\text{ps}}{\text{nm.km}}$ at 1550 nm) which is called *anomalous* dispersion. DCFs are usually made to compensate the anomalous dispersion of SMFs in the C-band and so they

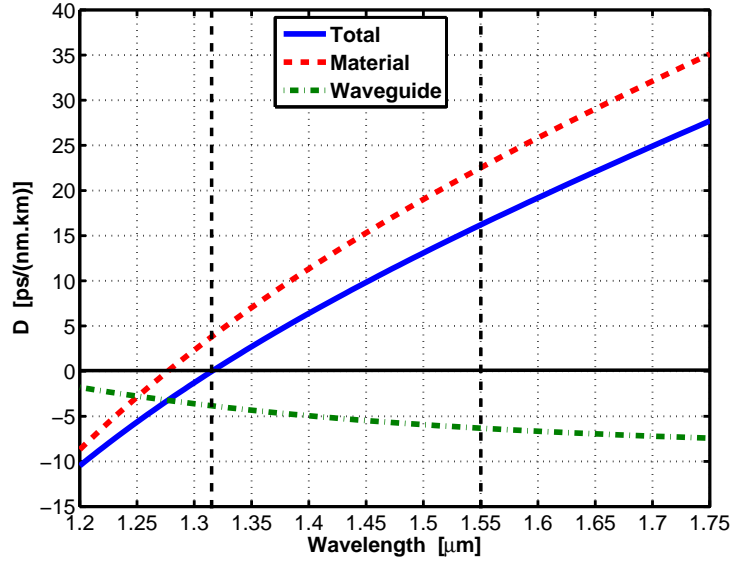


Figure 1.6 – Dispersion coefficient of a standard SMF versus wavelength including the material, waveguide and total dispersions.

have negative dispersion parameter ($\approx -42 \frac{\text{ps}}{\text{nm.km}}$ at 1550 nm) called *normal* dispersion. The zero-dispersion wavelength of DSFs is in the C-band ($\lambda_{\text{ZD}} \approx 1550$ nm) to provide specific propagation features for optical waves in special applications.

1.5 Nonlinear Fiber Optics

In silica glass where the inversion symmetry holds, the second order nonlinearity $\chi^{(2)}$ is zero and so the third order nonlinearity $\chi^{(3)}$ is dominant. The main contribution of $\chi^{(3)}$ is in the intensity-dependent refractive index which is assumed to be isotropic. Therefore, the nonlinear polarization in Eq. (1.25) can be approximated as

$$\begin{aligned} \mathbf{P}_{\text{NL}}(\mathbf{r}, t) &= \varepsilon_0 \int_{-\infty}^{+\infty} \chi_{\text{NL}}(t - t') \mathbf{E}^3(\mathbf{r}, t') dt' \approx \varepsilon_0 |\mathbf{E}(\mathbf{r})|^2 \int_{-\infty}^{+\infty} \chi_{\text{NL}}(t - t') \mathbf{E}(\mathbf{r}, t') dt' \\ &= \varepsilon_0 |\mathbf{E}(\mathbf{r})|^2 (\chi_{\text{NL}}(t) * \mathbf{E}(\mathbf{r}, t)). \end{aligned} \quad (1.72)$$

Eq. (1.72) can be treated linearly and so by taking its Fourier transform we have

$$\hat{\mathbf{P}}_{\text{NL}}(\mathbf{r}, \omega) = \varepsilon_0 |\mathbf{E}(\mathbf{r})|^2 \hat{\chi}_{\text{NL}}(\omega) \hat{\mathbf{E}}(\mathbf{r}, \omega). \quad (1.73)$$

Considering both linear and nonlinear polarizations and the definition of ε_r as $\hat{\mathbf{D}} = \varepsilon_0 \varepsilon_r \hat{\mathbf{E}}$, we find

$$\hat{\mathbf{D}} = \varepsilon_0 \hat{\mathbf{E}} + \hat{\mathbf{P}} = \varepsilon_0 \hat{\mathbf{E}} + \hat{\mathbf{P}}_{\text{L}} + \hat{\mathbf{P}}_{\text{NL}} = \varepsilon_0 (1 + \hat{\chi}_{\text{L}} + \hat{\chi}_{\text{NL}} |\mathbf{E}|^2) \hat{\mathbf{E}}, \quad (1.74)$$

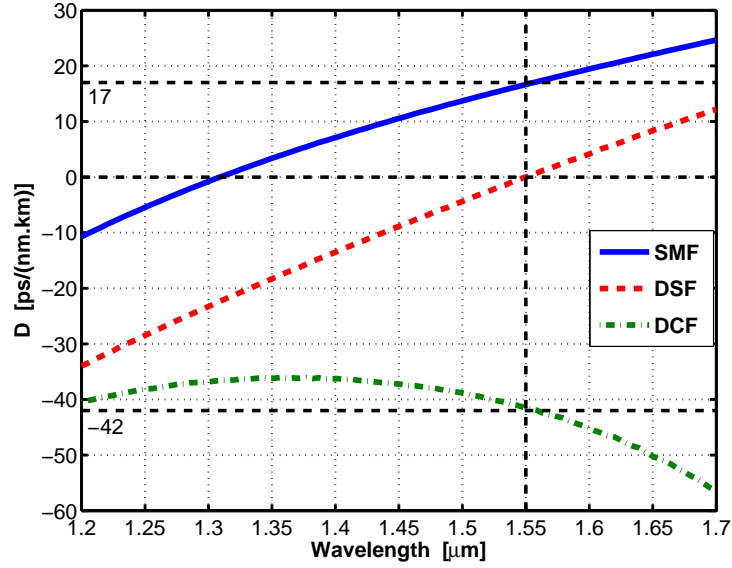


Figure 1.7 – Dispersion parameter for different types of optical fibers, standard SMF, DSF, and DCF versus wavelength.

and so $\varepsilon_r = 1 + \hat{\chi}_L + \hat{\chi}_{NL}|\mathbf{E}|^2$. The linear part of ε_r defines the linear refractive index as $n_0 = \sqrt{1 + \hat{\chi}_L}$ and since its nonlinear part is much smaller than the linear part, the following approximation can be made:

$$\begin{aligned} n = \sqrt{\varepsilon_r} &= (1 + \hat{\chi}_L + \hat{\chi}_{NL}|\mathbf{E}|^2)^{\frac{1}{2}} = (1 + \hat{\chi}_L)^{\frac{1}{2}} \left(1 + \frac{\hat{\chi}_{NL}|\mathbf{E}|^2}{1 + \hat{\chi}_L} \right)^{\frac{1}{2}} = n_0 \left(1 + \frac{\hat{\chi}_{NL}|\mathbf{E}|^2}{n_0^2} \right)^{\frac{1}{2}} \\ &\approx n_0 \left(1 + \frac{\hat{\chi}_{NL}}{2n_0^2} |\mathbf{E}|^2 \right) = n_0 + \frac{\hat{\chi}_{NL}}{2n_0} |\mathbf{E}|^2 \end{aligned} \quad (1.75)$$

Using the definition of intensity in Eq. (1.46), the refractive index in Eq. (1.75) can be expressed in terms of field intensity as follows:

$$n = n_0 + n_2 I = n_0 + \frac{\hat{\chi}_{NL}}{n_0^2 \varepsilon_0 c} I, \quad (1.76)$$

where n_2 is called the Kerr coefficient and its typical value for fused silica is $2.2 - 3.2 \times 10^{-20} \frac{\text{m}^2}{\text{W}}$. Since the susceptibility $\hat{\chi}_{NL}$ is a complex number, the refractive index is also complex as $n = n_0 + n_2^r I + i n_2^i I$. Considering the propagation term e^{inkz} , we have

$$e^{inkz} = e^{ikz(n_0 + n_2^r I + i n_2^i I)} = e^{-n_2^i I k z} e^{i n_0 k z} e^{i n_2^r I k z}. \quad (1.77)$$

The first exponential function on the right-hand side of Eq. (1.77) shows an intensity-dependent gain or loss in propagation depending on the sign of n_2^i . This term represents scattering processes such as stimulated Raman scattering (SRS) and stimulated Brillouin scattering (SBS).

The last term in Eq. (1.77) shows an intensity-dependent phase modulation which is the origin of a variety of nonlinear processes including self-phase modulation (SPM), cross-phase modulation (XPM), modulation instability (MI), optical parametric amplification (OPA), and four-wave mixing (FWM).

1.5.1 Kerr Effect

By the Kerr effect we mean the modification of real-valued refractive index linearly proportional to optical intensity. Therefore, the imaginary part of the Kerr coefficient is usually neglected in dealing with the quasi-instantaneous nonlinear processes originated from intensity-dependent phase modulation. The origin of the Kerr effect is the electric polarization caused by the nonlinear response of bound electrons to an intense electric field. It is worth mentioning that the Kerr effect can be modified by adding dopants to silica. An empirical expression for GeO₂-doped fibers is given by [46],

$$n_2 = 2.507 + 0.505\Delta \quad [\times 10^{-20} \text{ m}^2/\text{W}], \quad (1.78)$$

where Δ is the relative refractive index difference. An important parameter in nonlinear fiber optics closely related to the Kerr coefficient is the nonlinear coefficient γ [$\frac{\text{W}^{-1}}{\text{km}}$] defined as [3],

$$\gamma \triangleq k \frac{n_2}{A_{\text{eff}}} = \frac{\omega}{c} \frac{n_2}{A_{\text{eff}}} = \frac{2\pi}{\lambda} \frac{n_2}{A_{\text{eff}}}. \quad (1.79)$$

The nonlinear coefficient γ depends not only on the dopant through the Kerr coefficient n_2 but also upon the mode field distribution via the effective area A_{eff} . Table 1.2 presents the important parameters of four different types of optical fibers, namely, standard SMF, DSF, DCF, and highly non-linear fiber (HNLF) [46]. It is clear from the table that as the dopant

Fiber	SMF	DSF	DCF	HNLF
α [dB/km]	0.2	0.2	0.4	0.7
A_{eff} [μm^2]	85	50	20	12
γ [W^{-1}/km]	1.8	2.7	5.0	15

Table 1.2 – Characteristics of Optical Fibers @ 1550 nm.

increases to make a larger contrast between the core and cladding refractive indices and thus have smaller effective area, both attenuation and nonlinear coefficients increase. Modeling the propagation of light in optical fibers in the presence of the Kerr nonlinearity leads to a nonlinear partial differential equation (PDE) called the nonlinear Schrödinger equation (NLSE) which is thoroughly dealt with in the next chapter.

2 Nonlinear Schrödinger Equation

In this chapter we will see how Maxwell's equations result in the nonlinear Schrödinger equation (NLSE) in optical fibers and which characteristics such an equation imposes on the lightwave propagating in the fiber. First, the complete derivation of the scalar NLSE in optical fibers is presented using the results of the previous chapter. In this analysis the important approximation of slowly varying envelope (SVE) is introduced. Then, several solutions for the NLSE in different propagation regimes are provided. Different combinations of dispersion and nonlinearity are considered and for each of them available analytical solutions are discussed. As a numerical method for solving the NLSE in its general form, the well-know split-step Fourier method is thoroughly investigated. Finally, The experimental results of an interferometric method for measuring the nonlinear coefficient of optical fibers based on the nonlinear phenomenon of self-phase modulation (SPM) are presented.

2.1 Nonlinear Wave Equation

The general form of wave equation in nonlinear optics can be derived from Maxwell's equations in a nonmagnetic ($\mathbf{B} = \mu_0 \mathbf{H}$), isotropic, source-free ($\rho = 0$ and $\mathbf{J} = 0$) medium given by [41]

$$\nabla \times \mathbf{E} = -\partial_t \mathbf{B}, \quad (2.1a)$$

$$\nabla \times \mathbf{B} = \frac{1}{\epsilon_0 c^2} \partial_t \mathbf{D}, \quad (2.1b)$$

$$\nabla \cdot \mathbf{D} = 0, \quad (2.1c)$$

$$\nabla \cdot \mathbf{B} = 0, \quad (2.1d)$$

where the electric flux density can be expressed as $\mathbf{D} = \epsilon_0 \mathbf{E} + \mathbf{P}$. Taking the curl of Eq. (2.1a) and substituting from Eq. (2.1b) we have the following general equation:

$$\nabla^2 \mathbf{E} - \nabla(\nabla \cdot \mathbf{E}) = \frac{1}{c^2} \partial_t^2 \mathbf{E} + \frac{1}{\epsilon_0 c^2} \partial_t^2 \mathbf{P}. \quad (2.2)$$

Now consider the intensity-dependant nonlinear effect expressed by

$$\mathbf{D} = \epsilon_0 \mathbf{E} + \mathbf{P} = \epsilon_0 \mathbf{E} + \mathbf{P}_L + \mathbf{P}_{NL} = \epsilon_0 (\delta(t) + \chi_L(t) + \chi_{NL}(t) |\mathbf{E}|^2) * \mathbf{E}, \quad (2.3)$$

Chapter 2. Nonlinear Schrödinger Equation

where $*$ denotes the time convolution. The second term in the left-hand side of Eq. (2.2) hampers the wave equation to be solved analytically. In almost all works in nonlinear optics this term is neglected [2], even though there are a few arguments against removing the term from the equation [49]. It is pointed out that in realistic cases the term $\nabla(\nabla \cdot \mathbf{E})$ is even larger than the terms due to nonlinearity kept in the equation [50]. However, we accept this approximation by the following argument based on Gauss's law in Eq. (2.1c):

$$\begin{aligned} \nabla \cdot \mathbf{D} = 0 \quad \Rightarrow \quad \nabla \cdot \mathbf{D} &= \nabla \cdot (\varepsilon_0(\delta(t) + \chi_L(t) + \chi_{NL}(t)|\mathbf{E}|^2) * \mathbf{E}) \\ &\approx \varepsilon_0(\delta(t) + \chi_L(t) + \chi_{NL}(t)|\mathbf{E}|^2) * \nabla \cdot \mathbf{E} = 0. \end{aligned} \quad (2.4)$$

Accepting the controversial approximation in Eq. (2.4) leads to $\nabla \cdot \mathbf{E} = 0$ and thus, $\nabla(\nabla \cdot \mathbf{E}) = 0$. This way, the general wave equation in Eq. (2.2) reduces to the following simpler one:

$$\nabla^2 \mathbf{E} = \frac{1}{c^2} \partial_t^2 \mathbf{E} + \frac{1}{\varepsilon_0 c^2} \partial_t^2 \mathbf{P}. \quad (2.5)$$

Taking the Fourier transform of Eq. (2.5) and using Eq. (2.3) with the assumption of slow variation for $|\mathbf{E}|^2$ compared to \mathbf{E} , result in

$$\nabla^2 \hat{\mathbf{E}}(\mathbf{r}, \omega) + \frac{\omega^2}{c^2} (1 + \hat{\chi}_L(\omega) + \hat{\chi}_{NL}(\omega)|\mathbf{E}|^2) \hat{\mathbf{E}}(\mathbf{r}, \omega) = 0. \quad (2.6)$$

Considering the vacuum wavenumber $k = \frac{\omega}{c}$ and the refractive index $n = \sqrt{1 + \hat{\chi}_L}$, Eq. (2.6) can be written as

$$\nabla^2 \hat{\mathbf{E}} + k^2 (n^2 + \hat{\chi}_{NL}|\mathbf{E}|^2) \hat{\mathbf{E}} = 0. \quad (2.7)$$

Eq. (2.7) is a nonlinear Helmholtz equation that models the intensity dependent refractive index. In order to solve this equation we use the results from the previous chapter. In single-mode fibers, weakly guiding approximation leads to the two orthogonally polarized modes $(E_x, 0, E_z)$ and $(0, E_y, E_z)$. In the scalar wave propagation either x -polarization or y -polarization is taken into account; here we consider the x -polarization. Moreover, the longitudinal component E_z is neglected compared to the transverse components. Therefore, the electric field can be expressed as

$$\hat{\mathbf{E}}(\mathbf{r}, \omega) = F_{\perp}(x, y) \hat{E}(z, \omega) \hat{\mathbf{x}}, \quad (2.8)$$

where $F_{\perp}(x, y)$ is the transverse distribution of the field, $\hat{E}(z, \omega)$ is its longitudinal variation, and $\hat{\mathbf{x}}$ is the unit vector in the horizontal direction. Substituting Eq. (2.8) in Eq. (2.7) results in

$$(\nabla_{\perp}^2 F_{\perp}) \hat{E} + F_{\perp} \partial_z^2 \hat{E} + k^2 (n^2 + \hat{\chi}_{NL}|F_{\perp}|^2 |\hat{E}|^2) F_{\perp} \hat{E} = 0. \quad (2.9)$$

It has been proved in the previous chapter that $\nabla_{\perp}^2 F_{\perp} = (\beta^2 - n^2 k^2) F_{\perp}$; so Eq. (2.9) reduces to

$$(\partial_z^2 + \beta^2) F_{\perp} \hat{E} + k^2 \hat{\chi}_{NL} |F_{\perp}|^2 |\hat{E}|^2 \hat{E} = 0. \quad (2.10)$$

Multiplying Eq. (2.10) by F_{\perp}^* and taking its integral over the transverse plane results in

$$(\partial_z^2 + \beta^2) \hat{E} \iint |F_{\perp}|^2 dx dy + k^2 \hat{\chi}_{\text{NL}} |E|^2 \hat{E} \iint |F_{\perp}|^4 dx dy = 0. \quad (2.11)$$

According to the definition of effective area given in the previous chapter

$$\iint |F_{\perp}|^4 dx dy = \frac{1}{A_{\text{eff}}} \left(\iint |F_{\perp}|^2 dx dy \right)^2. \quad (2.12)$$

Substituting Eq. (2.12) in Eq. (2.11) results in

$$(\partial_z^2 + \beta^2) \hat{E} + k^2 \frac{\hat{\chi}_{\text{NL}}}{A_{\text{eff}}} |E|^2 \hat{E} \iint |F_{\perp}|^2 dx dy = 0. \quad (2.13)$$

We consider a normalization for the electric field from which the optical power can be calculated directly. Such normalization takes the optical intensity and mode area into account as follows:

$$A = E \sqrt{\frac{n \epsilon_0 c}{2} \iint |F_{\perp}|^2 dx dy} \quad (2.14)$$

It is easily seen that

$$|A|^2 = \underbrace{\frac{1}{2} n \epsilon_0 c |E|^2}_{\text{Intensity}} \underbrace{\iint |F_{\perp}|^2 dx dy}_{\text{Surface}}, \quad (2.15)$$

so $|A|^2$ denotes *optical power*; in other words, $P(z, t) = |A(z, t)|^2$. Substituting Eq. (2.14) in Eq. (2.13) results in the following expression:

$$(\partial_z^2 + \beta^2 + 2nk\gamma |A|^2) \hat{A} = 0, \quad (2.16)$$

in which $\gamma = k \frac{n_2}{A_{\text{eff}}}$ where $n_2 = \frac{\hat{\chi}_{\text{NL}}}{n^2 \epsilon_0 c}$. In order to proceed in solving Eq. (2.16) more restrictions must be put on the equation that is dealt with in the following section.

2.1.1 Slowly Varying Envelope

The evolution of wave packets or in fact wave envelopes propagating in a medium is of great importance in almost all applications of signal transmission. A strong tool giving an insight to such evolution is the slowly varying envelope (SVE) approximation. This approximation takes advantages of slow variation of the wave envelope compared to its phase variation due to the temporal oscillation or spatial propagation. Suppose that the optical field has a central frequency ω_0 and a propagation constant β_0 obtained from the dispersion relation $\beta_0 = \beta(\omega_0)$; this way the field can be expressed by $A(z, t) e^{i(\beta_0 z - \omega_0 t)}$ and its Fourier transform is given by $\hat{A}(z, \omega - \omega_0) e^{i\beta_0 z}$. Since the envelope varies slowly compared to the field oscillation, the frequency detuning $\Omega = \omega - \omega_0$ is normally much less than the optical frequency ω_0 , i.e. $|\Omega| \ll \omega_0$. According to Eq. (2.16) the second derivative of the envelope is needed and so it is

Chapter 2. Nonlinear Schrödinger Equation

derived as follows:

$$\partial_z^2 (\hat{A}(z, \Omega) e^{i\beta_0 z}) = e^{i\beta_0 z} (\partial_z^2 + 2i\beta_0 \partial_z - \beta_0^2) \hat{A}(z, \Omega). \quad (2.17)$$

Using the result of Eq. (2.17) in Eq. (2.16) leads to

$$(\partial_z^2 + 2i\beta_0 \partial_z + \beta^2 - \beta_0^2 + 2nk\gamma|A|^2) \hat{A} = 0, \quad (2.18)$$

By the slowly varying envelope approximation we mean

$$|\partial_z^2 A| \ll \beta_0 |\partial_z A|, \quad (2.19)$$

so that we can neglect the second-order derivative compared to the first-order one. Removing ∂_z^2 from Eq. (2.18) and dividing the equation by $2\beta_0$ we have

$$(i\partial_z + \frac{\beta^2 - \beta_0^2}{2\beta_0} + \frac{nk}{\beta_0} \gamma |A|^2) \hat{A} = 0. \quad (2.20)$$

The coefficients of Eq. (2.20) can be approximately evaluated as $nk \approx \beta_0$ and $\beta + \beta_0 \approx 2\beta_0$, so that the equation can be simplified to

$$i\partial_z \hat{A} + (\beta - \beta_0) \hat{A} + \gamma |A|^2 \hat{A} = 0. \quad (2.21)$$

Eq. (2.21) is in fact the nonlinear Schrödinger equation in the frequency domain and in order to convert it to the time domain, it is necessary to consider the dispersion relation $\beta = \beta(\omega)$ in detail. The dispersion relation can be expanded using a Taylor series around the central frequency ω_0 as follows:

$$\beta(\omega) = \sum_{m=0}^{\infty} \frac{\beta_m}{m!} (\omega - \omega_0)^m, \quad (2.22)$$

where the dispersion coefficient β_m is given by $\frac{d^m \beta}{d\omega^m} |_{\omega=\omega_0}$. Therefore, the coefficient $\beta - \beta_0$ in Eq. (2.21) is represented versus the frequency detuning $\Omega = \omega - \omega_0$ via

$$\beta - \beta_0 = \sum_{m=1}^{\infty} \frac{\beta_m}{m!} \Omega^m. \quad (2.23)$$

The time derivative ∂_t is represented by $-i\Omega$ in the frequency domain and the term Ω^m in Eq. (2.23) can be written as $i^m (-i\Omega)^m$, so Ω^m represents the time derivative $i^m \partial_t^m$ in the time domain. Taking the inverse Fourier transform of Eq. (2.21) and using Eq. (2.23) result in

$$i\partial_z A + \sum_{m=1}^{\infty} i^m \frac{\beta_m}{m!} \partial_t^m A + \gamma |A|^2 A = 0. \quad (2.24)$$

Eq. (2.24) is the general form of the scalar nonlinear Schrödinger equation in a lossless medium with instantaneous intensity-dependant refractive index. To include the fiber attenuation in

the equation we can simply add a damping term proportional to the field envelope with the damping coefficient of $\frac{\alpha}{2}$ (note that α is the power attenuation coefficient) as follows:

$$i\partial_z A + \sum_{m=1}^{\infty} i^m \frac{\beta_m}{m!} \partial_t^m A + i\frac{\alpha}{2} A + \gamma |A|^2 A = 0. \quad (2.25)$$

Eq. (2.25) is the nonlinear Schrödinger equation for lossy fibers and is its most general form we deal with in this dissertation. The equation can be generalized to include other effects such as delayed response of silica due to the Raman and Brillouin contribution to the Kerr coefficient [3].

2.1.2 Normalization of the NLSE

In order to solve the nonlinear Schrödinger equation both analytically and numerically, it is convenient to normalize the variables and functions. The first step is to remove the loss term from the NLSE in lossy media and normalizing the envelope by defining the normalized envelope $U(z, t)$ so that

$$A(z, t) = \sqrt{P_0} e^{-\frac{\alpha}{2}z} U(z, t), \quad (2.26)$$

where P_0 is the input peak power so that $|U(0, 0)| = 1$. It can be easily calculated that

$$\partial_z A = \sqrt{P_0} e^{-\frac{\alpha}{2}z} \left(\partial_z - \frac{\alpha}{2} \right) U. \quad (2.27)$$

Substituting $\partial_z A$ from Eq. (2.27) in the lossy NLSE given in Eq. (2.25) results in the following form of the equation:

$$i\partial_z U + \sum_{m=1}^{\infty} i^m \frac{\beta_m}{m!} \partial_t^m U + \gamma e^{-\alpha z} P_0 |U|^2 U = 0. \quad (2.28)$$

According to Eq. (2.28) the difference between lossless and lossy equations is in the coefficient of the nonlinear term. In the lossless case ($\alpha = 0$), the coefficient is γP_0 which is a constant; whilst in the lossy case, it equals $\gamma P_0 e^{-\alpha z}$ which is a function of the variable z . Such a difference makes a distinction in solving the equation with and without attenuation. Another modification to the NLSE can be the normalization of the independent variables. The position variable is normalized to the nonlinear length of the fiber defined as $L_{NL} = \frac{1}{\gamma P_0}$. In the case of time, it is more convenient to attach to the reference frame traveling with the envelope group velocity $v_g = \frac{1}{\beta_1}$; moreover, time can also be normalized to an arbitrary parameter T_0 representing for instance, pulse duration. Therefore, the following transformation for time and space are utilized:

$$\zeta \triangleq \frac{z}{L_{NL}} = \gamma P_0 z, \quad (2.29a)$$

$$\tau \triangleq \frac{t - z/v_g}{T_0} = \frac{t - \beta_1 z}{T_0}. \quad (2.29b)$$

Chapter 2. Nonlinear Schrödinger Equation

Changing the variables (z, t) to (ζ, τ) in Eq. (2.28) results in the following NLSE with normalized variables:

$$i\partial_{\zeta}U + \sum_{m=2}^{\infty} \frac{i^m \beta_m}{m! T_0^m \gamma P_0} \partial_{\tau}^m U + e^{-\frac{\alpha}{\gamma P_0} \zeta} |U|^2 U = 0. \quad (2.30)$$

Note that by the transformations in Eqs. (2.29), the series in Eq. (2.30) starts from the group velocity dispersion β_2 compared to Eq. (2.28) starting with β_1 . In standard SMFs working at 1550 nm, the group velocity dispersion (GVD) coefficient is dominant and all higher order dispersion coefficients can be safely neglected. In this case Eq. (2.30) is reduced to

$$i\partial_{\zeta}U - \text{sgn}(\beta_2) \frac{L_{\text{NL}}}{2L_D} \partial_{\tau}^2 U + e^{-L_{\text{NL}} \alpha \zeta} |U|^2 U = 0, \quad (2.31)$$

where $\text{sgn}(\beta_2)$ denotes the sign of the group velocity dispersion and $L_D = \frac{T_0^2}{|\beta_2|}$ is the dispersion length. Since the parameter T_0 is arbitrary, it can be chosen as $\sqrt{\frac{|\beta_2|}{\gamma P_0}}$ so that $L_D = L_{\text{NL}}$ and thus,

$$i\partial_{\zeta}U - \frac{\text{sgn}(\beta_2)}{2} \partial_{\tau}^2 U + e^{-L_{\text{NL}} \alpha \zeta} |U|^2 U = 0. \quad (2.32)$$

Throughout this dissertation we deal with standard SMFs working at the C-band where the GVD coefficient is dominant and so Eq. (2.32) is here the adopted form of the NLSE. The GVD coefficient β_2 [$\frac{\text{ps}^2}{\text{km}}$] can be expressed in terms of the dispersion parameter D [$\frac{\text{ps}}{\text{nm.km}}$] as follows:

$$\beta_2 = -\frac{\lambda}{\omega} D = -\frac{\lambda^2}{2\pi c} D. \quad (2.33)$$

For instance, in a standard SMF at 1550 nm where the dispersion parameter is $\approx 17 \frac{\text{ps}}{\text{nm.km}}$, the GVD coefficient is $\approx -22 \frac{\text{ps}^2}{\text{km}}$. It is evident from Eq. (2.32) that the sign of β_2 plays a role in the behavior of the NLSE. As we will see later light evolves differently in a nonlinear medium with normal ($\beta_2 > 0$) or anomalous ($\beta_2 < 0$) dispersion.

2.2 Solutions for the NLSE

There have been extensive efforts to find analytical solutions for the nonlinear Schrödinger equation in different conditions [51, 52]. Several solutions such as solitons [53] and breathers [54] have been obtained depending on initial conditions. However, in general case there is no analytical solution and thus, exploiting numerical methods is indispensable. In order to validate the employed numerical algorithm we need to compare it with some analytical results. The simplest temporal solution to the NLSE in a lossless medium is the fundamental *soliton* that can be utilized as a criterion for verifying numerical results. Before solving the NLSE, two pulse shapes commonly used in optics, i.e. *Gaussian* and *hyperbolic secant* are introduced and compared. For a temporal or spectral pulse $x(s)$ where s can be time or frequency, the

root-mean square (RMS) width σ_s is defined as [55]

$$\sigma_s^2 = \frac{\int_{-\infty}^{+\infty} (s - \mu_s)^2 |x(s)|^2 ds}{\int_{-\infty}^{+\infty} |x(s)|^2 ds}, \quad \text{where} \quad \mu_s = \frac{\int_{-\infty}^{+\infty} s |x(s)|^2 ds}{\int_{-\infty}^{+\infty} |x(s)|^2 ds}. \quad (2.34)$$

For a temporal pulse $x(t)$ and its Fourier transform $\hat{x}(\omega)$ there is a fundamental relation between their RMS widths known as Heisenberg's uncertainty principle which is derived using the Cauchy–Schwarz inequality and is given by [55]

$$\sigma_t \sigma_\omega \geq \frac{1}{2}. \quad (2.35)$$

Another definition for temporal and spectral width which is commonly used in optics is the full-width at half-maximum (FWHM) duration [41]. The FWHM of a pulse $x(s)$ is the distance between the positions at which $|x(s)|^2 = \frac{1}{2} |x_{\max}|^2$. The Gaussian and hyperbolic secant pulse shapes and their Fourier transforms are expressed as

$$x(t) = e^{-\frac{t^2}{2T_0^2}}, \quad \hat{x}(\omega) = \sqrt{2\pi} T_0 e^{-\frac{T_0^2 \omega^2}{2}}, \quad (2.36a)$$

$$y(t) = \text{sech}\left(\frac{t}{T_0}\right), \quad \hat{y}(\omega) = \pi T_0 \text{sech}\left(\frac{\pi T_0 \omega}{2}\right). \quad (2.36b)$$

An interesting point about these two pulse shapes is that their Fourier transform has the same shape as their temporal function. Table 2.1 shows different parameters of the Gaussian and sech pulses given in Eqs. (2.36). It is clear from the table that for the Gaussian pulse $\sigma_t \sigma_\omega = \frac{1}{2}$;

Pulse	σ_t	σ_ω	T_{FWHM}	Ω_{FWHM}
Gaussian	$\frac{T_0}{\sqrt{2}}$	$\frac{1}{T_0 \sqrt{2}}$	$2\sqrt{\ln 2} T_0$	$\frac{2\sqrt{\ln 2}}{T_0}$
sech	$\frac{\pi T_0}{2\sqrt{3}}$	$\frac{1}{T_0 \sqrt{3}}$	$2 \ln(\sqrt{2} + 1) T_0$	$\frac{4 \ln(\sqrt{2} + 1)}{\pi T_0}$

Table 2.1 – Temporal and Spectral Widths.

in fact, it is the only pulse satisfying equality in Heisenberg's uncertainty principle. In the case of sech pulse, $\sigma_t \sigma_\omega = \frac{\pi}{6}$ which is certainly greater than $\frac{1}{2}$. On the other hand, $T_{\text{FWHM}} \Omega_{\text{FWHM}}$ is equal to $4 \ln 2 \approx 2.773$ for the Gaussian pulse, and $\frac{8}{\pi} \ln^2(\sqrt{2} + 1) \approx 1.978$ for the sech pulse. Another interesting point about these two signals is that although $\sigma_t \sigma_\omega$ of the Gaussian pulse is less than that of the sech pulse, its $T_{\text{FWHM}} \Omega_{\text{FWHM}}$ is larger. Fig. 2.1 compares the temporal and spectral shapes of the Gaussian and sech pulses for the FWHM temporal width of unity ($T_{\text{FWHM}} = 1$). Using such pulses, certain solutions of the NLSE are presented in the coming sections.

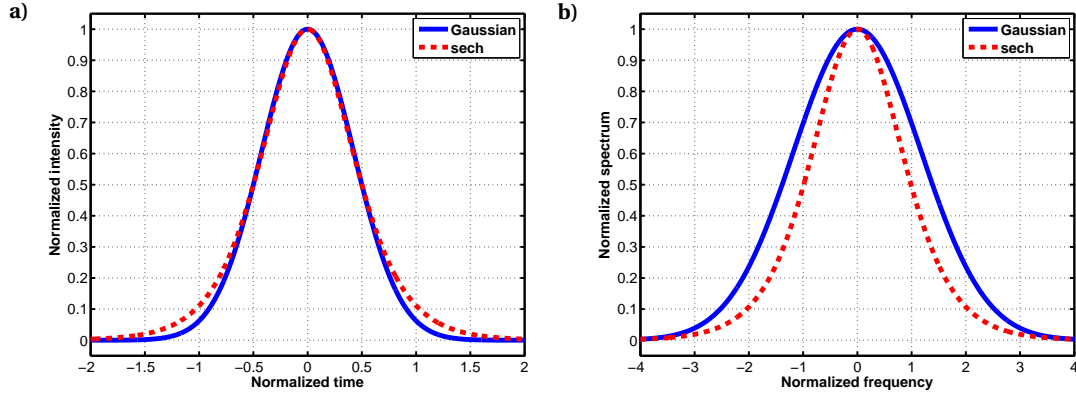


Figure 2.1 – Comparison of the Gaussian and sech pulses with $T_{FWHM} = 1$; a) Temporal intensity, b) Spectral intensity.

2.2.1 Propagation in Linear and Dispersive Media

If the nonlinear term in the NLSE is neglected, only remains the dispersion effect and Eq. (2.28) reduces to

$$i\partial_z U + \sum_{m=1}^{\infty} i^m \frac{\beta_m}{m!} \partial_t^m U = 0. \quad (2.37)$$

Taking the Fourier transform of Eq. (2.37) and substituting ∂_t by $-i\Omega$ result in

$$i\partial_z \hat{U} + \hat{U} \sum_{m=1}^{\infty} \frac{\beta_m}{m!} \Omega^m = 0. \quad (2.38)$$

Eq. (2.38) is a first-order linear differential equation and its solution is

$$\hat{U}(z, \Omega) = \hat{U}(0, \Omega) e^{iz \sum_{m=1}^{\infty} \frac{\beta_m}{m!} \Omega^m} \quad (2.39)$$

The temporal shape of pulses can be obtained by taking the inverse Fourier transform of Eq. (2.39) which depends on the initial pulse shape $U(0, t)$. It is clear from the expression that propagation does not affect the spectrum of the traveling signal, i.e. $|\hat{U}(z, \Omega)|^2 = |\hat{U}(0, \Omega)|^2$. However, the temporal shape can dramatically change in a linear dispersive medium. As an example, suppose that a Gaussian pulse given in Eq. (2.36) is launched into a standard SMF where the second-order dispersion coefficient is dominant. According to Eq. (2.39) the propagating pulse has the following Fourier transform at position z :

$$\hat{U}(z, \Omega) = \sqrt{2\pi} T_0 e^{-\frac{T_0^2}{2} \Omega^2} e^{iz(\beta_1 \Omega + \frac{\beta_2}{2} \Omega^2)} = \sqrt{2\pi} T_0 e^{i\beta_1 z \Omega} e^{-\frac{\Omega^2}{2} (T_0^2 - i\beta_2 z)}. \quad (2.40)$$

The temporal pulse is obtained by taking the inverse Fourier transform of Eq. (2.40) as follows:

$$U(z, t) = \frac{1}{\sqrt{1 - i\frac{\beta_2 z}{T_0^2}}} e^{-\frac{(t - \beta_1 z)^2}{2(T_0^2 - i\beta_2 z)}}. \quad (2.41)$$

This way the pulse intensity is given by

$$|U(z, t)|^2 = \frac{1}{\sqrt{1 + \left(\frac{\beta_2 z}{T_0^2}\right)^2}} e^{-\frac{(t - \beta_1 z)^2}{T_0^2 \left(1 + \left(\frac{\beta_2 z}{T_0^2}\right)^2\right)}}. \quad (2.42)$$

It is deduced from Eq. (2.42) that the propagating pulse remains Gaussian, but its temporal width increases while its spectral shape does not change. The following broadening factor determines the amount of increase in the temporal width of the pulse at the output of a fiber of length L :

$$\frac{T_L}{T_0} = \sqrt{1 + \left(\frac{L}{L_D}\right)^2}, \quad (2.43)$$

where $L_D = \frac{T_0^2}{|\beta_2|}$ is the fiber dispersion length. For example, a Gaussian pulse with the FWHM of 30 ps and the peak power of 100 mW is launched at the input of a 40-km long fiber with the GVD of $-22 \frac{\text{ps}^2}{\text{km}}$. Fig. 2.2a compares the input and output of the fiber and shows clearly the temporal broadening due to propagation; while it is implied from Fig. 2.2b that the pulse spectrum remains unchanged during propagation.

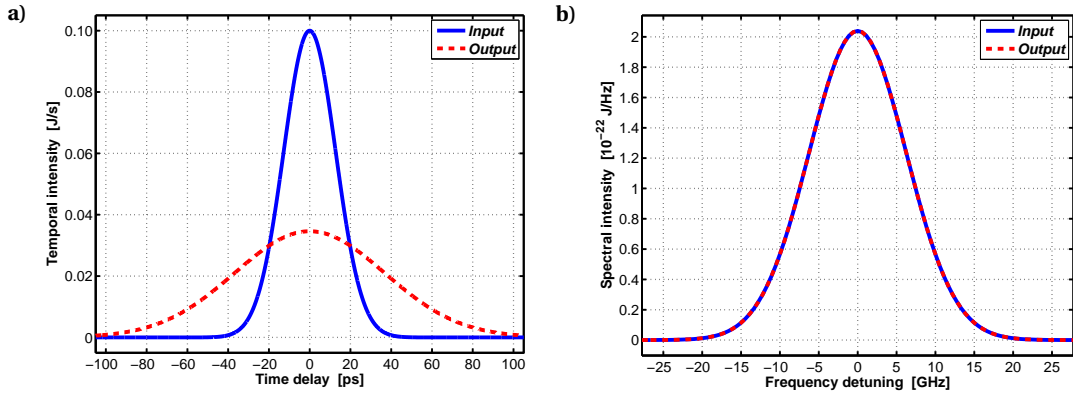


Figure 2.2 – Comparison of the input and output of a fiber of 40 km with $\beta_2 = -22 \frac{\text{ps}^2}{\text{km}}$ for a Gaussian pulse with the FWHM of 30 ps; a) Temporal intensity, b) Spectral intensity.

2.2.2 Propagation in Nonlinear and Nondispersive Media

A medium with pure nonlinearity gives a direct insight to the main contribution of the Kerr effect in optical fibers, i.e. self-phase modulation (SPM). Therefore, it is essential to analyze a non-dispersive Kerr medium in details. In such a medium all the dispersion coefficients β_m are null for $m \geq 2$ and thus Eq. (2.30) is simplified to

$$i\partial_\zeta U + e^{-\frac{\alpha}{\gamma P_0} \zeta} |U|^2 U = 0. \quad (2.44)$$

Chapter 2. Nonlinear Schrödinger Equation

Although Eq. (2.44) is a nonlinear differential equation, it is integrable and can be solved analytically [56]. The key point in solving the equation is to show that the field intensity $|U(\zeta, \tau)|$ is independent of position ζ . It can be demonstrated as follows:

$$\begin{aligned} & \overbrace{\left(i\partial_\zeta U + e^{-\frac{\alpha}{\gamma P_0}\zeta} |U|^2 U \right)}^{=0} U^* - \overbrace{\left(i\partial_\zeta U + e^{-\frac{\alpha}{\gamma P_0}\zeta} |U|^2 U \right)^*}^{=0} U = \\ & iU^* \partial_\zeta U + e^{-\frac{\alpha}{\gamma P_0}\zeta} |U|^4 - (-iU \partial_\zeta U^* + e^{-\frac{\alpha}{\gamma P_0}\zeta} |U|^4) = \\ & i(U^* \partial_\zeta U + U \partial_\zeta U^*) = i\partial_\zeta (U^* U) = i\partial_\zeta |U|^2 = 0. \end{aligned} \quad (2.45)$$

Since $\partial_\zeta |U|^2 = 0$, it is evident that $|U|$ can be treated as a constant with respect to ζ . Rearranging Eq. (2.44) gives the following well-known differential equation

$$\frac{\partial_\zeta U}{U} = i|U|^2 e^{-\frac{\alpha}{\gamma P_0}\zeta}, \quad (2.46)$$

whose right-hand side is purely exponential with respect to ζ and can be integrated analytically. Assuming a general initial pulse $U(0, \tau)$ and integrating over the interval $[0, z]$ lead to

$$U(\zeta, \tau) = U(0, \tau) \exp \left(i\gamma P_0 |U|^2 \frac{1 - e^{-\frac{\alpha}{\gamma P_0}\zeta}}{\alpha} \right). \quad (2.47)$$

Transforming the variables according to Eq. (2.29) with T_0 of unity, the solution is expressed by

$$U(z, t) = U(0, t - \beta_1 z) e^{i\gamma P_0 |U(0, t - \beta_1 z)|^2 \frac{1 - e^{-\alpha z}}{\alpha}}. \quad (2.48)$$

There are several important points in Eq. (2.48) to which attention must be paid. Firstly, the pulse shape is not affected by a purely Kerr medium because $|U(z, t)| = |U(0, t - \beta_1 z)|$. Secondly, the field experiences a phase modulation proportional to the intensity of the field itself; that is why it is called the self-phase modulation (SPM). Thirdly, for a fiber of length L the induced phase is proportional to the effective length of the fiber defined as [3]

$$L_{\text{eff}} = \frac{1 - e^{-\alpha L}}{\alpha}. \quad (2.49)$$

It is easily seen that for lossless fibers where $\alpha = 0$, we have $L_{\text{eff}} = L$. Moreover, the maximum of effective length is given by $\frac{1}{\alpha}$ which can be obtained by letting L go to infinity. As an example, for standard fibers with $\alpha = 0.2 \frac{\text{dB}}{\text{km}}$, the maximum effective length is ≈ 21.7 km. According to Eq. (2.48) the nonlinear phase experienced by a normalized optical field U is given by

$$\Phi_{\text{NL}} = \gamma P_0 |U|^2 L_{\text{eff}} = |U|^2 \frac{L_{\text{eff}}}{L_{\text{NL}}}. \quad (2.50)$$

Since the field is normalized, the maximum phase shift is given by $\gamma P_0 L_{\text{eff}} = L_{\text{eff}}/L_{\text{NL}}$; for example for a very long fiber ($L_{\text{eff}} \approx 21$ km) with $\gamma = 1.5 \frac{\text{W}^{-1}}{\text{km}}$, an optical pulse with a peak power 100 mW experience a nonlinear phase shift of around π rad. Although SPM does not

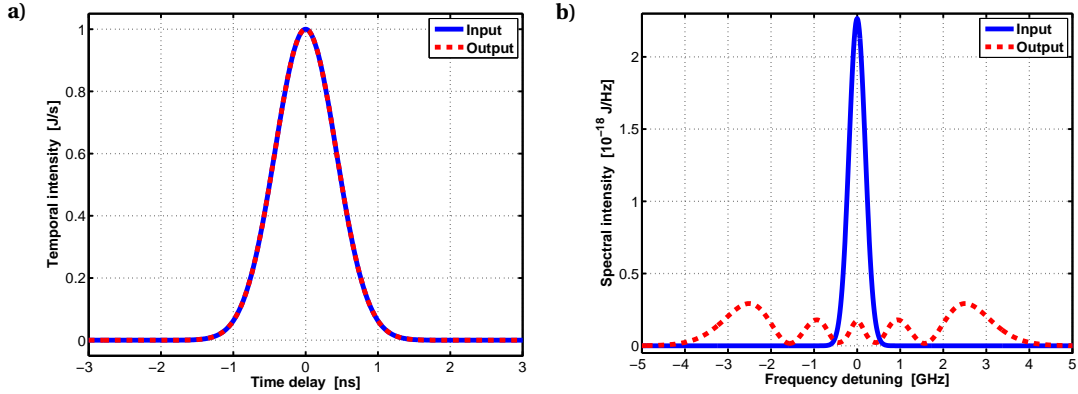


Figure 2.3 – Numerical comparison of the normalized input and output of a 10-km fiber with $\gamma = 1.8 \frac{\text{W}^{-1}}{\text{km}}$ and $\alpha = 0.2 \frac{\text{dB}}{\text{km}}$ for a Gaussian pulse with the FWHM of 1 ns and the peak power of 1 W; a) Temporal intensity, b) Spectral intensity.

affect the temporal shape of optical pulses, it can change their spectrum substantially. For example, suppose a Gaussian pulse with a peak power 1 W and a FWHM 1 ns is launched into a 10-km long fiber with $\alpha = 0.2 \frac{\text{dB}}{\text{km}}$ and $\gamma = 1.8 \frac{\text{W}^{-1}}{\text{km}}$. Fig. 2.3 compares the normalized input and output pulses in the time and frequency domains. As it is clear from Fig. 2.3a, the pulse shape remains unchanged in propagation whilst Fig. 2.3b shows the oscillatory behaviour of the spectrum due to SPM [57]. The fluctuations of the spectrum due to self-phase modulation, described numerically in Fig. 2.3b can also be observed experimentally. To do so, an experiment illustrated in Fig. 2.4 has been carried out using a 10.6-km dispersion-shifted fiber (DSF) with $\alpha = 0.24 \frac{\text{dB}}{\text{km}}$ and $\gamma = 2.9 \frac{\text{W}^{-1}}{\text{km}}$. The output of a continuous-wave (CW) laser at 1551 nm is modulated using a semiconductor optical amplifier (SOA) driven by a pulse generator. The modulated light is amplified by an erbium-doped fiber amplifier (EDFA) and its peak power is regulated by a variable optical attenuator (VOA) and monitored by a calibration setup, then launched into the fiber. The output spectrum is measured by an optical spectrum analyser (OSA). Fig. 2.5 shows the measured spectrum at the output of the fiber.

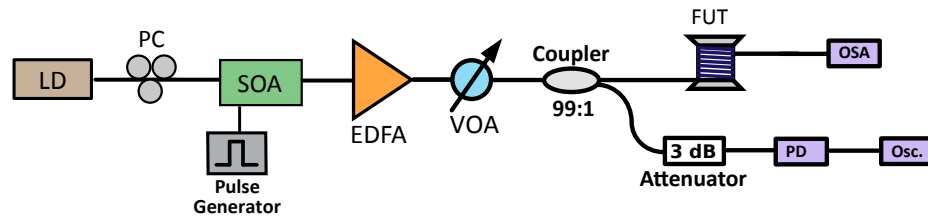


Figure 2.4 – Scheme of the experimental setup for SPM measurement. LD: laser diode, PC: polarization controller, SOA: semiconductor optical amplifier, EDFA: erbium-doped fiber amplifier, VOA: variable optical attenuator, FUT: fiber under test, OSA: optical spectrum analyzer, PD: photo-detector, Osc.: Oscilloscope.

The oscillatory behavior of the spectrum is obvious from the figure; we can also see that by boosting the peak power the number of spectral extrema increases because of inducing more phase due to SPM. It should be noted that the zero-dispersion wavelength of the used fiber is located around 1562 nm so that the fiber has normal dispersion at the laser wavelength of

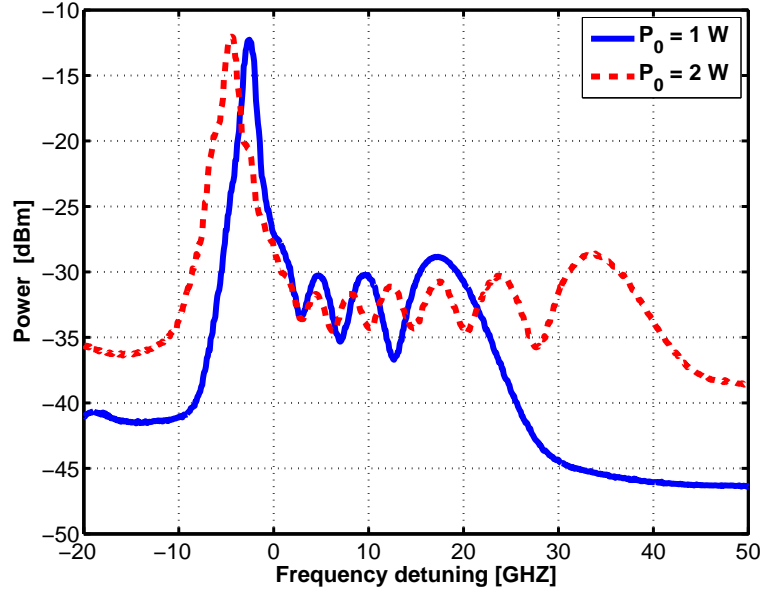


Figure 2.5 – Experimental observation of spectral oscillations due to self phase modulation.

1551 nm. Therefore, there is no modulation instability (MI) to affect the spectrum of light and hamper the observation of SPM-induced spectral fluctuations. It is also worth mentioning that the asymmetry in the measured spectrum is due to the asymmetry in the generated pulses because the SPM-induced phase is highly dependent on the pulse shape.

2.2.3 Propagation in Nonlinear and Dispersive Media

When both dispersion and nonlinearity exist in a medium, they interact with each other and based on their magnitude and characteristics, different phenomenon can be observed. Unfortunately, there is no analytical solution for the NLSE in its general form, yet in some special cases it is possible to have closed-form solutions providing an insight on how the interaction of dispersion and nonlinearity takes place. In this section, the special case of *soliton* propagation is investigated as a solution to the NLSE. Solitons are referred to the pulses that keep their temporal and spectral shapes unchanged during the propagation in a nonlinear dispersive medium. In fact, dispersion and nonlinearity interact in a way that the effect of one is exactly compensated by the other's. Suppose a lossless fiber with the nonlinear coefficient $\gamma > 0$ and the GVD coefficient β_2 in the anomalous regime, i.e. $\text{sgn}(\beta_2) < 0$, so that Eq. (2.32) reduces to

$$i\partial_\zeta U + \frac{1}{2}\partial_\tau^2 U + |U|^2 U = 0. \quad (2.51)$$

In this case, if a hyperbolic secant pulse is launched into the fiber, i.e. $U(0, \tau) = \text{sech}(\tau)$, a solution to Eq. (2.51) can be expressed by $U(\zeta, \tau) = \text{sech}(\tau)e^{i\zeta/2}$ referred to as the *fundamental*

soliton; the traveling soliton is given by

$$U(z, t) = \text{sech}\left(\frac{t - \beta_1 z}{T_0}\right) e^{i \frac{\gamma P_0}{2} z}, \quad (2.52)$$

where $T_0 = \sqrt{\frac{|\beta_2|}{\gamma P_0}}$ is the pulse width. It is seen that the width of soliton depends upon the peak power of pulse so it is important to have a lossless medium in order to keep the peak power unchanged and so the pulse width. Another interesting point about the fundamental soliton is its self-phase modulation which is proportional to half the peak power. The input pulse can be $N \text{sech}(\tau)$ where N is an integer; in the case of integers higher than 1, higher-order solitons propagate in the fiber. For instance, when $N = 2$, the second-order soliton is given by [3]

$$U(\zeta, \tau) = 4 \frac{\cosh(3\tau) + 3e^{4i\zeta} \cosh(\tau)}{\cosh(4\tau) + 4\cosh(2\tau) + 3\cos(4\zeta)} e^{i \frac{\zeta}{2}}. \quad (2.53)$$

It should be noted that in contrast to the fundamental soliton, higher-order solitons alter their shape periodically with period $\frac{\pi}{2} L_{\text{NL}}$. Fig 2.6a shows the propagation of the fundamental

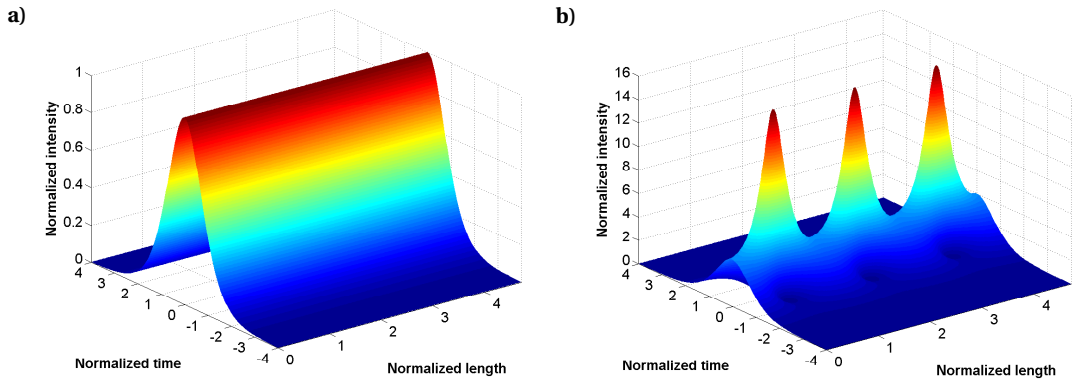


Figure 2.6 – Spatiotemporal distribution of solitons in optical fibers for a) Fundamental soliton, b) Second-order soliton.

soliton in optical fibers. It is clear that the shape of the pulse preserves during the propagation which makes it a promising candidate for optical communications in dispersive media. However, because of attenuation the pulse power dissipates and its shape deviates from the initial one and thus it should be used in low dissipation regime or with amplification. Fig. 2.6b illustrates the spatiotemporal distribution of the second-order soliton showing the periodic change of the pulse shape during propagation. Solitons are among very rare solutions of the nonlinear Schrödinger equation and they propagate in very special conditions. However, their importance is in providing analytical solutions; in other words, numerical algorithms for simulating the NLSE can be evaluated using solitons. All the numerical methods used in this work have been verified in this way.

2.3 Split-Step Fourier Method

As we have seen in the previous sections, analytical solutions for the nonlinear Schrödinger equation are available for very specific conditions. In real optical systems however, practical conditions make systems so complicated that they cannot be described by analytical solutions. Therefore, numerical methods are indispensable for simulating real conditions in an optical system. For the special case of nonlinear fiber optics, the most used numerical algorithm is the split-step Fourier method [3]. This algorithm simulates the propagation of light in optical fiber step by step considering either dispersion or nonlinearity [58]. In other words, the fiber is treated as a dispersive but linear in the frequency domain; and nonlinear but non-dispersive in the time domain. The reason for commuting from time to frequency lies in the fact that the NLSE's solution is known for pure nonlinearity in the time domain and for pure dispersion in the frequency domain. It can be summarized in the following two expressions assuming two positions z_n and z_{n+1} on the fiber for the NLSE given in Eq. (2.28):

$$\text{Dispersion: } \hat{U}(z_{n+1}, \Omega) = \hat{U}(z_n, \Omega) e^{i(z_{n+1}-z_n) \sum_{m=1}^{\infty} \frac{\beta_m}{m!} \Omega^m}, \quad (2.54a)$$

$$\text{Nonlinearity: } U(z_{n+1}, t) = U(z_n, t) e^{i\gamma P_0 |U|^2 \frac{e^{-\alpha z_n} - e^{-\alpha z_{n+1}}}{\alpha}}. \quad (2.54b)$$

The idea behind the split-step Fourier method is depicted in Fig. 2.7 where an optical fiber of length L is divided into uniform pieces of length Δz . The effect of dispersion is calculated by the dispersion operator \hat{D} in the frequency domain, described in Eq. (2.54a); while the nonlinearity operator N given in Eq. (2.54b) is responsible for simulating the Kerr effect in the time domain. The fast Fourier transform (FFT) algorithm and its inverse are utilized for commuting from time to frequency to speed up the numerical computation [59]. It can

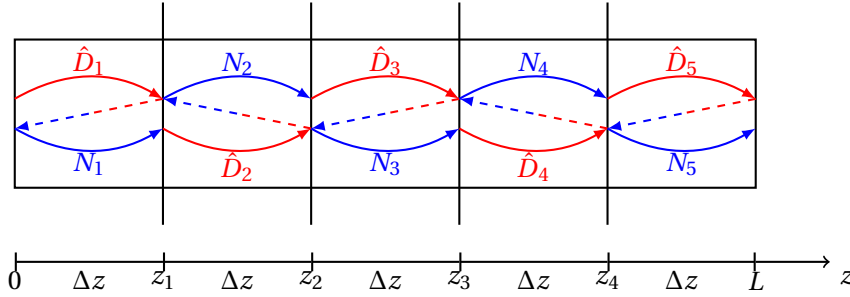


Figure 2.7 – Illustration of the split-step Fourier method; \hat{D} stands for the dispersion operator and N for the nonlinear operator.

be proved that the accuracy of the split-step Fourier method illustrated in Fig. 2.7 is of the second order of the step size, i.e. $(\Delta z)^2$ [3]. This accuracy can be easily increased to the third order $(\Delta z)^3$ without increasing the computational cost by symmetrizing the algorithm [60]. Fig. 2.8 shows the mechanism of the symmetric split-step Fourier method. The only difference with the ordinary algorithm is the initial and final half-steps which reduce the error in the method. It is evident that the smaller the step size Δz is, the less the calculation error will be. However, by decreasing the step size the processing time increases. Therefore, there is a

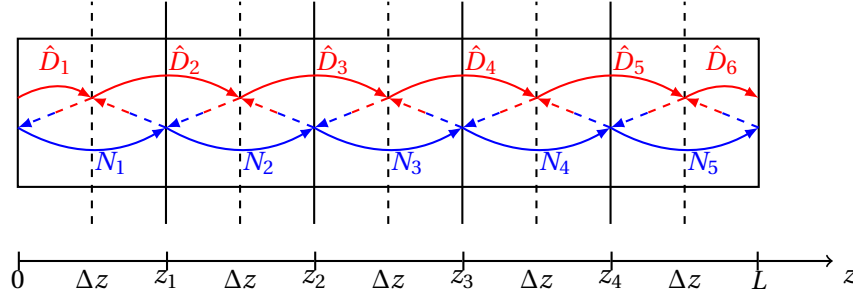


Figure 2.8 – Illustration of the symmetric split-step Fourier method

trade-off between the numerical error and consumed time [61]. As a rule of thumb, a step size less than the dispersion length L_D and the nonlinear length L_{NL} is a good choice. To make sure that the selected step size does not make systematic error, it is necessary to compare the time energy and spectral energy before and after propagation using Parseval's theorem given by [55]

$$\int_{-\infty}^{+\infty} |x(t)|^2 dt = \frac{1}{2\pi} \int_{-\infty}^{+\infty} |\hat{x}(\omega)|^2 d\omega. \quad (2.55)$$

Additionally, specific analytical solutions such as solitons can be used to verify the validity of numerical algorithms. Finally, it should be noted that the split-step Fourier method is trustworthy as long as the slowly varying envelope approximation is valid. Therefore, in situations like few-cycle pulses other numerical methods such as finite-difference time domain (FDTD) must be applied directly to Maxwell's equations. As an example of using the split-step Fourier method, consider a 25-km standard SMF with $\alpha = 0.2 \frac{\text{dB}}{\text{km}}$, $\beta_2 = -22 \frac{\text{ps}^2}{\text{km}}$, and $\gamma = 1.6 \frac{\text{W}^{-1}}{\text{km}}$. A Gaussian pulse with the peak power of 1 W and the FWHM of 30 ps is launched into the fiber. The output of the fiber has been calculated by running a split-step program in MATLAB®. Fig. 2.9 compares the input and output of the fiber in the time and frequency domains. As it is evident from the figure, the interaction of dispersion and the Kerr effect

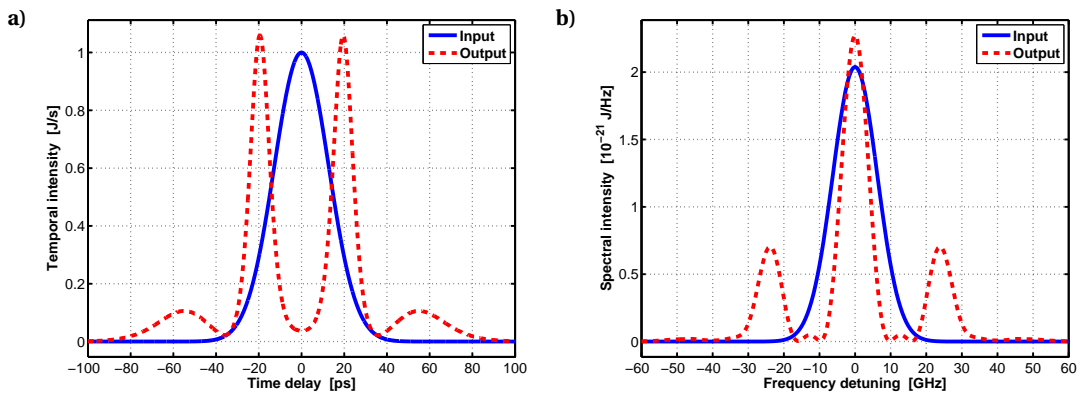


Figure 2.9 – Propagation of a Gaussian pulse in an optical fiber evaluated by the split-step Fourier method: a) Temporal evolution, b) Spectral evolution.

can change the temporal and spectral shapes of the pulse substantially compared to the conditions where there is either dispersion or nonlinearity. Fig. 2.9a shows that how a single pulse propagating in a nonlinear dispersive medium can be broken up to multiple pulses; while Fig. 2.9b demonstrates the emergence of spectral components in the pulse due to nonlinearity.

2.4 SPM-Based Measurement of Nonlinear Coefficient

The Kerr effect or the intensity-dependent refractive index causes only self-phase modulation (SPM) on a monochromatic wave in a non-dispersive medium; so SPM is the result of pure Kerr effect and can be used to measure the nonlinear coefficient of a medium efficiently. This phenomenon broadens the spectrum of optical pulses while it does not affect their temporal shape except adding a phase proportional to optical intensity. Self phase modulation was first observed in CS₂ (carbon disulfide that is a colorless liquid) in 1967 [62]. Then, it was demonstrated in an optical fiber whose core was filled with CS₂ in 1974 [63]. The thorough analysis and demonstration of SPM in silica-core fibers was carried out in 1978 by Stolen and Lin [57]. The induced phase on an optical pulse due to SPM is in proportion to its shape and thus, in order to have a uniform phase modulation a rectangular pulse must be used. The induced phase by a rectangular pulse is given by

$$\Phi_{NL} = \gamma P_0 L_{eff}. \quad (2.56)$$

Since the induced phase is proportional to the nonlinear coefficient, it is possible to obtain the nonlinear coefficient of a fiber by measuring the amount of self-phase modulation. A typical instrument of measuring phase is an interferometer that translates the phase difference to intensity that can be easily detected. Here we use a self-aligned interferometer for measuring the nonlinear coefficient of different types of optical fibers [64]. The scheme of a self-aligned interferometer for measuring the nonlinear coefficient is shown in Fig. 2.10. The main advantage of this technique for measuring the Kerr effect is that it can be applied to all types of optical fibers with normal and anomalous dispersions because the measurement is carried out on optical pulses in time domain; while other methods are based on the spectral measurement and thus can only be used for fibers with normal dispersion that do not suffer from spectral broadening due to modulation instability. The working principle of the self-

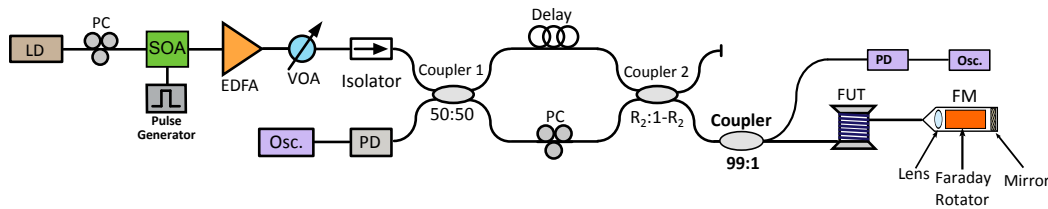


Figure 2.10 – Scheme of a self-aligned interferometer for nonlinear coefficient measurement. LD: laser diode, PC: polarization controller, SOA: semiconductor optical amplifier, VOA: variable optical attenuator, PD: Photo-detector, Osc.: oscilloscope, FUT: fiber under test, FM: Faraday mirror

aligned interferometer is explained in Fig. 2.11 [65]. An optical pulse is generated and boosted, then split into two pulses via the first coupler. The two pulses are combined together in the second coupler but with different delays and coupling ratios. Two pulses travel through the fiber under test (FUT) and then reflect from a Faraday mirror. After traveling back through the same path, they are detected by a photo-detector and acquired via an oscilloscope. Since the forward and backward pulses experience the same delay arm (self-aligned), three pulses are measured in the oscilloscope so that the middle pulse is the interference of two pulses. Since the two interfering pulses travel the same length, they have the same linear phase due to propagation; while they experience different nonlinear phase from SPM because of their different power levels. This way, it is possible to measure the induced nonlinear phase without any contribution of propagation phase.

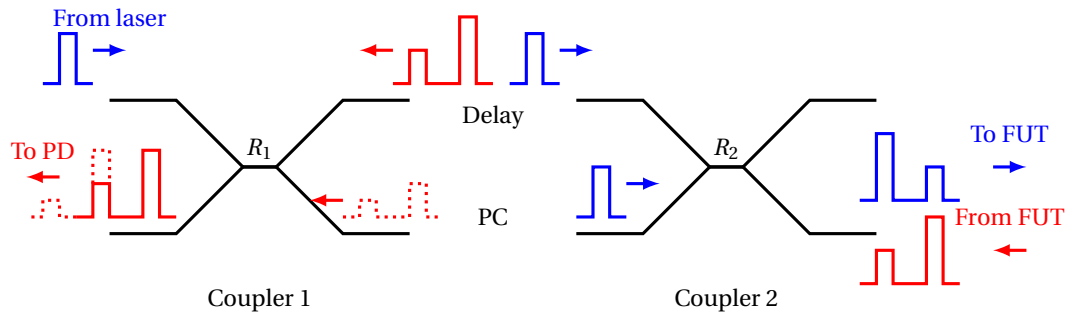


Figure 2.11 – Illustration of the interferometry setup. The forward traveling pulses are depicted in blue while the returning signals are drawn in red.

The polarization controller in one of the interferometer's arms is essential to maximize the interference of the two optical pulses by matching their polarization state. Moreover, the Faraday mirror used at the end of the FUT, reflects the orthogonal state of the incident polarization and thus, the optical pulse traveling in the fiber experiences two orthogonal polarizations. This way, all polarization effects due to random birefringence and environmental perturbations are cancelled [66]. As it is illustrated in the experimental setup of Fig. 2.10, the Faraday mirror includes a collimating lens, an ordinary mirror and a Faraday rotator. The Faraday rotator is an *optically active* medium working based on the magneto-optic effect. As light propagates through the Faraday rotator, its *plane* of polarization rotates and the angle of rotation is determined by the length of the medium, in this case 45° . Moreover, the plane of polarization in a Faraday mirror rotates in the same direction regardless of the propagation direction. Therefore, the backward wave also experiences a polarization plane rotation of 45° and thus the final rotation will be 90° . It must be noted that this argument is true for linear (planar) polarizations, while the Faraday mirror has no effect on circular polarizations. Actually, circular polarizations are eigenstates of a Faraday rotator. However, the ordinary mirror alters the handedness of circular polarizations and thus transforms a circular polarization to its orthogonal state. An elliptic polarization can be expressed in terms of a linear and a circular polarization, so the linear part of the reflected polarization state is transformed to its orthogonal counterpart by the Faraday rotator and its circular part is changed to an

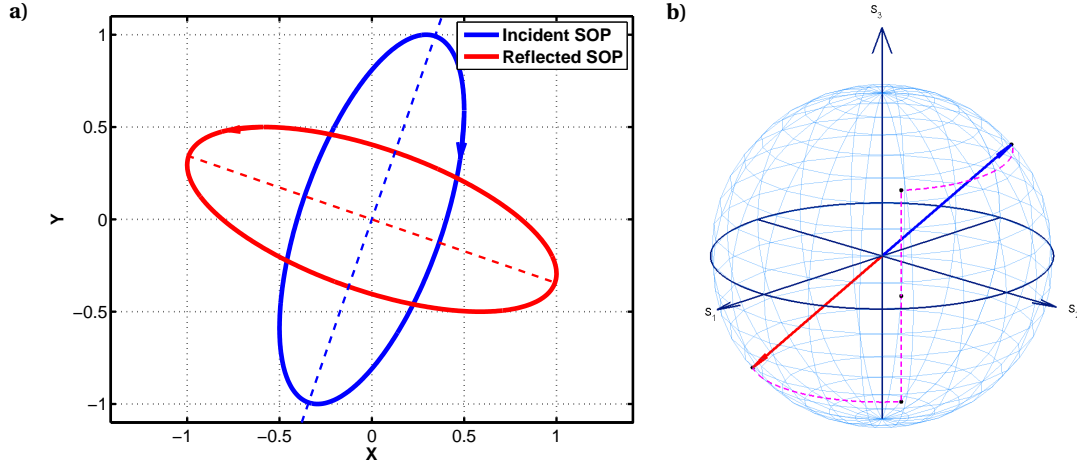


Figure 2.12 – Function of the Faraday mirror in reflecting the orthogonal polarization state of the incident wave: a) Incident and reflected states of polarization (SOP), b) Stokes representation of the Faraday mirror on the Poincaré sphere.

orthogonal one by the ordinary mirror. This way, every polarization state reflected from the Faraday mirror is orthogonal to its corresponding incident polarization.

Fig. 2.12 describes the function of the Faraday mirror used in this experiment. A righthanded (clockwise) elliptic polarization state depicted in Fig. 2.12a enters the Faraday mirror and the corresponding reflected one is a lefthanded (counterclockwise) elliptic polarization illustrated in the figure. As it is clear, the major axes of the two ellipses are perpendicular and the handedness of the polarization states is opposite. Fig. 2.12b demonstrates how the Faraday mirror works using the Stokes representation of the state of polarization (SOP) on the Poincaré sphere. The incident polarization state is rotated by 45° as it passes through the Faraday rotator. It is equivalent to a 90° rotation around the S_3 axis on the Poincaré sphere as it is shown in Fig. 2.12b; in fact, the Faraday rotator keeps S_3 unchanged. Then, the ordinary mirror reflect the incident light by altering its handedness and thus, by changing S_3 to $-S_3$ while keeping S_1 and S_2 fixed. On the Poincaré sphere it is represented by a reflection against the equator plane. Travelling again through the Faraday rotator, the reflected light experiences another 45° rotation in the same direction and equivalently, a rotation of 90° around the S_3 axis of the Poincaré sphere. This way, the final point on the Poincaré sphere is the antipodal of the initial one, demonstrating a polarization state orthogonal to the initial one.

2.4.1 Mathematical Analysis of the Self-Aligned Interferometer

In this section, the thorough analysis of the self-aligned interferometer for measuring the nonlinear coefficient is presented. This analysis demonstrates that the optimal ratio for the first coupler is 50%. Before analyzing the setup it is essential to describe the behaviour of a coupler in the field domain. Fig. 2.13 describes the output fields of a coupler with power ratio R versus its input fields. Such a description can be easily proved by applying the conservation of energy to input and output ports. It is clear that in a coupler with power ratio R , an input optical field is split into two branches with field ratios \sqrt{R} and $-i\sqrt{1-R}$ showing a 90°

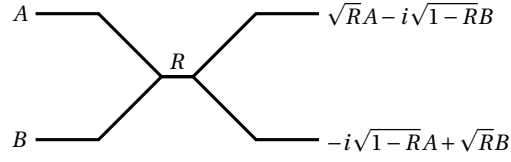


Figure 2.13 – Output ports of a coupler with power ratio R versus its inputs in the field domain.

phase difference. In order to analyze the self-aligned interferometer illustrated in Fig. 2.10, we consider the two interfering pulses as SL (short-long) and LS (long-short) showing that the first pulse travels through the short path and reflects back via the long path while the opposite holds for the second. Therefore, the following phase shifts experienced by the optical pulses can be defined:

1. Φ_D : Phase shift due to the delay in the long arm of the interferometer made by a 90-m long SME.
2. Φ_{PC-SL} and Φ_{PC-LS} : Phase shifts induced by the polarization controller (PC) in the short arm of the interferometer. It should be noted that although both pulses pass the same PC, they undergo different phase shifts depending on their input state of polarization. This way, the PC provides a degree of freedom on the phase difference between the two pulses.
3. $\Phi_{LN} = 2n_0kL$: Linear phase shift due to traveling twice across the FUT. n_0 is the linear refractive index, $k = \frac{2\pi}{\lambda}$ is the wavenumber and L is the fiber length.
4. Φ_{NL-SL} , ϕ_{NL-LS} : Nonlinear phase shifts acquired by each pulse which are obviously different because of different power levels.
5. Φ_{FM} : Phase shift due to reflection on the Faraday mirror.

The optical field of each interfering pulse at the input of the photo-detector can be expressed by

$$A_{SL} = i A_{in} e^{-\alpha L} (1 - R_1) \sqrt{R_2(1 - R_2)} e^{-i\Phi_{SL}}, \quad (2.57a)$$

$$A_{LS} = -i A_{in} e^{-\alpha L} R_1 \sqrt{R_2(1 - R_2)} e^{-i\Phi_{LS}}, \quad (2.57b)$$

where A_{in} is the input field of the first coupler; the phase shifts induced on the interfering pulses are given by

$$\Phi_{SL} = 2n_0kL + \Phi_{FM} + \Phi_D + \Phi_{PC-SL} + \Phi_{NL-SL}, \quad (2.58a)$$

$$\Phi_{LS} = 2n_0kL + \Phi_{FM} + \Phi_D + \Phi_{PC-LS} + \Phi_{NL-LS}. \quad (2.58b)$$

The interference of the two middle pulses is given by

$$A_{out} = A_{SL} + A_{LS} = i A_{in} e^{-\alpha L} \sqrt{R_2(1 - R_2)} \left((1 - R_1) e^{-i\Phi_{SL}} - R_1 e^{-i\Phi_{LS}} \right), \quad (2.59)$$

Chapter 2. Nonlinear Schrödinger Equation

so that the intensity of the pulse detected by the photo-detector is obtained as

$$\begin{aligned} P_{\text{out}} &= |A_{\text{out}}|^2 = |A_{\text{in}}|^2 e^{-2\alpha L} R_2(1-R_2) |(1-R_1)e^{-i\Phi_{\text{SL}}} - R_1 e^{-i\Phi_{\text{LS}}}|^2 \\ &= P_{\text{in}} e^{-2\alpha L} R_2(1-R_2) (1-2R_1(1-R_1)(1+\cos(\Phi_{\text{SL}}-\Phi_{\text{LS}}))). \end{aligned} \quad (2.60)$$

It can be easily seen that the visibility of P_{out} or its maximum to minimum ratio is optimal when $R_1 = \frac{1}{2}$ meaning that the first coupler must be 50:50. Using such a coupler leads to the following detected pulse:

$$P_{\text{out}} = P_{\text{in}} e^{-2\alpha L} R_2(1-R_2) \sin^2\left(\frac{\Phi_{\text{SL}}-\Phi_{\text{LS}}}{2}\right). \quad (2.61)$$

By using Eqs. (2.58) it is seen that the phase difference is given by only the nonlinear phase due to SPM and the phase induced by the polarization controller as follows:

$$\Phi_{\text{SL}} - \Phi_{\text{LS}} = \Phi_{\text{PC-SL}} - \Phi_{\text{PC-LS}} + \Phi_{\text{NL-SL}} - \Phi_{\text{NL-LS}}. \quad (2.62)$$

The polarization controller provides a degree of freedom that can be exploited by calibrating the PC in a linear regime (low power pulses) so that the detected pulse is maximal. It means that the phase difference induced by the PC is π rad; substituting Eq. (2.62) after calibration in Eq. (2.61) results in

$$P_{\text{out}} = P_{\text{in}} e^{-2\alpha L} R_2(1-R_2) \cos^2\left(\frac{\Phi_{\text{NL}}}{2}\right), \quad (2.63)$$

where $\Phi_{\text{NL}} = \Phi_{\text{NL-SL}} - \Phi_{\text{NL-LS}}$ is the phase difference experienced by two interfering pulses due to SPM. Eq. (2.63) indicates that when the nonlinear phase difference is π rad, the two pulses interfere destructively and thus they cancel out. Therefore, as the input power increases, the system transforms from the linear to nonlinear regime and the detected middle pulse decreases from its maximum to zero. The nonlinear phase difference due to SPM can be written

$$\Phi_{\text{NL}} = \Phi_{\text{NL-SL}} - \Phi_{\text{NL-LS}} = \gamma L_{\text{eff}} \left(\underbrace{\frac{1}{2} R_2 P_{\text{in}}}_{P_{\text{high}}} - \underbrace{\frac{1}{2} (1-R_2) P_{\text{in}}}_{P_{\text{low}}} \right), \quad (2.64)$$

where P_{high} and P_{low} are easily measured by the calibration circuit shown in Fig. 2.10 at the input of the FUT. Moreover, it is clear from Eq. (2.64) that the second coupler must be unbalanced unless the nonlinear phase is zero; in the experiment a 90:10 coupler has been used.

2.4.2 Experimental Results

After calibrating the polarization control in the linear or low-power regime, the peak power of the input pulse is increased to induce the phase difference on the two interfering pulses so that they cancel completely; at such a condition, according to Eq. (2.61) the nonlinear phase

difference is π rad and so by measuring the low and high powers at the input of the FUT we can calculate the nonlinear coefficient using Eq. (2.64) as follows:

$$\gamma = \frac{\pi}{L_{\text{eff}}(P_{\text{high}} - P_{\text{low}})}. \quad (2.65)$$

It is worth mentioning that the nonlinear coefficient measured in this way for standard optical fibers with random birefringence has a correction factor due to averaging over the polarization states of light that change randomly during the propagation. It has been shown theoretically [67] and experimentally [68] that such a correction factor must be $\frac{8}{9}$ so that the nonlinearity versus the Kerr coefficient is given by

$$\gamma = \frac{8}{9} \frac{2\pi}{\lambda} \frac{n_2}{A_{\text{eff}}}. \quad (2.66)$$

This experiment has been done for a variety of fibers, including standard single-mode fiber (SMF), dispersion-shifted fiber (DSF), and dispersion-compensating fiber (DCF) with different lengths. As an example, Fig. 2.14 shows the measured pulses for a 4-km DCF. The input pulse of 6-ns duration is plotted in Fig. 2.14a and the middle pulse resulted from the interference of two optical pulses is plotted in Fig. 2.14b. It shows clearly that the interference pulse is null at

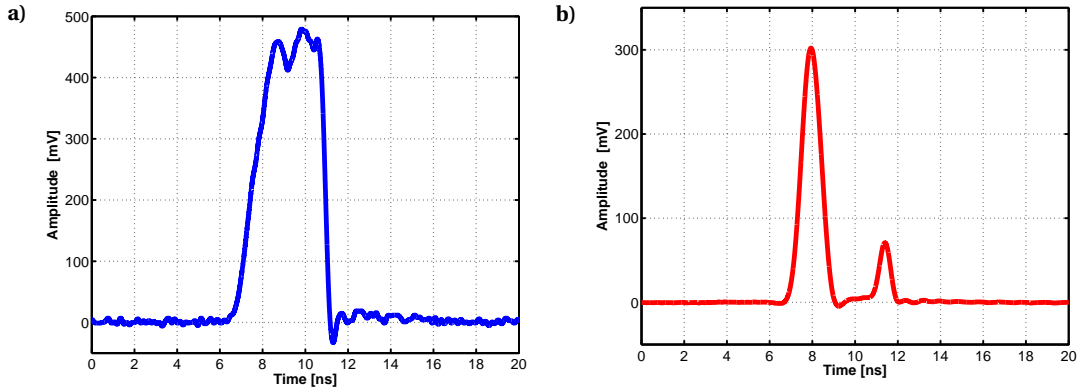


Figure 2.14 – Acquired pulses of the self-aligned interferometer for measuring the nonlinear coefficient of optical fibers a) Input pulse, b) Interfering pulse.

its middle part demonstrating a π phase shift due to SPM. It should be noticed that the tail and head parts of the interference pulse are not zero because the generated pulse is obviously not a perfect rectangle. Moreover, the input pulse shown in Fig. 2.14a is not symmetric and thus, the induced SPM is different in its head and tail as it is evident in the interference pulse shown in Fig. 2.14b. Table 2.2 represents the measured value of the nonlinear coefficient of different fibers available in the laboratory [65]. Several spools of optical fibers with different lengths have been measured using the self-aligned interferometric method. The measured nonlinear coefficients lie clearly in the typical range of γ for different kinds of optical fibers. The optical fiber in the last row of Table 2.2 is a special step-index optical fiber with the core diameter of around 5 micron and thus its effective area is about 4 times less than a standard SMF, so its nonlinear coefficient must be 4 times higher than a typical SMF.

Chapter 2. Nonlinear Schrödinger Equation

Type	Length [km]	γ [W^{-1}/km]
SMF	11.1	1.6
SMF	25.4	1.0
SMF	25.5	1.8
DSF	8.7	3.1
DSF	10.6	2.9
DSF	13.1	2.3
DSF	25.6	3.3
DCF	4.0	4.5
DCF	4.6	4.4
Special	4.8	4.0

Table 2.2 – Measured Nonlinear Coefficients.

Since fiber manufacturers use different types of refractive index profile with different amounts of dopants even for one kind of optical fiber, it is not surprising to see different values for γ . For instance, the nonlinear coefficient of standard SMFs can vary in a range of 1 to $2 \frac{\text{W}^{-1}}{\text{km}}$ depending on their refractive index profile [46], which is in accordance with the measured nonlinearity in Table. 2.2. The measured values of the nonlinear coefficient for different optical fibers given in Table. 2.2 are useful for analyzing any experiments involving the Kerr effect, especially for modeling the phenomenon of modulation instability (MI) in optical fibers which is the subject of the following chapters.

3 Modulation Instability Gain

The aim of this chapter is to derive the analytical form of modulation instability (MI) gain in optical fibers. Starting from the phase matching formalism of four-wave mixing (FWM) in both degenerate and non-degenerate cases, we proceed to the *linear stability analysis* of the nonlinear Schrödinger equation (NLSE) to investigate the small-signal behavior of a dispersive Kerr medium driven by a strong continuous-wave (CW) optical pump. Based on this analysis, the signal and idler fields are rigorously derived for two considerably different cases of lossless and lossy optical fibers. By using such fields, the gain of optical parametric amplification (OPA) which is inherently the same as MI is obtained for the phase-sensitive and phase-insensitive regimes. Moreover, using the characteristics of noise as a random process it is demonstrated that the gain of noise-seeded modulation instability is the sum of signal and idler gains. The gain spectrum of modulation instability in both lossless and lossy fibers is analytically derived and an appropriate approximation for the case of lossy fibers is presented. The MI gain spectrum in all cases are plotted and compared with the numerical results obtained from a Monte Carlo simulation of the NLSE solved by the split-step Fourier method. Finally, the modulation instability gain spectra, experimentally measured for different optical fibers are presented.

3.1 Dispersion Coefficients

Since the Kerr effect is a third-order nonlinear process, it leads to a four-wave mixing between frequency components of optical signals. Therefore, the conservation of photon energy $\hbar\omega$ leads to a symmetrical frequency band around a central frequency and thus the conservation of photon momentum $\hbar\beta(\omega)$ indicates that only even components of the propagation constant participate in the phase-matching condition. It will be mathematically proved when analysing the MI gain. Therefore, separating the propagation constant to even and odd functions is helpful in the analysis of the processes originating from the Kerr effect. Consider the propagation constant β at frequency $\omega = \omega_0 + \Omega$, where ω_0 is the central frequency and Ω is the frequency detuning so that $\Omega \ll \omega_0$. The Taylor expansion of the propagation constant

around the central frequency can be written as

$$\begin{aligned}
 \beta(\omega_0 + \Omega) &= \sum_{m=0}^{\infty} \frac{\beta_m}{m!} \Omega^m = \beta_0 + \sum_{m=1}^{\infty} \frac{\beta_m}{m!} \Omega^m = \beta_0 + \delta\beta \\
 &= \beta_0 + \sum_{m=1}^{\infty} \frac{\beta_{2m-1}}{(2m-1)!} \Omega^{2m-1} + \sum_{m=1}^{\infty} \frac{\beta_{2m}}{(2m)!} \Omega^{2m} \\
 &= \beta_0 + \delta\beta_o + \delta\beta_e,
 \end{aligned} \tag{3.1}$$

in which $\beta_0 = \beta(\omega_0)$ is the propagation constant at the central frequency and the dispersion coefficient β_m is given by $\frac{d^m \beta}{d\omega^m} |_{\omega=\omega_0}$. Besides, $\delta\beta_o$ and $\delta\beta_e$ denote the odd and even parts of the dispersion relation, respectively. Since $\delta\beta_e$ has a critical role in the Kerr effect processes, it is important to analyze it further. From a practical point of view when using standard SMFs in the C-band, the group-velocity dispersion β_2 is dominant and we can neglect higher order coefficients; so $\delta\beta_e = \frac{\beta_2}{2} \Omega^2$. However, when DSFs are used in the C-band, β_2 is so low that β_4 must also be taken into account which means $\delta\beta_e = \frac{\beta_2}{2} \Omega^2 + \frac{\beta_4}{24} \Omega^4$. It should be noted that for a pump wavelength around the zero-dispersion wavelength of an optical fiber, the group-velocity dispersion coefficient β_2 is approximated by the third-order dispersion as follows [69]:

$$\beta_2 \approx (\omega_0 - \omega_{zd}) \beta_3, \tag{3.2}$$

where ω_{zd} shows the zero-dispersion frequency. Moreover, the third-order dispersion coefficient is given by the dispersion slope of the fiber via the following relation [70]:

$$\beta_3 = \left(\frac{\lambda^2}{2\pi c} \right)^2 \frac{dD}{d\lambda}, \tag{3.3}$$

in which D is the dispersion parameter and $\frac{dD}{d\lambda}$ is the dispersion slope provided by fiber manufacturers. For instance, the nominal value of dispersion slope for an SMF at its zero-dispersion wavelength is $0.07 \frac{\text{ps}}{\text{nm}^2 \text{km}}$ [69].

3.1.1 Phase Matching in FWM

In the process of four-wave mixing (FWM) four photons interact together, two of them are annihilated and the other two are created. The four-wave mixing is the mechanism behind the two-pump parametric amplification and oscillation; so the terms of pump, signal and idler are adopted from the literature on parametric processes [69]. If ω_1 and ω_2 are the frequencies of the annihilated photons and ω_s and ω_i are those of the created photons, the principle of energy conservation dictates $\omega_1 + \omega_2 = \omega_s + \omega_i$. Such a relation forces a symmetry on the frequency diagram of the process illustrated in Fig. 3.1, where $2\Omega_p$ indicates the frequency difference between the pumps and Ω is the frequency detuning of the signal and idler around the central frequency ω_0 . The phase mismatch between the created and annihilated photons

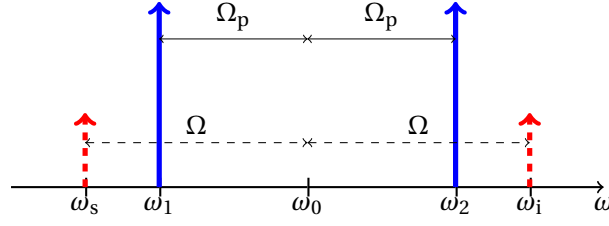


Figure 3.1 – Frequency diagram of the FWM process.

can be derived as follows:

$$\begin{aligned}
 \Delta\beta &= (\beta(\omega_s) + \beta(\omega_i)) - (\beta(\omega_1) + \beta(\omega_2)) \\
 &= \beta(\omega_0 - \Omega) + \beta(\omega_0 + \Omega) - \beta(\omega_0 - \Omega_p) - \beta(\omega_0 + \Omega_p) \\
 &= (\beta_0 - \delta\beta_o(\Omega) + \delta\beta_e(\Omega)) + (\beta_0 + \delta\beta_o(\Omega) + \delta\beta_e(\Omega)) \\
 &\quad - (\beta_0 - \delta\beta_o(\Omega_p) + \delta\beta_e(\Omega_p)) - (\beta_0 + \delta\beta_o(\Omega_p) + \delta\beta_e(\Omega_p)) \\
 &= 2(\delta\beta_e(\Omega) - \delta\beta_e(\Omega_p))
 \end{aligned} \tag{3.4}$$

Eq. (3.4) indicates that only the even terms of dispersion are effective in the phase matching of the FWM process. The phase mismatch in Eq. (3.4) can be obviously expressed as $\beta_2(\Omega^2 - \Omega_p^2)$ for SMFs and $\beta_2(\Omega^2 - \Omega_p^2) + \frac{\beta_4}{12}(\Omega^4 - \Omega_p^4)$ for DSFs in the C-band.

3.1.2 Phase Matching in Degenerate FWM

In a medium with third-order nonlinearity it is possible to have four-wave mixing using only one pump. In this process two pump photons at the same frequency are annihilated and two photons at signal and idler frequencies are created. Therefore, the principle of energy conservation indicates that $\omega_s + \omega_i = 2\omega_0$ and thus its frequency diagram is like what is depicted in Fig. 3.2. It is worth mentioning that degenerate FWM must not be confused with

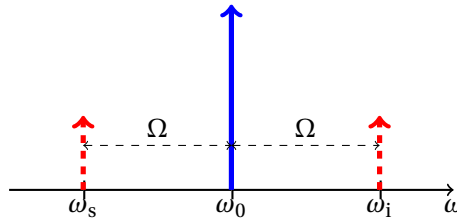


Figure 3.2 – Frequency diagram of the degenerate FWM process.

the three-wave mixing process that occurs in media with second-order nonlinearity where $\omega_s + \omega_i = \omega_0$. Similar to FWM, the phase mismatch between the generated and destroyed

photons are obtained as follows:

$$\begin{aligned}\Delta\beta &= \beta(\omega_s) + \beta(\omega_i) - 2\beta(\omega_0) = \beta(\omega_0 - \Omega) + \beta(\omega_0 + \Omega) - 2\beta(\omega_0) \\ &= (\beta_0 - \delta\beta_o(\Omega) + \delta\beta_e(\Omega)) + (\beta_0 + \delta\beta_o(\Omega) + \delta\beta_e(\Omega)) - 2\beta_0 \\ &= 2\delta\beta_e(\Omega)\end{aligned}\tag{3.5}$$

Eq. (3.5) shows that only the even part of the dispersion relation is effective in the phase matching condition of the process. Again the phase mismatch can be written in terms of dispersion coefficients as $\beta_2\Omega^2$ for SMFs and $\beta_2\Omega^2 + \frac{\beta_4}{12}\Omega^4$ for DSFs in the C-band. The degenerate FWM process is the mechanism behind single pump optical parametric amplifiers and modulation instability that will be thoroughly investigated in the following sections.

3.2 Linear Stability Analysis

Linear systems are known to be stable in a sense that any bounded input cannot result in an unbounded output. However, it is not the case for nonlinear systems which means that a nonlinear system may or may not be stable. Therefore, stability analysis is critical in investigating nonlinear systems and thus for the nonlinear Schrödinger equation (NLSE) too. The idea behind the stability analysis is to add a small perturbation to the stationary solution of the nonlinear system and follow the perturbation behavior during the system evolution. Since the perturbing signal is assumed to be small compared to the stationary solution, the nonlinear system's behavior is linearized and so it is called linear stability analysis [3]; moreover, the system function in such conditions is considered as the small-signal gain. As seen in the previous chapter, the nonlinear Schrödinger equation is given by

$$i\partial_z U + \sum_{m=1}^{\infty} i^m \frac{\beta_m}{m!} \partial_t^m U + \gamma P_0 e^{-\alpha z} |U|^2 U = 0.\tag{3.6}$$

The stationary solution is independent of time and thus considering $\partial_t = 0$, Eq. (3.6) results in the following time-independent equation:

$$i d_z U + \gamma P_0 e^{-\alpha z} |U|^2 U = 0.\tag{3.7}$$

Considering the boundary condition $U(z=0) = 1$ for the normalized envelope U , the following stationary solution for Eq. (3.7) is obtained:

$$U(z) = e^{i\gamma P_0 \frac{1-e^{-\alpha z}}{\alpha}}.\tag{3.8}$$

The stationary solution given in Eq. (3.8) represents the self-phase modulation (SPM) of the optical field. Such a solution is an equilibrium point for the nonlinear Schrödinger equation. An immediate question is that whether this equilibrium point is stable or unstable. For linear equations every solution or in fact every equilibrium point is stable but for nonlinear equations it depends on the type of nonlinearity and equation coefficients. For the NLSE it is seen that the stability of the solution depends on the sign of dispersion coefficients. In the case of instability,

the process is called *modulation instability* that happens in the anomalous dispersion regime. In order to analyse the stability of the solution in Eq. (3.8), the linear stability analysis is applied by adding a perturbing signal to the steady-state solution and substituting in Eq. (3.6). If the normalized perturbing signal is $\epsilon(z, t)$ so that $|\epsilon| \ll 1$, the perturbing solution of the NLSE will be given by

$$U(z, t) = U(z)(1 + \epsilon(z, t)) = e^{i\gamma P_0 \frac{1-\epsilon^{-\alpha z}}{\alpha}} (1 + \epsilon(z, t)). \quad (3.9)$$

By substituting Eq. (3.9) in the NLSE of Eq. (3.6), it can be derived that $\epsilon(z, t)$ satisfies the following nonlinear equation:

$$i\partial_z \epsilon + \sum_{m=1}^{\infty} i^m \frac{\beta_m}{m!} \partial_t^m \epsilon + \gamma P_0 e^{-\alpha z} (1 + \epsilon)(\epsilon + \epsilon^* + |\epsilon|^2) = 0, \quad (3.10)$$

where ϵ^* is the complex conjugate of ϵ . Since $|\epsilon| \ll 1$, higher order terms of ϵ can be neglected and the linearized perturbation equation is obtained as follows:

$$i\partial_z \epsilon + \sum_{m=1}^{\infty} i^m \frac{\beta_m}{m!} \partial_t^m \epsilon + \gamma P_0 e^{-\alpha z} (\epsilon + \epsilon^*) = 0. \quad (3.11)$$

Eq. (3.11) is linear and thus it can be solved in the Fourier domain. Considering a single pump scenario illustrated in Fig. 3.2, the perturbation contains a signal at frequency detuning $-\Omega$ and an idler at Ω represented by

$$\epsilon(z, t) = f(z)e^{i\Omega t} + h(z)e^{-i\Omega t}, \quad (3.12)$$

where f and h denote the signal and idler, respectively. The derivatives of the perturbation needed for Eq. (3.11) are given by

$$\frac{\partial \epsilon}{\partial z} = \frac{df}{dz} e^{i\Omega t} + \frac{dh}{dz} e^{-i\Omega t}, \quad (3.13a)$$

$$\frac{\partial^m \epsilon}{\partial t^m} = (i\Omega)^m f e^{i\Omega t} + (-i\Omega)^m h e^{-i\Omega t}. \quad (3.13b)$$

Substituting Eq. (3.12) and Eqs. (3.13) in the linear perturbation equation results in

$$\begin{aligned} i\partial_z \epsilon + \sum_{m=1}^{\infty} i^m \frac{\beta_m}{m!} \partial_t^m \epsilon + \gamma P_0 e^{-\alpha z} (\epsilon + \epsilon^*) \\ = \left[i \frac{df}{dz} + \delta\beta(-\Omega)f + \gamma P_0 e^{-\alpha z} (f + h^*) \right] e^{i\Omega t} \\ + \left[i \frac{dh}{dz} + \delta\beta(\Omega)h + \gamma P_0 e^{-\alpha z} (h + f^*) \right] e^{-i\Omega t} = 0, \end{aligned} \quad (3.14)$$

Chapter 3. Modulation Instability Gain

in which $\delta\beta(\pm\Omega)$ is defined in Eq. (3.1). The following two coupled equations governing the signal and idler are immediately inferred from Eq. (3.14):

$$i\frac{df}{dz} + \delta\beta(-\Omega)f + \gamma P_0 e^{-\alpha z}(f + h^*) = 0, \quad (3.15a)$$

$$i\frac{dh}{dz} + \delta\beta(\Omega)h + \gamma P_0 e^{-\alpha z}(h + f^*) = 0. \quad (3.15b)$$

Moreover, the dispersion coefficients can be expressed in terms of the odd and even parts so that $\delta\beta(\Omega) = \delta\beta_e(\Omega) + \delta\beta_o(\Omega)$ and $\delta\beta(-\Omega) = \delta\beta_e(\Omega) - \delta\beta_o(\Omega)$. This way, the coupled equations are rewritten as

$$i\frac{df}{dz} + (\delta\beta_e - \delta\beta_o)f + \gamma P_0 e^{-\alpha z}(f + h^*) = 0, \quad (3.16a)$$

$$i\frac{dh}{dz} + (\delta\beta_e + \delta\beta_o)h + \gamma P_0 e^{-\alpha z}(h + f^*) = 0. \quad (3.16b)$$

In order to solve Eqs. (3.16) two initial conditions are necessary. The initial values of signal and idler, i.e. $f(0)$ and $h(0)$ are normally available and the initial values of signal and idler derivatives are obtained from Eqs. (3.16) as follows:

$$f'(0) = i(\delta\beta_e - \delta\beta_o + \gamma P_0)f(0) + i\gamma P_0 h^*(0), \quad (3.17a)$$

$$h'(0) = i(\delta\beta_e + \delta\beta_o + \gamma P_0)h(0) + i\gamma P_0 f^*(0). \quad (3.17b)$$

Linear stability analysis provides a set of coupled equations for signal and idler as represented in Eqs. (3.16). By solving those equations the signal and idler fields and so the gains can be obtained. However, when the medium is considered to be lossless so that the attenuation coefficient is null, solving Eqs. (3.16) will be much simpler than the case of considering a lossy medium. Moreover, the simplicity of solution gives insight into the evolution of the process so the next section is devoted to the stability analysis of lossless optical fibers.

3.2.1 Lossless Fibers

Neglecting attenuation in optical fibers, i.e. $\alpha = 0$, reduces the signal and idler equations given in Eqs. (3.16) to the following:

$$i\frac{df}{dz} + (\delta\beta_e - \delta\beta_o + \gamma P_0)f + \gamma P_0 h^* = 0, \quad (3.18a)$$

$$i\frac{dh}{dz} + (\delta\beta_e + \delta\beta_o + \gamma P_0)h + \gamma P_0 f^* = 0. \quad (3.18b)$$

Uncoupling Eqs. (3.18) by taking their second derivative leads to the following second-order ordinary differential equations for signal and idler:

$$\frac{d^2f}{dz^2} + 2i\delta\beta_o\frac{df}{dz} + [\delta\beta_e(\delta\beta_e + 2\gamma P_0) - (\delta\beta_o)^2]f = 0, \quad (3.19a)$$

$$\frac{d^2h}{dz^2} - 2i\delta\beta_o\frac{dh}{dz} + [\delta\beta_e(\delta\beta_e + 2\gamma P_0) - (\delta\beta_o)^2]h = 0. \quad (3.19b)$$

Eqs. (3.19) are second-order linear differential equations with *constant* coefficients and thus, they can be solved in terms of exponential or hyperbolic functions with initial conditions as follows:

$$f(z) = e^{-i\delta\beta_0 z} \left(f(0) \cosh(gz) + \frac{f'(0) + i\delta\beta_0 f(0)}{g} \sinh(gz) \right), \quad (3.20a)$$

$$h(z) = e^{i\delta\beta_0 z} \left(h(0) \cosh(gz) + \frac{h'(0) - i\delta\beta_0 h(0)}{g} \sinh(gz) \right), \quad (3.20b)$$

where the exponent g is given by

$$g^2 = (\gamma P_0)^2 - (\gamma P_0 + \delta\beta_e)^2 = -\delta\beta_e(2\gamma P_0 + \delta\beta_e). \quad (3.21)$$

Note that g^2 can be positive or negative depending on the even-order dispersion coefficients and the input power; when g^2 is positive or equivalently g is real, the hyperbolic functions represent an exponential amplification or actually the system is unstable. However, for negative g^2 or imaginary g , the hyperbolic functions modify to ordinary sine and cosine and thus, there will be no amplification and in fact the system is stable. The condition for instability or amplification can be simply deduced from Eq. (3.21) to be as follows:

$$\delta\beta_e < 0 < 2\gamma P_0 + \delta\beta_e. \quad (3.22)$$

Substituting the initial values $f'(0)$ and $h'(0)$ from Eqs. (3.17) into Eqs. (3.20) results in

$$f(z) = e^{-i\delta\beta_0 z} \left(f(0) \cosh(gz) + i \frac{(\gamma P_0 + \delta\beta_e) f(0) + \gamma P_0 h^*(0)}{g} \sinh(gz) \right), \quad (3.23a)$$

$$h(z) = e^{i\delta\beta_0 z} \left(h(0) \cosh(gz) + i \frac{(\gamma P_0 + \delta\beta_e) h(0) + \gamma P_0 f^*(0)}{g} \sinh(gz) \right). \quad (3.23b)$$

Eqs. (3.23) can be rearranged to be expressed in terms of signal and idler initial conditions as follows:

$$f(z) = e^{-i\delta\beta_0 z} \left(f(0) \left[\cosh(gz) + i \frac{\gamma P_0 + \delta\beta_e}{g} \sinh(gz) \right] + h^*(0) \left[i \frac{\gamma P_0}{g} \sinh(gz) \right] \right), \quad (3.24a)$$

$$h(z) = e^{i\delta\beta_0 z} \left(h(0) \left[\cosh(gz) + i \frac{\gamma P_0 + \delta\beta_e}{g} \sinh(gz) \right] + f^*(0) \left[i \frac{\gamma P_0}{g} \sinh(gz) \right] \right). \quad (3.24b)$$

Eqs. (3.24) are the most general forms of signal and idler fields in a dispersive Kerr medium. Depending on their initial conditions several systems can be extracted from these fields such as optical parametric amplification (OPA) in phase-sensitive (PS) or phase-insensitive (PI) scenarios and also modulation instability (MI).

3.2.2 Optical Parametric Amplification

In the case of phase-insensitive OPA, a small signal along with a strong pump is launched into a fiber, while at the input there is no idler. Therefore, the initial conditions are given by

Chapter 3. Modulation Instability Gain

$f(0) = 1$ and $h(0) = 0$ leading to the following signal and idler fields obtained from Eqs. (3.24):

$$f(z) = e^{-i\delta\beta_0 z} \left(\cosh(gz) + i \frac{\gamma P_0 + \delta\beta_e}{g} \sinh(gz) \right), \quad (3.25a)$$

$$h(z) = e^{i\delta\beta_0 z} \left(i \frac{\gamma P_0}{g} \sinh(gz) \right). \quad (3.25b)$$

The signal and idler intensity gains can be simply calculated by taking the absolute square of the fields as follows [71]:

$$G_s = |f(z)|^2 = \cosh^2(gz) + \frac{(\gamma P_0 + \delta\beta_e)^2}{g^2} \sinh^2(gz) = 1 + \frac{(\gamma P_0)^2}{g^2} \sinh^2(gz), \quad (3.26a)$$

$$G_i = |h(z)|^2 = \frac{(\gamma P_0)^2}{g^2} \sinh^2(gz). \quad (3.26b)$$

It is clearly seen from Eqs. (3.26) that $G_s - G_i = 1$. According to Eq. (3.21), the maximum of g^2 occurs when $\delta\beta_e = -\gamma P_0$. In such a condition $g = \gamma P_0$ and the maximal signal and idler gains are given by $1 + \sinh^2(\gamma P_0 z)$ and $\sinh^2(\gamma P_0 z)$, respectively. When the frequency detuning is null and so the phase mismatch is zero, according to Eq. (3.21), g is zero and the signal and idler gains are obtained from Eqs. (3.26) as $1 + (\gamma P_0 z)^2$ and $(\gamma P_0 z)^2$, respectively. In the case of phase-sensitive OPA, we assume that the initial signal and idler have the same amplitude but different phase shift so that $f(0) = 1$ and $h(0) = e^{-i\Phi}$. Substituting these initial values in the general form of the fields given by Eqs. (3.24) and taking its absolute square result in the following gain function:

$$G = |f(z)|^2 = |h(z)|^2 = G_s + G_i - 2\sqrt{G_s G_i} \sin\left(\Phi - \frac{\gamma P_0 + \delta\beta_e}{g} \tanh(gz)\right), \quad (3.27)$$

where the signal and idler gains are given in Eqs. (3.26). It is evident from Eq. (3.27) that the gain depends on the initial phase difference between the signal and idler and it can fluctuate as the optical wave propagates along the fiber because the sine term in the expression depends on position z . The maximum and minimum of the phase-sensitive gain are obtained when the sine term in Eq. (3.27) is -1 and $+1$, respectively. Such gains are called in-phase and quadrature and are expressed as

$$G_P = G_s + G_i + 2\sqrt{G_s G_i} = (\sqrt{G_s} + \sqrt{G_i})^2, \quad (3.28a)$$

$$G_Q = G_s + G_i - 2\sqrt{G_s G_i} = (\sqrt{G_s} - \sqrt{G_i})^2. \quad (3.28b)$$

It can be easily seen from Eqs. (3.28) and Eqs. (3.26) that $G_P G_Q = (G_s - G_i)^2 = 1$. Fig. 3.3 shows several parametric gains in an OPA at an arbitrary frequency detuning where $\delta\beta_e = -\frac{\gamma P_0}{2}$. The phase-insensitive signal and idler gains are plotted in Fig. 3.3a showing an exponential growth versus the interaction length. Different phase-sensitive gains originating from different initial phase differences are depicted in Fig. 3.3b. It is evident that phase-sensitive gains are bounded between two curves corresponding to the in-phase and quadrature gains given in Eq. (3.28).

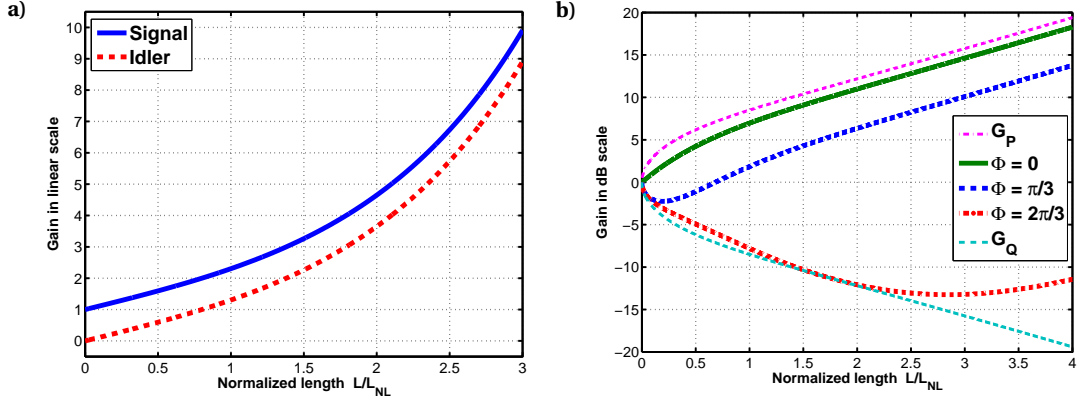


Figure 3.3 – OPA gain versus fiber length for $\delta\beta_e = -\frac{\gamma P_0}{2}$: a) Phase insensitive b) Phase sensitive.

3.2.3 Modulation Instability Gain

In noise-seeded modulation instability the initial conditions are determined by the noise at signal and idler frequencies. Any type of noise such as the thermal or quantum noise travelling with the pump signal can be a source of fluctuation on the pump intensity and as a result of modulation instability can lead to a huge oscillation on a continuous-wave (CW) lightwave. The main source of noise is the amplified spontaneous emission (ASE) generated by erbium-doped fiber amplifiers (EDFA). Assuming a flat spectrum for the ASE in the spectral band of modulation instability, we can attribute the whiteness property to the noise. It means that the temporal samples of the noise at different instances are uncorrelated. However, we need the spectral samples at the signal and idler frequencies. It has been proved in Appendix A that the Fourier transform of a white noise is also white and so its frequency samples are uncorrelated. This way, the initial conditions $f(0)$ and $h(0)$ in Eqs. (3.24) are two zero-mean uncorrelated random variables with normalized variance, i.e.

$$\mathbb{E}[f(0)] = \mathbb{E}[h(0)] = 0, \quad \mathbb{E}[f(0)h(0)] = 0, \quad \mathbb{E}[|f(0)|^2] = \mathbb{E}[|h(0)|^2] = 1, \quad (3.29)$$

where \mathbb{E} denotes the expected value. Moreover, Eqs. (3.24) can be written as a linear combination of the initial conditions in a compact way

$$f(z) = e^{-i\delta\beta_0 z} (f(0)A(z) + h^*(0)B(z)), \quad (3.30a)$$

$$h(z) = e^{i\delta\beta_0 z} (h(0)A(z) + f^*(0)B(z)), \quad (3.30b)$$

in which the signal and idler fields A and B are given by

$$A(z) = \cosh(gz) + i \frac{\gamma P_0 + \delta\beta_e}{g} \sinh(gz), \quad (3.31a)$$

$$B(z) = i \frac{\gamma P_0}{g} \sinh(gz). \quad (3.31b)$$

Chapter 3. Modulation Instability Gain

It has been seen in the previous section that $G_s = |A(z)|^2$ and $G_i = |B(z)|^2$. Taking the absolute square of $f(z)$ given in Eq. (3.30a) results in

$$|f(z)|^2 = |f(0)|^2 |A(z)|^2 + |h(0)|^2 |B(z)|^2 + 2\Re[f(0)h(0)A(z)B^*(z)], \quad (3.32)$$

in which \Re represents the real part. The modulation instability gain or noise gain G_n is obtained by taking the ensemble average of Eq. (3.32) and using the characteristics of the initial conditions in Eq. (3.29) as follows:

$$\begin{aligned} G_n &= \mathbb{E}[|f(z)|^2] = \mathbb{E}[|f(0)|^2] |A(z)|^2 + \mathbb{E}[|h(0)|^2] |B(z)|^2 + 2\Re[\mathbb{E}[f(0)h(0)] A(z)B^*(z)] \\ &= G_s + G_i = 1 + 2G_i = 2G_s - 1. \end{aligned} \quad (3.33)$$

Eq. (3.33) demonstrates that the modulation instability gain is the sum of the signal and idler gains. Since the signal and idler in noise-seeded MI are uncorrelated noise samples, their gains sum up incoherently to construct the MI gain which is equal to

$$G_n = 1 + 2 \frac{(\gamma P_0)^2}{g^2} \sinh^2(gz). \quad (3.34)$$

The modulation instability gain is in fact the gain experienced by the noise propagating with the pump lightwave. Considering that $G_s \gg 1$, the MI gain in Eq. (3.33) can be approximated as $G_n \approx 2G_s$ which means the noise gain is 3 dB higher than the signal gain. Moreover, the noise figure (NF) of a phase-insensitive OPA, defined as the ratio of the input to output signal-to-noise ratios (SNR), can be calculated as follows:

$$\text{NF} \triangleq \frac{\text{SNR}_{\text{in}}}{\text{SNR}_{\text{out}}} = \frac{\frac{S_{\text{in}}}{N_{\text{in}}}}{\frac{S_{\text{out}}}{N_{\text{out}}}} = \frac{N_{\text{out}}}{N_{\text{in}}} \frac{S_{\text{in}}}{S_{\text{out}}} = \frac{G_n}{G_s} = \frac{2G_s - 1}{G_s} = 2 - \frac{1}{G_s}. \quad (3.35)$$

Eq. (3.35) proves this well-known fact that the noise figure of phase-insensitive optical parametric amplifiers in the high-gain regime ($G_s \gg 1$) is 2 (3 dB) [69, 72].

3.3 Modulation Instability in Lossy Fibers

Opposite to the modulation instability gain in lossless optical fibers, the MI gain formula for lossy fibers is rather complicated. It can be expressed in terms of modified Bessel [73], Hankel [74], ordinary Bessel [75], or Whittaker [76] functions all with complex-valued orders which make them difficult to calculate. In this section we expand the approach taken by Michel E. Marhic [75] to obtain the MI gain based on the Bessel functions and then an approximate formula for the gain is investigated. The general form of coupled equations for signal and idler are given in Eqs. (3.16). Uncoupling the equations by taking the second derivative results in the following second-order differential equation for $f(z)$:

$$\frac{d^2 f}{dz^2} + (\alpha + 2i\delta\beta_0) \frac{df}{dz} + [\delta\beta_e(\delta\beta_e + 2\gamma P_0 e^{-\alpha z}) - (\delta\beta_0)^2 - i\alpha(\delta\beta_e - \delta\beta_0)] f = 0. \quad (3.36)$$

It is evident that by letting $\alpha = 0$ in Eq. (3.36), the case of lossless fiber given in Eq. (3.19a) is obtained. Solving Eq. (3.36) is not as simple as the lossless case because one of the coefficients of the equation is not a constant and depends on the variable z . In order to simplify the equation the function $u(z)$ is defined as

$$u(z) = e^{(\frac{\alpha}{2} + i\delta\beta_o)z} f(z). \quad (3.37)$$

Therefore, the first and second derivatives of f are expressed in terms of u as

$$\frac{df}{dz} = e^{-(\frac{\alpha}{2} + i\delta\beta_o)z} \left[\frac{du}{dz} - \left(\frac{\alpha}{2} + i\delta\beta_o \right) u \right], \quad (3.38a)$$

$$\frac{d^2f}{dz^2} = e^{-(\frac{\alpha}{2} + i\delta\beta_o)z} \left[\frac{d^2u}{dz^2} - 2 \left(\frac{\alpha}{2} + i\delta\beta_o \right) \frac{du}{dz} + \left(\frac{\alpha}{2} + i\delta\beta_o \right)^2 u \right]. \quad (3.38b)$$

Using the expressions in Eqs. (3.38), it can be seen that Eq. (3.36) reduces to the following simplified second-order differential equation:

$$\frac{d^2u}{dz^2} = \left[\left(\frac{\alpha}{2} + i\delta\beta_e \right)^2 - 2\delta\beta_e\gamma P_0 e^{-\alpha z} \right] u. \quad (3.39)$$

Since the phase mismatch is given by $\Delta\beta = 2\delta\beta_e$, Eq. (3.39) can also be written as

$$\frac{d^2u}{dz^2} = \left[\left(\frac{\alpha + i\Delta\beta}{2} \right)^2 - \Delta\beta\gamma P_0 e^{-\alpha z} \right] u. \quad (3.40)$$

Although Eq. (3.40) looks simpler than Eq. (3.36), it is not straightforward to solve because its coefficient still depends on the variable z . In order to proceed in solving the equation we need to define the variable x in terms of z so that

$$x^2 = \frac{4\gamma P_0 \Delta\beta}{\alpha^2} e^{-\alpha z}. \quad (3.41)$$

Considering Eq. (3.41), we have $\frac{dx}{dz} = -\frac{\alpha}{2}x$ and thus the first and second derivatives of u are obtained as

$$\frac{du}{dz} = -\frac{\alpha}{2}x \frac{du}{dx}, \quad (3.42a)$$

$$\frac{d^2u}{dz^2} = \frac{\alpha^2}{4} \left(x^2 \frac{d^2u}{dx^2} + x \frac{du}{dx} \right). \quad (3.42b)$$

Substituting Eqs. (3.41) and (3.42) in Eq. (3.40) leads to the following fundamental equation governing u :

$$x^2 \frac{d^2u}{dx^2} + x \frac{du}{dx} + (x^2 - \nu^2)u = 0 \quad (3.43)$$

in which $\nu = 1 + i\frac{\Delta\beta}{\alpha}$. Eq. (3.43) is the general form of Bessel's differential equation whose solutions can be expressed in terms of the Bessel functions of the first kind J_ν and $J_{-\nu}$. Con-

Chapter 3. Modulation Instability Gain

sidering the two initial conditions $u(x_0)$ and $u'(x_0)$ where $x_0 = \frac{2}{\alpha} \sqrt{\gamma P_0 \Delta \beta}$ is obtained from Eq. (3.41), the general solution of Bessel's equation is given by [77]

$$u(x) = \frac{1}{W(J_\nu(x_0), J_{-\nu}(x_0))} \left[(u(x_0)J'_{-\nu}(x_0) - u'(x_0)J_{-\nu}(x_0))J_\nu(x) + (u'(x_0)J_\nu(x_0) - u(x_0)J'_\nu(x_0))J_{-\nu}(x) \right], \quad (3.44)$$

where the Wronskian of J_ν and $J_{-\nu}$ is defined and obtained as follows [77]:

$$\begin{aligned} W(J_\nu(x_0), J_{-\nu}(x_0)) &\triangleq \begin{vmatrix} J_\nu(x_0) & J_{-\nu}(x_0) \\ J'_\nu(x_0) & J'_{-\nu}(x_0) \end{vmatrix} \\ &= J_\nu(x_0)J'_{-\nu}(x_0) - J_{-\nu}(x_0)J'_\nu(x_0) = -\frac{2\sin(\pi\nu)}{\pi x_0}. \end{aligned} \quad (3.45)$$

According to Eq. (3.37) we have $f(z) = e^{-(\frac{\alpha}{2} + i\delta\beta_0)z} u(x_0 e^{-\frac{\alpha}{2}z})$ and thus, the initial conditions for f can be written as:

$$f(0) = u(x_0), \quad (3.46a)$$

$$f'(0) = -\left(\frac{\alpha}{2} + i\delta\beta_0\right)u(x_0) - \frac{\alpha}{2}x_0 u'(x_0). \quad (3.46b)$$

On the other hand the initial condition $f'(0)$ can be expressed in terms of $f(0)$ and $h(0)$ using Eq. (3.17) and thus, $u'(x_0)$ is given by

$$u'(x_0) = -\frac{\alpha + i(\Delta\beta + 2\gamma P_0)}{\alpha x_0} f(0) - \frac{2i\gamma P_0}{\alpha x_0} h^*(0). \quad (3.47)$$

Using the initial condition in Eq. (3.47) and the Wronskian in Eq. (3.45), the function f can be expressed in terms of the initial conditions as

$$f(z) = e^{-i\delta\beta_0 z} (f(0)A(z) + h^*(0)B(z)), \quad (3.48)$$

where the signal and idler field gains $A(z)$ and $B(z)$ are obtained as

$$\begin{aligned} A(z) = \frac{\pi\gamma P_0 e^{-\frac{\alpha}{2}z}}{i\alpha \sin(\pi\nu)} &\left\{ \left(1 + \frac{\Delta\beta - i\alpha}{2\gamma P_0}\right) \left[J_{-\nu}(x_0)J_\nu(x_0 e^{-\frac{\alpha}{2}z}) - J_\nu(x_0)J_{-\nu}(x_0 e^{-\frac{\alpha}{2}z}) \right] \right. \\ &\left. - i\sqrt{\frac{\Delta\beta}{\gamma P_0}} \left[J'_{-\nu}(x_0)J_\nu(x_0 e^{-\frac{\alpha}{2}z}) - J'_\nu(x_0)J_{-\nu}(x_0 e^{-\frac{\alpha}{2}z}) \right] \right\}, \end{aligned} \quad (3.49a)$$

$$B(z) = \frac{\pi\gamma P_0 e^{-\frac{\alpha}{2}z}}{i\alpha \sin(\pi\nu)} \left[J_{-\nu}(x_0)J_\nu(x_0 e^{-\frac{\alpha}{2}z}) - J_\nu(x_0)J_{-\nu}(x_0 e^{-\frac{\alpha}{2}z}) \right]. \quad (3.49b)$$

Since the envelope U in the nonlinear Schrödinger equation given by Eq. (3.6) is normalized to $e^{-\frac{\alpha}{2}z}$, the signal and idler intensity gains are obtained from $G_s = e^{-\alpha z}|A(z)|^2$ and $G_i =$

$e^{-\alpha z}|B(z)|^2$ for which the following relation is proved:

$$G_s = e^{-\alpha z} + G_i. \quad (3.50)$$

In order to prove Eq. (3.50) it is sufficient to demonstrate that $|A(z)|^2 = 1 + |B(z)|^2$, but it is not straightforward from Eqs. (3.49). Therefore, another approach is adopted to prove the useful expression given in Eq. (3.50). Starting from the identity $\frac{d|f(z)|^2}{dz} = \frac{d(ff^*)}{dz} = f \frac{df^*}{dz} + f^* \frac{df}{dz}$ and using the signal and idler coupled equations in Eqs. (3.15), the coupled equations governing the signal and idler intensities are obtained as follows:

$$\frac{d|f(z)|^2}{dz} = 2\gamma P_0 e^{-\alpha z} \Im[f(z)h(z)], \quad (3.51a)$$

$$\frac{d|h(z)|^2}{dz} = 2\gamma P_0 e^{-\alpha z} \Im[f(z)h(z)], \quad (3.51b)$$

where \Im denotes the imaginary part. Eqs. (3.51) imply that $\frac{d|f(z)|^2}{dz} = \frac{d|h(z)|^2}{dz}$ whose integration from 0 to z results in

$$|f(z)|^2 - |f(0)|^2 = |h(z)|^2 - |h(0)|^2. \quad (3.52)$$

By setting the initial conditions $f(0) = 1$ and $h(0) = 0$, Eqs. (3.30) result in $f(z) = e^{-i\delta\beta_0 z} A(z)$ and $h(z) = e^{i\delta\beta_0 z} B(z)$. Substituting these expressions in Eq. (3.52) leads to $|A(z)|^2 = 1 + |B(z)|^2$ which is the proof of Eq. (3.50). The idler gain can be simply obtained from Eq. (3.49b) as follows:

$$G_i = e^{-\alpha z} |B(z)|^2 = \left(\frac{\pi\gamma P_0 e^{-\alpha z}}{\alpha \sinh(\pi \frac{\Delta\beta}{\alpha})} \right)^2 \left| J_{-\nu}(x_0) J_{\nu}(x_0 e^{-\frac{\alpha}{2} z}) - J_{\nu}(x_0) J_{-\nu}(x_0 e^{-\frac{\alpha}{2} z}) \right|^2. \quad (3.53)$$

It is worth mentioning that the value of $\sin(\pi\nu)$ in deriving Eq. (3.53) is calculated based on $\nu = 1 + i \frac{\Delta\beta}{\alpha}$ as $\sin(\pi(1 + i \frac{\Delta\beta}{\alpha})) = -i \sinh(\pi \frac{\Delta\beta}{\alpha})$. In the case of signal gain it is not necessary to calculate it directly from the signal field in Eq. (3.49a) and it can be simply obtained from the idler gain using $G_s = e^{-\alpha z} + G_i$. Moreover, the modulation instability gain is given by the sum of signal and idler gains so, $G_n = e^{-\alpha z} + 2G_i$. This way, the general formula for modulation instability gain in lossy optical fibers in terms of fiber characteristics α and γ , input power P_0 and phase mismatch $\Delta\beta$ is given by

$$G_n = e^{-\alpha z} + 2 \left(\frac{\pi\gamma P_0 e^{-\alpha z}}{\alpha \sinh(\pi \frac{\Delta\beta}{\alpha})} \right)^2 \left| J_{-1-i\frac{\Delta\beta}{\alpha}} \left(\frac{2}{\alpha} \sqrt{\Delta\beta\gamma P_0} \right) J_{1+i\frac{\Delta\beta}{\alpha}} \left(\frac{2}{\alpha} \sqrt{\Delta\beta\gamma P_0 e^{-\alpha z}} \right) - J_{1+i\frac{\Delta\beta}{\alpha}} \left(\frac{2}{\alpha} \sqrt{\Delta\beta\gamma P_0} \right) J_{-1-i\frac{\Delta\beta}{\alpha}} \left(\frac{2}{\alpha} \sqrt{\Delta\beta\gamma P_0 e^{-\alpha z}} \right) \right|^2. \quad (3.54)$$

Numerical evaluation of Eq. (3.54) is extremely difficult because the Bessel functions with complex-valued orders like $\nu = \pm 1 \pm i \frac{\Delta\beta}{\alpha}$ are hard to evaluate. For instance, MATLAB® is not

Chapter 3. Modulation Instability Gain

able to calculate such functions; however, stronger mathematical softwares like Mathematica® evaluates the Bessel functions with complex orders. To avoid the complexity of evaluating Eq. (3.54) it is necessary to approximate the expression by a simpler one. One straightforward method is the modification of the MI gain in lossless fibers to include the attenuation coefficient α by changing the position variable z to its effective value $z_{\text{eff}} = \frac{1-e^{-\alpha z}}{\alpha}$ and multiplying by the attenuation factor $e^{-\alpha z}$. Therefore, the approximated MI gain for lossy optical fibers is expressed as

$$G_n \approx e^{-\alpha z} \left(1 + 2 \frac{(\gamma P_0)^2}{g^2} \sinh^2(g z_{\text{eff}}) \right), \quad (3.55)$$

in which the exponent g is given by

$$g^2 = (\gamma P_0)^2 - \left(\gamma P_0 + \frac{\Delta\beta}{2} \right)^2 = -\Delta\beta \left(\gamma P_0 + \frac{\Delta\beta}{4} \right). \quad (3.56)$$

When the attenuation coefficient is zero, $z_{\text{eff}} = z$ and the approximate in Eq. (3.55) becomes exactly equal to the MI gain in lossless fibers given in Eq. (3.34). In order to give an insight to the validity of such a simple approximation a theorem is proved to show that the exact value of the MI gain in Eq. (3.54) at zero phase mismatch is equal to its approximate value obtained from Eq. (3.55). In other words,

$$\lim_{\Delta\beta \rightarrow 0} G_n = e^{-\alpha z} (1 + 2(\gamma P_0 z_{\text{eff}})^2). \quad (3.57)$$

To demonstrate this theorem it is sufficient to prove that the idler gain in Eq. (3.53) tends to $e^{-\alpha z}(\gamma P_0 z_{\text{eff}})^2$ when $\Delta\beta$ and so x_0 go to zero. The Bessel functions are approximated as follows when their arguments x and the imaginary part of their orders $\frac{\Delta\beta}{\alpha}$ tend to zero [77]:

$$J_{-1-i\frac{\Delta\beta}{\alpha}}(x) \approx \frac{1}{\Gamma(-i\frac{\Delta\beta}{\alpha})} \left(\frac{x}{2} \right)^{-1-i\frac{\Delta\beta}{\alpha}}, \quad (3.58a)$$

$$J_{1+i\frac{\Delta\beta}{\alpha}}(x) \approx \frac{1}{\Gamma(2+i\frac{\Delta\beta}{\alpha})} \left(\frac{x}{2} \right)^{1+i\frac{\Delta\beta}{\alpha}}, \quad (3.58b)$$

in which Γ is the Gamma function defined as

$$\Gamma(s) = \int_0^\infty t^{s-1} e^{-t} dt. \quad (3.59)$$

Substituting the approximate relations of Eqs. (3.58) in the idler gain of Eq. (3.53) results in

$$G_i \approx \left(\frac{\pi \gamma P_0 e^{-\alpha z}}{\alpha \sinh(\pi \frac{\Delta\beta}{\alpha})} \right)^2 \left| \frac{e^{\frac{\alpha+i\Delta\beta}{2} z} - e^{-\frac{\alpha+i\Delta\beta}{2} z}}{\Gamma(-i\frac{\Delta\beta}{\alpha}) \Gamma(2+i\frac{\Delta\beta}{\alpha})} \right|^2. \quad (3.60)$$

Using the properties of the gamma function, it can be seen that [77]

$$\left| \Gamma\left(-i\frac{\Delta\beta}{\alpha}\right) \Gamma\left(2+i\frac{\Delta\beta}{\alpha}\right) \right|^2 = \frac{\pi^2 + \left(\pi\frac{\Delta\beta}{\alpha}\right)^2}{\sinh^2\left(\pi\frac{\Delta\beta}{\alpha}\right)} \quad (3.61)$$

Substituting Eq. (3.61) in Eq. (3.60) leads to

$$G_i \approx e^{-\alpha z} \frac{(\gamma P_0)^2}{\alpha^2 + \Delta\beta^2} \left| e^{\frac{i\Delta\beta}{2}z} - e^{-\alpha z - \frac{i\Delta\beta}{2}z} \right|^2. \quad (3.62)$$

As $\Delta\beta$ tends to zero, the idler gain in Eq. (3.62) approaches to

$$G_i \approx e^{-\alpha z} (\gamma P_0)^2 \left(\frac{1 - e^{-\alpha z}}{\alpha} \right)^2 = e^{-\alpha z} (\gamma P_0 z_{\text{eff}})^2, \quad (3.63)$$

which is obviously the expected approximate idler gain and thus the result in Eq. (3.57) is established.

3.4 MI Gain Spectrum

In this section the gain spectrum of modulation instability is investigated. It is shown that the MI gain spectrum includes two symmetric sidebands around the central frequency and its bandwidth depends on the dispersion characteristic of the fiber as well as the input power. In order to evaluate the theoretical model for modulation instability gain in lossless and lossy optical fibers as well as its approximate, the Monte Carlo simulation on the nonlinear Schrödinger equation is carried out. For every ensemble sample of the input noise, the NLSE is solved by the split-step Fourier method to evaluate the propagation along the fiber and then the output spectrum are averaged to reduce the variance and obtain the expected value of spectrum. For standard single-mode fibers in the telecom band at 1550 nm where the group-velocity dispersion β_2 is dominant, the linear phase mismatch $\Delta\beta$ given by Eq. (3.5) can be expressed as $\beta_2\Omega^2$ in which $\Omega = \omega - \omega_0$ is the frequency detuning around the pump frequency ω_0 . Replacing $\Delta\beta$ by $\beta_2\Omega^2$ in the MI gain given by Eq. (3.34) for a lossless fiber with length L and anomalous dispersion results in the following gain spectrum:

$$G_n(\Omega) = 1 + \frac{\sinh^2\left(2\gamma P_0 L \sqrt{\left(\frac{\Omega}{\Omega_c}\right)^2 \left(1 - \left(\frac{\Omega}{\Omega_c}\right)^2\right)}\right)}{2\left(\frac{\Omega}{\Omega_c}\right)^2 \left(1 - \left(\frac{\Omega}{\Omega_c}\right)^2\right)}, \quad (3.64)$$

where Ω_c denotes the cutoff frequency in which the exponent g is null and

$$\Omega_c = \sqrt{\frac{4\gamma P_0}{|\beta_2|}}. \quad (3.65)$$

Chapter 3. Modulation Instability Gain

It can be calculated from Eq. (3.64) that the maximal gain which is equal to $1 + 2 \sinh^2(\gamma P_0 L)$ occurs at the following frequency:

$$\Omega_{\max} = \pm \frac{\Omega_c}{\sqrt{2}} = \pm \sqrt{\frac{2\gamma P_0}{|\beta_2|}}. \quad (3.66)$$

It can also be deduced from Eq. (3.64) that the gain at $\Omega = 0$ and $\Omega = \pm\Omega_c$ is equal to $1 + (\gamma P_0 L)^2$ which is a quadrature dependance on the pump power and fiber length.

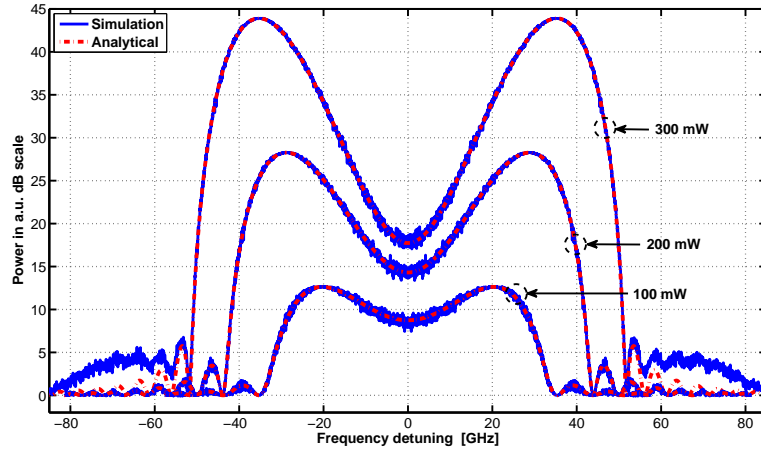


Figure 3.4 – MI gain spectrum for a 10-km lossless SMF with different input powers, quantum-level background noise and typical parameters $\beta_2 = -22 \frac{\text{ps}^2}{\text{km}}$ and $\gamma = 1.8 \frac{\text{W}^{-1}}{\text{km}}$.

Fig. 3.4 plots the MI gain spectrum for an SMF with different levels of input power, 100, 200 and 300 mW, and compares the numerical and analytical solutions. While the analytical results (dashed red lines) are obtained directly from the MI gain formula in Eq. (3.64), the numerical results (continuous blue lines) have been obtained by applying a Monte Carlo simulation to the nonlinear Schrödinger equation, solved by using the split-step Fourier method. It is evident that the simulation and the theoretical gain are in perfect agreement. The small discrepancy between theory and simulation observed outside the main MI sidelobes, for the case of 300 mW input power is due to the higher-order modulation instability [78], which is neglected in the analytical model and only occurs at rather high power levels. It is also clearly seen from Fig. 3.4 that the MI bandwidth and the frequency of maximal gain increase by boosting the pump power. For lossy optical fibers the exact gain spectrum is obtained from Eq. (3.54) by changing $\Delta\beta$ to $-\beta_2|\Omega|^2$ for anomalous dispersion as follows:

$$G_n(\Omega) = e^{-\alpha z} + 2 \left(\frac{\pi \gamma P_0 e^{-\alpha z}}{\alpha \sinh\left(\frac{\pi |\beta_2|}{\alpha} \Omega^2\right)} \right)^2 \left| J_{-1+i\frac{|\beta_2|}{\alpha}\Omega^2} \left(\frac{2i\Omega}{\alpha} \sqrt{|\beta_2| \gamma P_0} \right) J_{1-i\frac{|\beta_2|}{\alpha}\Omega^2} \left(\frac{2i\Omega}{\alpha} \sqrt{|\beta_2| \gamma P_0 e^{-\alpha z}} \right) - J_{1-i\frac{|\beta_2|}{\alpha}\Omega^2} \left(\frac{2i\Omega}{\alpha} \sqrt{|\beta_2| \gamma P_0} \right) J_{-1+i\frac{|\beta_2|}{\alpha}\Omega^2} \left(\frac{2i\Omega}{\alpha} \sqrt{|\beta_2| \gamma P_0 e^{-\alpha z}} \right) \right|^2. \quad (3.67)$$

As mentioned before, it is not straightforward to plot the gain formula in Eq. (3.67) by MATLAB®; therefore we use Mathematica® for plotting the analytical formula while the numerical simulation of the NLSE for obtaining the gain is performed in MATLAB® to which the analytical results are imported from Mathematica® for comparison.

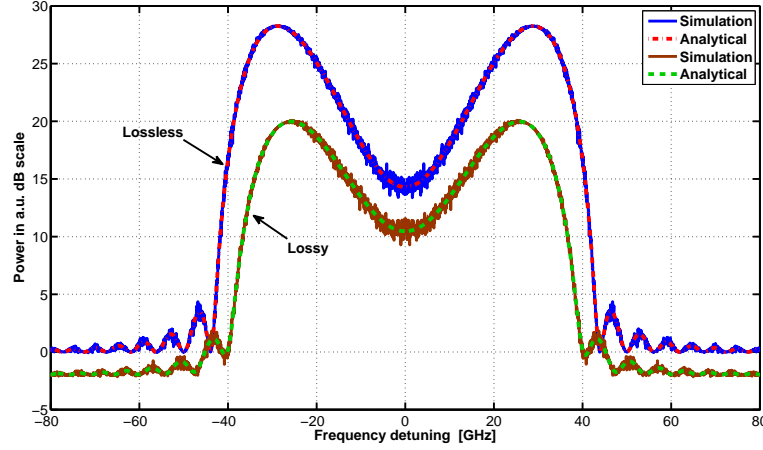


Figure 3.5 – Comparison of MI gain spectrum between a 10-km lossless SMF and a 10-km lossy one with $\alpha = 0.2 \frac{\text{dB}}{\text{km}}$ at the input power of 200 mW and typical parameters $\beta_2 = -22 \frac{\text{ps}^2}{\text{km}}$ and $\gamma = 1.8 \frac{\text{W}^{-1}}{\text{km}}$. Perfect agreement between the NLSE simulation and the analytical solution is also demonstrated for both cases.

Fig. 3.5 compares the MI gain spectrum in a 10-km lossy fiber with that of a lossless fiber showing clearly how the power attenuation decreases the gain value and shrinks its bandwidth. Moreover, the gain spectrum of the lossy fiber is plotted from the analytical formula given in Eq. (3.67). The perfect agreement between the numerical simulation and analytical result demonstrates the accuracy of the MI gain formula for lossy optical fibers expressed by Eq. (3.67). It is worth noting that the negative baseline level (−2 dB) for the lossy case is simply a consequence of the attenuation of the 10-km fiber which is equal to $10 \times 0.2 = 2$ dB. In order to avoid the complexity of the gain formula in Eq. (3.67) for further analytical results it is essential to provide a simpler form for the gain spectrum. An approximate formula similar to Eq. (3.64) is derived from the approximate gain in Eq. (3.55) as follows:

$$G_n(\Omega) \approx e^{-\alpha z} \left(1 + \frac{\sinh^2 \left(2\gamma P_0 L_{\text{eff}} \sqrt{\left(\frac{\Omega}{\Omega_c} \right)^2 \left(1 - \left(\frac{\Omega}{\Omega_c} \right)^2 \right)} \right)}{2 \left(\frac{\Omega}{\Omega_c} \right)^2 \left(1 - \left(\frac{\Omega}{\Omega_c} \right)^2 \right)} \right), \quad (3.68)$$

in which the effective length L_{eff} of the fiber is given by $\frac{1-e^{-\alpha L}}{\alpha}$. The approximate gain formula in Eq. (3.68) is clearly much simpler than the exact one in Eq. (3.67). Moreover, its only difference with the lossless gain in Eq. (3.64) is in the attenuation factor $e^{-\alpha z}$ and the effective length L_{eff} .

Fig. 3.6 compares the exact value of gain obtained by numerical simulations with its approximate value resulted from Eq. (3.68). Firstly, it is clear from the plots that the approximate

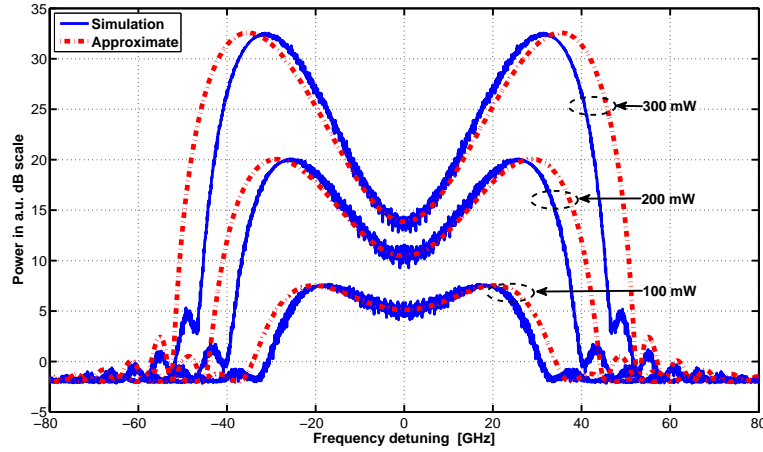


Figure 3.6 – MI gain spectrum for a 10-km lossy SMF with different input powers, quantum-level background noise and typical parameters $\alpha = 0.2 \frac{\text{dB}}{\text{km}}$, $\beta_2 = -22 \frac{\text{ps}^2}{\text{km}}$ and $\gamma = 1.8 \frac{\text{W}^{-1}}{\text{km}}$. Comparison between the NLSE simulation and the analytical approximation.

and exact values of the gain at the central frequency, where the phase mismatch is null, is identical; the fact that has been proved in the previous section as a sign for the accuracy of this approximation. Moreover, it is important to notice that the differences between the exact and approximate gains are mostly in the bandwidth of the MI gain and not in the peak gain value. Actually, the approximate gain predicts a wider spectral band because it neglects the power attenuation in the cutoff frequency; while considering the effective length instead of the length in its exponent leads to a correct gain value in the approximation.

3.5 Experimental Observation of MI Spectrum

This section is devoted to experimental measurements of the modulation instability spectrum in different optical fibers. The results show that in the small-signal gain regime the spectrum is the same as what the theory predicts which has two symmetric sidebands; while in the high-power regime, higher order modulation instability produces more sidebands which are not included in the analytical gain. Moreover, the highly nonlinear interaction can be achieved by further increasing the input peak power leading to a supercontinuum-like spectrum. The experimental setup is illustrated in Fig. 3.7. The CW light generated by a distributed feed-back (DFB) laser diode at 1551.7 nm is converted to a pulse train by an electro-optical modulator (EOM). The modulating pulse train with a repetition period of 500 ns and a pulse duration of 6 ns is generated by an HP 8131A pulse generator to drive the EOM. The light pulses are boosted by a low-noise erbium-doped fiber amplifier (EDFA) and are attenuated by a variable optical attenuator (VOA). A 99:1 coupler is used to split the light into two branches, the 1% branch for monitoring the peak power and the 99% one for launching the light into the fiber under test (FUT). For monitoring the input peak power, a power calibration unit comprising a fixed 3-dB attenuator, a DC-coupled photo-detector and an oscilloscope are utilized; the fixed attenuator prevents the photo-detector from saturation. Before launching the light pulses into the fiber a circulator is used to measure the back-scattering from the fiber, especially to

3.5. Experimental Observation of MI Spectrum

monitor the stimulated Brillouin scattering (SBS) to avoid power depletion due to SBS. The forward and backward spectra are measured using an optical spectrum analyser (OSA) with a resolution of 0.01 nm. The peak power of the pulse launched into the FUT is proportional to the pulse voltage acquired by the oscilloscope; this way, for each level of input peak power, the forward and backward spectra are captured by the OSA.

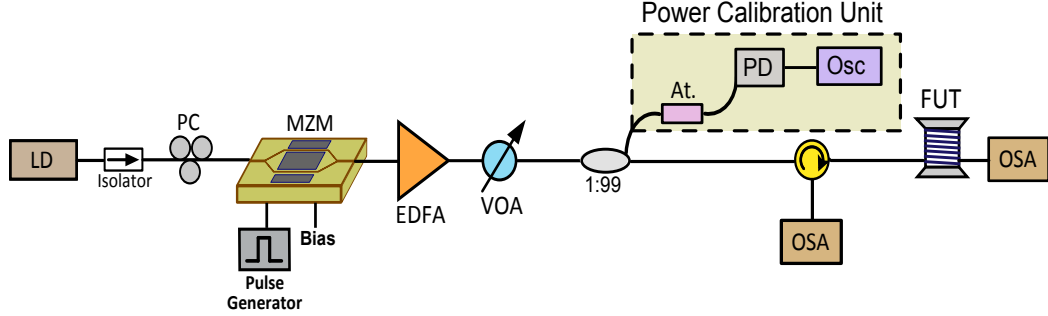


Figure 3.7 – Experimental setup for measuring MI spectrum. LD: laser diode, PC: polarization controller, MZM: Mach-Zehnder modulator, VOA: variable optical attenuator, PD: photo-detector, Osc: oscilloscope, FUT: fiber under test, At.: 3-dB fixed attenuator, OSA: optical spectrum analyzer.

Figure 3.8 plots the output spectrum of a 25.4 km long standard SMF for different levels of input peak power. We can see the onset of modulation instability at powers around 100 mW and by increasing the optical power the gain grows in value and expands in frequency. Until 200 mW, only the first-order modulation instability is evident but for more input power, the second-order MI is clearly shown. At higher powers around 500 mW the nonlinear interaction between all frequency components are considerable and so the spectrum looks like a flat but band-limited super continuum. However, in low-power or small signal conditions the spectrum looks like what is expected from theory.

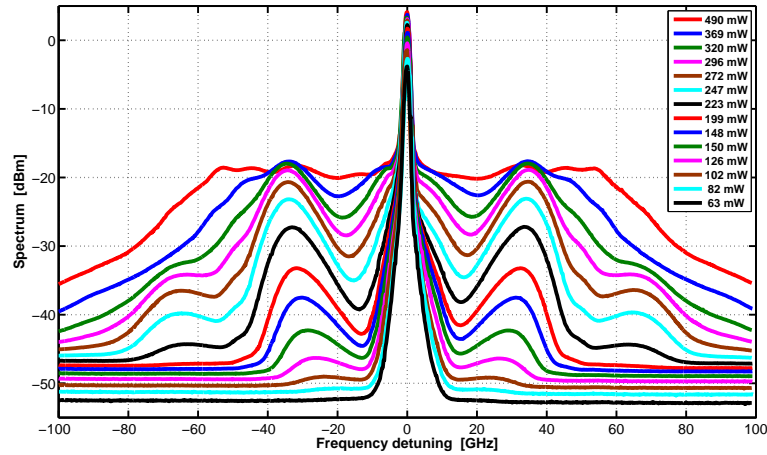


Figure 3.8 – MI spectra measured for different levels of input power in a standard SMF with $L = 25.4$ km and $\gamma = 1.0 \frac{\text{W}^{-1}}{\text{km}}$.

The same results for an 11.1 km long standard SMF are depicted in Fig. 3.9. It is evident from

the figure that the input power for MI onset is more than 200 mW which is higher than the previous fiber's MI onset power because the current fiber is shorter in length. It demonstrates experimentally how critical the interaction length given by L_{eff} is in the onset of modulation instability. For this fiber also other phenomena like second-order MI for powers more than 500 mW and high interaction regime at around 1 W are evident from the plots in Fig 3.8.

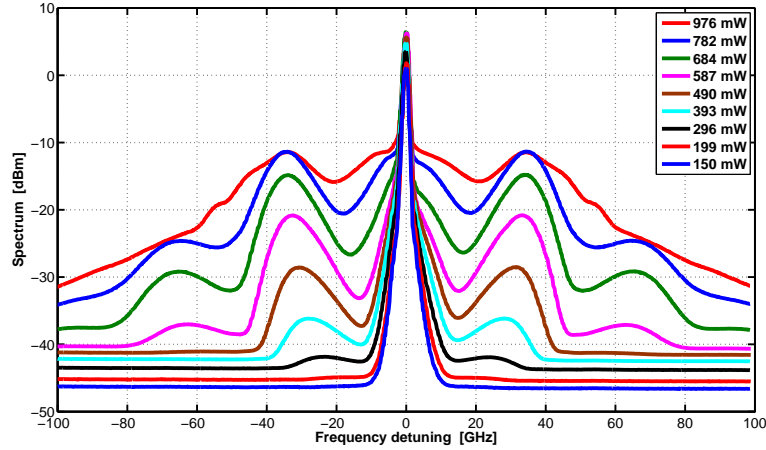


Figure 3.9 – MI spectra measured for different levels of input power in a standard SMF with $L = 11.1$ km and $\gamma = 1.6 \frac{\text{W}^{-1}}{\text{km}}$.

An 8.7 km long DSF is used to measure the modulation instability spectrum which is shown in Fig. 3.10. Since the fiber's zero-dispersion wavelength is 1500 nm, the dispersion coefficient is less than that of standard SMFs and thus the MI spectrum in DSFs is wider which is evident from the figure. For instance, at the power level of around 300 mW, the frequency of maximal gain happens to be around 80 GHz for the DSF while it is about 35 GHz for the utilized SMFs. Although the fiber length is shorter than the 11.1 km SMe, the MI onset power is less because the nonlinear coefficient of DSFs is higher than that of SMFs.

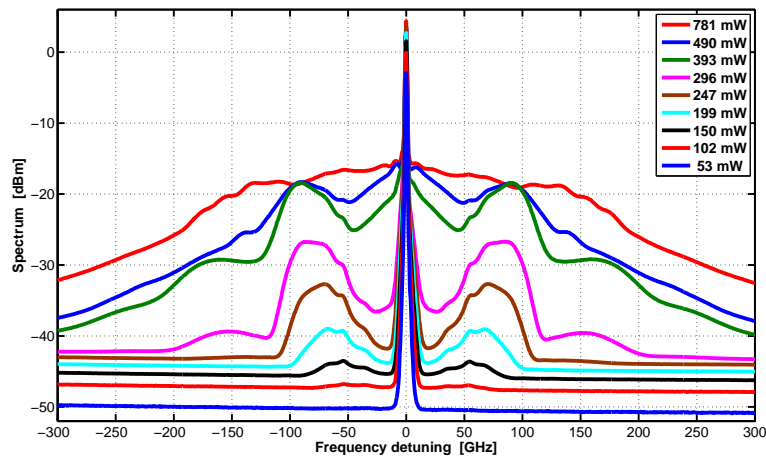


Figure 3.10 – MI spectra measured for different levels of input power in a DSF with $L = 8.7$ km and $\gamma = 3.1 \frac{\text{W}^{-1}}{\text{km}}$.

3.5. Experimental Observation of MI Spectrum

Fig. 3.11 shows the MI spectrum measured at the output of a 4.8 km long special fiber. The fiber's refractive index profile is a step index with the core diameter of around $4\ \mu\text{m}$ and so the effective area is one quarter of a typical standard SMF. Therefore, this fiber's nonlinear coefficient is four times bigger than that of a standard SMF. Actually, its measured nonlinear coefficient is $\gamma = 4.0\ \frac{\text{W}^{-1}}{\text{km}}$; for the detail see the previous chapter. As it is evident from the figure, the MI onset power is around 150 mW which is quite low for a step-index fiber with the length of 4.8 km. This is exactly because of its higher nonlinear coefficient due to the lower effective area. The fluctuations in the MI spectra of this fiber can be a result of fluctuations in phase matching conditions due to non-uniformity of the fiber's structure.

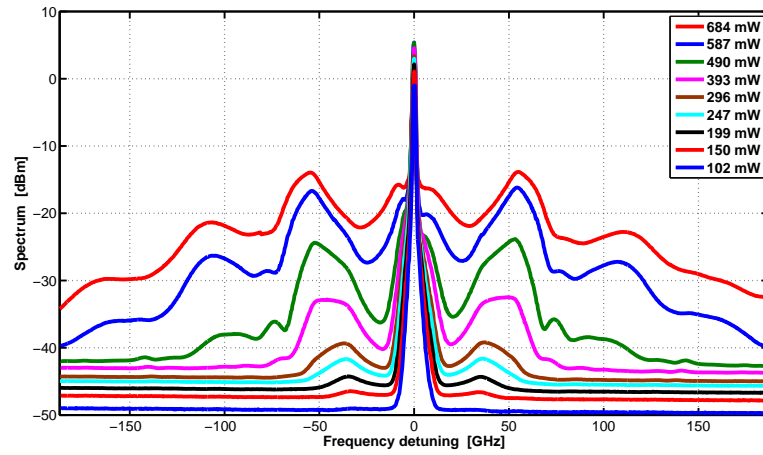


Figure 3.11 – MI spectra measured for different levels of input power in a special fiber with $L = 4.8\ \text{km}$ and $\gamma = 4.0\ \frac{\text{W}^{-1}}{\text{km}}$.

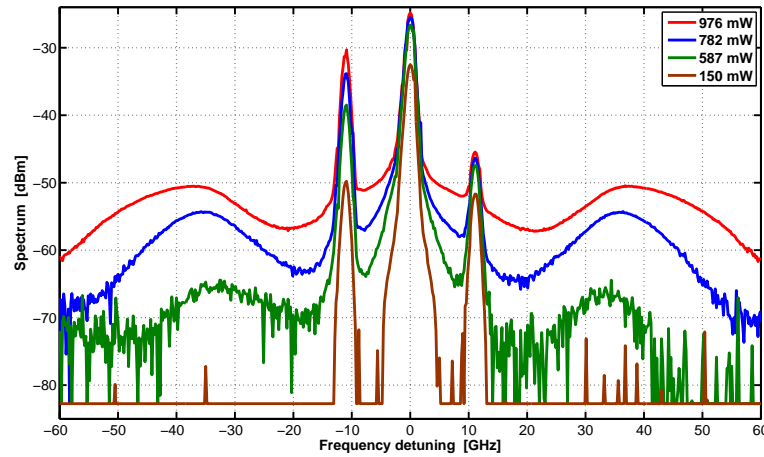


Figure 3.12 – Back scattered spectra measured from the 11.1 km long standard SMF for different levels of input power showing the Brillouin backscattering of the pump and the Rayleigh backscattering of the MI spectrum.

In the experimental setup illustrated in Fig. 3.7 there is a possibility to measure the backscattered light from the fiber under test. It is important to monitor the back reflection, especially

for avoiding high levels of stimulated Brillouin scattering that can deplete the pump hugely and decrease the Kerr interaction in the fiber substantially. Fig. 3.12 depicts the measured spectra back scattered from the 11.1 km long standard SMF. The central component in the spectra shows the Rayleigh backscattering while the narrow-band Stokes and anti-Stokes component at around 11 GHz illustrate a combination of the stimulated and spontaneous Brillouin scattering processes. It is evident from the figure that the stimulated Brillouin backscattering at the highest input peak power (≈ 1 W) is still less than the Rayleigh backscattering. The main reason for that is the short pulse duration (≈ 6 ns) that enhances the Brillouin critical power substantially. Moreover, the modulation instability spectra seen in the back reflection for high powers are the Rayleigh backscattering of the forward travelling MI spectra. The modulation instability spectrum that has been obtained analytically in this chapter and demonstrated experimentally is utilized in the following chapter to make a model for the MI characteristics of an optical fiber such as the depletion length due to MI and the critical power for the onset of modulation instability.

4 MI Critical and Optimal Power

A critical power for a nonlinear process is intuitively defined as the power below which nonlinear effects can be neglected. Critical powers for nonlinear inelastic scattering processes in optical fibers, namely stimulated Raman scattering (SRS) and stimulated Brillouin scattering (SBS) were proposed for the first time by R. G. Smith in 1972 [79]. The analysis by Smith led to the following well-known formulas for critical powers of forward SRS P_{critR} and backward SBS P_{critB} :

$$P_{\text{critR}} = \frac{16A_{\text{eff}}}{g_{\text{R}}L_{\text{eff}}}, \quad (4.1a)$$

$$P_{\text{critB}} = \frac{21A_{\text{eff}}}{g_{\text{B}}L_{\text{eff}}}, \quad (4.1b)$$

where A_{eff} is the mode effective area and L_{eff} is the fiber effective length. g_{R} and g_{B} denote the Raman and Brillouin gain in the medium, respectively. These formulas have been widely used in fiber optics, even though there are controversies on their accuracy [80, 81]. For instance, pump depletion along with low fiber attenuation is taken into account for SRS in [82] and for SBS in [83], leading to critical powers less than in Eqs. (4.1b) which means the estimations proposed by Smith are an upper bound for critical powers. This chapter is devoted to finding a similar formula for the critical power of modulation instability (MI). First we investigate the behaviour of pump power along the fiber using the numerical analysis of the nonlinear Schrödinger equation; especially the recurrence phenomenon and the impact of background noise on the pump power evolution are analyzed. Then, a mathematical model for the critical power of modulation instability is presented by using the MI gain spectrum derived in the previous chapter and by introducing the notion of depletion ratio. Additionally, the model is extended to obtain the maximal output power and its corresponding optimal input power in a fiber-optic system suffering from modulation instability. For validating the model an experiment is carried out in which a Brillouin distributed fiber sensor is utilized to measure the power evolution and MI behaviour along an optical fiber. Moreover, a quick analysis of pump-probe interaction in distributed fiber sensors due to stimulated Brillouin scattering is provided for understanding the working principles of the experimental setup. Finally the results of experimental measurement are analyzed and compared with the theoretical model and numerical simulation for evaluating the accuracy of the proposed model.

4.1 Power Evolution

As a high power CW or quasi-CW lightwave propagates in an optical fiber, the power transfers gradually from the pump to the frequency bands around the light wavelength due to the process of modulation instability originating from the noisy fluctuations on the pump intensity. This power transfer, called pump depletion, decreases the pump power drastically and it is the most detrimental effect in many distributed fiber sensors [12, 9, 11]. Therefore, monitoring the power evolution along an optical fiber is important for investigating the performance of distributed sensors. This section is devoted to the analysis of pump power as the lightwave propagates along an optical fiber. Assume that a CW lightwave of power P_0 generated by a narrow-band laser at frequency ω_0 is launched into an optical fiber of length L . The power at pump frequency along the fiber is denoted by $P(z)$ where z is the position along the fiber varying from 0 to L . Obviously, we have $P(0) = P_0$ which is the input pump power. In a linear system where there is no nonlinear interaction, the only cause affecting the pump power is the linear loss due to absorption and scattering which is represented by the attenuation coefficient α . Therefore, in the ideal linear situation, the power evolution is given by the exponential function $P_0 e^{-\alpha z}$. In real conditions where there is inevitable nonlinear interaction, the power along the fiber can be far away from the ideal exponential decay. This gap is caused by the pump depletion due to nonlinear effects like modulation instability. In order to quantify such a difference between the ideal and real conditions a local *depletion ratio* is defined as follows:

$$r(z) \triangleq \frac{\text{depleted power}}{\text{ideal power}} = \frac{P_0 e^{-\alpha z} - P(z)}{P_0 e^{-\alpha z}} = 1 - \frac{P(z)}{P_0 e^{-\alpha z}}. \quad (4.2)$$

Since there is no other coherent source except the pump we can assume that $P(z)$ is always less than $P_0 e^{-\alpha z}$ and so the depletion ratio in Eq. (4.2) is positive. On the other hand, its maximum is 1 and so, $0 \leq r(z) \leq 1$. In order to get rid of the attenuation factor in the power evolution, the normalized pump power along the fiber is defined as

$$p(z) \triangleq \frac{\text{actual power}}{\text{ideal power}} = \frac{P(z)}{P_0 e^{-\alpha z}}. \quad (4.3)$$

Clearly, we have $p(z) + r(z) = 1$. In the linear regime where there is no pump depletion, $p(z) = 1$ for every position z along the fiber; while any deviation from the constant function implies the existence of depletion due to nonlinear phenomena. In order to investigate the power evolution along the fiber or the variations of $p(z)$, several numerical simulations have been carried out.

Fig. 4.1 depicts the pump power evolution along a lossless standard SMF for several levels of input power. As the pump propagates along the fiber, its power transfers to MI sidebands and so it decreases. It is clear from the figure that by increasing the input power, the pump depletion due to MI starts at earlier positions and evolves faster. Besides showing pump depletion, the oscillatory behavior of the pump power propagating through the fiber is evident from the figure. This phenomenon, which is responsible for transferring power from signal back to pump, is called the Fermi-Pasta-Ulam (FPU) recurrence [84] and it has been theoretically studied and experimentally demonstrated in optical fibers [85, 86, 87]. Since the background

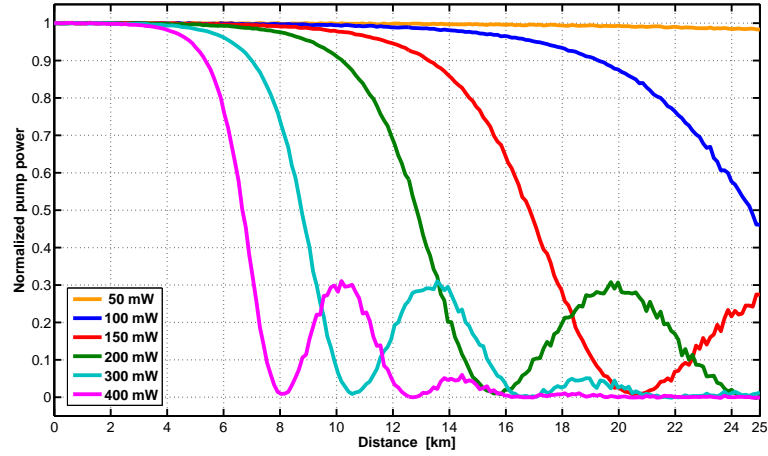


Figure 4.1 – Pump power evolution along a lossless SMF of 25 km with $\gamma = 1.8 \frac{\text{W}^{-1}}{\text{km}}$ and $\beta_2 = -22 \frac{\text{ps}^2}{\text{km}}$, in the presence of noise with a power spectral density of $-121 \frac{\text{dBm}}{\text{Hz}}$. Each plot is normalized to its corresponding input pump power.

noise plays the role of signal in modulation instability and it is not in coherence with the pump, full recurrence cannot happen and so the oscillation of power in Fig. 4.1 damps.

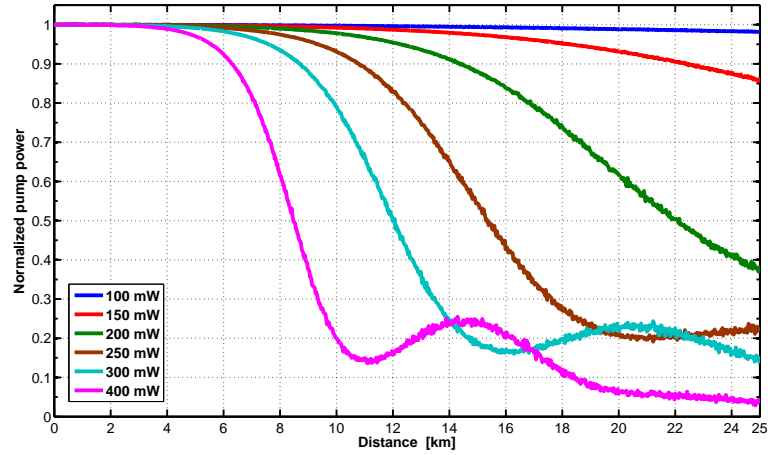


Figure 4.2 – Pump power evolution along an SMF of 25 km with $\alpha = 0.2 \frac{\text{dB}}{\text{km}}$, $\gamma = 1.8 \frac{\text{W}^{-1}}{\text{km}}$ and $\beta_2 = -22 \frac{\text{ps}^2}{\text{km}}$, in the presence of noise with a power spectral density of $-121 \frac{\text{dBm}}{\text{Hz}}$. The vertical axis shows $p(z)$ meaning that the pump power is normalized to $P_0 e^{-\alpha z}$ to discard the effect of the fiber attenuation on the curves.

Fig. 4.2 shows the power evolution in a lossy optical fiber. To discard the effect of loss for the sake of visibility, the normalized power which is the pump power divided by $P_0 e^{-\alpha z}$ is plotted in the figure. Compared to the lossless case in Fig. 4.1, the fiber attenuation delays the occurrence of modulation instability and reduces the strength of FPU recurrence. For example, the pump power starts to deplete at position 15 km along the lossless fiber for the input power of 100 mW, while the propagation in the lossy fiber remains in the linear regime and thus no depletion occurs.

4.1.1 Impact of Background Noise on the MI Evolution

It is worth mentioning that modulation instability and optical parametric amplification are in essence the same process, both being originated by the Kerr effect; for this reason sometimes the two terms are interchangeably used in the literature [88]. However if the focus is placed on the subtle differences, it should be noticed that in OPA a deterministic signal and the background noise within the OPA spectral band are amplified via energy transfer from a high-power pump to a signal and idler through a four-photon mixing process [89]. Spontaneous modulation instability is however solely seeded by the background noise present in the spectral band of MI, so that the background noise plays the simultaneous roles of signal and idler for modulation instability [90]; it is therefore essential to take into account the randomness inherent in noise when analyzing modulation instability. The strong impact of the background noise level on the MI evolution has been shown theoretically [91, 92] and experimentally [93, 94, 95]; thus neglecting this effect would certainly lead to a discrepancy between the experimental data and any theoretical model [10]. Since the modulation instability process is seeded by the background noise in its spectral band, the noise strength which is determined by its power spectral density (PSD) must have a critical role in the onset of modulation instability and thus, the evolution of pump power during the process. In order to demonstrate it the simulations in Fig. 4.2 have been redone for the same fiber and input powers but with a noise PSD of $10 \frac{\text{dB}}{\text{Hz}}$ more; the results are plotted in Fig. 4.3. It is evident from the comparison of the two figures that the noise level has a considerable effect on the MI evolution and thus, the pump depletion. For instance, when the input power is 150 mW, the amount of depletion at the fiber end ($L = 25 \text{ km}$) is 15% for the noise PSD of $-121 \frac{\text{dBm}}{\text{Hz}}$ from Fig. 4.2, while it is more than 65% from Fig. 4.3 for the noise level of $-111 \frac{\text{dBm}}{\text{Hz}}$.

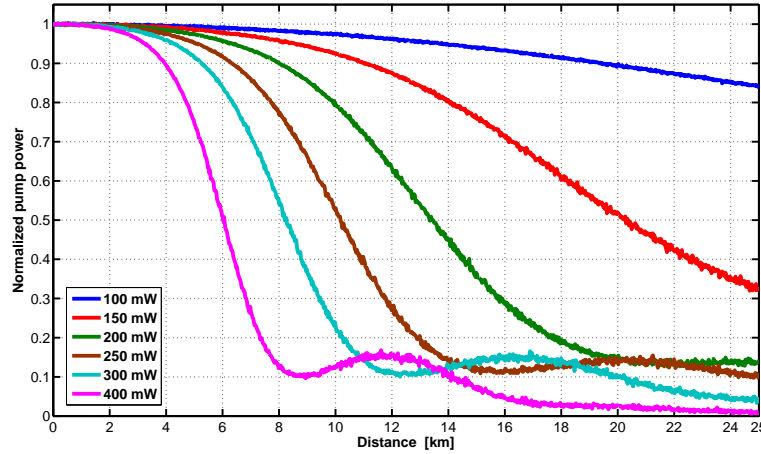


Figure 4.3 – Pump power evolution along an SMF of 25 km with $\alpha = 0.2 \frac{\text{dB}}{\text{km}}$, $\gamma = 1.8 \frac{\text{W}^{-1}}{\text{km}}$ and $\beta_2 = -22 \frac{\text{ps}^2}{\text{km}}$, in the presence of noise with a power spectral density of $-111 \frac{\text{dBm}}{\text{Hz}}$. The vertical axis shows $p(z)$ meaning that the pump power is normalized to $P_0 e^{-\alpha z}$ to discard the effect of the fiber attenuation on the curves.

From another perspective, we can see that 50% of depletion in the case of 200-mW input power occurs after 22-km propagation in fiber while for the higher noise level it happens by less than 14 km propagation. In order to see the impact of noise on the pump power depletion,

the output pump power of a 10 km long standard SMF is numerically simulated versus its input power for different levels of noise power spectral density and it is plotted in Fig. 4.4. A broad range of noise levels has been considered spanning from the quantum noise PSD $\frac{\hbar\omega_0}{2}$, which is around $-161 \frac{\text{dBm}}{\text{Hz}}$ at 1550 nm, up to $-101 \frac{\text{dBm}}{\text{Hz}}$ using the power step of $10 \frac{\text{dB}}{\text{Hz}}$. The figure self-explains how strong the noise level influences the onset and behavior of modulation instability. It is evidently seen from the figure that increasing the noise level seeds more MI and thus, reduces the output pump power as a consequence of the increased pump depletion. Therefore, the input pump power for which modulation instability starts to be significant crucially depends on the noise level present in the system.

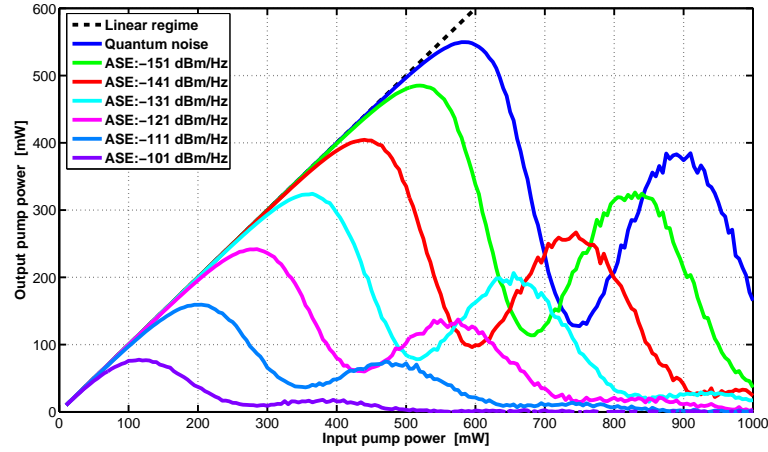


Figure 4.4 – Output pump power versus input power for an SMF of length $L = 10$ km with $\alpha = 0.2 \frac{\text{dB}}{\text{km}}$, $\gamma = 1.8 \frac{\text{W}^{-1}}{\text{km}}$ and $\beta_2 = -22 \frac{\text{ps}^2}{\text{km}}$ for different levels of noise power spectral density. The pump power is normalized to $e^{-\alpha L}$ to remove the effect of the fiber attenuation on the curves.

4.2 Modeling the MI Critical Power

This section is devoted to obtaining a mathematical model for the critical power of noise-seeded modulation instability. The model is based on the modulation instability gain spectrum derived in the previous chapter. The idea behind it is to obtain the amount of pump depletion by simply calculating the power transferred from the pump to the MI spectral band. The strength of this approach is in taking all frequency components of the nonlinear interaction into account. The transferred power is simply calculated by integrating over the entire modulation instability spectrum; in doing so there are two issues to which attention should be paid. First, the available analytical gain spectrum is obtained in small signal gain or actually undepleted pump power regime. Therefore, the model should be used in low depletion conditions. In distributed sensors it is tried to avoid strong pump depletion and thus, assuming the system to be in the low depletion regime is plausible. Secondly, the MI gain spectrum is not analytically integrable and thus there is no closed-form exact value for the depleted power. Therefore, it is essential to approximate the spectral integral; to do so, Laplace's method of integration is utilised which has a high accuracy in evaluating the integrals involving exponential functions. The essentials of Laplace's method are described in Appendix B. As it has been

Chapter 4. MI Critical and Optimal Power

seen in the previous chapter, the modulation instability or noise gain at the end of an optical fiber of length L with an attenuation coefficient α and an input power P_0 can be approximated by

$$G_n \approx e^{-\alpha L} (1 + G_p) = e^{-\alpha L} \left(1 + 2 \frac{(\gamma P_0)^2}{g^2} \sinh^2(g L_{\text{eff}}) \right), \quad (4.4)$$

where the exponent g is given in terms of the fiber nonlinear coefficient γ and the linear phase mismatch $\Delta\beta$ as follows:

$$g^2 = (\gamma P_0)^2 - \left(\gamma P_0 + \frac{\Delta\beta}{2} \right)^2. \quad (4.5)$$

The gain in Eq. (4.4) is divided into two parts: the unitary term demonstrating the existence of noise independent from the pump wave and the net gain G_p which is responsible for the power transferred from the pump into the MI sidebands. According to the previous chapter, when the second order dispersion is dominant, i.e. the linear phase mismatch $\Delta\beta$ is given by $\beta_2(\omega - \omega_0)^2$, the net gain can be expressed as

$$G_p(\omega) = \frac{\sinh^2 \left(2\gamma P_0 L_{\text{eff}} \sqrt{\left(\frac{\omega - \omega_0}{\Omega_c} \right)^2 \left(1 - \left(\frac{\omega - \omega_0}{\Omega_c} \right)^2 \right)} \right)}{2 \left(\frac{\omega - \omega_0}{\Omega_c} \right)^2 \left(1 - \left(\frac{\omega - \omega_0}{\Omega_c} \right)^2 \right)}, \quad (4.6)$$

in which Ω_c is given by $\sqrt{\frac{4\gamma P_0}{|\beta_2|}}$. Assume that $S_n(\omega)$ in $\frac{W}{\text{Hz}}$ denotes the one-sided power spectral density of the background noise traveling with the pump. The power transferred or depleted from the pump into the modulation instability sidebands can be obtained by the following spectral integral:

$$P_{\text{MI}} = \frac{1}{2\pi} \int_0^\infty S_n(\omega) e^{-\alpha L} G_p(\omega) d\omega = \frac{e^{-\alpha L}}{2\pi} \int_0^\infty S_n(\omega) G_p(\omega) d\omega. \quad (4.7)$$

The integral in Eq. (4.7) can be calculated over the spectral lobes of the MI gain from $\omega_0 - m\Omega_c$ to $\omega_0 + m\Omega_c$ where m is a positive integer showing the number of spectral sidebands taken into account for calculating the depleted power. Since most of power is in the first side lobes of the MI symmetric spectrum, m can be set to 1 with fairly acceptable accuracy. However, the larger m the more accurate the approximation will be; ideally, m should tend to infinity. Moreover, in a real system, the main source of noise launched into optical fibers comes from the amplified spontaneous emission (ASE) generated in optical amplifiers, such as the commonly-used erbium-doped fiber amplifiers (EDFA). Since the MI spectral width is quite narrow (less than 1 nm) compared to the ASE linewidth (more than 30 nm), the noise spectral density can be assumed to be flat or white and so it is independent of frequency. Therefore, the MI power in

Eq. (4.7) is calculated by

$$P_{\text{MI}} = \frac{e^{-\alpha L}}{2\pi} \int_0^\infty S_n(\omega) G_p(\omega) d\omega \approx \frac{e^{-\alpha L} S_n}{2\pi} \int_{\omega_0 - m\Omega_c}^{\omega_0 + m\Omega_c} G_p(\omega) d\omega. \quad (4.8)$$

The second integral in Eq. (4.8) can be modified by normalizing and centering the frequency variable through $x = \frac{\omega - \omega_0}{\Omega_c}$,

$$\int_{\omega_0 - m\Omega_c}^{\omega_0 + m\Omega_c} G_p(\omega) d\omega = \Omega_c \int_{-m}^{+m} G_p(x) dx, \quad (4.9)$$

where the net gain $G_p(x)$ is obtained from Eq. (4.6) and is given by

$$G_p(x) = \frac{\sinh^2\left(2\gamma P_0 L_{\text{eff}} \sqrt{x^2(1-x^2)}\right)}{2x^2(1-x^2)}. \quad (4.10)$$

Substituting Eq. (4.9) in Eq. (4.8) and letting m go to infinity result in

$$P_{\text{MI}} = \frac{e^{-\alpha L} S_n \Omega_c}{2\pi} \lim_{m \rightarrow \infty} \int_{-m}^{+m} G_p(x) dx = \frac{e^{-\alpha L} S_n \Omega_c}{2\pi} \int_{-\infty}^{+\infty} G_p(x) dx. \quad (4.11)$$

It is interesting to note that the net gain function $G_p(x)$ is a real-valued nonnegative and even function for all real numbers, as explained hereafter. It is clearly seen that $G_p(-x) = G_p(x)$ and thus, the function is even. For x where $|x| < 1$, it is evident from Eq. (4.10) that $G_p(x)$ is real and positive. For x equal to 0 and ± 1 , the function acquires the value of $2(\gamma P_0 L_{\text{eff}})^2$ which is obviously positive. However, for x where $|x| > 1$, it is not clear and the following argument is needed; when $|x| > 1$, it is true that $1 - x^2 < 0$, so $\sqrt{x^2(1-x^2)} = i\sqrt{x^2(x^2-1)}$ where the term $\sqrt{x^2(x^2-1)}$ is a real number and i denotes the imaginary unit. On the other hand, for the hyperbolic and trigonometric sine functions the identity $\sinh(iu) = i \sin(u)$ always holds. So,

$$\begin{aligned} \sinh\left(2\gamma P_0 L_{\text{eff}} \sqrt{x^2(1-x^2)}\right) &= \sinh\left(2i\gamma P_0 L_{\text{eff}} \sqrt{x^2(x^2-1)}\right) \\ &= i \sin\left(2\gamma P_0 L_{\text{eff}} \sqrt{x^2(x^2-1)}\right), \end{aligned} \quad (4.12)$$

and accordingly,

$$\begin{aligned} \sinh^2\left(2\gamma P_0 L_{\text{eff}} \sqrt{x^2(1-x^2)}\right) &= i^2 \sin^2\left(2\gamma P_0 L_{\text{eff}} \sqrt{x^2(x^2-1)}\right) \\ &= -\sin^2\left(2\gamma P_0 L_{\text{eff}} \sqrt{x^2(x^2-1)}\right). \end{aligned} \quad (4.13)$$

Therefore, the net gain $G_p(x)$ in Eq. (4.10) for the variable x where $|x| > 1$, is written as

$$\begin{aligned} G_p(x) &= \frac{\sinh^2\left(2\gamma P_0 L_{\text{eff}} \sqrt{x^2(1-x^2)}\right)}{2x^2(1-x^2)} = \frac{-\sin^2\left(2\gamma P_0 L_{\text{eff}} \sqrt{x^2(x^2-1)}\right)}{-2x^2(x^2-1)} \\ &= \frac{\sin^2\left(2\gamma P_0 L_{\text{eff}} \sqrt{x^2(x^2-1)}\right)}{2x^2(x^2-1)}. \end{aligned} \quad (4.14)$$

Chapter 4. MI Critical and Optimal Power

Eq. (4.14) clearly demonstrates that $G_p(x)$ for $|x| > 1$ is a real-valued nonnegative function. Therefore, the integral in Eq. (4.11) for calculating the depleted power is a positive number well-defined as

$$I = \int_{-\infty}^{+\infty} G_p(x) dx = \int_{-\infty}^{+\infty} \frac{\sinh^2 \left(2\gamma P_0 L_{\text{eff}} \sqrt{x^2(1-x^2)} \right)}{2x^2(1-x^2)} dx. \quad (4.15)$$

The integral in Eq. (4.15) has no analytical solution, so to obtain a closed-form solution, it is necessary to approximate it. Since the integral involves the hyperbolic sine function which is an exponential form, Laplace's method is a promising approximation for calculating it. Actually, the same method has been used to derive accurate critical powers for the SRS and SBS processes [96, 97]. The method and its proof have been explained in Appendix B. Consider two non-exponential real functions $f(x)$ and $g(x)$ so that f has its maximum at x_0 where $g(x_0)$ is positive. Laplace's method states that for a positive number s , the following approximation is held [98]:

$$\int_{-\infty}^{+\infty} g(x) e^{sf(x)} dx \approx g(x_0) e^{sf(x_0)} \sqrt{\frac{2\pi}{s|f''(x_0)|}}, \quad (4.16)$$

where $f''(x_0)$ is the second derivative of f at x_0 . Since f has a maximum at x_0 , the exponential function $e^{sf(x)}$ has a sharp peak at x_0 . The same thing happens for the hyperbolic function in $G_p(x)$. The maximum of G_p occurs at $x_0^2 = \frac{1}{2}$ and its first zero happens to be at $x^2 = \frac{1}{2} + \frac{1}{2} \sqrt{1 + \left(\frac{\pi}{\gamma P_0 L_{\text{eff}}} \right)^2}$, showing how sharp the gain function is, especially when $\gamma P_0 L_{\text{eff}} \gg 1$; so Laplace's method is appropriate to be applied to the integral in Eq. (4.15). In order to use Laplace's theorem, the following exponential approximation is first considered for the hyperbolic sine:

$$\sinh^2(u) = \left(\frac{e^u - e^{-u}}{2} \right)^2 \approx \frac{e^{2u}}{4}, \quad \text{for } u \gg 1. \quad (4.17)$$

$G_p(x)$ has its two equal maxima at $x_0 = \pm \frac{1}{\sqrt{2}}$ where $G_p(x_0) = 2 \sinh^2(\gamma P_0 L_{\text{eff}}) \approx \frac{e^{2\gamma P_0 L_{\text{eff}}}}{2}$ is a good approximation assuming $\gamma P_0 L_{\text{eff}} \gg 1$. Therefore, the integral in Eq. (4.15) can be approximated by

$$I = \int_{-\infty}^{+\infty} G_p(x) dx \approx \int_{-\infty}^{+\infty} \frac{\exp \left(4\gamma P_0 L_{\text{eff}} \sqrt{x^2(1-x^2)} \right)}{8x^2(1-x^2)} dx. \quad (4.18)$$

The integral in Eq. (4.18) by analogy with Laplace's formula in Eq. (4.16) leads to the following definitions for the parameter s and functions f and g :

$$f(x) = \sqrt{x^2(1-x^2)}, \quad (4.19a)$$

$$g(x) = \frac{1}{8x^2(1-x^2)}, \quad (4.19b)$$

$$s = 4\gamma P_0 L_{\text{eff}}. \quad (4.19c)$$

For $x_0 = \pm \frac{1}{\sqrt{2}}$, it is easily seen that $f(x_0) = g(x_0) = \frac{1}{2}$ and $f''(x_0) = -4$. Applying Laplace's method to Eq. (4.18) and considering two equal maxima at $\pm \frac{1}{\sqrt{2}}$, we have the following approximate closed-form value for I :

$$I = \int_{-\infty}^{+\infty} G_p(x) dx \approx 2g(x_0) e^{sf(x_0)} \sqrt{\frac{2\pi}{s|f''(x_0)|}} = \frac{\sqrt{\pi} e^{2\gamma P_0 L_{\text{eff}}}}{2\sqrt{2\gamma P_0 L_{\text{eff}}}}. \quad (4.20)$$

Substituting Eq. (4.20) in the MI depleted power given by Eq. (4.11) and considering the cutoff frequency $\Omega_c = \sqrt{\frac{4\gamma P_0}{|\beta_2|}}$ result in

$$P_{\text{MI}} = \frac{S_n e^{2\gamma P_0 L_{\text{eff}} - \alpha L}}{2\sqrt{2\pi|\beta_2|L_{\text{eff}}}}. \quad (4.21)$$

Eq. (4.21) is a closed-form formula for the power in the modulation instability sidebands depleted from pump. On the other hand, setting a depletion ratio R at the position L along the fiber, i.e. $r(L) = R$, the MI power can be obtained based on Eq. (4.2) as

$$P_{\text{MI}} = P_0 e^{-\alpha L} R. \quad (4.22)$$

Combining Eq. (4.21) and Eq. (4.22) leads to the following expression:

$$S_n e^{2\gamma P_0 L_{\text{eff}}} = 2P_0 R \sqrt{2\pi|\beta_2|L_{\text{eff}}}. \quad (4.23)$$

Eq. (4.23) is a transcendental equation that can be considered for either P_0 or L_{eff} as its variable. For a fixed input power P_0 , the effective length obtained from Eq. (4.23) corresponds to a fiber length where there is $R\%$ depletion due to modulation instability. The fiber length corresponding to the calculated effective length is named *depletion length* [99] and is given by $L_D = -\alpha^{-1} \ln(1 - \alpha L_{\text{eff}})$. On the other hand, if we consider the input power P_0 as the variable and the fiber length as a parameter, Eq. (4.23) gives an input power of an optical fiber for which there is $R\%$ depletion at the position L corresponding to the effective length $L_{\text{eff}} = \alpha^{-1}(1 - e^{-\alpha L})$. The power obtained so is called *critical power* [100] and is denoted by P_{crit} . Defining the critical gain or exponent $\sigma_{\text{crit}} = 2\gamma P_{\text{crit}} L_{\text{eff}}$, Eq. (4.23) can be rewritten as

$$e^{\sigma_{\text{crit}}} = \frac{R\sqrt{2\pi|\beta_2|}}{S_n\gamma\sqrt{L_{\text{eff}}}} \sigma_{\text{crit}}. \quad (4.24)$$

Eq. (4.24) can be easily solved by simple numerical approaches like the bisection method to obtain the critical exponent σ_{crit} and thus, the critical power P_{crit} by the following expression:

$$P_{\text{crit}} = \frac{\sigma_{\text{crit}}}{2\gamma L_{\text{eff}}}. \quad (4.25)$$

Since the critical exponent in Eq. (4.24) depends on the effective length through the term $\sqrt{L_{\text{eff}}}$ in the equation, the critical power in Eq. (4.25) is not exactly in inverse proportion to the effective length. However, for long optical fibers the effective length $L_{\text{eff}} = \alpha^{-1}(1 - e^{-\alpha L})$ can

be approximated by $L_\infty = \alpha^{-1}$ and so Eq. (4.24) modifies to the the following expression:

$$e^{\sigma_{\text{crit}}} = \frac{R\sqrt{2\pi\alpha|\beta_2|}}{S_n\gamma}\sigma_{\text{crit}}, \quad (4.26)$$

whose solution σ_{crit} is independent from fiber length. As an example, consider a standard SMF with typical parameters $\alpha = 0.2 \frac{\text{dB}}{\text{km}}$, $\beta_2 = -22 \frac{\text{ps}^2}{\text{km}}$ and $\gamma = 1.8 \frac{\text{W}^{-1}}{\text{km}}$. Substituting all the numerical parameters in Eq. (4.26), taking its logarithm and expressing the noise power spectral density S_n in $\frac{\text{dBm}}{\text{Hz}}$ instead of $\frac{\text{W}}{\text{Hz}}$, result in the following equation for σ_{crit} :

$$\sigma_{\text{crit}} - \ln(\sigma_{\text{crit}}) = \ln(R) - \left(\frac{S_n}{10} + 9\right)\ln(10) + \frac{\ln(2)}{2}. \quad (4.27)$$

For a tolerable depletion ratio R and a noise power spectral density S_n the critical exponent σ_{crit} and thus, the critical power P_{crit} are calculated from Eq. (4.27) independent from fiber length; for instance, if a system tolerates a maximum depletion of 10%, i.e. $R = 0.1$, and the background noise level launched into the fiber is $-121 \frac{\text{dBm}}{\text{Hz}}$, Eq. (4.27) is reduced to $\sigma_{\text{crit}} - \ln(\sigma_{\text{crit}}) = 5.18$, whose solution is 7.15. So, for a 25-km standard SMF the critical input power that induces at most 10% of depletion at the fiber end can be simply calculated from Eq. (4.25) to be around 135 mW. This value actually agrees very well with experimental observation reported in the literature [95]. It should be clarified that the depletion ratio in this case is 10% only at the end of the fiber (25 km), and it is certainly lower at shorter distances along the fiber. In order to evaluate the accuracy of the model, the analytical solutions given by Eq. (4.24) and Eq. (4.26) are compared with the numerical simulation of the nonlinear Schrödinger equation (NLSE). It should be noted that by simulating the NLSE all aspects of its corresponding real system including the pump depletion and fiber length are taken into account. However, Eq. (4.24), called Model I, neglects the effect of pump depletion in the modulation instability gain and Eq. (4.26), called Model II, removes the effect of fiber length in addition to neglecting the pump depletion.

Fig. 4.5 plots the critical gain σ_{crit} versus the fiber length calculated in three ways: the

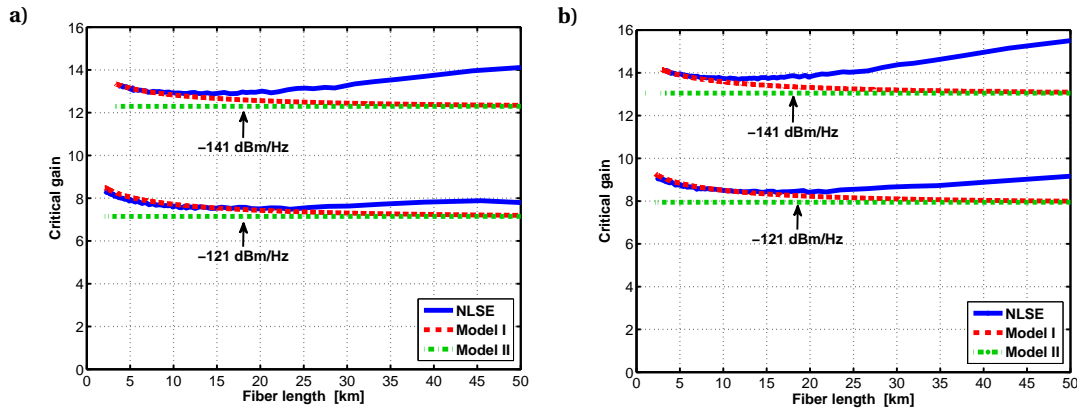


Figure 4.5 – Critical gain versus fiber length obtained from the NLSE, Model I and Model II for a) $R = 10\%$ and b) $R = 20\%$, using two values of noise PSD: -121 and $-141 \frac{\text{dBm}}{\text{Hz}}$.

simulation of the NLSE, the solution of Model I in Eq. (4.24), and the solution of Model II in Eq. (4.26). Two levels of ASE noise, namely -141 and $-121 \frac{\text{dBm}}{\text{Hz}}$, along with two depletion ratios, i.e. 10% and 20%, are assumed in the figure to describe how σ_{crit} varies with the amount of tolerable depletion R and the noise power spectral density S_n . As it is evident from Fig. 4.5, all four samples have the same behavior. In short length regime the NLSE and Model I are in good agreement since the undepleted pump approximation is accurately valid; while Model II has a discrepancy since the effective length approximation (i.e. assuming $L_{\text{eff}} = \alpha^{-1} = 21.7 \text{ km}$) is not accurate in short ranges, where L_{eff} is clearly shorter than α^{-1} . On the other hand, in long fibers the solution of the analytical model differs from the simulation of the NLSE due to the loss of accuracy of the undepleted pump approximation for long propagation lengths leading to more nonlinear interaction. However, Model II approximates the solution of Model I asymptotically in long distances. Actually, it is worth mentioning that the constant critical gain obtained from Model II determines in all cases a safe and relatively accurate limit on the peak power to avoid a certain amount of MI depletion, keeping in mind that the real critical power could be slightly higher for a real system. It should also be noticed that since the MI gain is here calculated using the undepleted pump approximation, the lower the depletion ratio, the more accurate the model is and thus the obtained value for σ_{crit} . This is evident when comparing Fig. 4.5a with Fig. 4.5b. Since the variation of σ_{crit} with respect to fiber length turns out to be negligible when compared to the effect of other factors such as noise and tolerable depletion ratio, a constant critical gain σ_{crit} can be calculated with an acceptable approximation by using Eq. (4.26) independently from the fiber length.

4.2.1 Optimal Input and Maximal Output Power

Since the maximum sensing distance and performance of Brillouin distributed fiber sensors are determined by the signal-to-noise ratio (SNR) at the far end of the sensing fiber [101], it is critical to obtain the maximum achievable power at the fiber end and its corresponding optimal input pump power. As long as there is no depletion due to nonlinear interactions such as modulation instability and stimulated Raman and Brillouin scattering, the pump power follows the exponential decay and thus, at the output of a sensing fiber of length L , the pump power is $P_0 e^{-\alpha L}$ where P_0 is the input pump power. Therefore, in the linear regime, as P_0 increases the output power and thus the SNR increase proportionally. However, nonlinearity, especially modulation instability depletes the pump power and surprisingly the increase in the input pump power can lead to a decrease in the output pump power and thus a degradation in the sensing distance and system performance. To show this behaviour, a numerical simulation on the power evolution has been done for a 10 km fiber and the result is depicted in Fig. 4.6.

It is clearly seen from the figure that by increasing the input pump power from 150 mW to 200 mW and then even to 250 mW where the nonlinearity is still negligible, the output power increases. However, further increase of the input power slightly raises the output power until reaching the input power of 275 mW; after that the output power starts to decrease substantially. For instance, the output powers corresponding to the input powers of 250 mW and 300 mW are the same and equal to 147 mW. So the optimal input power is around 275 mW and its corresponding output power which is 152 mW is the maximum achievable power at

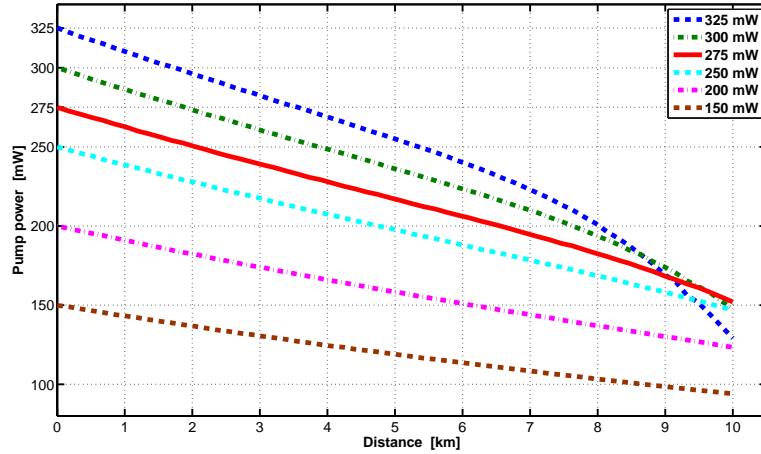


Figure 4.6 – Pump power evolution along a standard SMF of length $L = 10$ km with $\alpha = 0.2 \frac{\text{dB}}{\text{km}}$, $\gamma = 1.8 \frac{\text{W}^{-1}}{\text{km}}$ and $\beta_2 = -22 \frac{\text{ps}^2}{\text{km}}$ for different levels of input power around the optimal pump power 275 mW. The noise PSD is $-121 \frac{\text{dBm}}{\text{Hz}}$.

the fiber end. In this section we find the maximal output power and its corresponding optimal input power based on the analytical model proposed in the previous part. Assume a fiber of length L with characteristics α , β_2 and γ in a system with a noise power spectral density of S_n . If $P(z)$ denotes the actual power along the fiber, the input and output pump powers can be expressed by $P_0 = P(z = 0)$ and $P_L = P(z = L)$. On the other hand, if P_{MI} represents the power transferred to the MI sidebands, the actual output power can be expressed as

$$P_L = P_0 e^{-\alpha L} - P_{\text{MI}}, \quad (4.28)$$

where $P_0 e^{-\alpha L}$ is the ideal output power obtained from attenuation assuming no nonlinearity. An analytical formula for P_{MI} has been proposed in Eq. (4.21) using Laplace's method; its substitution in Eq. (4.28) results in

$$P_L = \left(P_0 - \frac{S_n e^{2\gamma P_0 L_{\text{eff}}}}{2\sqrt{2\pi|\beta_2|L_{\text{eff}}}} \right) e^{-\alpha L}. \quad (4.29)$$

Eq. (4.29) represents the output power P_L versus the input power P_0 . The optimal input power corresponding to the maximal output power is simply derived via the following simple optimization equation:

$$\frac{dP_L}{dP_0} = 0. \quad (4.30)$$

Moreover, since the depleted power is an exponential function of the input power, its derivative with respect to P_0 is proportional to the depleted power itself; in other words, Eq. (4.21) gives

$$\frac{dP_{\text{MI}}}{dP_0} = (2\gamma L_{\text{eff}}) P_{\text{MI}}. \quad (4.31)$$

Taking the derivative of Eq. (4.29) with respect to P_0 and solving Eq. (4.30) lead to the following optimal input power in terms of fiber and system characteristics:

$$P_{\text{opt}} = \frac{1}{2\gamma L_{\text{eff}}} \ln \left(\frac{\sqrt{2\pi|\beta_2|}}{S_n \gamma \sqrt{L_{\text{eff}}}} \right). \quad (4.32)$$

Corresponding to the optimal input power given in Eq. (4.32), the maximal output power is obtained from Eq. (4.29) to be

$$P_{\text{max}} = \frac{e^{-\alpha L}}{2\gamma L_{\text{eff}}} \left[\ln \left(\frac{\sqrt{2\pi|\beta_2|}}{S_n \gamma \sqrt{L_{\text{eff}}}} \right) - 1 \right] = \frac{e^{-\alpha L}}{2\gamma L_{\text{eff}}} \ln \left(\frac{\sqrt{2\pi|\beta_2|}}{e S_n \gamma \sqrt{L_{\text{eff}}}} \right). \quad (4.33)$$

The depleted pump power transferred to the MI spectral band at the optimal condition is simply given by

$$P_{\text{dep}} = \frac{e^{-\alpha L}}{2\gamma L_{\text{eff}}}, \quad (4.34)$$

where all the powers satisfy $P_{\text{max}} + P_{\text{dep}} = P_{\text{opt}} e^{-\alpha L}$. Fig. 4.7 plots the output pump power versus the input power of a standard SMF with length 10 km obtained by numerical simulation. It clearly shows the optimal input power in which the output power is maximal. Moreover, the depleted power is shown to be the difference between the ideal exponential decay and the actual nonlinear condition. Applying the fiber and system characteristics to Eq. (4.32) and Eq. (4.33) results in $P_{\text{opt}} = 436$ mW and $P_{\text{max}} = 253$ mW which are in agreement with the numerical simulation in Fig. 4.7. In addition, since the optimal input power occurs at

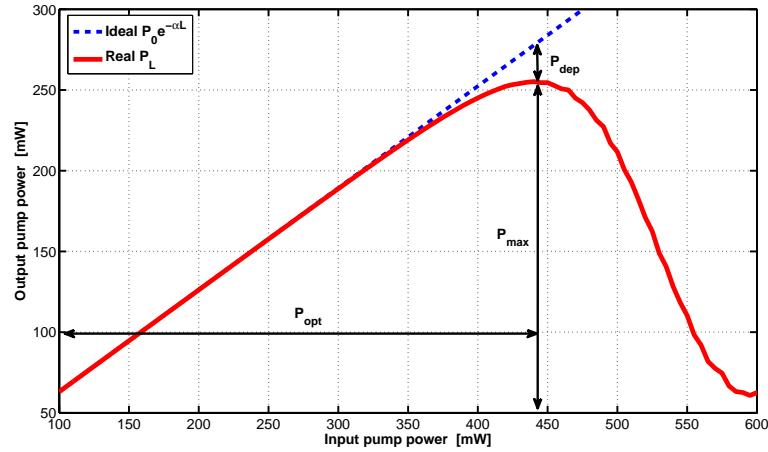


Figure 4.7 – Output pump power versus input pump power for a standard SMF of length $L = 10$ km with $\alpha = 0.2 \frac{\text{dB}}{\text{km}}$, $\gamma = 1.8 \frac{\text{W}^{-1}}{\text{km}}$ and $\beta_2 = -22 \frac{\text{ps}^2}{\text{km}}$; the noise PSD is $-141 \frac{\text{dBm}}{\text{Hz}}$. The optimal input power, maximal output power and depleted power are shown.

the first maximal point deviated from the ideal straight line in Fig. 4.7, the corresponding depletion ratio $\frac{P_{\text{dep}}}{P_{\text{opt}} e^{-\alpha L}}$ happens to be very low. For the example of Fig. 4.7 it is around 8%; in practice, considering an upper bound of 20% is relatively safe. The optimal input power given

Chapter 4. MI Critical and Optimal Power

in Eq. (4.32) is plotted in Fig. 4.8 versus the fiber length for different levels of background noise PSD. The figure demonstrates the asymptotic behavior of optimal input power for long fibers where $L_{\text{eff}} \approx L_{\infty} = \alpha^{-1}$, so that the asymptote is given by

$$\lim_{L \rightarrow \infty} P_{\text{opt}} = \frac{\alpha}{2\gamma} \ln \left(\frac{\sqrt{2\pi|\beta_2|\alpha}}{S_n\gamma} \right). \quad (4.35)$$

For instance, the optimal power for a long SMF where the noise PSD is $-121 \frac{\text{dBm}}{\text{Hz}}$ is calculated from Eq. (4.35) to be $\approx 96 \text{ mW}$ which is also clear from Fig. 4.8. It is also evident from the figure

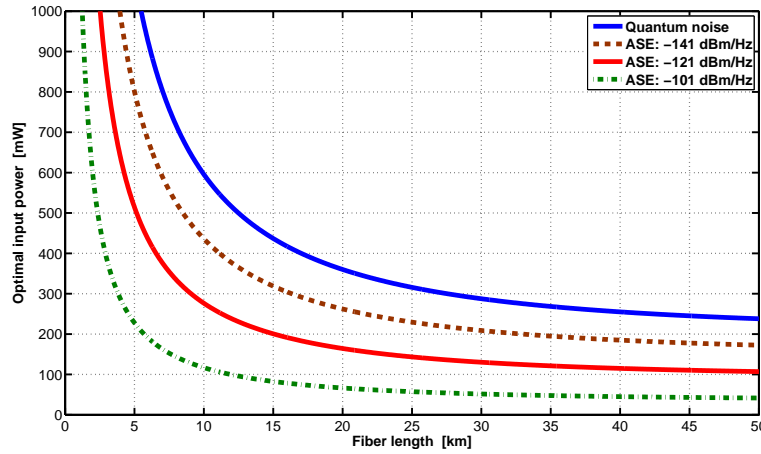


Figure 4.8 – Optimal input power versus fiber length for different levels of background noise PSD: -161 (quantum noise), -141 , -121 and $-101 \frac{\text{dBm}}{\text{Hz}}$. Fiber characteristics are $\alpha = 0.2 \frac{\text{dB}}{\text{km}}$, $\gamma = 1.8 \frac{\text{W}^{-1}}{\text{km}}$ and $\beta_2 = -22 \frac{\text{ps}^2}{\text{km}}$.

that by increasing the level of background noise PSD, the optimal input power reduces; in fact, according to Eq. (4.32) the optimal power decreases linearly by the noise power spectral density when S_n is expressed in decibel.

4.3 Brillouin Optical Time Domain Analysis

For validating the model proposed in the previous section an experiment has been done based on the Brillouin distributed sensing whose implementation setup and working principles are presented in this section. Brillouin distributed optical fiber sensors are among the most common distributed sensors for measuring environmental quantities such as temperature and strain [102, 103]. There are several techniques for implementing Brillouin distributed sensors like Brillouin optical time-domain reflectometry (BOTDR) which is based on the linear phenomenon of spontaneous Brillouin scattering [104, 105], and Brillouin optical time-domain analysis (BOTDA) based on the nonlinear process of stimulated Brillouin scattering (SBS) [6, 106]. The SBS process's narrow-band spectral response can be exploited to induce gain or loss on a specific frequency and thus, it provides a promising tool for measuring the longitudinal variations of parameters such as chromatic dispersion [107], parametric gain [108], power evolution along the fiber [109]. Therefore, it makes sense to use a BOTDA

system for analyzing the longitudinal behaviour of modulation instability to validate the proposed model in this work.

Before going to the details of a BOTDA sensor, it is necessary to review the phenomenon of stimulated Brillouin scattering. The existence of an inelastic scattering of light waves due to their interaction with sound waves was predicted by the French physicist Léon Brillouin (1889-1969) [110] and the Russian physicist Leonid Mandelstam (1879-1944) [111] independently in the 1920s. Such a scattering referred to as the Brillouin scattering can happen spontaneously by thermally-excited acoustic phonons in a medium or might be stimulated by the acoustic wave originating from the electrostriction of medium because of high-intensity incident light [2]. Therefore, the spontaneous Brillouin scattering is linearly proportional to the incident light; whilst the stimulated Brillouin scattering (SBS) varies nonlinearly with respect to the intensity of optical waves due to the nonlinear phenomenon of electrostriction. SBS was experimentally observed for the first time by Chiao *et al.* in 1964 using a pulsed ruby laser as a light source and two crystals namely, quartz (SiO₂) and sapphire (Al₂O₃) as media [112]. The Brillouin frequency shift (BFS) measured by a Fabry-Pérot interferometer in the experiment is 29.7 GHz for quartz and 62.1 GHz for sapphire at the laser wavelength of 694 nm. Ippen and Stolen demonstrated the SBS process in optical fibers employing a pulsed xenon-ion laser as a pump and a single-mode silica fiber with a core diameter of 3.8 μm as a medium [113]. The measured BFS is 32.2 GHz at 535 nm showing that the velocity of sound must be around 5.89 $\frac{\text{km}}{\text{s}}$ at that acoustic frequency in the fiber. A thorough mathematical description of both stimulated Brillouin scattering and stimulated Raman scattering (SRS) has been carried out by Shen and Bloembergen using both classical electromagnetism and quantum mechanics [114]. Here, the classical approach to the stimulated Brillouin scattering based on the acoustic wave propagation is presented in details. In this approach the source of acoustic wave is the electrostrictive force originating from the interference of two counter-propagating optical waves called pump and probe.

4.3.1 Pump-Probe Interaction in Stimulated Brillouin Scattering

Suppose a medium for light propagation such as an optical fiber with density $\rho_0 + \tilde{\rho}$, where ρ_0 is the average density of the medium and $\tilde{\rho}$ is its fluctuation around ρ_0 . It is shown that the density fluctuation $\tilde{\rho}(z, t)$ is governed by the following wave equation in a one-dimensional propagating medium such as optical fibers [2]:

$$\frac{\partial^2 \tilde{\rho}}{\partial t^2} - v^2 \frac{\partial^2 \tilde{\rho}}{\partial z^2} - \Gamma \frac{\partial}{\partial t} \frac{\partial^2 \tilde{\rho}}{\partial z^2} = -\frac{\epsilon_0 \gamma_e}{2} \frac{\partial^2 \langle \tilde{E}^2 \rangle}{\partial z^2}, \quad (4.36)$$

where v is the acoustic velocity in the medium and Γ is a damping coefficient expressed in terms of the thermodynamic parameters of the medium such as shear and bulk viscosities. ϵ_0 is the vacuum permittivity and γ_e is the electrostrictive constant. The right-hand side of Eq. (4.36) is the electrostrictive source of acoustic wave in which $\langle \tilde{E}^2 \rangle$ shows the time average of the total electric field in the medium obtained from the superposition of the forward electric field \tilde{E}_p called the pump and the backward field \tilde{E}_s called the probe. The forward and backward

Chapter 4. MI Critical and Optimal Power

fields are given by

$$\tilde{E}_p(z, t) = E_p(z, t) e^{i(k_p z - \omega_p t)} + c.c., \quad (4.37a)$$

$$\tilde{E}_s(z, t) = E_s(z, t) e^{i(-k_s z - \omega_s t)} + c.c., \quad (4.37b)$$

where $c.c.$ denotes the complex conjugate of previous terms. In Eqs. (4.37), E_p and E_s are slowly varying envelopes of the pump and probe fields; $k_p = \frac{n\omega_p}{c}$ and $k_s = \frac{n\omega_s}{c}$ are the pump and probe wavenumbers oscillating at pump frequency ω_p and probe frequency ω_s , respectively. The electrostriction term in the right side of Eq. (4.36) is obtained using the expressions in Eqs. (4.37) as follows:

$$-\frac{\epsilon_0 \gamma_e}{2} \frac{\partial^2 \langle \tilde{E}^2 \rangle}{\partial z^2} = \frac{\epsilon_0 \gamma_e}{2} (k_p + k_s)^2 E_p E_s^* e^{i(k_p + k_s)z - i(\omega_p - \omega_s)t} + c.c., \quad (4.38)$$

It is seen from Eq. (4.38) that the electrostrictive source in the acoustic wave equation is a traveling wave with frequency $\Omega = \omega_p - \omega_s$ and wavenumber $q = k_p + k_s$. The idea behind the pump-probe approach is to fix the pump frequency and then sweep the probe frequency so that the frequency detuning Ω changes and q follows it according to

$$q = k_p + k_s = \frac{n\omega_p}{c} + \frac{n\omega_s}{c} = \frac{n}{c} (2\omega_p - \Omega). \quad (4.39)$$

Therefore, the acoustic wave is a forward traveling wave with frequency Ω and wavenumber q that can be expressed by

$$\tilde{\rho}(z, t) = \rho e^{i(qz - \Omega t)} + c.c. \quad (4.40)$$

Substituting Eqs. (4.38), (4.39) and (4.40) in Eq. (4.36) results in the following spectrum for the acoustic wave:

$$\rho = \frac{\gamma_e \epsilon_0 E_p E_s^*}{\nu^2 - \left(\frac{\nu c}{n} \frac{\Omega}{2\omega_p - \Omega} \right)^2 - i\Gamma\Omega}. \quad (4.41)$$

The phase-matching condition in which the acoustic wave phase is in quadrature with both pump and probe phases is obtained when Eq. (4.41) is purely imaginary regardless of E_p and E_s . Therefore,

$$\nu^2 - \left(\frac{\nu c}{n} \frac{\Omega}{2\omega_p - \Omega} \right)^2 = 0. \quad (4.42)$$

Eq. (4.42) has two solutions, one represents the Stokes frequency Ω_S and the other is the anti-Stokes frequency Ω_A of the stimulated Brillouin scattering given by

$$\Omega_S = \frac{2\nu}{\frac{c}{n} + \nu} \omega_p, \quad (4.43a)$$

$$\Omega_A = \frac{2\nu}{\frac{c}{n} - \nu} \omega_p. \quad (4.43b)$$

As it is clear from Eqs. (4.43), there is a slight difference between the Stokes and anti-Stokes Brillouin frequency shifts. This frequency difference can also be derived using the relativistic Doppler effect [115]. Since the acoustic velocity v is negligible compared to the speed of light in fibers, i.e. $v \ll \frac{c}{n}$, the Brillouin frequency shift Ω_B can be attributed to both Stokes and anti-Stokes components by approximating Eqs. (4.43) as follows:

$$\Omega_B = \frac{2nv}{c} \omega_p. \quad (4.44)$$

In optical fibers where the acoustic velocity is around $v = 5900 \frac{\text{m}}{\text{s}}$ and the effective refractive index is $n = 1.446$, the Brillouin frequency shift for a pump wavelength at 1550 nm is obtained from Eq. (4.44) to be approximately 11 GHz. The spectrum in Eq. (4.41) can be simplified by using the approximation $2\omega_p - \Omega \approx 2\omega_p$ justified by $\Omega \ll \omega_p$. This way,

$$\rho = \frac{\gamma_e \epsilon_0 E_p E_s^*}{v^2 \left(1 - \frac{\Omega^2}{\Omega_B^2}\right) - i\Gamma\Omega}. \quad (4.45)$$

Another approximation that can be applied to Eq. (4.45) is $\Omega_B^2 - \Omega^2 = (\Omega_B + \Omega)(\Omega_B - \Omega) \approx 2\Omega_B(\Omega_B - \Omega)$, because the frequency detuning Ω varies in the order of Brillouin bandwidth Γ_B , which turns out to be $\ll \Omega_B$, around the Brillouin frequency shift Ω_B and thus, $\Omega \approx \Omega_B$. This approximation leads to the following normalized Brillouin gain spectrum:

$$g(\Omega) = \frac{1}{1 + 2i \frac{\Omega - \Omega_B}{\Gamma_B}}, \quad (4.46)$$

in which the phonon decay rate Γ_B is given by

$$\Gamma_B = \left(\frac{2n\omega_p}{c}\right)^2 \Gamma = \frac{16\pi^2 n^2}{\lambda_p^2} \Gamma. \quad (4.47)$$

For single mode fibers at the telecom wavelength of 1550 nm, $\frac{\Gamma_B}{2\pi} \approx 27$ MHz. Therefore, the phonon decay time is $\Gamma_B^{-1} \approx 6$ ns. Moreover, Eq. (4.47) indicates that the Brillouin bandwidth is in quadratic proportion to the pump frequency while the Brillouin frequency shift increases linearly with the pump frequency according to Eq. (4.44). In order to see the longitudinal evolution of pump and probe, it is more convenient to consider their intensity I or power P defined by $P = A_{\text{eff}} I = \frac{n\epsilon_0 c}{2} |E|^2 A_{\text{eff}}$, where A_{eff} is the mode effective area. Using the wave equations describing the pump and probe propagation coupled through the acoustic wave, it can be demonstrated that the coupled equations governing the intensity or power of the pump and probe in the CW or quasi-CW regime are given by [4, 3]

$$\frac{dP_p}{dz} = -\frac{g_B}{A_{\text{eff}}} P_p P_s - \alpha P_p, \quad (4.48a)$$

$$\frac{dP_s}{dz} = -\frac{g_B}{A_{\text{eff}}} P_p P_s + \alpha P_s, \quad (4.48b)$$

Chapter 4. MI Critical and Optimal Power

where the Brillouin gain is obtained from Eq. (4.46) as follows:

$$g_B(\Omega) = g_0 \Re[g(\Omega)] = g_0 |g(\Omega)|^2 = g_0 \frac{\left(\frac{\Gamma_B}{2}\right)^2}{(\Omega - \Omega_B)^2 + \left(\frac{\Gamma_B}{2}\right)^2}, \quad (4.49)$$

in which $g_0 \approx 5 \times 10^{-11} \frac{\text{m}}{\text{W}}$ is the maximum Brillouin gain and \Re denotes the real part. Eq. (4.49) shows a Lorentzian distribution for the Brillouin gain spectrum whose FWHM bandwidth is Γ_B and it has the property $\Re[g(\Omega)] = |g(\Omega)|^2$. The Lorentzian distribution for Brillouin gain spectrum has been experimentally demonstrated to be almost perfectly accurate [116]. Fig. 4.9 depicts the Brillouin gain spectrum given in Eq. (4.49) for standard optical fibers. The FWHM spectral width of 27 MHz shows how narrowband the Brillouin process is and so it can be utilized as a narrowband filter for selecting an optical wavelength. In the small-signal regime

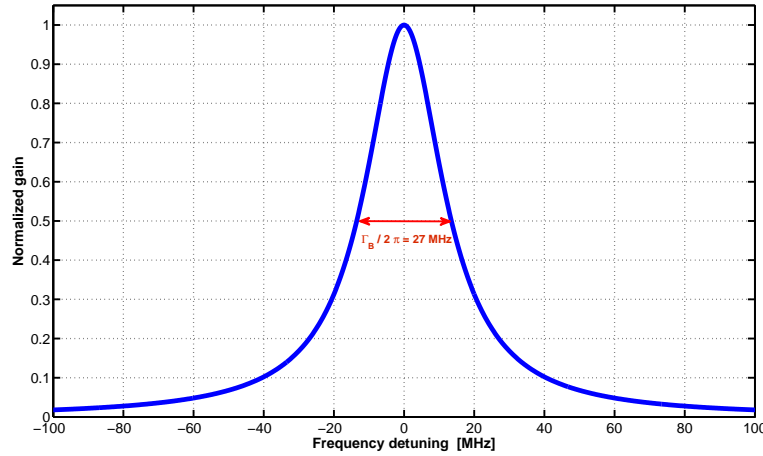


Figure 4.9 – Normalized Brillouin gain spectrum showing a Lorentzian function with a FWHM spectral width of 27 MHz.

where the pump can be considered undepleted, the pump equation is simply approximated by $\frac{dP_p}{dz} = -\alpha P_p$, and thus $P(z) = P_0 e^{-\alpha z}$ where P_0 is the input pump power. Substituting the exponential pump power in the probe equation of Eqs. (4.48) leads to

$$\frac{dP_s}{dz} = \left(\alpha - \frac{g_B}{A_{\text{eff}}} P_0 e^{-\alpha z} \right) P_s. \quad (4.50)$$

Consider a fiber of length L into the far end of which the probe power $P_s(L)$ is launched. With this boundary condition, Eq. (4.50) gives the following solution:

$$P_s(z) = P_s(L) e^{\alpha(z-L)} \exp \left(\frac{g_B P_0}{A_{\text{eff}}} \frac{e^{-\alpha z} - e^{-\alpha L}}{\alpha} \right). \quad (4.51)$$

The first exponential function in Eq. (4.51) shows the power attenuation while the second one represents the power amplification due to the SBS process. Moreover, at the input of the fiber

where $z = 0$, the backscattered power is detected to be

$$P_s(0) = P_s(L) e^{\frac{g_B P_0 L_{\text{eff}}}{A_{\text{eff}}} - \alpha L}, \quad (4.52)$$

in which $L_{\text{eff}} = \frac{1-e^{-\alpha L}}{\alpha}$ is the fiber effective length. When the system is in the quasi-CW regime where the pump is a square pulse covering the segment ΔL of the fiber length, L_{eff} is replaced by ΔL and thus the exponent in the gain function is so low that it can be approximated by

$$e^{\frac{g_B P_0 \Delta L}{A_{\text{eff}}}} \approx 1 + \frac{g_B P_0 \Delta L}{A_{\text{eff}}}, \quad \text{when} \quad \frac{g_B P_0 \Delta L}{A_{\text{eff}}} \ll 1. \quad (4.53)$$

In BOTDA sensors, a relatively intense pump pulse of length ΔL is launched into the near end ($z = 0$) of the sensing optical fiber and a low-power CW probe of power P_b is injected to its far end ($z = L$). Assume that the pulse power at the position z along the fiber is denoted by $P(z)$ and so the net Brillouin gain is $\frac{g_B \Delta L}{A_{\text{eff}}} P(z)$. At the same position the probe power is $P_b e^{-\alpha(L-z)}$ and thus, the amplified power by the Brillouin interaction is $\frac{g_B \Delta L}{A_{\text{eff}}} P(z) P_b e^{-\alpha(L-z)}$. As this amplified power travels to the input of the fiber, it suffers from the fiber attenuation by the factor of $e^{-\alpha z}$. Therefore, the detected Brillouin-amplified power at the fiber input is obtained as [101]

$$\frac{g_B \Delta L}{A_{\text{eff}}} P(z) P_b e^{-\alpha(L-z)} e^{-\alpha z} = \frac{g_B P_b e^{-\alpha L} \Delta L}{A_{\text{eff}}} P(z). \quad (4.54)$$

The importance of Eq. (4.54) is that the Brillouin gain detected from the amplified probe signal is proportional to the local pump power $P(z)$ along the fiber. Therefore, it is possible to measure the longitudinal evolution of optical power propagating in optical fibers using a BOTDA sensor. When the pump power is not large enough to excite considerable nonlinear interaction and thus, pump depletion, the power evolution follows the exponential decay $P_0 e^{-\alpha z}$. Therefore, the ideal trace of the detected Brillouin gain is an exponential decay and any deviation from that is the result of pump depletion due to nonlinear effects, in this case modulation instability. Fig. 4.10 depicts the power evolution along an optical fiber which is proportional to the detected Brillouin gain. The solid lines have been obtained by simulating the nonlinear Schrödinger equation while the dashed lines represents the ideal exponential decay. It is evident from the figure that for low input power like 150 mW the power variation matches almost perfectly the exponential function while by increasing the input power the nonlinear interaction and thus, the pump depletion enhances the deviation from the ideal power evolution.

4.3.2 Validating Experimental Setup

In order to validate the analytical model and numerical results regarding the longitudinal evolution of modulation instability, a standard BOTDA system [6] has been utilized to obtain experimental results. This system is based on a pump-probe interaction, in which a high-power pump pulse and a continuous-wave probe signal are launched into the opposite ends of an optical fiber under test. While the high-power pump pulse induces modulation instability

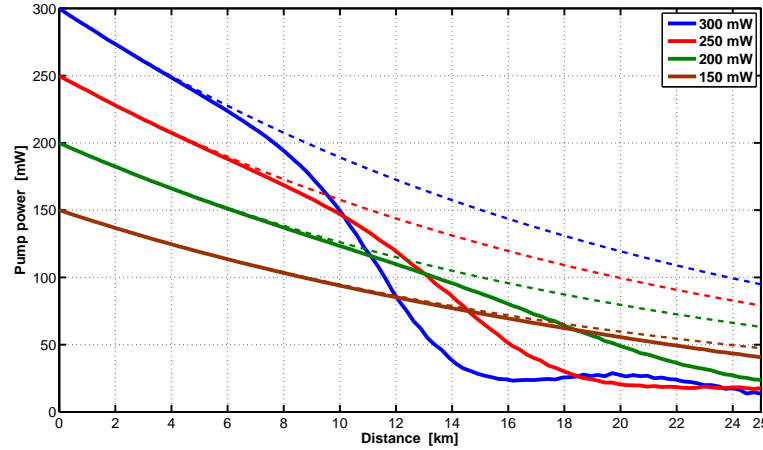


Figure 4.10 – Pump power evolution along an SMF of length $L = 25$ km with $\alpha = 0.2 \frac{\text{dB}}{\text{km}}$, $\gamma = 1.8 \frac{\text{W}^{-1}}{\text{km}}$ and $\beta_2 = -22 \frac{\text{ps}^2}{\text{km}}$ for different levels of input power. The noise power spectral density is $-121 \frac{\text{dBm}}{\text{Hz}}$. The simulations of the NLSE are shown in solid lines and the exponential decays are plotted by dashed curves.

in the fiber, the low-power probe signal is simply used to measure the longitudinal evolution of the pump power through the Brillouin gain. Since the Brillouin gain is proportional to the pump power in the small gain approximation, the longitudinal evolution of pump pulse and any depletion induced by MI can be directly mapped by analyzing the Brillouin gain affecting the probe power. The scheme of the experimental setup is sketched in Fig. 4.11.

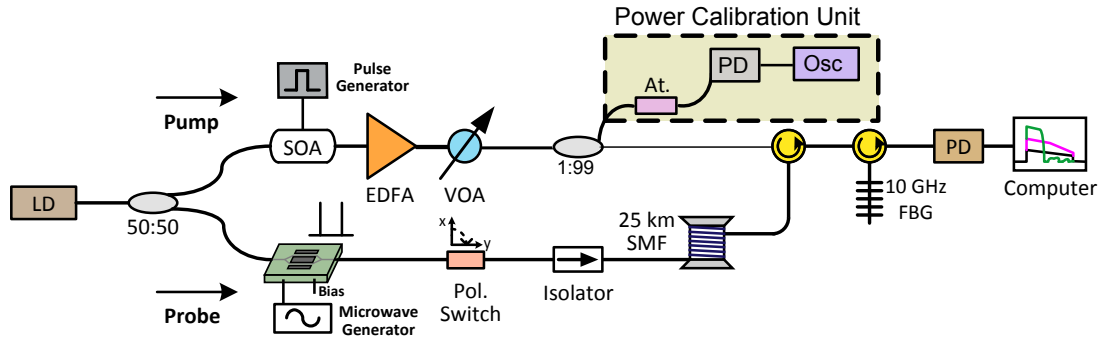


Figure 4.11 – Experimental setup based on a standard BOTDA scheme; LD: laser diode; SOA: semiconductor optical amplifier; EDFA: erbium-doped fiber amplifier; VOA: variable optical attenuator; FBG: fiber Bragg grating; At.: 10 dB attenuator; PD: photodetector; Osc: Oscilloscope; EOM: electric-optic modulator; SMF: single-mode fiber.

The light from a distributed feedback (DFB) laser diode (LD) at 1551.1 nm is split into pump and probe branches by a 50:50 coupler. A semiconductor optical amplifier (SOA) is used to shape pulses of 20 ns with a high extinction ratio (>50 dB) and a repetition period of 300 μs , longer than the return-trip time in the fiber. Pump pulses are amplified by a low-noise EDFA and attenuated by a variable optical attenuator (VOA) to precisely adjust different levels of pump peak power. A power calibration unit shown in the dashed box, is used for monitoring the peak power launched into the fiber under test (FUT), which is in this case a 25.5 km

long standard SMF. For the probe branch, an electro-optic modulator (EOM) is employed to generate a two-sideband probe with a suppressed carrier, and a polarization switch is inserted to eliminate the polarization dependence of the SBS gain. An optical isolator in the probe branch is used to stop the pump pulses propagating back into the output of the EOM. A 10-GHz fiber Bragg grating (FBG) is employed to filter out one of the probe sidebands and the Rayleigh backscattered light from the pulses, so that only one of the probe sidebands is detected by a 125 MHz photo-detector (PD). Finally, a computer acquisition card is used to record the time-domain traces of the detected signal.

It is important to mention that the FUT has a very uniform Brillouin gain throughout the fiber, ensuring that the recorded time-domain trace at a given pump-probe frequency offset is proportional to the pump power at each fiber position, discarding any potential effect induced by spectral variations of the Brillouin gain. This way, the acquired traces can show a reliable profile of the longitudinal evolution of the pump power along the fiber. It is also noteworthy that the probe power is kept very low in comparison with the pump power, so that the SBS-induced depletion can be safely neglected [8] and the traces only include the effect of modulation instability. The optical fiber utilized in this experiment is a standard SMF of length 25.5 km with typical the attenuation of $0.2 \frac{\text{dB}}{\text{km}}$ and anomalous GVD coefficient of $\beta_2 = -22 \frac{\text{ps}^2}{\text{km}}$. The nonlinear coefficient of the fiber under test has been measured using a self-aligned interferometer with a Faraday mirror, as described in Chapter 2; the measured nonlinear coefficient is $\gamma = 1.8 \frac{\text{W}^{-1}}{\text{km}}$.

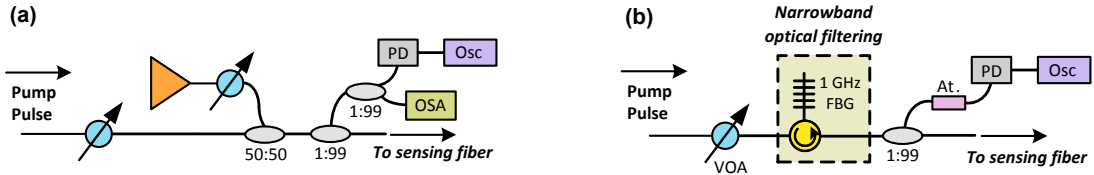


Figure 4.12 – Two modifications to the standard BOTDA system; used to analyze the impact of noise on the behavior of modulation instability: (a) Scheme used to couple ASE noise co-propagating with the pump pulses; (b) Scheme used to filter out ASE noise from the pump pulses.

Fig. 4.12 sketches two modifications in the standard BOTDA configuration to quantitatively verify the impact of ASE noise on modulation instability. In Fig. 4.12a, an EDFA is used as a source of ASE noise which is coupled to the pump pulses through a 50:50 coupler. The level of noise spectral density is controlled via a variable optical attenuator. Using this configuration, the evolution of the pump power during propagation along the fiber can be investigated in presence of different levels of co-propagating background noise, seeding modulation instability at different levels. On the other hand, Fig. 4.12b shows a configuration designed for filtering the ASE noise (within the MI spectral band) generated by the EDFA used to boost the pump pulses. The filter includes a circulator and a narrowband FBG with a bandwidth of 1 GHz. Since the spectral band of modulation instability is in the range of a few tens of GHz, the 1 GHz filter used in this configuration can filter most of the ASE noise within the MI bandwidth.

4.4 Experimental Validation of the Model

Using the BOTDA system illustrated in Fig. 4.11, the longitudinal power evolution of an optical pulse during its propagation along an optical fiber can be obtained by measuring the local linear Brillouin amplification [6]. In the performed experiment, pump pulses have duration of 20 ns, corresponding to a spatial resolution of 2 m, and traces have been acquired with 2000 times averaging. The pump-probe frequency offset has been set to the average Brillouin frequency shift (BFS) of the fiber which is 10.84 GHz, so that the measured longitudinal power evolution can be mostly attributed to modulation instability and fiber attenuation. In order to ensure this, the BFS of the fiber has been measured, verifying negligible longitudinal variations.

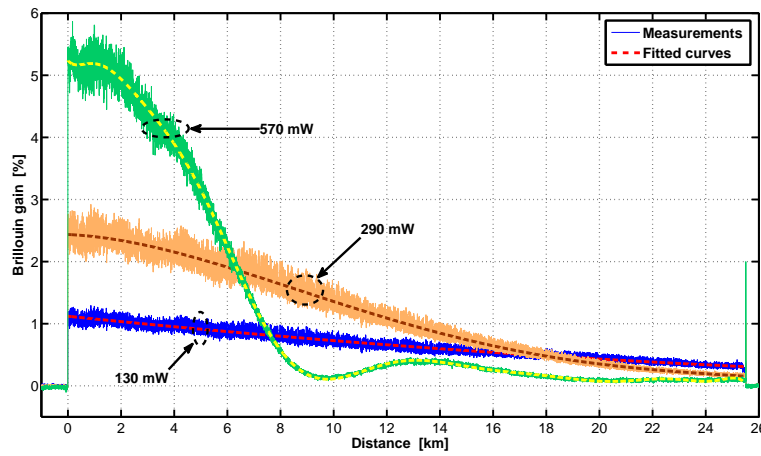


Figure 4.13 – Brillouin traces along with their fitted curves, for three different values of input pump power: 130 mW, 290 mW, and 570 mW.

Fig. 4.13 shows the pulse peak power evolution along the optical fiber under test for three different input pump powers: 130 mW, 290 mW and 570 mW. For the case of the lowest power, i.e. 130 mW, it is possible to observe the natural exponential power decay given by the fiber attenuation; however, as pulse power increases, the peak power evolution changes due to the onset of modulation instability. Comparing the curves in Fig. 4.13, it is interesting to notice that increasing the input power of an optical signal launched into the fiber can even decrease the signal power propagating at far distances as a consequence of the pump depletion induced by modulation instability. In other words, increasing the input power does not necessarily enhance the power propagating throughout the fiber at the original wavelength, but sometimes can degrade it due to nonlinear distortions, such as modulation instability. At high input power, the Fermi-Pasta-Ulam recurrence phenomenon turns out evident, as shown by the oscillatory behavior in Fig. 4.13 for a pump power of 570 mW. An important aspect to mention is that, since the depletion is oscillatory it is possible to assume that modulation instability is dominant and the depletion induced by other processes, such as stimulated Raman and Brillouin scattering, is negligible. The measured longitudinal traces have been fitted to smooth curves as shown by the dashed lines in Fig. 4.13 using the smoothing spline method [117]. This method is appropriate for fitting a smooth function to a set of noisy

data [118]. This way, the experimental measurements of the pump power evolution which is proportional to the measured Brillouin gain can be represented smoothly by discarding the effect of noise, thus providing a clean reference for comparing with the analytical model and simulation data.

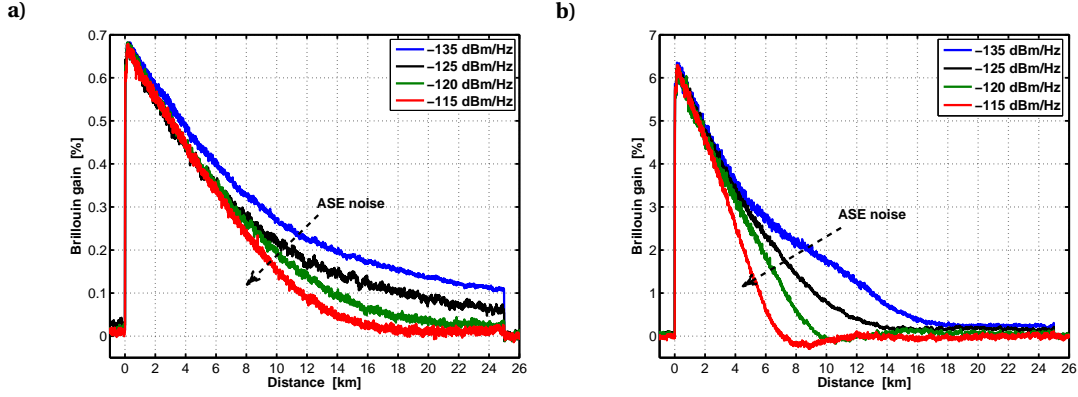


Figure 4.14 – Longitudinal BOTDA traces for different noise PSD values, ranging from -135 up to $-115 \frac{\text{dBm}}{\text{Hz}}$, and for an input peak power of a) 60 mW and b) 500 mW.

In order to investigate the impact of the background noise on the onset and behavior of modulation instability, an EDFA has been used to introduce noise into the system based on the scheme shown in Fig. 4.12a. The longitudinal BOTDA traces obtained with an input pump power of 60 mW, for different levels of noise power spectral density are depicted in Fig. 4.14a. Under the lowest noise situation, the time-domain BOTDA trace can be measured with no distortion; however, when the ASE noise increases, MI is seeded enough to deplete the pump. This behavior experimentally validates that the onset of modulation instability depends not only on the peak pump power which is kept fixed in this case, but also on the power level of the background noise co-propagating with the pump within the MI spectral band. Fig. 4.14b reports similar results, but for an input peak power of 500 mW. In this case, modulation instability substantially distorts the expected exponential decay of the pulse power along the fiber as a consequence of the high input power, even at low noise conditions. However, it is possible to observe that the presence of ASE noise further seeds MI, increasing the amount of pump depletion. The results validate the behavior described in Fig. 4.4 and demonstrate the key role of the noise spectrum in the analytical model. It is worth noting that the small negative level obtained in the measured gain shown in Fig. 4.14b for the noise power spectral density of $-115 \frac{\text{dBm}}{\text{Hz}}$ does not have any relation to the MI evolution, but results in the measurement process simply from the uneven and limited-bandwidth response of the photo-detector.

A second test to verify the effect of noise on modulation instability has been carried out employing the scheme in Fig. 4.12b. In this case most of the ASE noise co-propagating with the pump pulses is filtered out, thus providing a potential reduction of the seeding of MI. Fig. 4.15 shows how filtering the ASE noise within the MI spectral band changes the onset of MI and thus decreases the pump depletion. The comparison between filtered and non-filtered pump cases clearly highlights the importance of background noise in seeding MI and how

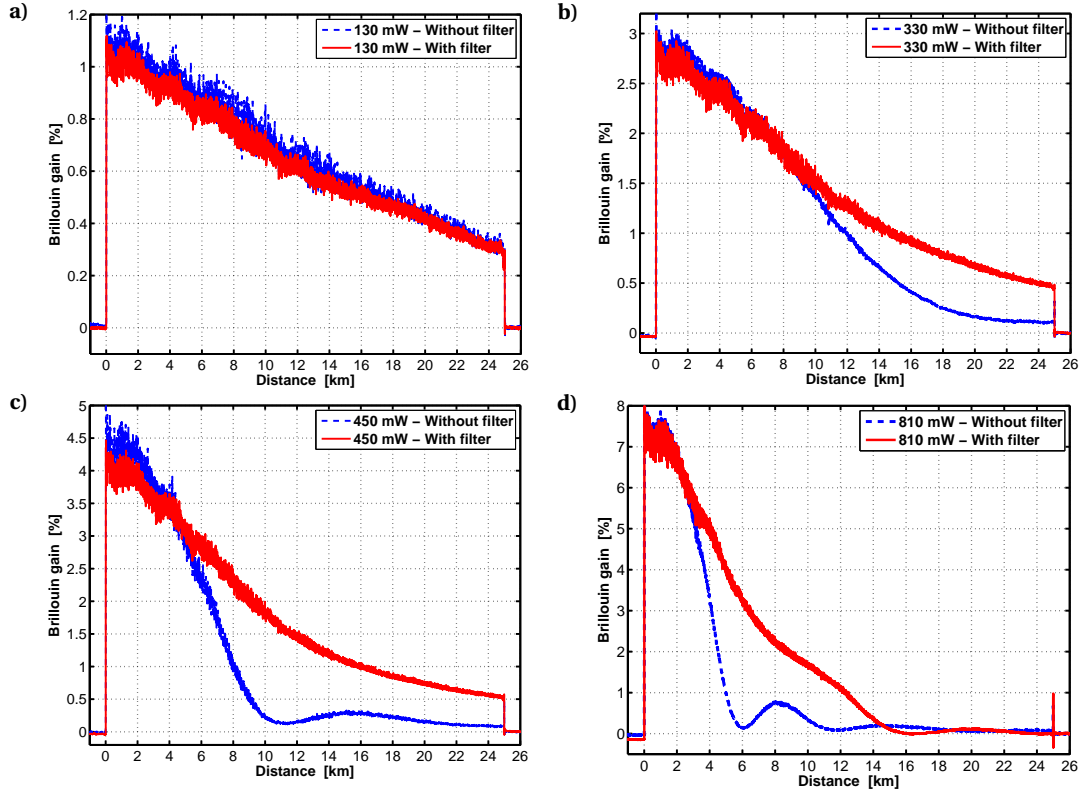


Figure 4.15 – BOTDA traces for filtered and non-filtered ASE noise cases with different peak power levels: a) 130 mW, b) 330 mW, c) 450 mW and d) 810 mW.

filtering can mitigate its impact. According to Fig. 4.15a and Fig. 4.15d the filter does little in very low or very high peak power regimes; while it is evident from Fig. 4.15b and Fig. 4.15c that inserting a narrowband filter in the MI spectral band can be very effective in delaying the onset of modulation instability and thus decreasing the pump depletion due to MI.

The impact of ASE noise filtering on the behavior of modulation instability and thus, on the performance of BOTDA sensors is demonstrated in Fig. 4.16 where the characteristics of a BOTDA systems are compared for two cases: with and without a 1-GHz filter in the MI spectral band. Fig. 4.16a shows the Brillouin gain measured at the end of the FUT as a function of the pump power, illustrating the effect of filtering on the output pulse power. It can be observed that the amount of MI-induced depletion decreases significantly by filtering out the ASE noise in the spectral band of modulation instability. This leads to higher output pulse power with respect to the case in which the noise is not filtered out, especially for high power regime. It should be noted that the residual noise passing through the 1-GHz filter still induces some level of MI, thus inducing also some pump depletion, but at higher pump powers. This explains why the red curve in Fig. 4.16a does not follow a perfect straight line as a function of the input power, but shows a clear behavior of pump depletion. It should be emphasized that even with a perfect filter covering only the bandwidth of the propagating signal, MI will always occur if there is co-propagating noise. This is because the MI gain at pump wavelength

4.4. Experimental Validation of the Model

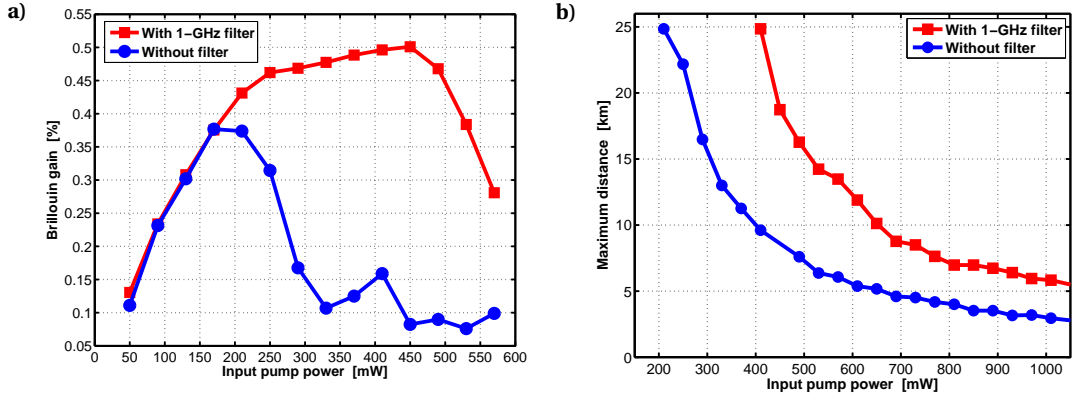


Figure 4.16 – Effect of ASE on the BOTDA performance: a) SBS gain measured in the last meters of the 25 km SMF versus input pump power, with and without narrowband optical filtering, b) Comparison of maximum distance reached by the pump before 50% of power depletion, with and without filter.

is not null, which means that any in-band noise co-propagating along the fiber will always seed MI, inducing some level of depletion, which essentially depends upon the noise PSD and bandwidth of the optical filter. Moreover, the curve corresponding to the no-filter case in Fig. 4.16a shows a similar behavior as the numerical simulations illustrated in Fig. 4.4; while the case of filtered noise looks different which can also be a result of non-white or colored noise due to filtering. Fig. 4.16b shows an experimental comparison of the maximum distance that the pump power can reach before being depleted by 50%. The figure clearly shows the improvement in the performance of BOTDA systems by reducing the ASE noise and thus decreasing the amount of pump depletion due to modulation instability. Tolerating 50% of pump depletion at the fiber end, we can launch an input power of 400 mW with filtering while without the filter it must be around 200 mW. In other words, by injecting 400 mW into the fiber, 50% depletion occurs at 10 km along the fiber without filtering, while by using the filter it happens at 25 km.

Fig. 4.17 compares the critical power obtained from the experimental measurement with

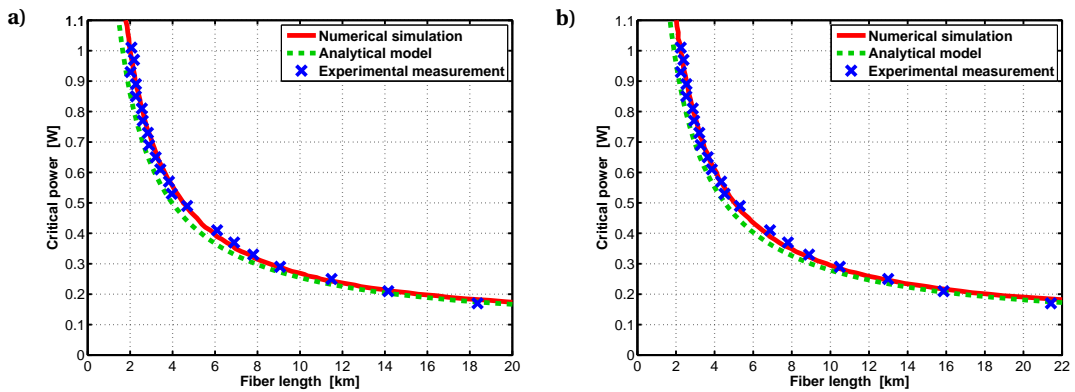


Figure 4.17 – Critical power P_{crit} versus fiber length obtained by numerical simulations, experimental measurements and analytical model for two depletion ratios: a) 10% and b) 20%.

the results of numerical simulations and analytical model II. In order to acquire the critical power versus the fiber length from the experimental data, the fiber position showing a certain depletion ratio is extracted from the measured BOTDA traces, thus obtaining the respective depletion length for different input pump powers. This way, the input pump power leading to a given depletion length corresponds to the MI critical power for a fiber of length equal to the calculated depletion length. The numerical results are obtained by applying the split-step Fourier method and Monte Carlo simulation to the nonlinear Schrödinger equation. Solving Eq. (4.26) or equivalently Eq. (4.27) in this case, results in the critical power given by the analytical model. The experimental results and the numerical simulations match almost perfectly, mostly because in simulation the pump depletion is taken into account. On the other hand, the critical power obtained from the analytical model follows exactly the measurements and simulations but with a slight difference; in fact the proposed model provides a fairly tight lower bound for the critical power ensuring a safe limit for avoiding a certain amount of depletion due to modulation instability.

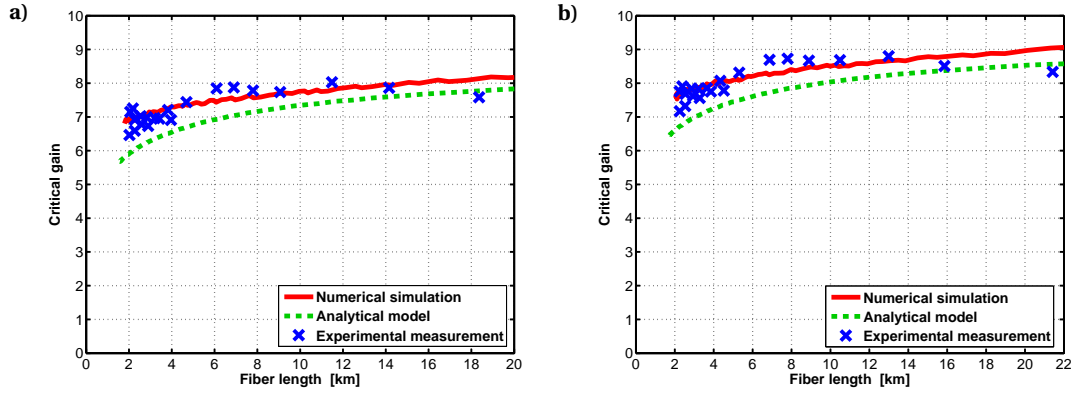


Figure 4.18 – Critical gain σ_{crit} versus fiber length for two depletion ratios: a) 10% and b) 20%; the plots compare measurements, simulations and results of the proposed analytical model.

Fig. 4.18 shows the critical gain σ_{crit} versus the fiber length for two depletion ratios, i.e. 10% and 20%. It must be noted that in contrast to Fig. 4.5, the model does not give a straight horizontal line because of the non-uniform ASE noise power used when measuring the different pump power conditions. According to the experimental setup illustrated in Fig. 4.11 the input power level is adjusted by a variable optical attenuator in a 10-dB range. Therefore, the ASE noise generated by the EDFA is also modified in the same range, thus leading to a different behavior when compared to Fig. 4.5, in which a constant ASE noise is assumed. Under this condition, Fig. 4.17 and Fig. 4.18 demonstrate a good agreement between measurement, simulation and analytical solution so that the discrepancy between the experimental and analytical results is negligible showing an acceptable accuracy for the analytical model to predict an MI critical power in fiber-optic systems. Actually, the experimental results presented in this section and compared with the proposed model proof the validity of the analytical formula in Eq. (4.21) for depleted power due to modulation instability in relatively low depletion ratios. Therefore, the formulas for optimal input power in Eq. (4.32) and maximal output power in Eq. (4.33) obtained from the MI depleted power in Eq. (4.21), are experimentally trustworthy.

5 Polarization Modulation Instability

Brillouin optical time domain analysis (BOTDA) sensing systems rely on the nonlinear process of stimulated Brillouin scattering (SBS). This inelastic scattering occurs when two counter-propagating optical waves, called pump and probe, with a frequency difference of the Brillouin frequency shift (BFS) interact or actually interfere. Therefore, SBS is sensitive to the polarization state of the pump and probe. The polarization dependence of the Brillouin gain in polarization-maintaining (PM) fibers was experimentally demonstrated by Stolen [119]. He showed that in high birefringence (Hi-Bi) fibers when the pump and probe are launched orthogonally into slow and fast axes, the Brillouin gain is negligible. More importantly, when the pump is injected at 45° with the birefringence axes, the Brillouin gain is more or less uniform for all polarization states of the probe. However, the situation is different in non-PM fibers because their birefringence changes randomly both in magnitude and direction. Horiguchi *et al.* demonstrated in an experiment that the overall Brillouin gain of a pump-probe interaction in standard single-mode fibers (SMF) can vary a factor two depending on the pump and probe polarizations [120]. This was mathematically proved using the Stokes representation of polarization states in a random birefringence medium containing two counter-propagating light waves [121]. More mathematical analysis shows the high sensitivity of SBS on the interacting pump and probe state of polarization (SOP) [122]. Therefore, in BOTDA sensors the polarization-dependent Brillouin gain, sometimes called *polarization fading*, is a challenge to be dealt with.

The classical techniques for eliminating the polarization noise in BOTDA are based on the electromechanical systems such as polarization scramblers and polarization switches. Electromechanical components make BOTDA sensors less robust and impose time-consuming averaging in order to obtain a polarization independent measurement. Recently, a technique for eliminating the polarization noise has been proposed exploiting the Brillouin gain for the Stokes component and the Brillouin loss for the anti-Stokes component of the probe while these components are orthogonally polarized [123]. The technique is based on the balanced detection of the Stokes and anti-Stokes components of the probe experiencing both Brillouin gain and loss. The detection scheme can be simplified to a self-heterodyne detector by using two orthogonally polarized pumps and leaving the probe components in parallel polarization [124]. Moreover, in this system since the peak power of pump pulses is divided to two orthogonally polarized components, the modulation instability (MI) is mitigated or

equivalently more pump power can be launched into the sensing fiber without a considerable pump depletion due to MI [125]. This way, the signal-to-noise ratio (SNR) of the system can be enhanced but not as much as expected because although the scalar modulation instability of each pump component reduces, a vector modulation instability occurs due to the interaction of two orthogonal components [126]. This chapter is devoted to the performance analysis of a BOTDA sensor deploying orthogonally polarized pumps and the comparison of such a system with the ordinary one from the MI point of view.

5.1 Manakov System

The fundamental mode propagating in a single-mode fiber is HE_{11} which is a hybrid mode including two degenerate modes. Therefore, even a single-mode fiber, in fact, supports two orthogonally polarized modes with the same spatial distribution. Using the weakly guiding approximation, the two modes are shown to be linearly polarized along orthogonal axes, for instance the x - and y -axis; so they are represented by HE_{11x} and HE_{11y} . If n_x and n_y denote the refractive indices of x and y principal axes, respectively, the *modal birefringence* is defined as

$$B_m = |n_x - n_y|. \quad (5.1)$$

Assuming $n_x > n_y$, the x -axis is called the *slow* axis and the y -axis is called the *fast* axis because $\frac{c}{n_x} < \frac{c}{n_y}$ in which c is the speed of light in vacuum. The phase difference induced on the polarization components of the optical field by the birefringence is expressed by

$$\phi = n_x kL - n_y kL = (n_x - n_y)kL = B_m kL, \quad (5.2)$$

where $k = \frac{2\pi}{\lambda}$ is the vacuum wavenumber and L is the propagation length. The *beat length* L_B of a fiber is defined as the length in which the induced phase difference between the two polarization components is 2π and according to Eq. (5.2) it is given by

$$L_B = \frac{2\pi}{(n_x - n_y)k} = \frac{\lambda}{n_x - n_y} = \frac{\lambda}{B_m}. \quad (5.3)$$

L_B is the minimum propagation length over which the input and output polarization states return to identical. The typical value of birefringence for standard optical fibers is in the order of 10^{-8} and thus, the beat length of standard fibers is in the range of tens of meters (< 100 m) at telecom wavelengths around $1.5 \mu\text{m}$. Two general techniques are utilized for manufacturing birefringent or polarization maintaining (PM) fibers; one is by breaking the circular symmetry of the fiber core into an elliptic shape that achieves a birefringence of 10^{-6} or equivalently a beat length of ≈ 1 m. The other method uses stress-induced birefringence reaching up to 10^{-4} equivalent to a beat length of ≈ 1 cm. The commercially available PANDA and BOW-TIE are among such high-birefringence (Hi-Bi) fibers. However, in standard optical fibers extensively used in communications and sensing systems, birefringence changes in a random manner both in value and in orientation of the slow and fast axes. Therefore, stochastic analysis is

necessary to describe lightwave characteristics in such optical fibers [127, 128]. An important parameter in randomly varying birefringent fibers is the *correlation length* l_c which is defined as the length over which two polarization components remain correlated and it is of the order of 10 m for standard fibers. Another parameter is the polarization mode dispersion (PMD) which is the pulse broadening due to the different group velocities of two polarization modes. In a fiber of length L with group velocities $v_{gx} = \frac{1}{\beta_{1x}}$ and $v_{gy} = \frac{1}{\beta_{1y}}$, the PMD-induced pulse broadening is given by the following variance [129]:

$$\sigma_T^2 = 2(\beta_{1x} - \beta_{1y})^2 l_c^2 \left(e^{-\frac{L}{l_c}} + \frac{L}{l_c} - 1 \right). \quad (5.4)$$

For long fibers where $L \gg l_c$, the exponential function in Eq. (5.4) can be neglected and thus, the pulse broadening is expressed by

$$\sigma_T = |\beta_{1x} - \beta_{1y}| \sqrt{2l_c L} = D_p \sqrt{L}, \quad (5.5)$$

where $D_p = \sqrt{2l_c} |\beta_{1x} - \beta_{1y}|$ is called the PMD parameter and its value is ranged from 0.01 to $2 \frac{\text{ps}}{\sqrt{\text{km}}}$; the PMD parameter in low-PMD fiber is around $0.05 \frac{\text{ps}}{\sqrt{\text{km}}}$. Now, we can analyze light propagation in an optical fiber having birefringence.

5.1.1 Mathematical Derivation of the Manakov System

First, we consider a deterministic (non-random) linear birefringence and then, we apply randomness to our analysis. Let A_x and A_y denote the slowly varying envelope of the x -polarized and y -polarized fields with corresponding frequencies ω_1 and ω_2 and propagation constants $\beta_x(\omega)$ and $\beta_y(\omega)$. The time- and longitudinal variations of the optical vector field can be expressed by

$$\mathbf{A}(z, t) = \hat{\mathbf{x}} A_x(z, t) e^{i(\beta_{0x} z - \omega_1 t)} + \hat{\mathbf{y}} A_y(z, t) e^{i(\beta_{0y} z - \omega_2 t)} + \text{c.c.}, \quad (5.6)$$

where $\hat{\mathbf{x}}$ and $\hat{\mathbf{y}}$ represent the unit vectors along the x - and y -axis, respectively. c.c. denotes the complex conjugate of the previous terms and $\beta_{0x} = \beta_x(\omega_1)$ and $\beta_{0y} = \beta_y(\omega_2)$ show the propagation constants at the pump wavelengths. In a linearly birefringent fiber, the general form of the two coupled nonlinear Schrödinger equations governing the slowly varying envelopes is given by [3]

$$\frac{\partial A_x}{\partial z} + \beta_{1x} \frac{\partial A_x}{\partial t} + \frac{i\beta_2}{2} \frac{\partial^2 A_x}{\partial t^2} + \frac{\alpha}{2} A_x = i\gamma \left(|A_x|^2 + \frac{2}{3} |A_y|^2 \right) A_x + \frac{i\gamma}{3} A_x^* A_y^2 e^{-2i\Delta\beta z}, \quad (5.7a)$$

$$\frac{\partial A_y}{\partial z} + \beta_{1y} \frac{\partial A_y}{\partial t} + \frac{i\beta_2}{2} \frac{\partial^2 A_y}{\partial t^2} + \frac{\alpha}{2} A_y = i\gamma \left(|A_y|^2 + \frac{2}{3} |A_x|^2 \right) A_y + \frac{i\gamma}{3} A_y^* A_x^2 e^{2i\Delta\beta z}, \quad (5.7b)$$

in which α is the attenuation coefficient, $\gamma = \frac{n_2 k}{A_{\text{eff}}}$ is the nonlinear coefficient and $\Delta\beta = \beta_{0x} - \beta_{0y}$ is proportional to the modal birefringence B_m . In general, $\beta_{1x} \neq \beta_{1y}$ so that $|\beta_{1x} - \beta_{1y}|$ represent the group velocity mismatch (GVM) between the two principal axes. It is also assumed that the group velocity dispersion (GVD) coefficient β_2 is the same for both

Chapter 5. Polarization Modulation Instability

polarizations that is acceptable as long as the optical frequencies ω_1 and ω_2 are relatively close to each other and thus, β_2 can be attributed to the central frequency $\omega_0 = \frac{\omega_1 + \omega_2}{2}$. Defining $\beta_1 = \frac{\beta_{1x} + \beta_{1y}}{2}$ and $\delta = \frac{\beta_{1x} - \beta_{1y}}{2}$ leads to $\beta_{1x} = \beta_1 + \delta$ and $\beta_{1y} = \beta_1 - \delta$, where β_1 can be attributed to the central frequency ω_0 . By changing the time variable from t to $t - \beta_1 z$, the reference frame moves with the average group velocity and the coupled equations in Eq. (5.7) are written as

$$\frac{\partial A_x}{\partial z} + \delta \frac{\partial A_x}{\partial t} + \frac{i\beta_2}{2} \frac{\partial^2 A_x}{\partial t^2} + \frac{\alpha}{2} A_x = i\gamma \left(|A_x|^2 + \frac{2}{3} |A_y|^2 \right) A_x + \frac{i\gamma}{3} A_x^* A_y^2 e^{-2i\Delta\beta z}, \quad (5.8a)$$

$$\frac{\partial A_y}{\partial z} - \delta \frac{\partial A_y}{\partial t} + \frac{i\beta_2}{2} \frac{\partial^2 A_y}{\partial t^2} + \frac{\alpha}{2} A_y = i\gamma \left(|A_y|^2 + \frac{2}{3} |A_x|^2 \right) A_y + \frac{i\gamma}{3} A_y^* A_x^2 e^{2i\Delta\beta z}. \quad (5.8b)$$

The phase terms $e^{\pm 2i\Delta\beta z}$ in Eqs. (5.8) can be removed by defining the following phase-shifted envelopes:

$$U(z, t) = A_x(z, t) e^{+i\frac{\Delta\beta}{2} z}, \quad (5.9a)$$

$$V(z, t) = A_y(z, t) e^{-i\frac{\Delta\beta}{2} z}. \quad (5.9b)$$

Using Eqs. (5.9) in the coupled equations results in

$$\frac{\partial U}{\partial z} + \delta \frac{\partial U}{\partial t} + \frac{i\beta_2}{2} \frac{\partial^2 U}{\partial t^2} + \frac{\alpha - i\Delta\beta}{2} U = i\gamma \left(|U|^2 + \frac{2}{3} |V|^2 \right) U + \frac{i\gamma}{3} U^* V^2, \quad (5.10a)$$

$$\frac{\partial V}{\partial z} - \delta \frac{\partial V}{\partial t} + \frac{i\beta_2}{2} \frac{\partial^2 V}{\partial t^2} + \frac{\alpha + i\Delta\beta}{2} V = i\gamma \left(|V|^2 + \frac{2}{3} |U|^2 \right) V + \frac{i\gamma}{3} V^* U^2. \quad (5.10b)$$

In randomly varying birefringent fibers, the random rotation of the principal axes along with a random phase difference between the two axes results in the following transformation of the envelopes [130]:

$$\begin{bmatrix} U' \\ V' \end{bmatrix} = \begin{bmatrix} \cos\theta & e^{i\phi} \sin\theta \\ -e^{-i\phi} \sin\theta & \cos\theta \end{bmatrix} \begin{bmatrix} U \\ V \end{bmatrix}, \quad (5.11)$$

where θ is a uniform random variable over the interval $[0, 2\pi]$ and ϕ is also a random variable uniformly distributed over $[-\frac{\pi}{2}, \frac{\pi}{2}]$ independent from θ [3]. Besides random rotation of the birefringence axes, the modal birefringence $\Delta\beta$ also changes randomly along the fiber. In a reasonably accurate model, $\Delta\beta$ is represented by a Gaussian stochastic process with zero average and exponentially decaying correlation, valid for all positions z , z_1 and z_2 along the fiber as follows [3]:

$$\mathbb{E}[\Delta\beta(z)] = 0, \quad (5.12a)$$

$$\mathbb{E}[\Delta\beta(z_1)\Delta\beta(z_2)] = \sigma^2 e^{-\frac{|z_1 - z_2|}{l_c}}, \quad (5.12b)$$

in which \mathbb{E} denotes the expected value operation. σ^2 is the variance and l_c is the correlation length of birefringence fluctuations. Substituting the transformation given by Eq. (5.11) in

Eqs. (5.10) and averaging over θ , ϕ and $\Delta\beta$ using Eqs. (5.12), and dropping the primes, we find that [131]

$$\frac{\partial U}{\partial z} + \delta \frac{\partial U}{\partial t} + \frac{i\beta_2}{2} \frac{\partial^2 U}{\partial t^2} + \frac{\alpha}{2} U = \frac{8}{9} i\gamma (|U|^2 + |V|^2) U, \quad (5.13a)$$

$$\frac{\partial V}{\partial z} - \delta \frac{\partial V}{\partial t} + \frac{i\beta_2}{2} \frac{\partial^2 V}{\partial t^2} + \frac{\alpha}{2} V = \frac{8}{9} i\gamma (|U|^2 + |V|^2) V. \quad (5.13b)$$

The group velocity mismatch (GVM) in Eqs. (5.13) represented by δ can be removed using the following phase transformation [132]:

$$u(z, t) = U(z, t) e^{i\left(\frac{\delta^2}{2\beta_2} z - \frac{\delta}{\beta_2} t\right)}, \quad (5.14a)$$

$$v(z, t) = V(z, t) e^{i\left(\frac{\delta^2}{2\beta_2} z + \frac{\delta}{\beta_2} t\right)}. \quad (5.14b)$$

Applying the transformation given by Eqs. (5.14) to Eqs. (5.13) leads to

$$\frac{\partial u}{\partial z} + i \frac{\beta_2}{2} \frac{\partial^2 u}{\partial t^2} + \frac{\alpha}{2} u = \frac{8}{9} i\gamma (|u|^2 + |v|^2) u, \quad (5.15a)$$

$$\frac{\partial v}{\partial z} + i \frac{\beta_2}{2} \frac{\partial^2 v}{\partial t^2} + \frac{\alpha}{2} v = \frac{8}{9} i\gamma (|u|^2 + |v|^2) v. \quad (5.15b)$$

The set of Eqs. (5.15) is called the Manakov system first described in [133]. It has been experimentally demonstrated that light propagation in standard optical fibers with relatively low PMD can be described accurately using the Manakov system in both anomalous [134] and normal [135] dispersion regimes. The coefficient $\frac{8}{9}$ which is a result of averaging over the whole Poincaré sphere, can be absorbed to the nonlinear coefficient by defining $\gamma = \frac{8}{9} \frac{n_2 k}{A_{\text{eff}}}$. This way, the Manakov system in Eqs. (5.15) is rewritten as

$$\frac{\partial u}{\partial z} + i \frac{\beta_2}{2} \frac{\partial^2 u}{\partial t^2} + \frac{\alpha}{2} u = i\gamma (|u|^2 + |v|^2) u, \quad (5.16a)$$

$$\frac{\partial v}{\partial z} + i \frac{\beta_2}{2} \frac{\partial^2 v}{\partial t^2} + \frac{\alpha}{2} v = i\gamma (|u|^2 + |v|^2) v. \quad (5.16b)$$

It is worth mentioning that in the Manakov system, as it is clear from Eq. (5.16), the self-phase modulation (SPM) terms $i\gamma|u|^2 u$ and $i\gamma|v|^2 v$ have equal strength to the cross-phase modulation (XPM) terms $i\gamma|u|^2 v$ and $i\gamma|v|^2 u$ which is a characteristic of randomly varying birefringent fibers. The Manakov system described in Eqs. (5.16) is used in the next section to model the propagation of orthogonally polarized light waves in a BOTDA system utilizing long standard SMFs.

5.1.2 Numerical Simulation of the Manakov System

In this section, numerical simulations of the Manakov system given in Eqs. (5.16) are carried out to obtain the longitudinal evolution of pump power and thus, the Brillouin gain in a BOTDA sensor with orthogonally-polarized pumps. Three different scenarios are considered: 1) a classical BOTDA containing one pump with peak power P_0 , 2) a BOTDA deploying two

pumps with parallel polarization each of which has a peak power of $\frac{P_0}{2}$ and with the frequency difference Δf , 3) a two-pump BOTDA with the same parameters but orthogonal states of polarization. In order to numerically solve the Manakov system in Eqs. (5.16), the split-step Fourier method described in Chapter 2 is utilized. Moreover, the background noise as a seeding signal for modulation instability is taken into account by applying a Monte Carlo simulation to the Manakov system. A standard SMF with typical characteristics at 1550 nm like the attenuation coefficient $\alpha = 0.2 \frac{\text{dB}}{\text{km}}$, GVD coefficient $\beta_2 = -22 \frac{\text{ps}^2}{\text{km}}$, nonlinear coefficient $\gamma = 1.8 \frac{\text{W}^{-1}}{\text{km}}$ is considered. It should be noted that the fiber must be long enough to guarantee the accuracy of the statistical averaging of the coupled nonlinear Schrödinger equations over the fiber random birefringence. It can be seen that for a standard fiber with a length of more than 1 km, during the propagation the state of polarization covers the Poincaré sphere almost completely [3]; the fiber length here is chosen 25 km being compatible with our experiment. The total pump power is chosen to be $P_0 = 250 \text{ mW}$, therefore, for the single-pump BOTDA the peak power is 250 mW, while the peak power of each pump in two-pump BOTDA is 125 mW. The frequency spacing between the two pumps are set to 20 GHz which is around twice the Brillouin frequency shift. The total noise power spectral density (PSD) is $-118 \frac{\text{dBm}}{\text{Hz}}$ which means that it is $-121 \frac{\text{dBm}}{\text{Hz}}$ in each polarization.

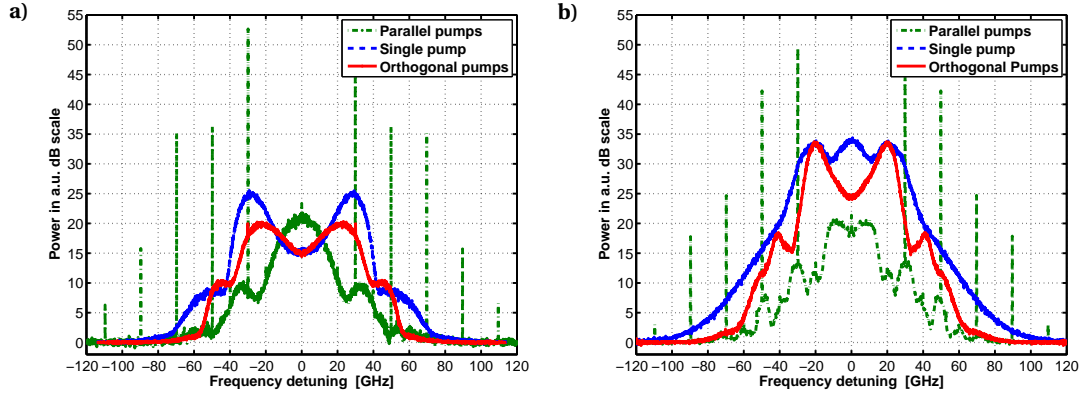


Figure 5.1 – Numerical simulation of modulation instability gain spectrum for a standard SMF with $\alpha = 0.2 \frac{\text{dB}}{\text{km}}$, $\beta_2 = -22 \frac{\text{ps}^2}{\text{km}}$, $\gamma = 1.8 \frac{\text{W}^{-1}}{\text{km}}$, and two fiber lengths a) $L = 10 \text{ km}$ and b) $L = 25 \text{ km}$ in three different scenarios. The frequency spacing between the pumps is $\Delta f = 20 \text{ GHz}$, the noise power spectral density is $-118 \frac{\text{dBm}}{\text{Hz}}$, and the total power is 250 mW. The curves are normalized to $e^{-\alpha L}$ to discard the effect of fiber loss.

Fig. 5.1 depicts the modulation instability gain spectrum in the three considered scenarios for two fiber lengths, 10 and 25 km. For the sake of visibility, the pump lines at 0 and $\pm 10 \text{ GHz}$ are removed from the plots. Firstly, the spectral lines in the figure demonstrates an efficient four-wave mixing (FWM) between the pumps with parallel polarizations while with orthogonally polarized pumps, FWM is highly suppressed [136] which is evident from the figure. Secondly, the MI gain in single-pump scenario is always higher than that of the orthogonal pumps whether in small-signal gain or low pump depletion plotted in Fig. 5.1a or in saturated gain or high pump depletion shown in Fig. 5.1b. Therefore, it is evident that a BOTDA with orthogonally polarized pumps can perform better than a single-pump BOTDA in the sense

of pump depletion due to modulation instability. To confirm this claim, the longitudinal evolution of pump power during the propagation along the fiber is simulated for the three considered scenarios. In the two-pump scenarios the total pump power is obtained by adding the two pump powers incoherently which is proportional to the total Brillouin gain in a BOTDA system. Fig. 5.2 shows the simulation results of pump power evolution. The case of parallel pumps demonstrates a highly oscillating pump power due to the FWM between the pumps. Hence, this scenario is not applicable in BOTDA systems. However, in other scenarios where FWM is efficiently suppressed there are no abrupt changes in the longitudinal variation of the pump power. On the other hand, it is interesting to observe the behavior of the orthogonally polarized pumps, which shows a considerable improvement in terms of pump depletion compared to the standard single-pump configuration. For instance, the pump depletion ratio at the fiber end (25 km) is more than 70% for a single-pump setup while it is less than 40% when orthogonally polarized pumps are deployed.

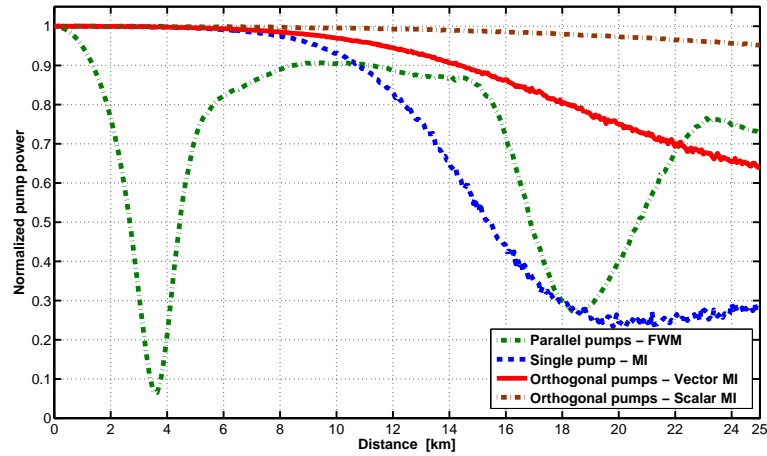


Figure 5.2 – Longitudinal pump power evolution along a 25 km SMF with $\alpha = 0.2 \frac{\text{dB}}{\text{km}}$, $\beta_2 = -22 \frac{\text{ps}^2}{\text{km}}$, and $\gamma = 1.8 \frac{\text{W}^{-1}}{\text{km}}$ in three practical scenarios plus a fictitious case. The frequency spacing between the pumps is $\Delta f = 20 \text{ GHz}$, the noise power spectral density is $-118 \frac{\text{dBm}}{\text{Hz}}$, and the total power is 250 mW. The curves are normalized to $e^{-\alpha z}$ to discard the effect of fiber loss.

Fig. 5.2 also includes a fourth fictitious scenario (the plot close to a straight line) in which there is no interaction between two orthogonal pumps and thus no vector modulation instability occurs. Actually, each pump has its own scalar modulation instability and its corresponding power depletion. Comparing the power evolution in two cases of orthogonally polarized pumps with and without vector modulation instability, we find that how significant the interaction of two pumps and the power depletion can be. It proves that assuming the same performance, it is not possible to double the pump power by splitting it into two orthogonal pumps because in addition to scalar modulation instability of each pump there is a vector modulation instability due to the interaction of the pumps. It is worth mentioning that the power evolution of parallel pumps can be exploited for extracting the fiber parameters γ and β_2 . More specifically, the position and the depth of the first dip in the curve highly depends on the dispersion and nonlinear coefficients. Moreover, this dip is almost independent from

the system noise level because it is the result of energy transfer between pumps and not the interaction of pumps and noise. Therefore, by measuring the longitudinal evolution of pump power in a two-pump BOTDA with parallel polarizations the fiber characteristics can be extracted almost accurately.

5.2 BOTDA with Orthogonally Polarized Pumps

Pump probe interaction through the nonlinear process of stimulated Brillouin scattering (SBS) provides an amplification or gain when the probe is in the Stokes zone of the pump, while in the anti-Stokes region it induces a loss on the probe. Traditional single-pump BOTDA sensors can exploit either the gain or the loss mechanism of SBS for measuring the environmental parameters like temperature and strain. However, in two-pump BOTDA systems, it is required to use the gain and loss mechanisms simultaneously. Fig. 5.3 illustrates the conceptual design of a BOTDA with orthogonally-polarized pumps. On the one hand, the probe spectral lines are in the Stokes region of the horizontal pump and thus, they experience a gain due to the energy transfer from that pump. On the other hand, the vertical pump induces a loss on the probe lines because they are located in its anti-Stokes zone.

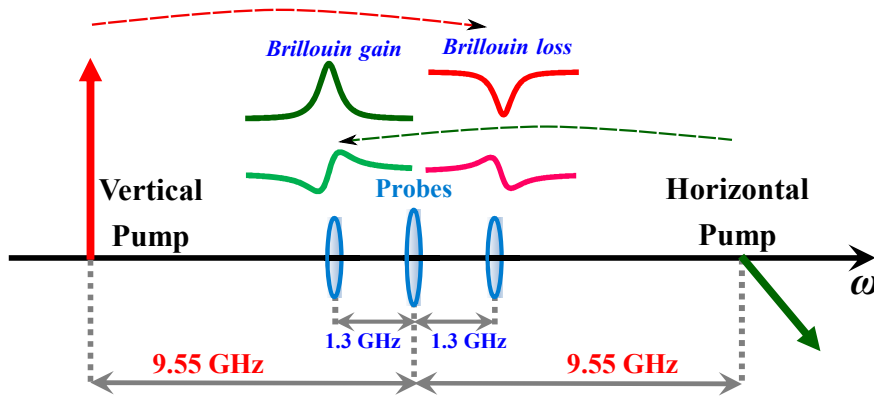


Figure 5.3 – Brillouin interactions of the probe spectral lines with the orthogonally-polarized pumps. The vertical pump induces a Brillouin loss on the probe, while the horizontal pump provides a Brillouin gain. The BFS is $9.55 + 1.3 = 10.85$ GHz.

The efficiency of gain and loss on each probe line highly depends on the frequency difference between them. The scheme in Fig. 5.3 is designed so that the upper probe line experiences an efficient loss due to the vertical pump because the frequency difference between them is $9.55 + 1.3 = 10.85$ GHz which is the Brillouin frequency shift (BFS) in standard optical fibers; and for the same reason the lower probe line sees an efficient gain from the horizontal pump. If I_p denotes the intensity of each pump, the small-signal gain induced by the horizontal pump is expressed by $1 + g_h I_p L_{\text{eff}}$, where g_h is the Brillouin gain of the horizontal pump. Similarly, if g_v represents the Brillouin gain of the vertical pump, the small signal loss due to the vertical pump is expressed by $1 - g_v I_p L_{\text{eff}}$. By measuring the difference between the gain and loss, the net signal is detected to be $(1 + g_h I_p L_{\text{eff}}) - (1 - g_v I_p L_{\text{eff}}) = (g_h + g_v) I_p L_{\text{eff}}$ and it automatically compensates the polarization fading.

5.2.1 Experimental Setup of Two-Pump BOTDA

The experimental setup implementing exactly the conceptual design given in Fig. 5.3 is portrayed in Fig. 5.4. The output of a laser source at 1550.5 nm is split into two branches using an optical coupler. In the pump branch, the continuous-wave (CW) light is shaped into a train of optical square pulses with a pulse duration of 50 ns and a repetition period of 300 μ s using a Mach-Zehnder electro-optic modulator (MZ-EOM) driven by an RF switch. The switch is turned on and off by a pulse generator and at the same time, a microwave oscillator at 9.55 GHz modulates the pump pulses to generate two spectral lines around the laser frequency. The carrier at the laser wavelength is highly suppressed by the bias voltage applied to the intensity modulator. The modulated lightwave passes through a polarization controller (PC), a differential group delay (DGD) module and a programmable optical filter (POF), depicted inside a dashed box in Fig. 5.4. These optical components together allow us to implement the three scenarios mentioned in the previous section for the study of modulation instability, i.e. orthogonal pumps, parallel pumps and single pump.

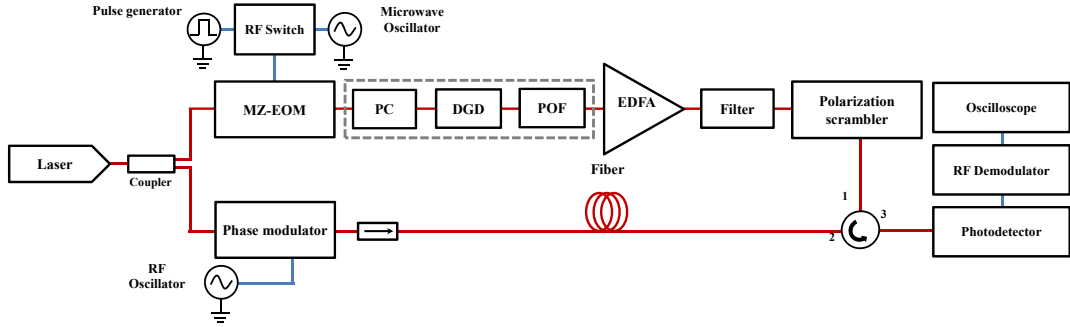


Figure 5.4 – Experimental setup for implementing three variations of a BOTDA sensor: 1) single pump, 2) parallel pumps and 3) orthogonal pumps. PC: polarization controller; DGD: differential group delay; POF: programmable optical filter; RF: radio frequency; MZ-EOM: Mach-Zehnder electro-optic modulator.

The polarization controller allows the linearly-polarized light at the output of the intensity modulator to be properly aligned into the DGD module. This birefringent material generates a wavelength-dependent phase shift difference between its axes expressed by $\theta = 2\pi\Delta f\Delta\tau$, in which $\Delta\tau$ is the differential group delay introduced by the birefringence in the DGD module and Δf is the frequency spacing between the optical waves [125], in this case 19.1 GHz. Therefore, depending on the wavelength difference and the angle of the linearly-polarized incident light, the birefringent material can provide different states of polarization at its output. Two orthogonally-polarized pulses can be obtained if the incident angle into the birefringent material is set to 45° and $\theta = \pi$. The incident angle is achieved by the polarization controller, while condition on θ is fulfilled by choosing a DGD module with $\Delta\tau = 26$ ps. The generation of pulses with parallel polarizations only requires to adjust the incident angle to one of the principal axes of the DGD module. Finally, for making a standard single-wavelength pulse, the programmable optical filter is adjusted to select only one of the sidebands. Once the desired pump signal is generated, it is boosted by an erbium-doped fiber amplifier (EDFA), whose amplified spontaneous emission noise is filtered out by a 1 nm optical filter.

In the probe branch, the CW lightwave is modulated by an electro-optic phase modulator driven by a 1.3 GHz signal generator. This modulation frequency is selected so that the upper (lower) sideband of the phase modulation interacts with the lower (upper) sideband of the pump to implement the conceptual design in Fig. 5.3. After interacting via stimulated Brillouin scattering, the probe signal is directed to a photodetector playing the role of a self-heterodyne detection scheme. Since the probe has three spectral lines in which the two sidebands are in opposite phase because of the electro-optic phase modulator, the detected signal at 1.3 GHz is the difference between the Brillouin gain and loss as desired for implementing the scheme in Fig. 5.3. The detected radio frequency (RF) signal at 1.3 GHz is transformed to a base-band signal using the RF demodulator. Finally, the BOTDA signal is acquired by an oscilloscope.

5.2.2 Comparison of the Model and Measurements

Here, the experimental measurements obtained from a BOTDA system with three different configurations are compared with the numerical simulations obtained from the theoretical model given by the Manakov system. The local Brillouin gain which is proportional to the pump power distributed along the fiber is measured to obtain the evolution of pump power as it propagates through the fiber. Therefore, the measurement must be similar to the simulation results depicted in Fig. 5.2 except that the experimental results include the attenuation effect and thus, an exponential decay. A 25 km long SMF (its exact length is 24760 m) is employed as the sensing fiber under test (FUT). The main objective is to compare the performance of a single-pump BOTDA and a double-pump BOTDA with orthogonal polarizations from the modulation instability point of view. However, the configuration of double-pump BOTDA with parallel polarization is also implemented to extract the fiber characteristics from its experimental measurement. As mentioned before, the coherent interaction of the parallel pumps through the four-wave mixing process can be exploited to extract dispersion and nonlinear coefficients. Therefore, it is necessary to measure this scenario even though it is not desired from the BOTDA perspective. Fitting the measurement results with the numerical simulation of the system, we find the dispersion and nonlinear coefficients. It is worth mentioning again that the Manakov system is numerically solved using the split-step Fourier method while the noise is taken into account by performing a Monte Carlo simulation.

Fig. 5.5 compares the experimental and simulation results. The measured BOTDA trace of the single-pump configuration along with its corresponding simulation is plotted in both sub-figures of Fig. 5.5. Moreover, the exponential decay due to the fiber attenuation is depicted to demonstrate the behaviour of an ideal BOTDA system free from the pump depletion due to nonlinear effects. Comparing the single-pump and ideal cases, we find that there is a 50% depletion at the fiber end (≈ 25 km) in the single-pump configuration. In addition to the single-pump BOTDA, Fig. 5.5a depicts the pump power evolution in the double-pump BOTDA with parallel polarizations. The deep dip in the trace is because of the FWM between the pumps and it can be used to extract the fiber dispersion and nonlinear coefficients by fitting the numerical simulation to the experimental results which leads to the parameters $\beta_2 = -23 \frac{\text{ps}^2}{\text{km}}$, and $\gamma = 1.0 \frac{\text{W}^{-1}}{\text{km}}$ for the FUT. Moreover, Fig. 5.5a demonstrates that two-pump BOTDA systems with parallel polarizations are not suitable as sensors due to high pump

5.2. BOTDA with Orthogonally Polarized Pumps

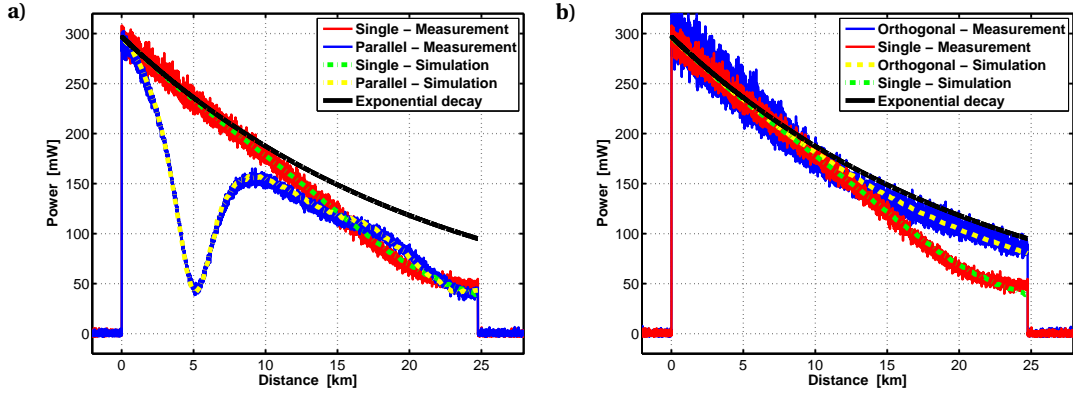


Figure 5.5 – Measured and simulated power evolution in a 25 km SMF with a total input power of 300 mW, for a) single pump with 300 mW and double parallel pumps each of which with 150 mW, and b) single pump with 300 mW and double orthogonal pumps each of which with 150 mW. The system parameters are: $\alpha = 0.2 \frac{\text{dB}}{\text{km}}$, $\beta_2 = -23 \frac{\text{ps}^2}{\text{km}}$, and $\gamma = 1.0 \frac{\text{W}^{-1}}{\text{km}}$. The frequency spacing between the pumps is 19.1 GHz and the noise power spectral density is $-109 \frac{\text{dBm}}{\text{Hz}}$. The undepleted exponential decay corresponding to the ideal situation is also plotted.

depletion.

The main result of this study is shown in Fig. 5.5b where the single-pump BOTDA is compared with a double-pump one of orthogonal polarizations. First of all, it is evident from the figure that the numerical simulation of the Manakov system given in Eqs. (5.16) is in an excellent agreement with the experimental results, demonstrating the validity of the model and its accuracy in analyzing a two-pump BOTDA from the MI perspective. Secondly, Fig. 5.5b demonstrates that a double-pump BOTDA system with orthogonal polarizations outperforms a classical single-pump one as long as the MI pump depletion matters. Obvious differences in the pump power evolution can be observed in the last 10 km of fiber, where the power of the single pump is depleted by approximately 50% as a result of scalar modulation instability, while the total power in the two orthogonal pulses is only depleted by around 10% due to vector or polarization modulation instability. This represents an improvement slightly less than 3 dB in the sensor response at the end of the fiber, enabling a sensing range extension of around 7 km while maintaining the same SNR [101].

In order to evaluate the performance improvement provided by the use of orthogonally polarized pumps, the measured depletion ratio at the fiber end is compared in Fig. 5.6 with the single-pump case for different levels of input pump power. As it is evident from the figure, the depletion ratio using a single pump is clearly much higher than when using double pumps with orthogonal polarizations. As an example, tolerating a depletion ratio of about 20%, the input pump power can be increased from around 220 mW to 320 mW employing orthogonally-polarized pumps. This represents a 1.5-fold improvement in the input pump power supported by the system before inducing distortions in the pump evolution traces. Furthermore, for pump powers below 300 mW, the depletion ratio grows from 15% using orthogonally polarized pumps up to more than 50% using the single pump configuration, which also confirms the advantage of a BOTDA with orthogonally polarized pumps. It is worth

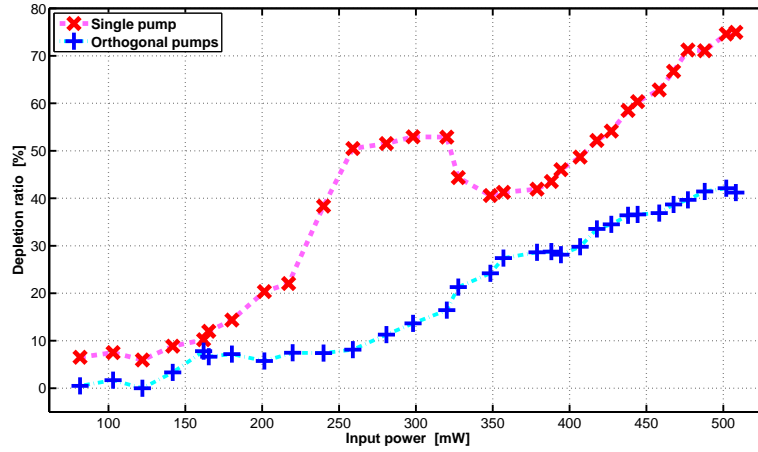


Figure 5.6 – Measured pump depletion ratio versus total input power at the fiber end (≈ 25 km distance) for two cases: 1) single pump and 2) double pumps with orthogonal polarizations.

mentioning that the oscillatory behavior of the single pump case in Fig. 5.6 is due to the FPU recurrence phenomenon.

Finally, it is seen that the Manakov system is a reasonably accurate model for evaluating the power evolution in a Brillouin distributed sensor employing two orthogonally polarized pumps. It is also demonstrated that although the pump depletion due to the scalar modulation instability reduces by splitting the pump power into two orthogonally polarized pumps, the vector or polarization modulation instability originating from the interaction of the pumps induces a pump depletion limiting the performance improvement. Therefore, the maximum pump power allowed to be launched into a BOTDA sensor is determined by the pump depletion due to the polarization MI described by the Manakov system. Such a maximum power is obtained when two pumps with orthogonal polarizations are utilized and it is shown to be higher than the allowable power for a single-pump BOTDA.

Conclusions

This dissertation analyzes the main limitation for increasing the sensing distance of distributed optical fiber sensors, i.e. pump depletion due to modulation instability (MI). A mathematical model for predicting the critical, optimal and maximal powers is proposed and verified by experiment and simulation. Methods for mitigating modulation instability in optical fibers are presented. The results of this thesis are given below.

Suppose a fiber-optic system with the input pump power of P_0 comprising a background noise with the power spectral density S_n . For a standard single-mode fiber (SMF) of length L with attenuation coefficient α , group-velocity dispersion β_2 , and nonlinearity γ , the power depleted from the pump due to modulation instability is given

$$P_{\text{MI}} = \frac{S_n e^{2\gamma P_0 L_{\text{eff}} - \alpha L}}{2\sqrt{2\pi|\beta_2|}L_{\text{eff}}}. \quad (1)$$

This formula shows the impact of background noise level, dispersion, attenuation and nonlinearity on the amount of depleted power due to modulation instability. Specifically, increasing the group-velocity dispersion and decreasing the background noise are shown to be effective in reducing modulation instability.

Accepting a depletion ratio R for the aforementioned system, we can define a critical input power for which the output power experiences a depletion of $R\%$. Based on the depleted power in Eq. (1), the MI critical power for a tolerable depletion ratio R is expressed by an intuitively expected formula as

$$P_{\text{crit}} = \frac{\sigma_{\text{crit}}}{2\gamma L_{\text{eff}}}, \quad (2)$$

where the critical gain σ_{crit} is obtained from the following equation:

$$e^{\sigma_{\text{crit}}} = \frac{R\sqrt{2\pi|\beta_2|}}{S_n\gamma\sqrt{L_{\text{eff}}}}\sigma_{\text{crit}}. \quad (3)$$

The transcendental equation given by Eq. (3) can be simply solved by numerical methods in order to obtain the MI critical power from Eq. (2). The depletion ratio R provides a degree of freedom in evaluating the MI critical power so that it can be adapted to different fiber-optics systems based on application.

Conclusions

Maximizing the pump power at the fiber output in order to achieve the maximum signal-to-noise ratio (SNR) by performing an optimization based on Eq. (1) results in the following maximal output power:

$$P_{\max} = \frac{e^{-\alpha L}}{2\gamma L_{\text{eff}}} \ln \left(\frac{\sqrt{2\pi|\beta_2|}}{e S_n \gamma \sqrt{L_{\text{eff}}}} \right), \quad (4)$$

where $e \approx 2.71828$ is Euler's number. The optimal input pump power corresponding to the maximal output power is obtained from

$$P_{\text{opt}} = \frac{1}{2\gamma L_{\text{eff}}} \ln \left(\frac{\sqrt{2\pi|\beta_2|}}{S_n \gamma \sqrt{L_{\text{eff}}}} \right). \quad (5)$$

The optimal input power given in Eq. (5) can be very applicable in designing, testing and analyzing fiber-optic systems suffering from modulation instability such as distributed optical fiber sensors.

According to Eq. (1) and Eq. (4), the impact of modulation instability on distributed optical fiber sensors can be alleviated by modifying the fiber characteristics such as dispersion and nonlinearity. It is evident from Eq. (4) that by increasing the dispersion coefficient β_2 , maximal output power enhances slightly due to the logarithmic dependence. It can be justified considering that the MI bandwidth decreases while the MI gain remains unchanged so the total depleted power reduces. Another parameter is the nonlinear coefficient γ that can be much more effective than the dispersion coefficient in mitigating modulation instability. However, reducing γ through increasing the fiber effective area is useless in improving the performance of distributed fiber sensors, because the Raman and Brillouin gain coefficients also decrease with the same proportion.

Eq. (5) and Eq. (4) suggest a rather effective way to mitigate modulation instability by decreasing the level of background noise in the MI spectral band which is demonstrated experimentally in this thesis via utilizing a narrowband optical filter covering the MI spectral lobes around the pump wavelength. Moreover, by splitting the pump power into two orthogonally-polarized components at different wavelengths, it is possible to reduce the MI pump depletion. In this case the system performance is determined by the vector modulation instability originating from the two interacting pumps.

This work can be continued in several ways. For instance, the proposed analytical model for MI characteristics can be generalized to consider higher-order dispersions. The results will be applicable for dispersion-managed optical fibers such as dispersion-shifted fibers (DSF). Another path is to consider a colored or non-white characteristic for the background noise. This assumption will result in a different modulation instability gain spectrum and thus, different power depletion due to MI. Moreover, the experimental observation of such a colored-noise-seeded MI can be exciting.

Based on the model, obtaining optimum combinations of fiber characteristics and system parameters for different applications can also open the door for future work. Such optimal configurations will be useful in designing, manufacturing and testing distributed fiber sensors.

A White Noise

In this appendix, a few essential concepts for dealing with stochastic signals in general and white noise in particular are represented. White noise is a random signal with a constant power spectral density and so, it is necessary to define the power spectral density (PSD) of random signals. For a random power signal $x(t)$, the power spectral density $S_x(\omega)$ is defined as [137]

$$S_x(\omega) \triangleq \lim_{T \rightarrow \infty} \frac{\mathbb{E}[|\hat{x}_T(\omega)|^2]}{T}, \quad (\text{A.1})$$

where \mathbb{E} denotes the expected value operator and $\hat{x}_T(\omega)$ indicates the Fourier transform of the truncated signal as follows:

$$\hat{x}_T(\omega) = \int_{-\frac{T}{2}}^{+\frac{T}{2}} x(t) e^{i\omega t} dt. \quad (\text{A.2})$$

Obtaining the PSD of a random signal directly from Eq. (A.1) is cumbersome. Fortunately, for a broad range of random signals called *wide-sense stationary* or WSS signals, it is possible to calculate their PSD by taking the Fourier transform of their *autocorrelation* function, thanks to the well-known *Wiener-Khinchin* theorem in spectral analysis [137]. A random signal $x(t)$ is called wide-sense stationary when its expected value $\mathbb{E}[x(t)]$ is time independent and its correlation between two instants t_1 and t_2 depends only on the time difference $\tau = t_1 - t_2$. In this case the autocorrelation function is given by [138]

$$R_x(\tau) = \mathbb{E}[x(t + \tau)x^*(t)]. \quad (\text{A.3})$$

Accordingly, the Wiener-Khinchin theorem simply indicates that

$$S_x(\omega) = \mathcal{F}[R_x(\tau)] = \int_{-\infty}^{+\infty} R_x(\tau) e^{i\omega\tau} d\tau. \quad (\text{A.4})$$

The white noise signal $n(t)$ is a WSS stochastic signal with a zero average and a constant power spectral density, i.e. $\mathbb{E}[n(t)] = 0$ and $S_n(\omega) = \frac{N_0}{2}$, where N_0 is called one-sided power spectral density [138]. Since the white noise PSD is constant, according to the Wiener-Khinchin

Appendix A. White Noise

theorem its autocorrelation is a Dirac impulse function that can be expressed as

$$R_n(t_1, t_2) \triangleq \mathbb{E}[n(t_1)n^*(t_2)] = \frac{N_0}{2}\delta(t_1 - t_2). \quad (\text{A.5})$$

Eq. (A.5) indicates that for a white noise the samples at different instances are uncorrelated. This characteristic of noise provides a simplicity in the mathematical analysis of systems containing white noise. Here, we show that the same feature holds for the spectral samples of white noise. More precisely, we demonstrate that $\hat{n}(\omega)$, the Fourier transform of $n(t)$, is also a white process. It can be easily seen that the ensemble average of $\hat{n}(\omega)$ is null as follows:

$$\mathbb{E}[\hat{n}(\omega)] = \mathbb{E}\left[\int_{-\infty}^{+\infty} n(t)e^{i\omega t} dt\right] = \int_{-\infty}^{+\infty} \mathbb{E}[n(t)]e^{i\omega t} dt = 0. \quad (\text{A.6})$$

It is worth mentioning that the integration in Eq. (A.6) is not an ordinary integration; rigorously speaking it is a stochastic integral that needs to be defined in terms of stochastic processes. However, it is possible to deal with it as normal integration and roughly speaking the results are still pertinent. The autocorrelation function of $\hat{n}(\omega)$ is calculated as follows:

$$\begin{aligned} R_n(\omega_1, \omega_2) &= \mathbb{E}[\hat{n}(\omega_1)\hat{n}^*(\omega_2)] = \mathbb{E}\left[\int_{-\infty}^{+\infty} n(t)e^{i\omega_1 t} dt \int_{-\infty}^{+\infty} n^*(t')e^{-i\omega_2 t'} dt'\right] \\ &= \iint_{-\infty}^{+\infty} \mathbb{E}[n(t)n^*(t')]e^{i(\omega_1 t - \omega_2 t')} dt' dt = \frac{N_0}{2} \iint_{-\infty}^{+\infty} \delta(t - t')e^{i(\omega_1 t - \omega_2 t')} dt' dt \\ &= \frac{N_0}{2} \int_{-\infty}^{+\infty} e^{i(\omega_1 - \omega_2)t} dt = \pi N_0 \delta(\omega_1 - \omega_2). \end{aligned} \quad (\text{A.7})$$

Eq. (A.7) clearly shows that the samples of $\hat{n}(\omega)$ at different frequencies are uncorrelated. Therefore, the Fourier transform of white noise is also a white noise, i.e. a wide-sense stationary process with uncorrelated samples. This feature of white noise is useful in obtaining the gain spectrum of spontaneous modulation instability seeded by the background noise which is modeled as white noise.

B Laplace's Method

In this appendix a useful approximate formula for integrating exponential functions, called *Laplace's method* is discussed and proved. Suppose that the function $f(x)$ has a global maximum at x_0 at which its first derivative is null, i.e. $f'(x_0) = 0$, and its second derivative is negative, i.e. $f''(x_0) = -|f''(x_0)|$. The Taylor expansion of f can be written as

$$\begin{aligned} f(x) &= \sum_{n=0}^{\infty} \frac{f^{(n)}(x_0)}{n!} (x-x_0)^n \\ &= f(x_0) + f'(x_0)(x-x_0) + \frac{f''(x_0)}{2} (x-x_0)^2 + \sum_{n=3}^{\infty} \frac{f^{(n)}(x_0)}{n!} (x-x_0)^n \\ &= f(x_0) - \frac{|f''(x_0)|}{2} (x-x_0)^2 + \sum_{n=3}^{\infty} \frac{f^{(n)}(x_0)}{n!} (x-x_0)^n. \end{aligned} \quad (\text{B.1})$$

For a positive number s the exponential function $e^{sf(x)}$ can be expressed using Eq. (B.1) as follows:

$$e^{sf(x)} = e^{sf(x_0)} e^{-\frac{s|f''(x_0)|}{2} (x-x_0)^2} e^{\sum_{n=3}^{\infty} \frac{sf^{(n)}(x_0)}{n!} (x-x_0)^n}. \quad (\text{B.2})$$

Taking the integral of Eq. (B.2) over the whole real numbers results in

$$I = \int_{-\infty}^{+\infty} e^{sf(x)} dx = e^{sf(x_0)} \int_{-\infty}^{+\infty} e^{-\frac{s|f''(x_0)|}{2} (x-x_0)^2} e^{\sum_{n=3}^{\infty} \frac{sf^{(n)}(x_0)}{n!} (x-x_0)^n} dx. \quad (\text{B.3})$$

Applying the change of variable $z = \sqrt{s|f''(x_0)|} (x-x_0)$ to the integral in Eq. (B.3) leads to

$$I = \frac{e^{sf(x_0)}}{\sqrt{s|f''(x_0)|}} \int_{-\infty}^{+\infty} e^{-\frac{z^2}{2}} e^{\sum_{n=3}^{\infty} s^{1-\frac{n}{2}} k_n z^n} dz, \quad (\text{B.4})$$

in which $k_n = \frac{f^{(n)}(x_0)}{\sqrt{|f''(x_0)|^n}}$. The exponential function inside the integral in Eq. (B.4) can be expanded using the Taylor series as

$$e^{\sum_{n=3}^{\infty} s^{1-\frac{n}{2}} k_n z^n} = 1 + \frac{k_3}{s^{1/2}} z^3 + \frac{k_4}{s} z^4 + \frac{k_5}{s^{3/2}} z^5 + \left(\frac{k_3^2}{2s} + \frac{k_6}{s^2} \right) z^6 + \dots \quad (\text{B.5})$$

Appendix B. Laplace's Method

Note that the terms corresponding to $n = 1$ and $n = 2$ in the Taylor expansion of Eq. (B.5) are simply zeros. Substituting Eq. (B.5) in the integral of Eq. (B.4) results in

$$I = \frac{e^{sf(x_0)}}{\sqrt{s|f''(x_0)|}} \int_{-\infty}^{+\infty} \left[1 + \frac{k_3}{s^{1/2}} z^3 + \frac{k_4}{s} z^4 + \frac{k_5}{s^{3/2}} z^5 + \left(\frac{k_3^2}{2s} + \frac{k_6}{s^2} \right) z^6 + \dots \right] e^{-\frac{z^2}{2}} dz, \quad (\text{B.6})$$

The integration in Eq. (B.6) can be performed term-by-term; odd terms lead to zero and only even terms remain so it can be expressed as

$$I = \frac{e^{sf(x_0)}}{\sqrt{s|f''(x_0)|}} \left[\int_{-\infty}^{+\infty} e^{-\frac{z^2}{2}} dz + \frac{1}{s} \int_{-\infty}^{+\infty} \left(k_4 z^4 + \frac{k_3^2}{2} z^6 \right) e^{-\frac{z^2}{2}} dz + \frac{1}{s^2} \dots \right]. \quad (\text{B.7})$$

The first integral in the right-hand side of Eq. (B.7) is a Gaussian integral whose value is $\sqrt{2\pi}$ and so the expression can be written as

$$\begin{aligned} I &= e^{sf(x_0)} \sqrt{\frac{2\pi}{s|f''(x_0)|}} \left[1 + \frac{1}{s\sqrt{2\pi}} \left(\int_{-\infty}^{+\infty} \left(k_4 z^4 + \frac{k_3^2}{2} z^6 \right) e^{-\frac{z^2}{2}} dz + \frac{1}{s} \dots \right) \right] \\ &= e^{sf(x_0)} \sqrt{\frac{2\pi}{s|f''(x_0)|}} (1 + O(s^{-1})), \end{aligned} \quad (\text{B.8})$$

where $O(s^{-1})$ represents the part that decays as fast as $\frac{1}{s}$. Therefore, when s is large enough the following approximate formula for integration is obtained:

$$\int_{-\infty}^{+\infty} e^{sf(x)} dx \approx e^{sf(x_0)} \sqrt{\frac{2\pi}{s|f''(x_0)|}}. \quad (\text{B.9})$$

Eq. (B.9) is called Laplace's method for integration and it is useful in approximating integrals involving exponential-type functions such as hyperbolic functions. The formal statement of Laplace's method that has been proved in the above is given in the following theorem [139].

Theorem: Suppose a twice differentiable real-valued function $f(x)$ with a unique global maximum at x_0 so that $f''(x_0) < 0$. Then,

$$\lim_{s \rightarrow \infty} \frac{\int_{-\infty}^{+\infty} e^{sf(x)} dx}{e^{sf(x_0)} \sqrt{\frac{2\pi}{s|f''(x_0)|}}} = 1. \quad (\text{B.10})$$

The approximation in Eq. (B.9) can be generalized to consider the multiplication of a non-exponential function. In other words, suppose a smooth function $h(x)$ with positive value at x_0 where the maximum of $f(x)$ occurs. Then, Laplace's formula is simply modified to [98]

$$\int_{-\infty}^{+\infty} h(x) e^{sf(x)} dx \approx h(x_0) e^{sf(x_0)} \sqrt{\frac{2\pi}{s|f''(x_0)|}}. \quad (\text{B.11})$$

The approximation in Eq. (B.11) sometimes called the *steepest decent method* [77] or *saddle-point approximation* [140] is used for evaluating the power transferred into the MI spectrum.



Bibliography

- [1] L. Savage, "Sensing trouble: fiber-optics in civil engineering," *OSA Optics & Photonics News*, vol. 24, no. 3, pp. 26–33, 2013.
- [2] R. W. Boyd, *Nonlinear Optics*. Academic Press, 3rd ed., 2008.
- [3] G. P. Agrawal, *Nonlinear Fiber Optics*. Academic Press, 4th ed., 2006.
- [4] L. Thévenaz, *Advanced Fiber Optics: Concepts and Technology*. EPFL Press, 2011.
- [5] J. P. Dakin, D. J. Pratt, G. W. Bibby, and J. N. Ross, "Distributed optical fibre Raman temperature sensor using a semiconductor light source and detector," *Electronics Letters*, vol. 21, no. 13, p. 569, 1985.
- [6] T. Horiguchi and M. Tateda, "BOTDA-nondestructive measurement of single-mode optical fiber attenuation characteristics using Brillouin interaction: theory," *Journal of Lightwave Technology*, vol. 7, no. 8, pp. 1170–1176, 1989.
- [7] J. Juarez, E. Maier, K. N. Choi, and H. Taylor, "Distributed fiber-optic intrusion sensor system," *Journal of Lightwave Technology*, vol. 23, no. 6, pp. 2081–2087, 2005.
- [8] L. Thévenaz, S. F. Mafang, and J. Lin, "Effect of pulse depletion in a Brillouin optical time-domain analysis system.," *Optics Express*, vol. 21, no. 12, pp. 14017–35, 2013.
- [9] D. Alasia, M. González-Herráez, L. Abrardi, S. Martin-Lopez, and L. Thévenaz, "Detri-mental effect of modulation instability on distributed optical fiber sensors using stimu-lated Brillouin scattering," in *Proc. SPIE*, vol. 5855, pp. 587–590, 2005.
- [10] S. F. Mafang and L. Thévenaz, "Impact of Raman scattering and modulation instability on the performances of Brillouin sensors," in *Proc. SPIE*, vol. 7753, p. 77539V, 2011.
- [11] H. F. Martins, S. Martin-Lopez, P. Corredera, P. Salgado, O. Frazão, and M. González-Herráez, "Modulation instability-induced fading in phase-sensitive optical time-domain reflectometry.," *Optics Letters*, vol. 38, no. 6, pp. 872–4, 2013.
- [12] M. N. Alahbabi, Y. T. Cho, T. P. Newson, P. C. Wait, and A. H. Hartog, "Influence of modu-lation instability on distributed optical fiber sensors based on spontaneous Brillouin scattering," *Journal of the Optical Society of America B*, vol. 21, no. 6, p. 1156, 2004.

Bibliography

- [13] A. Hasegawa, "Generation of a train of soliton pulses by induced modulational instability in optical fibers," *Optics Letters*, vol. 9, no. 7, p. 288, 1984.
- [14] J. M. Dudley, J. L. Taylor, and eds., *Supercontinuum Generation in Optical Fibers*. Cambridge University Press, 2010.
- [15] A. Hasegawa and K. Tai, "Effects of modulational instability on coherent transmission systems," *Optics Letters*, vol. 14, no. 10, p. 512, 1989.
- [16] B. Hermansson and D. Yevick, "Modulational instability effects in PSK modulated coherent fiber systems and their reduction by optical loss," *Optics Communications*, vol. 52, no. 2, pp. 99–102, 1984.
- [17] K. Tai, A. Tomita, J. L. Jewell, and A. Hasegawa, "Generation of subpicosecond solitonlike optical pulses at 0.3 THz repetition rate by induced modulational instability," *Applied Physics Letters*, vol. 49, no. 5, p. 236, 1986.
- [18] A. Hasegawa and W. Brinkman, "Tunable coherent IR and FIR sources utilizing modulational instability," *IEEE Journal of Quantum Electronics*, vol. 16, no. 7, pp. 694–697, 1980.
- [19] K. Tai, A. Hasegawa, and A. Tomita, "Observation of modulational instability in optical fibers," *Physical Review Letters*, vol. 56, no. 2, pp. 135–138, 1986.
- [20] H. Itoh, G. M. Davis, and S. Sudo, "Continuous-wave-pumped modulational instability in an optical fiber," *Optics Letters*, vol. 14, no. 24, p. 1368, 1989.
- [21] G. Agrawal, "Modulation instability induced by cross-phase modulation," *Physical Review Letters*, vol. 59, no. 8, pp. 880–883, 1987.
- [22] G. Agrawal, P. Baldeck, and R. Alfano, "Modulation instability induced by cross-phase modulation in optical fibers," *Physical Review A*, vol. 39, no. 7, pp. 3406–3413, 1989.
- [23] P. Drummond, T. Kennedy, J. Dudley, R. Leonhardt, and J. Harvey, "Cross-phase modulational instability in high-birefringence fibers," *Optics Communications*, vol. 78, no. 2, pp. 137–142, 1990.
- [24] J. Rothenberg, "Modulational instability for normal dispersion," *Physical Review A*, vol. 42, no. 1, pp. 682–685, 1990.
- [25] G. Cappellini and S. Trillo, "Third-order three-wave mixing in single-mode fibers: exact solutions and spatial instability effects," *Journal of the Optical Society of America B*, vol. 8, no. 4, p. 824, 1991.
- [26] S. Trillo and S. Wabnitz, "Dynamics of the nonlinear modulational instability in optical fibers," *Optics Letters*, vol. 16, no. 13, p. 986, 1991.

-
- [27] J. M. Dudley, G. Genty, F. Dias, B. Kibler, and N. Akhmediev, "Modulation instability, Akhmediev Breathers and continuous wave supercontinuum generation," *Optics Express*, vol. 17, no. 24, p. 21497, 2009.
- [28] M. Erkintalo, G. Genty, B. Wetzell, and J. M. Dudley, "Akhmediev breather evolution in optical fiber for realistic initial conditions," *Physics Letters A*, vol. 375, no. 19, pp. 2029–2034, 2011.
- [29] K. Hammani, B. Wetzell, B. Kibler, J. Fatome, C. Finot, G. Millot, N. Akhmediev, and J. M. Dudley, "Spectral dynamics of modulation instability described using Akhmediev breather theory," *Optics Letters*, vol. 36, no. 11, p. 2140, 2011.
- [30] J. M. Dudley, F. Dias, M. Erkintalo, and G. Genty, "Instabilities, breathers and rogue waves in optics," *Nature Photonics*, vol. 8, no. 10, pp. 755–764, 2014.
- [31] B. Kibler, J. Fatome, C. Finot, G. Millot, F. Dias, G. Genty, N. Akhmediev, and J. M. Dudley, "The Peregrine soliton in nonlinear fibre optics," *Nature Physics*, vol. 6, no. 10, pp. 790–795, 2010.
- [32] D. Anderson and M. Lisak, "Modulational instability of coherent optical-fiber transmission signals," *Optics Letters*, vol. 9, no. 10, p. 468, 1984.
- [33] Y. Chen and A. W. Snyder, "Four-photon parametric mixing in optical fibers: effect of pump depletion," *Optics Letters*, vol. 14, no. 1, p. 87, 1989.
- [34] A. E. Ismagulov, S. A. Babin, E. V. Podivilov, M. P. Fedoruk, I. S. Shelemba, and O. V. Shtyrina, "Modulation instability of narrow-band nanosecond pulses propagating in anomalous-dispersion fibre," *Quantum Electronics*, vol. 39, no. 8, pp. 765–769, 2009.
- [35] S. A. Babin, A. E. Ismagulov, E. V. Podivilov, M. P. Fedoruk, I. S. Shelemba, and O. V. Shtyrina, "Modulation instability at propagation of narrowband 100-ns pulses in optical fibers of various types," *Laser Physics*, vol. 20, no. 2, pp. 334–340, 2010.
- [36] S. M. Kobtsev and S. V. Smirnov, "Influence of noise amplification on generation of regular short pulse trains in optical fibre pumped by intensity-modulated CW radiation," *Optics Express*, vol. 16, no. 10, p. 7428, 2008.
- [37] J. C. Maxwell, "A dynamical theory of the electromagnetic field," *Philosophical Transactions of the Royal Society of London*, vol. 155, pp. 459–512, 1865.
- [38] J. C. Maxwell, *A Treatise on Electricity and Magnetism*. Clarendon Press, 1873.
- [39] J. D. Jackson, *Classical Electrodynamics*. John Wiley & Sons, Inc., 3rd ed., 1999.
- [40] H. Hertz, *Electric Waves: Being Researches on the Propagation of Electric Action with Finite Velocity Through Space*. Dover Publications, 1893.

Bibliography

- [41] B. E. A. Saleh and M. C. Teich, *Fundamentals of Photonics*. John Wiley & Sons, Inc., 2nd ed., 2007.
- [42] J. D. Joannopoulos, S. G. Johnson, J. N. Winn, and R. D. Meade, *Photonic Crystals: Molding the Flow of Light*. Princeton University Press, 2nd ed., 2008.
- [43] S. A. Maier, *Plasmonics: Fundamentals and Applications*. Springer Science, 2007.
- [44] V. Lucarini, K.-E. Peiponen, J. J. Saarinen, and E. M. Vartiainen, *Kramers–Kronig Relations in Optical Materials Research*. Springer, 2005.
- [45] A. M. Weiner, *Ultrafast Optics*. John Wiley & Sons, Inc., 2009.
- [46] K. Oh and U.-C. Paek, *Silica Optical Fiber Technology for Devices and Components*. John Wiley & Sons, Inc., 2012.
- [47] K. Okamoto, *Fundamentals of Optical Waveguides*. Academic Press, 2nd ed., 2006.
- [48] D. Marcuse, “Gaussian approximation of the fundamental modes of graded-index fibers,” *Journal of the Optical Society of America*, vol. 68, no. 1, pp. 103–109, 1978.
- [49] C. Menyuk, “Application of multiple-length-scale methods to the study of optical fiber transmission,” *Journal of Engineering Mathematics*, vol. 875, pp. 113–136, 1999.
- [50] Y. Kodama, “Optical solitons in a monomode fiber,” *Journal of Statistical Physics*, vol. 39, no. 5-6, pp. 597–614, 1985.
- [51] C. Sulem and P.-L. Sulem, *Nonlinear Schrödinger Equation: Self-Focusing and Wave Collapse*. Springer, 1999.
- [52] M. J. Ablowitz, B. Prinari, and A. D. Trubatch, *Discrete and Continuous Nonlinear Schrödinger Systems*. Cambridge University Press, 2004.
- [53] Y. S. Kivshar and G. Agrawal, *Optical Solitons: From Fibers to Photonic Crystals*. Academic Press, 2003.
- [54] N. N. Akhmediev and A. Ankiewicz, *Solitons: Nonlinear Pulses and Beams*. Chapman & Hall, 1997.
- [55] R. N. Bracewell, *The Fourier Transform and Its Applications*. McGraw-Hill, 3rd ed., 2000.
- [56] V. E. Zakharov, *What Is Integrability?* Springer, 2012.
- [57] R. Stolen and C. Lin, “Self-phase-modulation in silica optical fibers,” *Physical Review A*, vol. 17, no. 4, pp. 1448–1453, 1978.
- [58] R. A. Fisher and W. K. Bischel, “Numerical studies of the interplay between self-phase modulation and dispersion for intense plane-wave laser pulses,” *Journal of Applied Physics*, vol. 46, no. 11, p. 4921, 1975.

- [59] H. Stone, "An algorithm for the machine calculation of complex Fourier series," *IEEE Transactions on Electronic Computers*, vol. 15, no. 4, pp. 680–681, 1966.
- [60] J. A. Fleck, J. R. Morris, and M. D. Feit, "Time-dependent propagation of high energy laser beams through the atmosphere," *Applied Physics*, vol. 10, no. 2, pp. 129–160, 1976.
- [61] O. Sinkin, R. Holzlohner, J. Zweck, and C. Menyuk, "Optimization of the split-step Fourier method in modeling optical-fiber communications systems," *Journal of Lightwave Technology*, vol. 21, no. 1, pp. 61–68, 2003.
- [62] F. Shimizu, "Frequency broadening in liquids by a short light pulse," *Physical Review Letters*, vol. 19, no. 19, pp. 1097–1100, 1967.
- [63] E. P. Ippen, "Self-phase modulation of picosecond pulses in optical fibers," *Applied Physics Letters*, vol. 24, no. 4, p. 190, 1974.
- [64] C. Vinegoni, M. Wegmuller, and N. Gisin, "Determination of nonlinear coefficient n_2/A_{eff} using self-aligned interferometer and Faraday mirror," *Electronics Letters*, vol. 36, no. 10, p. 886, 2000.
- [65] S. Zaslowski, M. Alem, and L. Thévenaz, "Measuring the nonlinear coefficient of optical fibers using self-phase modulation," *GFO Internal Reports*, 2014.
- [66] C. Vinegoni, M. Wegmuller, and N. Gisin, "Measurements of the nonlinear coefficient of standard, SMF, DSF, and DCF fibers using a self-aligned interferometer and a Faraday mirror," *IEEE Photonics Technology Letters*, vol. 13, no. 12, pp. 1337–1339, 2001.
- [67] P. K. A. Wai and C. R. Menyuk, "Polarization mode dispersion, decorrelation, and diffusion in optical fibers with randomly varying birefringence," *Journal of Lightwave Technology*, vol. 14, no. 2, pp. 148–157, 1996.
- [68] S. V. Chernikov and J. R. Taylor, "Measurement of normalization factor of n_2 for random polarization in optical fibers," *Optics Letters*, vol. 21, no. 19, p. 1559, 1996.
- [69] M. E. Marhic, *Fiber Optical Parametric Amplifiers, Oscillators and Related Devices*. Cambridge University Press, 2008.
- [70] G. P. Agrawal, *Fiber-Optic Communications Systems*. John Wiley & Sons, Inc., 3rd ed., 2002.
- [71] R. Stolen and J. Bjorkholm, "Parametric amplification and frequency conversion in optical fibers," *IEEE Journal of Quantum Electronics*, vol. 18, no. 7, pp. 1062–1072, 1982.
- [72] C. J. McKinstrie, M. Yu, M. G. Raymer, and S. Radic, "Quantum noise properties of parametric processes," *Optics Express*, vol. 13, no. 13, p. 4986, 2005.
- [73] M. Karlsson, "Modulational instability in lossy optical fibers," *JOSA B*, vol. 12, no. 11, pp. 2071–2077, 1995.

Bibliography

- [74] A. Carena, V. Curri, R. Guadino, P. Poggiolini, and S. Benedetto, "New analytical results on fiber parametric gain and its effects on ASE noise," *IEEE Photonics Technology Letters*, vol. 9, no. 4, pp. 535–537, 1997.
- [75] M. Marhic, V. Curri, and L. Kazovsky, "Bessel function solution for the gain of one-pump fiber optical parametric amplifier," in *Proceedings of IEEE Conference on Nonlinear Optics*, no. 3, pp. 221–223, IEEE, 1998.
- [76] S. Roy, M. Santagiustina, A. Willinger, G. Eisenstein, S. Combrie, and A. De Rossi, "Parametric gain and conversion efficiency in nanophotonic waveguides with dispersive propagation coefficients and loss," *Journal of Lightwave Technology*, vol. 32, no. 6, pp. 1177–1182, 2014.
- [77] G. B. Arfken, H. J. Weber, and F. E. Harris, *Mathematical Methods for Physics: A Comprehensive Guide*. Academic Press, 7th ed., 2013.
- [78] M. Erkintalo, K. Hammani, B. Kibler, C. Finot, N. Akhmediev, J. M. Dudley, and G. Genty, "Higher-order modulation instability in nonlinear fiber optics," *Physical Review Letters*, vol. 107, no. 25, p. 253901, 2011.
- [79] R. G. Smith, "Optical power handling capacity of low loss optical fibers as determined by stimulated Raman and Brillouin scattering.," *Applied Optics*, vol. 11, no. 11, pp. 2489–94, 1972.
- [80] V. I. Kovalev and R. G. Harrison, "Threshold for stimulated Brillouin scattering in optical fiber," *Optics Express*, vol. 15, no. 26, p. 17625, 2007.
- [81] A. Kobaykov, M. Sauer, and D. Chowdhury, "Stimulated Brillouin scattering in optical fibers," *Advances in Optics and Photonics*, vol. 2, no. 1, p. 1, 2009.
- [82] J. AuYeung and A. Yariv, "Spontaneous and stimulated Raman scattering in long low loss fibers," *IEEE Journal of Quantum Electronics*, vol. 14, no. 5, pp. 347–352, 1978.
- [83] S. Le Floch and P. Cambon, "Theoretical evaluation of the Brillouin threshold and the steady-state Brillouin equations in standard single-mode optical fibers," *Journal of the Optical Society of America A*, vol. 20, no. 6, p. 1132, 2003.
- [84] E. Fermi, J. Pasta, and S. Ulam, "Studies of nonlinear problems," *Collected Papers of Enrico Fermi*, vol. 2, pp. 977–988, 1965.
- [85] G. Van Simaey, P. Emplit, and M. Haelterman, "Experimental demonstration of the Fermi-Pasta-Ulam recurrence in a modulationally unstable optical wave," *Physical Review Letters*, vol. 87, p. 033902, jun 2001.
- [86] G. Van Simaey, P. Emplit, and M. Haelterman, "Experimental study of the reversible behavior of modulational instability in optical fibers," *Journal of the Optical Society of America B*, vol. 19, no. 3, p. 477, 2002.

-
- [87] A. Mussot, A. Kudlinski, M. Droques, P. Szriftgiser, and N. Akhmediev, "Fermi-Pasta-Ulam recurrence in nonlinear fiber optics: the role of reversible and irreversible losses," *Physical Review X*, vol. 4, no. 1, p. 011054, 2014.
- [88] K. Tai, A. Tomita, J. L. Jewell, and A. Hasegawa, "Generation of subpicosecond solitonlike optical pulses at 0.3 THz repetition rate by induced modulational instability," *Applied Physics Letters*, vol. 49, no. 5, p. 236, 1986.
- [89] C. J. McKinstrie, M. Yu, M. G. Raymer, and S. Radic, "Quantum noise properties of parametric processes," *Optics Express*, vol. 13, no. 13, p. 4986, 2005.
- [90] A. Carena, V. Curri, R. Guadino, P. Poggiolini, and S. Benedetto, "New analytical results on fiber parametric gain and its effects on ASE noise," *IEEE Photonics Technology Letters*, vol. 9, no. 4, pp. 535–537, 1997.
- [91] E. Brainis, D. Amans, and S. Massar, "Scalar and vector modulation instabilities induced by vacuum fluctuations in fibers: Numerical study," *Physical Review A*, vol. 71, no. 2, p. 023808, 2005.
- [92] S. M. Kobtsev and S. V. Smirnov, "Influence of noise amplification on generation of regular short pulse trains in optical fibre pumped by intensity-modulated CW radiation," *Optics Express*, vol. 16, no. 10, p. 7428, 2008.
- [93] K. Rolle, M. Alem, and L. Thévenaz, "Experimental results on threshold power for modulation instability," *GFO Internal Reports*, 2012.
- [94] W. Chen, Z. Meng, H. J. Zhou, and H. Luo, "Spontaneous and induced modulation instability in the presence of broadband spectra caused by the amplified spontaneous emission," *Laser Physics*, vol. 22, no. 8, pp. 1305–1309, 2012.
- [95] M. A. Soto, M. Alem, W. Chen, and L. Thévenaz, "Mitigating modulation instability in Brillouin distributed fibre sensors," in *Proc. SPIE*, vol. 8794, p. 87943J, 2013.
- [96] A. Kobaykov, M. Mehendale, M. Vasilyev, S. Tsuda, and A. F. Evans, "Stimulated Brillouin scattering in Raman-pumped fibers: a theoretical approach," *Journal of Lightwave Technology*, vol. 20, no. 8, pp. 1635–1643, 2002.
- [97] A. Kobaykov, S. A. Darmanyany, and D. Q. Chowdhury, "Exact analytical treatment of noise initiation of SBS in the presence of loss," *Optics Communications*, vol. 260, no. 1, pp. 46–49, 2006.
- [98] G. J. Gbur, *Mathematical Methods for Optical Physics and Engineering*. Cambridge University Press, 2011.
- [99] M. Alem, M. A. Soto, and L. Thévenaz, "Modelling the depletion length induced by modulation instability in distributed optical fibre sensors," in *Proc. SPIE*, vol. 9157, p. 91575S, 2014.

Bibliography

- [100] M. Alem, M. A. Soto, and L. Thévenaz, “Analytical model and experimental verification of the critical power for modulation instability in optical fibers,” *Optics Express*, vol. 23, no. 23, p. 29514, 2015.
- [101] M. A. Soto and L. Thévenaz, “Modeling and evaluating the performance of Brillouin distributed optical fiber sensors,” *Optics Express*, vol. 21, no. 25, p. 31347, 2013.
- [102] B. Culshaw and A. Kersey, “Fiber-optic sensing: a historical perspective,” *Journal of Lightwave Technology*, vol. 26, no. 9, pp. 1064–1078, 2008.
- [103] K. T. V. Grattan and T. Sun, “Fiber optic sensor technology: an overview,” *Sensors and Actuators A: Physical*, vol. 82, no. 1-3, pp. 40–61, 2000.
- [104] K. Shimizu, T. Horiguchi, Y. Koyamada, and T. Kurashima, “Coherent self-heterodyne Brillouin OTDR for measurement of Brillouin frequency shift distribution in optical fibers,” *Journal of Lightwave Technology*, vol. 12, no. 5, pp. 730–736, 1994.
- [105] T. Parker, M. Farhadiroushan, V. Handerek, and A. Roger, “A fully distributed simultaneous strain and temperature sensor using spontaneous Brillouin backscatter,” *IEEE Photonics Technology Letters*, vol. 9, no. 7, pp. 979–981, 1997.
- [106] T. Horiguchi, K. Shimizu, T. Kurashima, M. Tateda, and Y. Koyamada, “Development of a distributed sensing technique using Brillouin scattering,” *Journal of Lightwave Technology*, vol. 13, no. 7, pp. 1296–1302, 1995.
- [107] Kwang-Yong Song, M. Herraiez, and L. Thévenaz, “Mapping of chromatic-dispersion distribution along optical fibers with 20-m spatial resolution,” *Journal of Lightwave Technology*, vol. 23, no. 12, pp. 4140–4146, 2005.
- [108] A. Vedadi, D. Alasia, E. Lantz, H. Maillotte, L. Thévenaz, M. Gonzalez-Herraiez, and T. Sylvestre, “Brillouin optical time-domain analysis of fiber-optic parametric amplifiers,” *IEEE Photonics Technology Letters*, vol. 19, no. 3, pp. 179–181, 2007.
- [109] F. Alishahi, A. Vedadi, M. A. Shoaie, M. A. Soto, A. Denisov, K. Mehrany, L. Thévenaz, and C.-S. Brès, “Power evolution along phase-sensitive parametric amplifiers: an experimental survey,” *Optics Letters*, vol. 39, no. 21, p. 6114, 2014.
- [110] L. Brillouin, “Diffusion de la lumière et des rayons X par un corps transparent homogène: influence de l’agitation thermique,” *Ann. de Phys.*, vol. 17, pp. 88–122, 1922.
- [111] L. Mandelstam, “Light scattering by inhomogeneous media,” *Zh. Russ. Fiz-Khim. Ova.*, vol. 58, p. 381, 1926.
- [112] R. Chiao, C. Townes, and B. Stoicheff, “Stimulated Brillouin scattering and coherent generation of intense hypersonic waves,” *Physical Review Letters*, vol. 12, no. 21, pp. 592–595, 1964.

- [113] E. P. Ippen and R. H. Stolen, "Stimulated Brillouin scattering in optical fibers," *Applied Physics Letters*, vol. 21, no. 11, p. 539, 1972.
- [114] Y. R. Shen and N. Bloembergen, "Theory of stimulated Brillouin and Raman scattering," *Physical Review*, vol. 137, no. 6A, pp. A1787–A1805, 1965.
- [115] V. Chandrasekharan, "The exact equation for Brillouin shifts," *Journal de Physique*, vol. 26, no. 11, pp. 655–658, 1965.
- [116] M. Niklès, L. Thévenaz, and P. Robert, "Brillouin gain spectrum characterization in single-mode optical fibers," *Journal of Lightwave Technology*, vol. 15, no. 10, pp. 1842–1851, 1997.
- [117] T. J. Hastie and R. J. Tibshirani, *Generalized Additive Models*. Chapman & Hall, 1990.
- [118] C. De Boor, *A Practical Guide to Splines*. Springer, 2001.
- [119] R. Stolen, "Polarization effects in fiber Raman and Brillouin lasers," *IEEE Journal of Quantum Electronics*, vol. 15, no. 10, pp. 1157–1160, 1979.
- [120] T. Horiguchi, N. Shibata, Y. Azuma, and M. Tateda, "Brillouin gain variation due to a polarization-state change of the pump or Stokes fields in standard single-mode fibers," *Optics Letters*, vol. 14, no. 6, p. 329, 1989.
- [121] M. van Deventer and A. Boot, "Polarization properties of stimulated Brillouin scattering in single-mode fibers," *Journal of Lightwave Technology*, vol. 12, no. 4, pp. 585–590, 1994.
- [122] A. Zadok, E. Zilka, A. Eyal, L. Thévenaz, and M. Tur, "Vector analysis of stimulated Brillouin scattering amplification in standard single-mode fibers," *Optics Express*, vol. 16, no. 26, p. 21692, 2008.
- [123] A. Lopez-Gil, A. Dominguez-Lopez, S. Martin-Lopez, and M. Gonzalez-Herraez, "Simple method for the elimination of polarization noise in BOTDA using balanced detection and orthogonal probe sidebands," *Journal of Lightwave Technology*, vol. 33, no. 12, pp. 2605–2610, 2015.
- [124] J. Urricelqui, F. Lopez-Fernandino, M. Sagues, and A. Loayssa, "Polarization diversity scheme for BOTDA sensors based on a double orthogonal pump interaction," *Journal of Lightwave Technology*, vol. 33, no. 12, pp. 2633–2638, 2015.
- [125] J. Urricelqui, M. Alem, M. Sagues, L. Thévenaz, A. Loayssa, and M. A. Soto, "Mitigation of modulation instability in Brillouin distributed fiber sensors by using orthogonal polarization pulses," in *Proc. SPIE*, vol. 9634, p. 963433, 2015.
- [126] M. Alem, M. A. Soto, L. Thévenaz, J. Urricelqui, M. Sagues, and A. Loayssa, "Performance limit of two-pump Brillouin fiber sensors obtained by Manakov modulation instability," in *Spatiotemporal Complexity in Nonlinear Optics (SCNO)*, pp. 1–2, IEEE, 2015.

Bibliography

- [127] G. Foschini and C. Poole, "Statistical theory of polarization dispersion in single mode fibers," *Journal of Lightwave Technology*, vol. 9, no. 11, pp. 1439–1456, 1991.
- [128] P. K. A. Wai and C. R. Menyuk, "Polarization mode dispersion, decorrelation, and diffusion in optical fibers with randomly varying birefringence," *Journal of Lightwave Technology*, vol. 14, no. 2, pp. 148–157, 1996.
- [129] C. D. Poole, "Statistical treatment of polarization dispersion in single-mode fiber," *Optics Letters*, vol. 13, no. 8, p. 687, 1988.
- [130] P. K. A. Wai, C. R. Menyuk, and H. H. Chen, "Stability of solitons in randomly varying birefringent fibers," *Optics Letters*, vol. 16, no. 16, p. 1231, 1991.
- [131] P. K. A. Wai and C. R. Menyuk, "Polarization decorrelation in optical fibers with randomly varying birefringence," *Optics Letters*, vol. 19, no. 19, p. 1517, 1994.
- [132] B. Frisquet, B. Kibler, J. Fatome, P. Morin, F. Baronio, M. Conforti, G. Millot, and S. Wabnitz, "Polarization modulation instability in a Manakov fiber system," *Physical Review A*, vol. 92, no. 5, p. 053854, 2015.
- [133] S. V. Manakov, "On the theory of two-dimensional stationary self-focusing of electromagnetic waves," *Soviet Physics-JETP*, vol. 38, no. 2, pp. 248–253, 1974.
- [134] J. Fatome, I. El-Mansouri, J.-L. Blanchet, S. Pitois, G. Millot, S. Trillo, and S. Wabnitz, "Even harmonic pulse train generation by cross-polarization-modulation seeded instability in optical fibers," *Journal of the Optical Society of America B*, vol. 30, no. 1, p. 99, 2012.
- [135] B. Kibler, B. Frisquet, P. Morin, J. Fatome, F. Baronio, M. Conforti, G. Millot, and S. Wabnitz, "Manakov polarization modulation instability in normal dispersion optical fiber," in *Advanced Photonics*, p. NW2A.2, OSA, 2014.
- [136] B. Kibler, B. Frisquet, P. Morin, J. Fatome, F. Baronio, M. Conforti, G. Millot, and S. Wabnitz, "Observation of Manakov polarization modulation instability in the normal dispersion regime of randomly birefringent telecom optical fiber," in *European Conference on Optical Communication (ECOC)*, pp. 1–3, 2014.
- [137] P. Z. Peebles, *Probability, Random Variables and Random Signal Principles*. McGraw-Hill, 1987.
- [138] A. Papoulis, *Probability, Random Variables and Stochastic Processes*. McGraw-Hill, 3rd ed., 1991.
- [139] "Wikipedia: Laplace's method." https://en.wikipedia.org/wiki/Laplace's_method.
- [140] R. W. Butler, *Saddlepoint Approximations with Applications*. Cambridge University Press, 2007.

Mehdi Alem

CONTACT	Email: mehdi.alem@gmail.com	LinkedIn: https://www.linkedin.com/in/mehdi-alem-1a983755
EDUCATION	École Polytechnique Fédérale de Lausanne , Lausanne, Switzerland	
	Ph.D., Photonics, 2012 - 2016	
	<ul style="list-style-type: none">• Thesis Topic: <i>Impact of Modulation Instability on Distributed Optical Fiber Sensors</i>• Supervisor: Professor Luc Thévenaz	
	Sharif University of Technology , Tehran, Iran	
	M.S., Electrical Engineering, 2004 - 2006	
	<ul style="list-style-type: none">• Thesis Topic: <i>Analysis and Design of Optical Orthogonal Codes Using Matrix Algebra</i>• Supervisor: Professor Jawad A. Salehi	
	Isfahan University of Technology , Isfahan, Iran	
	B.S., Electrical Engineering, 2000 - 2004	
	<ul style="list-style-type: none">• Project Topic: <i>Analysis of Lifting Method in Wavelet Transform and Filter Bank</i>• Advisor: Professor Saeid Sadri	
RESEARCH INTERESTS	Photonics & Nonlinear Optics Fiber optics, modulation instability, stimulated Brillouin scattering, distributed fiber sensors, quantum optics, light-matter interaction, polarization effects optical frequency comb, solitons & breathers,	
	Optical Communications Statistical optical communications, optical multiplexing techniques, all-optical processing, eigenvalue division multiplexing, optical pulse shaping, optical networks, ultrashort pulse propagation	
	Applied Mathematics Numerical analysis of dynamical systems, nonlinear differential equations, split-step Fourier method, Monte Carlo simulation, stochastic analysis, statistical signal processing, information & coding theory	
RESEARCH EXPERIENCE	Group for Fiber Optics, EPFL , Lausanne, Switzerland	
	<i>Doctoral Assistant</i>	March 2012 to May 2016
	<ul style="list-style-type: none">• Experimental and theoretical investigation of scalar and vector modulation instability• Brillouin distributed optical fiber sensors• Optical sinc-shaped Nyquist pulse generation• Designing special optical fibers for tailoring nonlinear effects• Measuring optical fiber nonlinearity using self-phase modulation• Suppression of stimulated Brillouin scattering in optical fibers	
	Optical Networks Research Lab., SUT , Tehran, Iran	
	<i>Research Engineer</i>	September 2004 to September 2010
	<ul style="list-style-type: none">• Free space optical (FSO) communications• Optical code-division multiple-access (OCDMA) techniques• Fiber-to-the-home (FTTH) technology• Algorithms for optical orthogonal code (OOC) generation• Design and implementation of erbium-doped fiber amplifiers (EDFA)	

TRAINING COURSES	Summer Schools <ul style="list-style-type: none">• Spatiotemporal Complexity in Nonlinear Optics, <i>Lake Como School of Advanced Studies</i>, Como, Italy, Aug. 31 – Sept. 4, 2015.• Optical Fibre Sensors from Research to Real World, <i>COST Action OFSESA</i>, Chandolin, Switzerland, Sept. 1 – 3, 2014.• Symposium: Swiss Photonics Research, <i>European MSc in Photonics</i>, EPFL, Lausanne, Switzerland, July 9 – 11, 2013.• Optical Fiber Sensing, <i>COST Action OFSESA</i>, Madeira, Portugal, Sept. 3 – 5, 2012.																	
TEACHING ASSISTANCE	École Polytechnique Fédérale de Lausanne <table><tr><td>Lab in information technologies</td><td>Spring 2013 & Spring 2015</td></tr><tr><td>Introduction to photonics</td><td>Spring 2014</td></tr><tr><td>Nonlinear fiber optics</td><td>Fall 2013 & Spring 2016</td></tr></table> Sharif University of Technology <table><tr><td>Lab in digital communications</td><td>Fall 2007 & Spring 2008</td></tr><tr><td>Optical communications networks</td><td>Spring 2006</td></tr><tr><td>Statistical optical communications</td><td>Fall 2005</td></tr></table> Isfahan University of Technology <table><tr><td>Electromagnetism</td><td>Fall 2002, Spring & Fall 2003</td></tr></table>				Lab in information technologies	Spring 2013 & Spring 2015	Introduction to photonics	Spring 2014	Nonlinear fiber optics	Fall 2013 & Spring 2016	Lab in digital communications	Fall 2007 & Spring 2008	Optical communications networks	Spring 2006	Statistical optical communications	Fall 2005	Electromagnetism	Fall 2002, Spring & Fall 2003
Lab in information technologies	Spring 2013 & Spring 2015																	
Introduction to photonics	Spring 2014																	
Nonlinear fiber optics	Fall 2013 & Spring 2016																	
Lab in digital communications	Fall 2007 & Spring 2008																	
Optical communications networks	Spring 2006																	
Statistical optical communications	Fall 2005																	
Electromagnetism	Fall 2002, Spring & Fall 2003																	
PROFESSIONAL SERVICE	Referee Service <ul style="list-style-type: none">• <i>IEEE Photonics Technology Letter</i>• <i>IEEE Transactions on Communications</i>• <i>Elsevier Optics Communications</i>• <i>Springer Designs, Codes and Cryptography</i>• <i>Elsevier Sensors and Actuators A: Physical</i>																	
IT SKILLS	Numerical Analysis & Programming: <ul style="list-style-type: none">• MATLAB, Mathematica, C/C++, FORTRAN Simulation: <ul style="list-style-type: none">• COMSOL Multiphysics, OptiFiber, Microwave Office, OrCAD, PSpice Desktop Editing: <ul style="list-style-type: none">• L^AT_EX, WinEdt, Microsoft Office, InkScape																	
PROFESSIONAL MEMBERSHIP	Optical Society of America (OSA), student member, 2012–present																	
LANGUAGES	Persian: native	English: fluent	French: intermediate	German: novice														
HOBBIES	Playing Tar (Iranian traditional music instrument), watching movies, hiking, cycling, singing, reading																	
REFERENCES	References are available on demand.																	
	List of Publications																	
PATENT	[1] T. Schneider, C.-S. Brès, L. Thévenaz, M. A. Soto, M. Alem , M. A. Shoaie, and A. Vedadi “System and method for producing optical sinc-shaped pulses,” US 2015/0323781 A1, Nov. 2015.																	

REFEREED
JOURNAL
PUBLICATIONS

- [1] **M. Alem**, M. A. Soto, and L. Thévenaz, “Analytical model and experimental verification of the critical power for modulation instability in optical fibers,” *Optics Express* 23(23), Nov. 2015.
- [2] M. A. Soto, **M. Alem**, M. A. Shoaie, A. Vedadi, C.-S. Brès, L. Thévenaz, and T. Schneider, “Optical sinc-shaped Nyquist pulses of exceptional quality,” *Nature Communications* 4, Dec. 2013.
- [3] **M. Alem** and J. A. Salehi, “Spectral classification and multiplicative partitioning of constant-weight sequences based on circulant matrix representation of optical orthogonal codes,” *IEEE Transactions on Information Theory* 56(9), Sept. 2010.

CONFERENCE
PUBLICATIONS

- [1] J. Urricelquia, **M. Alem**, M. Saguesa, L. Thévenaz, A. Loayssaa, and M. A. Soto, “Mitigation of modulation instability in Brillouin distributed fiber sensors by using orthogonal polarization pulses,” *24th International Conference on Optical Fiber Sensors (OFS)*, SPIE, Oct. 2015.
- [2] **M. Alem**, J. Urricelquia, M. A. Soto, M. Saguesa, L. Thévenaz, and A. Loayssaa, “Performance limit of two-pump Brillouin fiber sensors obtained by Manakov modulation instability,” *Spatiotemporal Complexity in Nonlinear Optics (SCNO)*, IEEE, Sept. 2015.
- [3] **M. Alem**, M. A. Soto, and L. Thévenaz, “Random telegraph signal vs random binary sequence for suppressing the stimulated Brillouin backscattering,” *International OSA Networks of Students (IONS)*, OSA, June 2015.
- [4] C.-S. Brès, M. A. Soto, **M. Alem**, M. A. Shoaie, A. Vedadi, T. Schneider, and L. Thévenaz, “Towards highest spectral efficiency: Optical sinc-shaped Nyquist pulses generation from rectangular frequency comb,” *16th International Conference on Transparent Optical Networks (ICTON)*, IEEE, July 2014.
- [5] **M. Alem**, M. A. Soto, and L. Thévenaz, “Modelling the depletion length induced by modulation instability in distributed optical fibre sensors,” *23rd International Conference on Optical Fiber Sensors (OFS)*, SPIE, June 2014.
- [6] M. A. Soto, **M. Alem**, M. A. Shoaie, A. Vedadi, C.-S. Brès, T. Schneider, L. Thévenaz, “Optical sinc-shaped Nyquist pulses with very low roll-off generated from a rectangular frequency comb,” *Asia Communications and Photonics Conference (ACP)*, Postdeadline, OSA, Nov. 2013.
- [7] M. A. Soto, **M. Alem**, M. A. Shoaie, A. Vedadi, C.-S. Brès, T. Schneider, L. Thévenaz, “Highly tunable method to generate sinc-shaped Nyquist pulses from a rectangular frequency comb,” *Signal Processing in Photonic Communications*, OSA, July 2013.
- [8] M. A. Soto, **M. Alem**, M. A. Shoaie, A. Vedadi, C.-S. Brès, L. Thévenaz, and T. Schneider, “Generation of Nyquist sinc pulses using intensity modulators,” *CLEO: Science and Innovations*, OSA, June 2013.
- [9] M. A. Soto, **M. Alem**, W. Chen, and L. Thévenaz, “Mitigating modulation instability in Brillouin distributed fibre sensors,” *5th European Workshop on Optical Fibre Sensors (EWOFS)*, SPIE, May 2013.
- [10] T. Schneider, M. A. Soto, **M. Alem**, M. A. Shoaie, A. Vedadi, C.-S. Brès, and L. Thévenaz, “Optical Nyquist-pulse generation with a power difference to the ideal sinc-shape sequence of < 1%,” *ITG Symposium on Photonic Networks*, IEEE, May 2013.
- [11] **M. Alem**, L. Sepahi, M. Jazayerifar, and K. Kalbasi, “Optimum power allocation in parallel Poisson optical channel,” *10th International Conference on Telecommunications (ConTEL)*, IEEE, June 2009.